

# **Detectors and Physics at a Future Linear Collider**

Boruo Xu  
of King's College

A dissertation submitted to the University of Cambridge  
for the degree of Doctor of Philosophy



## Abstract

An electron-positron linear collider is an option for future large particle accelerator projects. Such a collider would focus on precision tests of the higgs boson properties. This thesis describes several studies related to the optimisation of high granular calorimeters. Three main areas were covered.

The performance of photon reconstruction is improved. Photon reconstruction algorithms were developed within PandoraPFA, a world-leading pattern-recognition software for particle flow calorimetry. A sophisticated pattern recognition algorithm was implemented, which uses the topological properties of electromagnetic showers to identify photon candidates and separate them from nearby particles. It performs clustering of the energy deposits in the detector, followed by topological characterisation of the clusters, with the results being considered by a multivariate likelihood analysis. This algorithm leads to a significant improvement in the reconstruction of both single photons and multiple photons in high energy jets.

Reconstruction and classification of tau lepton decay modes were studied. Tau decay products, such as photons, were reconstructed as separate entities. Utilising high granular calorimeters, the resolution of energy and invariant mass of the tau decay products is improved. A hypothesis test was performed for expected decay final states. A multivariate analysis was trained to classify decay final states with a data-driven machine learning method. The performance of tau decay classification is used for the electromagnetic calorimeter optimisation at the ILC or CLIC.

Sensitivity of higgs couplings at the CLIC was studied, using simulated double Higgs boson production. Algorithms were developed to

identify isolated high energy leptons, and results were fed into a multivariate analysis. The study was done for two CLIC energy scenarios. This sensitivity study of triple and quartic Higgs self-couplings is a part of scientific cases for the CLIC. This work provides further motivation for high granular particle flow calorimetry for a future electron-positron linear collider.

## Declaration

This dissertation is the result of my own work, except where explicit reference is made to the work of others, and has not been submitted for another qualification to this or any other university. This dissertation does not exceed the word limit for the respective Degree Committee.

Boruo Xu



## Acknowledgements

There are many people that I would like to thank for their help in my pursuit of a PhD degree. First of all, I would like express my most sincere gratitude to my parents, for their financial support and moral support. They have been supporting me for all this many years. Especially, when the PhD study became an intense and stressful exercise, they were able to put up with me and not abandon me. During a few months when I was really worried about not able to finish the PhD program and facing unemployment, they talked me through and gave me much consoling when I needed.

The next person I would like to thank is my supervisor, Mark Thomson. I was lucky to follow him to embark an incredible journey on an exciting project. I have received much useful guidance from him on numerous occasions. On one occasion, which influenced me greatly, was in the very early stage of my PhD study. I managed to make improvements to some algorithms. However, a study suggested that my improved algorithms were not as good as a rival algorithm by a certain metric. Feeling defeated and eager to prove myself, I wanted to repeat the studies just to prove that my algorithms are better. Mark suggested that it is more important to have a project to understand physics, rather than competing for the best performance defined by some arbitrary metrics, which taught me the importance of having the right priority in work, rather than engaging in meaningless competition, however tempting it may be.

I would also like to thank John Marshall for his constant support over the last four years. A large part of the improvement in coding skills is because of the help from John. There was a couple of months, where I had written my working algorithms in ugly codes, and had to rewrite my codes to meet PandoraPFA code standard. This refactorisation exercise indeed taught me a lot about the C++ coding concepts, as well as good coding habits. It was also him who introduced me to the wonderful world of git, which I hated in the beginning. Nevertheless, I was fortunate to have John as my second supervisor and coding mentor.

I was also extremely fortunate to have Steven Green as my colleague and my cherished friend. Other than the lovely, occasionally frustrating, four years that we spent in the same office, I was privileged to spend two years with Steve sampling the fine ale from local pubs on a regular basis. After the infamous “gin” incident, which was a great night, we continued to share our love of ale and pork scratchings in a much more civilised fashion. I was also honoured to be the usher on Steve’s wedding. The wedding was great. And we should have more boardgame nights.

Before moving on to external collaborators, I would also like to thank Joris de Vries for providing entertainments in the office, for embarking on numerous pub trips together, and for suffering together in the “ceiling” incident. I would also like to thank Jack Anthony and Andy Smith for enduring me in the same office, and the rest of the Cambridge HEP group for their support.

I would like to thank Philipp Roloff for his teaching on various techniques in a physics analysis; Rosa Simoniello for collaborating on the double Higgs production analysis. The analysis would take much longer to finish without their help. I would also like to thank André Sailer and Marko Petric for their support with the CLIC grid computing system. At this time of this thesis is written, I should probably still be the top user on the grid system, in terms of the cpu time, much thanks to their help. I also have to thank André for introducing me to Café de l’aviation. It was the best steak that I had in Europe. My gratitude also goes to Lucie Linssen, who was very kind to fund several of my trips to CERN. It was an enjoyable experience to work in CERN and it would be impossible without Lucie’s support. I would also like to thank the rest of CLICdp group in CERN for the friendly and the useful collaboration during my PhD.

My friends in Cambridge, whom I probably see on daily basis, deserve my a lot of my appreciation. It is them who made my PhD study in Cambridge lively and fun. I am again very luck not only to gain a PhD degree after another four years in Cambridge, but also to gain a group of good friends.

Apart from all the people that I have thanked above, there are a few extra people who proof-read my thesis: David Arvidsson, Sophie Morrison, and Laure-Anne Vincent. Thank you for the constructive suggestionss on my thesis.

Because of all the people that I have thanked, and those who I forget to thank, I was privileged to be able to spend four years to research on a topic that is truly interesting.

# Contents

<b>1. Introduction</b>	<b>1</b>
<b>2. Theoretical overview</b>	<b>5</b>
2.1. Overview of the Standard Model . . . . .	5
2.2. Quantum electrodynamics . . . . .	6
2.3. Quantum chromodynamics . . . . .	8
2.4. The electroweak interaction . . . . .	9
2.4.1. Spontaneous symmetry breaking . . . . .	10
2.5. Higgs Mechanism . . . . .	12
2.6. Higgs boson . . . . .	15
2.7. Yukawa couplings . . . . .	16
2.8. Beyond the Standard Model Higgs Models . . . . .	17
2.9. Tau pair polarisation correlations as a signature of Higgs boson . . . . .	20
<b>3. Detectors for Future Electron-Positron Linear Colliders</b>	<b>25</b>
3.1. International Linear Collider . . . . .	25
3.2. Compact Linear Colliders . . . . .	27
3.3. Physics at future linear colliders . . . . .	28
3.4. Detector requirements . . . . .	29
3.5. Particle Flow Calorimetry . . . . .	29
3.6. International Large Detector . . . . .	31
3.7. ILD sub-detectors . . . . .	32
3.7.1. Vertex Detector . . . . .	33
3.7.2. Tracking Detectors . . . . .	35
3.7.3. Electromagnetic Calorimeter . . . . .	36
3.7.4. Hadronic Calorimeter . . . . .	37
3.7.5. Solenoid, Yoke and Muon system . . . . .	38
3.7.6. Very Forward Calorimeters . . . . .	38

3.8.	Detector optimisation . . . . .	40
3.8.1.	Vertex detector optimisation . . . . .	40
3.8.2.	Electromagnetic calorimeter optimisation . . . . .	41
3.8.3.	Hadronic calorimeter optimisation . . . . .	41
3.9.	CLIC_ILD . . . . .	42
<b>4.</b>	<b>Simulation, reconstruction, and analysis software for Future Electron-positron Linear Colliders</b>	<b>45</b>
4.1.	Monte Carlo event generation . . . . .	46
4.2.	Event Simulation . . . . .	46
4.3.	Event Reconstruction . . . . .	46
4.4.	PandoraPFA event reconstruction . . . . .	47
4.4.1.	Track selection . . . . .	47
4.4.2.	Calorimeter selection . . . . .	48
4.4.3.	Particle Identification . . . . .	48
4.4.4.	Clustering . . . . .	49
4.4.5.	Topological cluster association . . . . .	50
4.4.6.	Track-cluster association . . . . .	51
4.4.7.	Re-clustering . . . . .	51
4.4.8.	Fragment removal . . . . .	52
4.4.9.	Particle Flow Object Creation . . . . .	53
4.5.	The CLIC specific simulation and reconstruction issue . . . . .	53
4.5.1.	Luminosity spectrum . . . . .	53
4.5.2.	Beam induced backgrounds . . . . .	54
4.5.3.	CLIC simulated particle masses . . . . .	55
4.7.	Analysis software . . . . .	57
4.7.1.	Monte Carlo truth linker . . . . .	57
4.7.2.	Jet algorithms . . . . .	57
4.7.3.	Longitudinally-invariant $k_t$ algorithm . . . . .	58
4.7.4.	Durham algorithm . . . . .	59
4.7.5.	Jet algorithm for the CLIC . . . . .	59
4.7.6.	The $y$ parameter . . . . .	59
4.8.	Multivariate Analysis . . . . .	60
4.8.1.	Optimisation and overfitting . . . . .	61
4.8.2.	Choice of models . . . . .	61
4.8.3.	Rectangular Cut model . . . . .	63

4.8.4. Projective Likelihood model . . . . .	63
4.8.5. Decision Tree model . . . . .	64
4.8.6. To improve decision tree . . . . .	66
4.8.7. Boosted Decision Tree model . . . . .	66
4.8.8. Optimisation of Boosted Decision Tree . . . . .	68
4.8.9. Multiple classes . . . . .	69
<b>5. Photon Reconstruction in PandoraPFA</b>	<b>71</b>
5.1. Electromagnetic shower . . . . .	72
5.2. Overview of photon reconstruction in PandoraPFA . . . . .	73
5.3. PHOTON RECONSTRUCTION algorithm . . . . .	74
5.3.1. Form photon clusters . . . . .	74
5.3.2. Find photon candidates . . . . .	75
5.3.3. Photon ID test . . . . .	76
5.3.4. Photon Fragment removal . . . . .	77
5.4. Two-dimensional peak-finding algorithm . . . . .	77
5.4.1. Initialise the two-dimensional histogram . . . . .	77
5.4.2. Project calorimeter hits to histogram . . . . .	79
5.4.3. Local peak identifying . . . . .	79
5.4.4. Associate non-peak bins to peaks . . . . .	79
5.4.5. Peak filtering . . . . .	80
5.4.6. Candidate close to track projection . . . . .	80
5.4.7. Inclusive mode . . . . .	81
5.5. Likelihood classifier for photon ID . . . . .	83
5.5.1. Variable used in the likelihood classifier . . . . .	83
5.5.2. Projective Likelihood classifier . . . . .	84
5.6. Photon fragment removal algorithm in the ECAL . . . . .	86
5.6.1. Transverse shower comparison cuts . . . . .	88
5.6.2. Low energy fragment cuts . . . . .	88
5.6.3. Small fragment cuts . . . . .	89
5.6.4. Small fragment forward region cuts . . . . .	89
5.6.5. Relative low energy fragment cuts . . . . .	89
5.6.6. Photon fragment recovery algorithm after the PHOTON RECON- STRUCTURE algorithm . . . . .	89
5.7. Photon fragment recovery algorithm in the HCAL . . . . .	92
5.7.1. Distance comparison cuts . . . . .	93

5.7.2. Projection comparison cuts . . . . .	93
5.7.3. Shower width comparison cuts . . . . .	93
5.7.4. Cone comparison cuts . . . . .	93
5.7.5. Energy comparison cuts . . . . .	94
5.8. Photon splitting algorithm . . . . .	94
5.9. Characterise the performance . . . . .	96
5.10. Compare with no photon reconstruction . . . . .	96
5.11. Compare with photon reconstruction in PandoraPFA version 1 . . . . .	99
5.12. Understand photon reconstruction improvement . . . . .	103
5.13. Current photon reconstruction performance . . . . .	103
<b>6. Tau Lepton Decay Modes Classification</b> . . . . .	<b>109</b>
6.1. Overview of the analysis . . . . .	110
6.2. Samples for the analysis . . . . .	111
6.2.1. Tau lepton decay modes . . . . .	111
6.3. Simulation and reconstruction . . . . .	111
6.4. Event pre-selection . . . . .	113
6.5. Variables used in the MVA . . . . .	114
6.5.1. PFOs number variables . . . . .	115
6.5.2. Invariant mass variables . . . . .	115
6.5.3. Energy variables . . . . .	115
6.5.4. Calorimetric information variables . . . . .	116
6.5.5. $\rho(\pi^-\pi^0)$ and $a_1(\pi^-\pi^0\pi^0)$ resonances reconstruction variables . . . . .	116
6.5.6. Separate $e^-$ from $\pi^-$ . . . . .	117
6.6. Multivariate Analysis . . . . .	119
6.7. Tau decay mode classification efficiency . . . . .	119
6.8. Electromagnetic calorimeter optimisation . . . . .	121
6.8.1. Tau hadronic decay correct classification efficiency . . . . .	123
6.9. Tau pair polarisation correlations as a signature of Higgs boson . . . . .	125
6.9.1. Event pre-selection . . . . .	126
6.9.2. Find tau decay products . . . . .	126
6.9.2.1. Direct tau searching . . . . .	127
6.9.2.2. Jet clustering . . . . .	127
6.9.2.3. Select tau candidates . . . . .	128
6.9.3. Boost tau decay products to Z decay rest frame . . . . .	129
6.9.4. Variables used in the MVA . . . . .	129

6.9.5. Multivariate analysis . . . . .	130
6.9.6. Result . . . . .	130
<b>7. Double Higgs Boson Production Analysis</b>	<b>133</b>
7.1. Analysis Strategy Overview . . . . .	134
7.2. Monte Carlo sample generation . . . . .	135
7.3. Lepton identification . . . . .	136
7.3.1. Electron and muon identification . . . . .	138
7.3.1.1. ISOLATEDLEPTONFINDER . . . . .	138
7.3.1.2. ISOLATEDLEPTONIDENTIFIER . . . . .	138
7.3.2. Tau lepton identification . . . . .	139
7.3.2.1. TAU <sub>FINDER</sub> . . . . .	141
7.3.2.2. ISOLATEDTAU <sub>IDENTIFIER</sub> . . . . .	142
7.3.3. Very forward electron identification . . . . .	144
7.3.4. Lepton identification performance . . . . .	145
7.4. Jet reconstruction . . . . .	147
7.4.1. Jet reconstruction optimisation . . . . .	148
7.5. Jet flavour tagging . . . . .	153
7.5.1. Mutually exclusive cuts for $\text{HH} \rightarrow b\bar{b}W^+W^-$ and $\text{HH} \rightarrow b\bar{b}b\bar{b}$ . . . . .	155
7.6. Jet pairing . . . . .	156
7.7. Pre-selection . . . . .	157
7.8. MVA variables . . . . .	159
7.8.1. Invariant mass variables . . . . .	164
7.8.2. Energy and momentum variables . . . . .	164
7.8.3. Lab-frame angle variables . . . . .	165
7.8.4. Boosted-frame angle variables . . . . .	165
7.8.5. Event shape variables . . . . .	166
7.8.6. b and c tag variables . . . . .	166
7.8.7. PFOs number variables . . . . .	167
7.8.8. Cuts to aid the MVA . . . . .	167
7.9. Multivariate analysis . . . . .	169
7.10. Signal selection results . . . . .	169
7.11. $\sqrt{s} = 3 \text{ TeV}$ analysis . . . . .	170
7.12. Semi-leptonic decay at $\sqrt{s} = 3 \text{ TeV}$ analysis . . . . .	177
7.13. Result interpretation . . . . .	178
7.14. Combined results . . . . .	181

7.15. Simultaneous couplings extraction . . . . .	181
<b>8. Summary</b>	<b>189</b>
<b>A. Double Higgs Boson Production Analysis</b>	<b>191</b>
A.1. Hadronic decay at $\sqrt{s} = 3 \text{ TeV}$ analysis . . . . .	191
<b>Bibliography</b>	<b>197</b>
<b>List of Figures</b>	<b>203</b>
<b>List of Tables</b>	<b>211</b>

*‘A Higgs-Boson walks into a church,  
the priest says  
“We don’t allow Higgs-Bosons in here.”  
The Higgs-Boson says  
“But without me, how can you have mass?”’*

— Reddit



# Chapter 1.

## Introduction

*'The journey of a thousand miles begins with a single step.'*

— Lao Zi, 604 BC - 531 BC

Future electron-positron linear colliders are capable of making precise measurements of the Higgs sector, as well as the top quark sector [1, 2]. At a high centre-of-mass energy, the collider could search for new physics, such as supersymmetry particles, and measure rare events, such as double Higgs production events. These measurements would be difficult for the current proton-proton collider, limited by the underlying QCD interaction. Therefore, it is important to optimise the design of the future particle detector for the linear colliders to improve the event reconstruction and to perform physics simulation studies to demonstrate the superiority of the linear collider.

Since twenty years ago, the high energy physics community has been considering a next-generation electron-positron collider after the Large Hadron Collider (LHC). Measurements from the LHC helped to establish a Standard Model of particle physics. Yet there are issues that Standard Model could not explain. For example, the origin of the masses of neutrinos and the particles account for cosmic dark matter are questions that need to be addressed. Precision measurements from a next-generation electron-positron collider will hopefully provide answers to some of these questions.

Precision measurements will help us to understand Standard Model (SM) better. In the autumn of 2012, experiments in LHC discovered a particle consistent with being the SM Higgs boson [3, 4]. However, is it known that there are limitations to the capability of the hadron colliders to measure properties of colour-singlet scalar particles. The

determination of the Higgs properties, whether it is a Standard Model Higgs, depends on the precise measurement on cross section of Higgs decay. At an electron-positron collider, it will be possible to measure many elementary particles to a high precision [5], providing a probe to physics beyond standard model.

Since the discovery of a particle consistent with the Standard Model Higgs boson at the LHC in 2012 [3, 4], the natural step for high energy physicists is to understand the Higgs. Yet limited by the underlying QCD interaction from proton-anti-proton collision, one has great difficulties in measuring the properties of the Higgs precisely. However, next generation electron-positron linear colliders could make precise measurements in the Higgs sector, as well as the top quark sector [1, 2].

The thesis begins with overview of relevant theories on particle physics in chapter 2. Firstly a brief review of the current best particle theory, Standard Model of Particle Physics, is provided, including a short overview of the quantum electrodynamics, quantum chromodynamics, and the electroweak interaction. The focus of the Standard Model discussion is on the Higgs mechanism and the Higgs boson in Standard Model. The discussion then moves on to theories beyond the Standard Model, with an example of a general parametrisation of the Higgs theory. The last part of the chapter is dedicated to the discussion on identifying a Higgs boson from vector bosons using tau pair decay channel.

In chapter 3, the detector models used in the thesis are described in details. A general overview of two future electron-positron linear colliders, the International Linear Collider (ILC) and the Compact Linear Collider (CLIC), is provided. After a short discussion on the physics program for these future colliders, the impact of physics and other requirements on the detector design is discussed. Afterwards, the International Large Detector, one detector option for the International Linear Collider, is discussed in details, followed by overviews on each sub-detector in the International Large Detector. The chapter finishes with a discussion on the modified International Large Detector detector concept for the Compact Linear Collider, where the modifications of the detector are highlighted.

In the next chapter, chapter 4, the software for event simulation and event reconstruction is discussed, followed by a discussion on the analysis software. The event reconstruction of future linear colliders share common software framework. Hence, the shared software for simulation and reconstruction is discussed first, with an emphasis on the PandoraPFA, a world-leading pattern-recognition software for particle flow calor-

metry. Some CLIC specific issues are highlighted afterwards. Analysis software, including jet algorithms, is presented. Lastly, the multivariate analysis is discussed in details, where different fitting models, optimisation, and overfitting are discussed.

Chapter 5 describes several PandoraPFA algorithms regarding photon reconstruction. One algorithm performs the initial photon forming and photon ID test. Three algorithms are developed for the photon fragment removals. And one algorithm is developed to split the accidentally merged photons. The core of identifying the photon is a two-dimensional peaking finding algorithm. Having discussed the algorithms, performances of these algorithms are provided. Comparison with event reconstruction without photon reconstruction is also provided.

In chapter 6, a classification of the tau lepton decay modes is presented. The analysis contains the sample selection, pre-selection cuts, and the use of the multivariate classifier for the classification. The performance of the tau decay mode classification will be given, followed by an electromagnetic calorimeter optimisation study using the tau decay mode classification. Lastly, the tau decay mode classification is further used in a proof-of-principle analysis to demonstrate the ability to use the tau pair polarisation correlation as a signature for Higgs boson.

In chapter 7, a full CLIC\_ILD detector simulation study has been performed for the double Higgs production channel,  $e^+e^- \rightarrow HH\nu_e\bar{\nu}_e$ , via  $W^+W^-$  fusion. Event generation and simulation will be discussed first. An overview of the analysis, including lepton finding and jet reconstruction, is presented, followed by an optimised multivariate analysis to distinguish signal from background processes. The optimised event selection is used to derive an estimate of the uncertainty on the cross section of double Higgs production at the CLIC. The event selection is further exploited to provide an estimate of the uncertainty on the measurements of trilinear Higgs self coupling and quartic coupling at the CLIC.



# Chapter 2.

## Theoretical overview

*'I believe it is impossible to be sure of anything.'*

— Han Fei Zi, 280 BC - 233 BC

This chapter provides a review of the Standard Model of Particle Physics, with an emphasis on the Higgs mechanism and the Higgs boson. A general parametrisation of the Higgs theory is discussed, which supplies the theoretical background for the physics analysis in chapter 7. Lastly a discussion of the usage of the tau pair polarisation correlations as a signature of Higgs boson is presented, which motivates the study in chapter 6.

### 2.1. Overview of the Standard Model

The Standard Model (SM) [6–9] is a quantum field theory concerning the fundamental particles and three fundamental interactions of nature: the electromagnetic; the weak; and the strong interactions. The fundamental particles in the SM consist of bosons and fermions. The bosons mediate the fundamental forces between particles: the photon is the force carrier of the electromagnetic force;  $W^+$ ,  $W^-$ , and Z bosons are the force carriers of the weak force; and the gluon, g, is the force carrier of the strong force. The properties of the force-exchange bosons and Higgs boson are listed in table 2.1.

The other fundamental particles are spin- $\frac{1}{2}$  fermions. For each fermion in the SM, there is an anti-fermion with the same mass and spin, but opposite charge. These

Force	Boson	Mass	Spin	Charge / $e$
Electromagnetic	photon	0	1	0
	$W^+$	80.385(15) GeV	1	1
	$W^-$	80.385(15) GeV	1	-1
Weak	Z	91.1876(21) GeV	1	0
Strong	gluon	0	1	0
-	Higgs	125.1(3) GeV	0	0

**Table 2.1:** Masses, spins, and charges of fundamental bosons in the SM. Values are taken from [6].

fermions have three generations. Each generation of fermions has the same interaction property, but different masses. Experimental evidences of three generations include the measurements of the Z boson decay-width, which strongly suggested three generations of neutrinos [10].

These fermions came in two distinct categories: leptons and quarks. The neutral leptons (the neutrinos) only experience the weak forces. The charged leptons ( $e^\pm, \mu^\pm, \tau^\pm$ ) experience the weak forces and the electromagnetic forces. Quarks experience all three fundamental forces described by the SM. Properties of these fermions are listed in table 2.2.

Many SM predictions have been experimentally verified. Some recent highlights include the discovery of the top quark in 1995 [11], the tau neutrino in 2000 [12], and the Higgs boson in 2012 [3, 4]. However, there are observations which are not explained by the SM. One issue is that the SM does not incorporate the gravitational force. Another issue is that the SM does not natively allow neutrino masses and mixings. The SM also does not explain the existence of the dark matter. There are many theories beyond the Standard Model (BSM) trying to provide an explanation for these issues. One example is the generalisation of the Higgs theory to allow non-SM coupling strengths [13, 14].

## 2.2. Quantum electrodynamics

QED is a quantum gauge field theory explaining electromagnetic interactions. Quantum field theory (QFT) is the theoretical framework for constructing quantum mechanical

Type	Generation	Fermion	Mass	Charge / $e$
Lepton	1	$e^-$	$0.548579909070(16) \text{ MeV}$	-1
		$\nu_e$	-	0
	2	$\mu^-$	$105.6583745(24) \text{ MeV}$	-1
		$\nu_\mu$	-	0
	3	$\tau^-$	$1776.86(12) \text{ MeV}$	-1
		$\nu_\tau$	-	0
Quark	1	u	$2.2_{-0.4}^{+0.6} \text{ MeV}$	$+\frac{2}{3}$
		d	$4.7_{-0.4}^{+0.5} \text{ MeV}$	$-\frac{1}{2}$
	2	c	$1270 \pm 30 \text{ MeV}$	$+\frac{2}{3}$
		s	$98_{-4}^{+8} \text{ MeV}$	$-\frac{1}{3}$
	3	t	$173210 \pm 510 \pm 710 \text{ MeV}$	$+\frac{2}{3}$
		b	$4180_{-30}^{+40} \text{ MeV}$	$-\frac{1}{3}$

**Table 2.2:** Masses and charges of the fundamental fermions in the SM. All fermions are spin- $\frac{1}{2}$  particles. For each fermion in the SM, there is an anti-fermion with the same mass and spin, but opposite charge. Neutrinos are known to have non-zero mass from the observation of neutrino flavour oscillations. The upper bound on the neutrino mass is 2 eV. For the top quark mass, the statistical uncertainties is listed first, followed by systematic uncertainties. Values are taken from [6].

models of fundamental particles. Particles are treated as excited states of the underlying physical field in the QFT. A gauge theory is a type of field theory in which the Lagrangian is invariant under a continuous group of local transformations. Gauge invariance or gauge symmetry refers to when a field is transformed, but the Lagrangian is not.

QED is an abelian gauge theory with the U(1) symmetry group. The gauge field, which mediates the interaction between the charged spin- $\frac{1}{2}$  fields, is the electromagnetic field, denoted  $A^\mu$ . The QED Lagrangian [15] for a spin- $\frac{1}{2}$  field interacting with the electromagnetic field is given by:

$$\mathcal{L}_{QED} = \bar{\psi} (i\gamma^\mu D_\mu - m) \psi - \frac{1}{4} F_{\mu\nu} F^{\mu\nu}, \quad (2.1)$$

where  $\psi$  is the spin- $\frac{1}{2}$  Dirac field satisfying the Dirac equation, given by the Lagrangian density:

$$\mathcal{L} = \bar{\psi} (i\gamma^\mu D_\mu - m) \psi, \quad (2.2)$$

where the  $\gamma^\mu$  are the Dirac gamma matrices with  $\mu \in \{0, 1, 2, 3\}$ ;  $\bar{\psi}$  is defined as  $\psi^\dagger \gamma^0$ ;  $F_{\mu\nu} = \partial_\mu A_\nu - \partial_\nu A_\mu$  is the electromagnetic field tensor;  $e$  is the coupling constant, which is equal to the electric charge;  $m$  is the mass of the electron; and the gauge covariant derivative is given by:

$$D_\mu \equiv \partial_\mu + ieA_\mu, \quad (2.3)$$

where  $A_\mu$  is the covariant four-vector potential of the electromagnetic field generated by the electron itself.

## 2.3. Quantum chromodynamics

Quantum chromodynamics (QCD) is the quantum field theory of strong interactions. QCD theory is invariant under local non-Abelian SU(3) transformations. There are eight gauge bosons, the gluons, corresponding to the eight ( $8 = 3^2 - 1$ ) generators of the SU(3) symmetry group. Gluons carry colour charges. There are three types of colour charge, sometimes labelled as red, green, and blue. Anti-particles carry anticolour. Quarks are associated with a single colour. Gluons are made up of a colour and an anticolour (or

superposition of colour–anticolour pair). The QCD Lagrangian is given by:

$$\mathcal{L}_{QCD} = \sum_{f \in u, d, s, c, b, t} \bar{\psi}_i \left( \left( i\gamma^\mu \partial_\mu - g_s \gamma^\mu G_\mu^a \frac{\lambda^a}{2} \right)_{ij} - m_f \delta_{ij} \right) \psi_j - \frac{1}{4} G_{\mu\nu}^a G^{a\mu\nu}, \quad (2.4)$$

where  $\psi$  represents a quark with a colour charge, indicated by  $i$  or  $j$ ;  $m$  controls the mass of the quark;  $g_s$  is the strong coupling constant;  $a$  is the colour charge;  $\lambda^a$  represents one of the eight Gell-Mann matrices; and  $G_{\mu\nu}^a$  represents the gauge invariant gluon field strength tensor, given by:

$$G_{\mu\nu}^a = \partial_\mu \gamma_\nu^a - \partial_\nu \gamma_\mu^a - g_s f_{abc} G_\mu^b G_\nu^c, \quad (2.5)$$

where  $G_\mu^b$  is the gluon field with colour charge  $b$ .

## 2.4. The electroweak interaction

The electroweak interaction can be thought as an extension to QED to incorporate the weak force, the force describing nuclear radioactive decay. The unification of the electromagnetic and the weak force is accomplished under an  $SU(2)_L \times U(1)$  gauge symmetry group. The corresponding gauge bosons are the three  $W$  bosons ( $W^1$ ,  $W^2$ , and  $W^3$ ) from  $SU(2)_L$  gauge symmetry, and the  $B$  boson from  $U(1)$  gauge symmetry. All gauge bosons are initially massless. Fermion mass terms are forbidden under  $SU(2)_L$  gauge symmetry.

The electroweak Lagrangian can be written as

$$\mathcal{L}_{Electroweak} = \mathcal{L}_{Boson} + \mathcal{L}_{Fermion} + \mathcal{L}_{Higgs} + \mathcal{L}_{Yukawa}. \quad (2.6)$$

First consider  $\mathcal{L}_{Boson}$ , given by:

$$\mathcal{L}_{Boson} = -\frac{1}{4} W_{\mu\nu}^i W^{i\mu\nu} - \frac{1}{4} B_{\mu\nu} B^{\mu\nu}, \quad (2.7)$$

$$W_{\mu\nu}^i = \partial_\nu W_\mu^i - \partial_\mu W_\nu^i - g \varepsilon^{ijk} W_\mu^j W_\nu^k, \quad (2.8)$$

$$B_{\mu\nu} = \partial_\nu B_\mu - \partial_\mu B_\nu, \quad (2.9)$$

where the  $B$  field is invariant under U(1) transformations; the  $W$  field is invariant under non-Abelian SU(2) transformations; and the indices,  $i$ ,  $j$ , and  $k$ , indicate three  $W$  fields.

The term  $\mathcal{L}_{Fermion}$  describes the massless fermion fields coupling to the fermions, and the propagation of the fermion fields. The left-handed ( $\psi_L$ ) and the right-handed fermions ( $\psi_R$ ) are treated differently. The right-handed fermions are singlets. The left-handed fermions are in doublets with the corresponding fermion of the same generation. The term  $\mathcal{L}_{Fermion}$  is given by:

$$\mathcal{L}_{Fermion} = \sum_{\psi \in fermions} \bar{\psi}_L \gamma^\mu D_\mu^L \psi_L + \bar{\psi}_R \gamma^\mu D_\mu^R \psi_R, \quad (2.10)$$

where covariant derivatives  $D_\mu^L$  and  $D_\mu^R$  are defined as

$$D_\mu^L = \partial_\mu + ig \frac{\tau_i}{2} W_\mu^i + ig' Y_\psi B_\mu, \quad (2.11)$$

$$D_\mu^R = \partial_\mu + ig' Y_\psi B_\mu. \quad (2.12)$$

The structure of this Lagrangian allows  $W$  and  $B$  fields to couple with left-handed fermions, but only allows the  $B$  field to couple with right-handed fermions. The  $\tau_i$  matrices are the generators of SU(2) and  $Y_\psi$  is the hypercharge associated with the fermion field  $\psi$ . The  $W$  field couples with strength  $g$  to the fermion field. The  $B$  field couples with strength  $g'$  to the particles carrying weak hypercharge  $Y$ .

The term  $\mathcal{L}_{Higgs}$  describes the Higgs field. After electroweak symmetry breaking of the Higgs field, the mass terms of the gauge bosons are introduced. The term  $\mathcal{L}_{Yukawa}$  produces the mass terms of the quarks and charged leptons. Firstly a general spontaneous symmetry breaking mechanism is provided, followed by a description of the electroweak symmetry breaking.

### 2.4.1. Spontaneous symmetry breaking

Consider a complex scalar field, with the Klein-Gordon Lagrangian:

$$\mathcal{L} = \partial^\mu \psi^* \partial_\mu \psi - m^2 |\psi|^2 = \partial_\mu \psi^* \partial_\mu \psi - V(\psi), \quad (2.13)$$

where  $m$  is the mass term and  $V(\psi)$  is the potential of the field  $\psi$ . This Lagrangian has a global symmetry  $\psi \rightarrow e^{i\phi}\psi$ . The potential can be modified to add an interaction term without breaking the invariance of the global symmetry:

$$V(\psi) = m^2|\psi|^2 + \lambda|\psi|^4, \quad (2.14)$$

where  $\lambda$  controls the interaction strength. This modified potential has a minimum at  $|\psi| = 0$  for  $m^2 > 0$ . However, if  $m^2 < 0$ , the minimum of the potential occurs when:

$$\frac{\partial V(\psi)}{\partial |\psi|} = 2m^2|\psi| + 4\lambda|\psi|^3 = 0, \quad (2.15)$$

leading to a non-negative expectation value for the field:

$$|\psi| = \sqrt{\frac{-m^2}{2\lambda}} \equiv \frac{\nu}{\sqrt{2}}, \quad (2.16)$$

where  $\nu = \sqrt{-m^2/\lambda}$ . The solution that minimises the potential is not unique; it corresponds to a circle of points in the complex  $\psi$  plane. By choosing any one of these points, which are degenerate in energy, the symmetry of  $\psi \rightarrow e^{i\phi}\psi$  is broken. This phenomenon is known as the spontaneous symmetry breaking.

A consequence of spontaneous symmetry breaking is that the perturbation of the field along the degenerate energy direction, which is the circle in complex  $\psi$  plane, have no associated potential energy. This is formalised as Goldstone's theorem [16, 17]. The theorem states that spontaneous symmetry breaking always implies the existence of a massless particle.

To demonstrate Goldstone's theorem, using the Lagrangian in equation 2.13 as an example, after the spontaneous symmetry breaking of the field, the perturbation of the field  $\psi$  near the field minimum point can be written as

$$\psi = \frac{1}{\sqrt{2}}(\nu + \psi_1 + i\psi_2), \quad (2.17)$$

where  $\nu = \sqrt{\frac{-m^2}{\lambda}}$  refers to the minimum point in the potential, and  $\psi_1$  and  $\psi_2$  are real scalar fields. Substituting  $\psi$  in the Lagrangian in equation 2.13 gives:

$$\mathcal{L} = \frac{1}{2}\partial^\mu\psi_1\partial_\mu\psi_1 + \frac{1}{2}\partial^\mu\psi_2\partial_\mu\psi_2 - m^2\psi_1^2 + \dots \quad (2.18)$$

The mass term for the  $\psi_1$  field is  $\sqrt{-m^2}$  whereas there is no mass term for the  $\psi_2$  field, as stated by the Goldstone's theorem.

In the previous example, the Lagrangian in equation 2.13 possesses the global symmetry of  $\psi \rightarrow e^{i\phi}\psi$ . Instead, if there is a local U(1) gauge symmetry of  $\psi \rightarrow e^{i\phi(x)}\psi$ , this implies a corresponding field  $A_\mu$ , which transforms as  $A_\mu \rightarrow A_\mu - \partial_\mu\phi(x)$ . For the gauge invariance, the covariant derivative becomes  $D_\mu = \partial_\mu + ieA_\mu$ . Hence the Lagrangian in equation 2.13 becomes:

$$\mathcal{L} = (D^\mu\psi)^*(D_\mu\psi) - m^2|\psi|^2 - \lambda|\psi|^4. \quad (2.19)$$

When the field is expanded around the minimum of the potential,  $\nu = \sqrt{\frac{-m^2}{\lambda}}$ , with  $m^2 < 0$ , the gauge boson mass term:

$$+ \frac{e^2\nu^2}{2}A^\mu A_\mu, \quad (2.20)$$

is obtained from the  $(D^\mu\psi)^*(D_\mu\psi)$  term in the Lagrangian. Therefore the spontaneous symmetry breaking of a gauge field gives rise to a gauge boson mass.

## 2.5. Higgs Mechanism

The Higgs mechanism is an extension of the example of the spontaneous symmetry breaking introduced in the previous section. It can provide mass terms for bosons and fermions. A complex scalar Higgs field,  $\Phi_H$ , transforms as a doublet of SU(2) with hypercharge  $Y = \frac{1}{2}$ . The Lagrangian is given by:

$$\mathcal{L}_{Higgs} = (D_\mu\Phi_H)^\dagger(D^\mu\Phi_H) - \mu^2\Phi_H^\dagger\Phi_H + \lambda(\Phi_H^\dagger\Phi_H)^2, \quad (2.21)$$

where  $\lambda$  and  $\mu$  are constants. The  $SU(2)_L \times U(1)$  symmetry of the electroweak Lagrangian demands that the covariant derivative of the Higgs field takes the form

$$D_\mu = \left( \partial_\mu + ig\frac{\tau_i}{2}W_\mu^i + ig'\frac{1}{2}B_\mu \right), \quad (2.22)$$

where  $g$  is the coupling constant of the  $SU(2)_L$  gauge symmetry;  $g'$  is the coupling constant of the  $U(1)$  gauge symmetry; and  $\tau_i$  is one of the Pauli matrices. The Higgs

potential is given by:

$$V(H) = \mu^2 \Phi_H^\dagger \Phi_H - \lambda (\Phi_H^\dagger \Phi_H)^2. \quad (2.23)$$

The Higgs potential is minimised when

$$\sqrt{\Phi_H^\dagger \Phi_H} = \frac{\nu}{\sqrt{2}} = \sqrt{\frac{\mu^2}{2\lambda}}. \quad (2.24)$$

By expanding the Higgs field about the minimum point of the potential, the non-zero vacuum expectation value (VEV) can be written as:

$$\langle \Phi_H \rangle = \begin{pmatrix} 0 \\ \frac{\nu}{\sqrt{2}} \end{pmatrix}, \quad (2.25)$$

with a real  $\nu$ . Substituting the Higgs VEV into the  $\mathcal{L}_{boson}$  in equation 2.21, the  $(D_\mu \Phi_H)^\dagger (D^\mu \Phi_H)$  becomes

$$-\frac{1}{8} \begin{pmatrix} 0 \\ \nu \end{pmatrix} \begin{pmatrix} gW_\mu^3 + g'B_\mu & g(W_\mu^1 - iW_\mu^2) \\ g(W_\mu^1 + iW_\mu^2) & -gW_\mu^3 + g'B_\mu \end{pmatrix} \begin{pmatrix} gW_\mu^3 + g'B_\mu & g(W_\mu^1 - iW_\mu^2) \\ g(W_\mu^1 + iW_\mu^2) & -gW_\mu^3 + g'B_\mu \end{pmatrix} \begin{pmatrix} 0 \\ \nu \end{pmatrix}. \quad (2.26)$$

Ignoring the negative sign, the expression simplifies to

$$\frac{\nu^2 g^2}{8} (W_\mu^1 - iW_\mu^2)(W_\mu^1 + iW_\mu^2) + \frac{\nu^2}{8} (gW_\mu^3 - g'B_\mu)^2. \quad (2.27)$$

The physical fields  $W_\mu^+$  and  $W_\mu^-$  can be identified with the first part of the equation 2.27, as

$$W_\mu^+ = \frac{1}{\sqrt{2}} (W_\mu^1 - iW_\mu^2), \quad (2.28)$$

$$W_\mu^- = \frac{1}{\sqrt{2}} (W_\mu^1 + iW_\mu^2). \quad (2.29)$$

The physical fields  $Z_\mu$  and  $A_\mu$  are associated with  $W_\mu^3$  and  $B_\mu$ . Since the Z boson is massive and the photon is massless, the second part of the equation 2.27 should give rise to Z boson mass term only, with no mass term for photon. This can be achieved by

rearranging the second part of the equation 2.27:

$$\frac{\nu^2}{8} (gW_\mu^3 - g'B_\mu)^2 = \frac{\nu^2(g^2 + g'^2)}{8} \left( \frac{g}{\sqrt{g^2 + g'^2}} W_\mu^3 - \frac{g'}{\sqrt{g^2 + g'^2}} B_\mu \right)^2. \quad (2.30)$$

A convenient way to connect  $g$  and  $g'$  is to use the Weinberg mixing angle [18], denoted as  $\theta_W$ . The Weinberg mixing angle is defined as

$$\cos(\theta_W) = \frac{g}{\sqrt{g^2 + g'^2}}, \quad (2.31)$$

$$\sin(\theta_W) = \frac{g'}{\sqrt{g^2 + g'^2}}. \quad (2.32)$$

The equation 2.30 can be rewritten in terms of the Weinberg mixing angle:

$$\frac{\nu^2(g^2 + g'^2)}{8} (\cos(\theta_W) W_\mu^3 - \sin(\theta_W) B_\mu)^2. \quad (2.33)$$

The physical field  $Z_\mu$  can be immediately identified as:

$$Z_\mu = \cos(\theta_W) W_\mu^3 - \sin(\theta_W) B_\mu. \quad (2.34)$$

Consequently, the physical field  $A_\mu$  with associated massless photon can be written as:

$$A_\mu = \sin(\theta_W) W_\mu^3 + \cos(\theta_W) B_\mu. \quad (2.35)$$

The equation 2.27 can be written in terms of the physical fields  $W_\mu^+$ ,  $W_\mu^-$ ,  $Z_\mu$  and  $A_\mu$ :

$$\frac{(g\nu)^2}{4} W_\mu^+ W^{-\mu} + \frac{(g^2 + g'^2)\nu^2}{8} Z_\mu Z^\mu. \quad (2.36)$$

The first term gives mass of the  $W^+$  and  $W^-$  vector bosons. The second term gives mass of the  $Z$  neutral vector boson. There is no mass term for the photon. The spontaneous symmetry breaking of the Higgs field breaks the electroweak  $SU(2)_L \times U(1)$  gauge symmetry to electromagnetism  $U(1)$  gauge symmetry. The masses of the  $W^+$ ,  $W^-$

and Z bosons are given by:

$$m_{W^+} = m_{W^-} = \frac{g\nu}{2}, \quad m_Z = \frac{\nu\sqrt{g^2 + g'^2}}{2} = \frac{m_W}{\cos(\theta_W)}. \quad (2.37)$$

## 2.6. Higgs boson

For the Higgs doublet complex field in the SM, there are four real scalar degrees of freedom. Three degrees of freedom are “eaten” to form the longitudinal polarisations of the  $W_\mu^\pm$  and  $Z_\mu$  fields. The remaining one real scalar degree of freedom forms the Higgs boson. The properties of the Higgs bosons can be shown in the unitary gauge, where three degrees of freedom are manifestly eaten. The Higgs field is given by:

$$H(x) = \frac{1}{\sqrt{2}} \begin{pmatrix} 0 \\ \nu + h(x) \end{pmatrix}, \quad (2.38)$$

where  $h(x)$  is the real scalar field of the Higgs boson and  $\nu$  the Higgs vacuum expectation value. The Higgs boson is not charged under electromagnetism as the field is real. The coupling of the Higgs boson to other fields can be calculated out by replacing  $\nu$  with  $\nu + h(x)$  in equation 2.36:

$$m_W^2 \left( \frac{2h}{\nu} + \frac{h^2}{\nu^2} \right) W_\mu^+ W^{-\mu} + \frac{m_Z^2}{2} \left( \frac{2h}{\nu} + \frac{h^2}{\nu^2} \right) Z_\mu Z^\mu. \quad (2.39)$$

The Higgs boson self-interaction terms are obtained by replacing  $\nu$  with  $\nu + h(x)$  the Higgs field potential in equation ??:

$$\frac{\mu^2}{2} (\nu + h)^2 - \frac{\lambda}{4} (\nu + h)^4 \supset -\lambda\nu^2 h^2 - \lambda\nu h^3 - \frac{\lambda}{4} h^4 \quad (2.40)$$

The quadratic term,  $-\lambda\nu^2 h^2$ , is the Higgs boson mass term,  $m_H = \sqrt{2\lambda}\nu$ . The terms in  $h^3$  and  $h^4$  give trilinear and quadlinear Higgs self-interaction terms.

Once the Higgs boson mass is known,  $\lambda$  can be determined and the Higgs boson decay widths and branching fractions can be calculated. Figure 2.1 shows the Higgs boson partial decay widths and the branching ratios as a function of the Higgs boson mass for different Higgs decay modes.

The Higgs boson mass is measured to be  $125.09 \pm 0.24$  GeV [6]. Because the Higgs boson is lighter than a pair of heavier particles such as  $W^+W^-$  or  $ZZ$ , the process  $H \rightarrow W^+W^-$  and  $H \rightarrow ZZ$  are forbidden kinematically. However, the quantum field theory allows such processes to happen, if one of the decay products is virtual and not on the mass shell. The virtual gauge boson subsequently decays to real on-mass-shell particles.

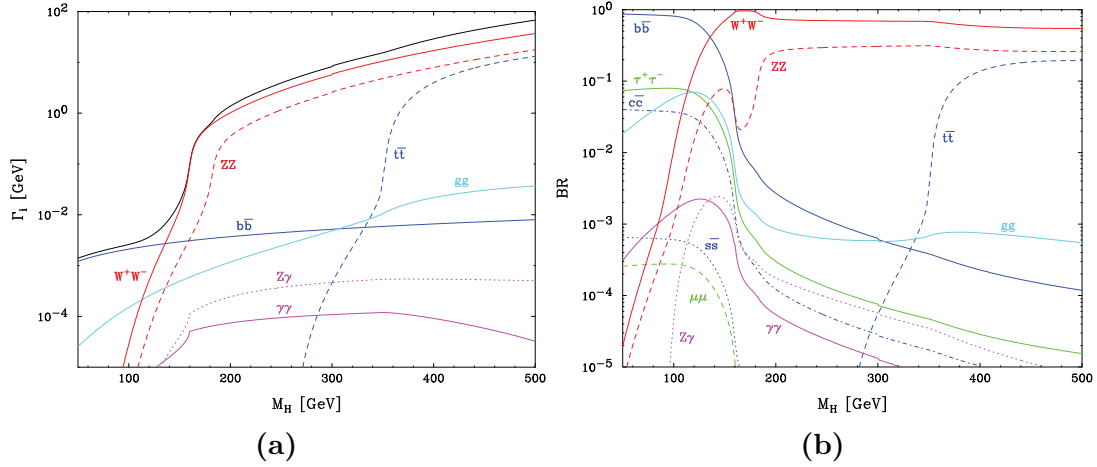


**Figure 2.1:** a) the Higgs boson partial decay widths, and b) Higgs boson branching ratios, plotted as a function of the Higgs boson mass,  $m_H$ . In a), the black curve shows the total decay width. Both figures are taken from [19].

## 2.7. Yukawa couplings

The Yukawa sector of the electroweak Lagrangian provides mass terms for quarks and charged leptons after the spontaneous symmetry breaking of the Higgs field. The corresponding term in the Lagrangian is:

$$\mathcal{L}_{Yukawa} = -\lambda^u \overline{q}_L \Phi_H^c u_R - \lambda^d \overline{q}_L \Phi_H d_R - \lambda^e \overline{l}_L \Phi_H e_R + h.c., \quad (2.41)$$

where  $q_L$  is the left-handed quark doublet field;  $u_R$  is the up-type right-handed quark singlet field;  $d_R$  is the down-type right-handed quark singlet field;  $l_L$  is the left-handed lepton doublet field;  $e_R$  is the right-handed charged lepton singlet field;  $\lambda$  is a constant;  $\Phi_H^c \equiv i\sigma^2 H^*$  is an SU(2) doublet field with hypercharge  $Y = -\frac{1}{2}$ ;  $h.c.$  indicates the Hermitian conjugate terms; and the Lagrangian is summed over all possible quarks and leptons. When the Higgs vacuum expectation value is substituted into  $\mathcal{L}_{Yukawa}$ , the

Yukawa interaction terms give the fermion mass terms:

$$m_u = \frac{\lambda^u \nu}{\sqrt{2}}, \quad m_d = \frac{\lambda^d \nu}{\sqrt{2}}, \quad m_e = \frac{\lambda^e \nu}{\sqrt{2}}. \quad (2.42)$$

## 2.8. Beyond the Standard Model Higgs Models

A number of BSM Higgs theories have been proposed. For example, the light Higgs could be a composite bound state of new strongly-interacting sector at the TeV scale. If the composite Higgs is pseudo Nambu-Goldstone boson from spontaneous global symmetry breaking, the Higgs can be naturally light [13]. In this model, the couplings of the Higgs would deviate from those in the SM for Higgs interactions at the TeV scale.

An important physics process for testing the Higgs theory is the double Higgs production via vector boson fusion at the TeV scale [20–22]. For the composite Higgs scenario, the scattering amplitude for this process increases with energy. It is difficult to measure the double Higgs production at the LHC due to the large SM background rate [21]. However, a multi-TeV linear electron-position collider, such as the Compact Linear Collider, would be able to measure the cross section for this process [23].

The study of double Higgs production via  $W^+W^-$  fusion can probe the Higgs trilinear self coupling,  $g_{HHH}$ , and quartic coupling,  $g_{WWHH}$ . The coupling  $g_{HHH}$  is associated with the terms in  $h^3$  in Higgs potential in equation 2.40. The coupling  $g_{WWHH}$  is associated with the terms in  $h^2$  in Higgs interaction terms with other fields in equation 2.39. Leading-order Feynman diagrams for double Higgs production via  $W^+W^-$  fusion are shown in figure 2.2. The diagram shown in figure 2.2a contains the triple Higgs vertex, which is sensitive to the Higgs trilinear self coupling  $g_{HHH}$ . The diagram in the figure 2.2b is sensitive to the quartic coupling  $g_{WWHH}$ . Figures 2.2c and 2.2d show Feynman diagrams for irreducible background processes containing two  $HW^+W^-$  vertices.

Following the assumption made in [21, 22], the self-interaction of the light scalar Higgs,  $h$ , and its coupling to other SM bosons can be described by a Lagrangian using the notation in [22]. In this description, after the electroweak symmetry breaking , the Lagrangian is given by:

$$\mathcal{L} = \frac{1}{2} (\partial_\mu h)^2 - V(h) + \left( m_W^2 W_\mu^+ W^{-\mu} + \frac{m_Z^2}{2} Z_\mu Z^\mu \right) \left[ 1 + 2a \frac{h}{\nu} + b \frac{h^2}{\nu^2} + \dots \right], \quad (2.43)$$

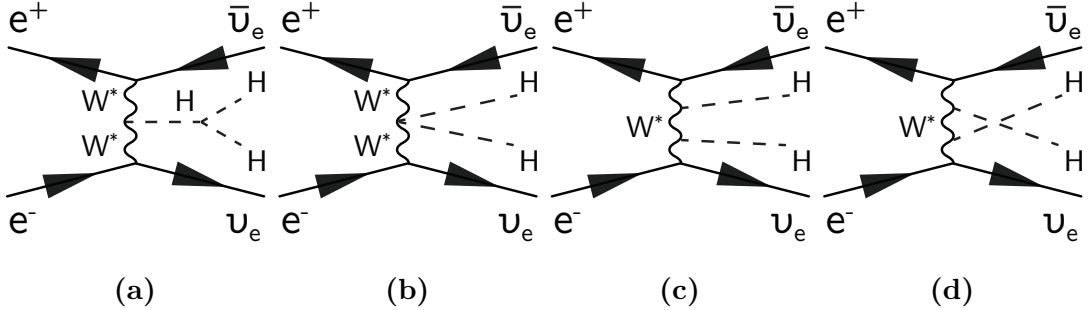


**Figure 2.2:** The main Feynman diagrams for the leading-order  $e^+e^- \rightarrow HH\nu_e\bar{\nu}_e$  processes.

where  $V(h)$  is the  $h$  field potential

$$V(h) = \frac{1}{2}m_h^2 h^2 + d_3 \left( \frac{m_h^2}{2\nu} \right) h^3 + d_4 \left( \frac{m_h^2}{8\nu^2} \right) h^4 + \dots, \quad (2.44)$$

and  $a$ ,  $b$ ,  $d_3$  and  $d_4$  are dimensionless parameters. Higher-order terms in  $h$  are omitted. The parameters  $a$  and  $b$  are proportional to the coupling strengths of the  $VVh$  and  $VVhh$  vertices, where  $V$  represents a vector boson and the parameters  $d_3$  and  $d_4$  are proportional to the trilinear and quadlinear  $h$  self-coupling strength, respectively. Comparing with the  $\mathcal{L}_{Higgs}$  in the SM (see equation 2.39 and equation 2.40), it can be seen that  $a = b = d_3 = d_4 = 1$  in the SM, and all higher order terms vanish. However, BSM Higgs model allow  $a, b, d_3, d_4$  to take different values.

Consider a pair of the longitudinal polarised vector bosons ( $V_L$ ) coupling to two  $h$  fields. The scattering amplitude for  $V_L V_L \rightarrow hh$  can be written as:

$$A = a^2 (A_{SM} + A_1 \delta_b + A_2 \delta_{d_3}), \quad (2.45)$$

where  $A_{SM}$  is the SM amplitude and:

$$\delta_b \equiv 1 - \frac{b}{a^2}, \quad (2.46)$$

$$\delta_{d_3} \equiv 1 - \frac{d_3}{a}. \quad (2.47)$$

The term  $A_1$  grows like the square of energy at a large center-of-mass energy,  $E \gg m_V$ . The terms  $A_{SM}$  and  $A_2$  have no energy dependence. Therefore, the parameter  $\delta_b$  controls the magnitude of the increasing of the scattering amplitude as a function of energy. In

an electron-positron collider, this scattering process can be studied via the double Higgs production  $e^+e^- \rightarrow \nu\bar{\nu}hh$  channel, where the cross section can be written as

$$\sigma = a^4 \sigma_{SM} (1 + A\delta_b + B\delta_{d_3} + C\delta_b\delta_{d_3} + D\delta_b^2 + E\delta_{d_3}^2), \quad (2.48)$$

where  $\sigma_{SM}$  is the SM cross section. Variables that increase with the increasing of the centre-of-mass energies are suitable for studying the cross section dependence on parameters  $\delta_b$  and  $\delta_{d_3}$ . Two examples of such variables are the invariant mass of the two Higgs system,  $m_{hh}$ , and the scalar sum of two Higgs transverse momenta,  $H_T$ . Figure 2.3 shows that the  $m_{hh}$  and  $H_T$  distributions are sensitive to the values of  $\delta_b$  and  $\delta_{d_3}$  [22]. The changes in the  $m_{hh}$  and  $H_T$  distributions can be related to the change in  $\delta_b$  and  $\delta_{d_3}$ . Therefore deviations of  $\delta_b$  and  $\delta_{d_3}$  from those SM values, 1, could be established using the  $m_{hh}$  and  $H_T$  distributions. It should be noted that figure 2.3 shows a generator-level study; detector effect will affect the distributions because of, for example, the loss of the reconstruction efficiency in the barrel/endcap gap region.

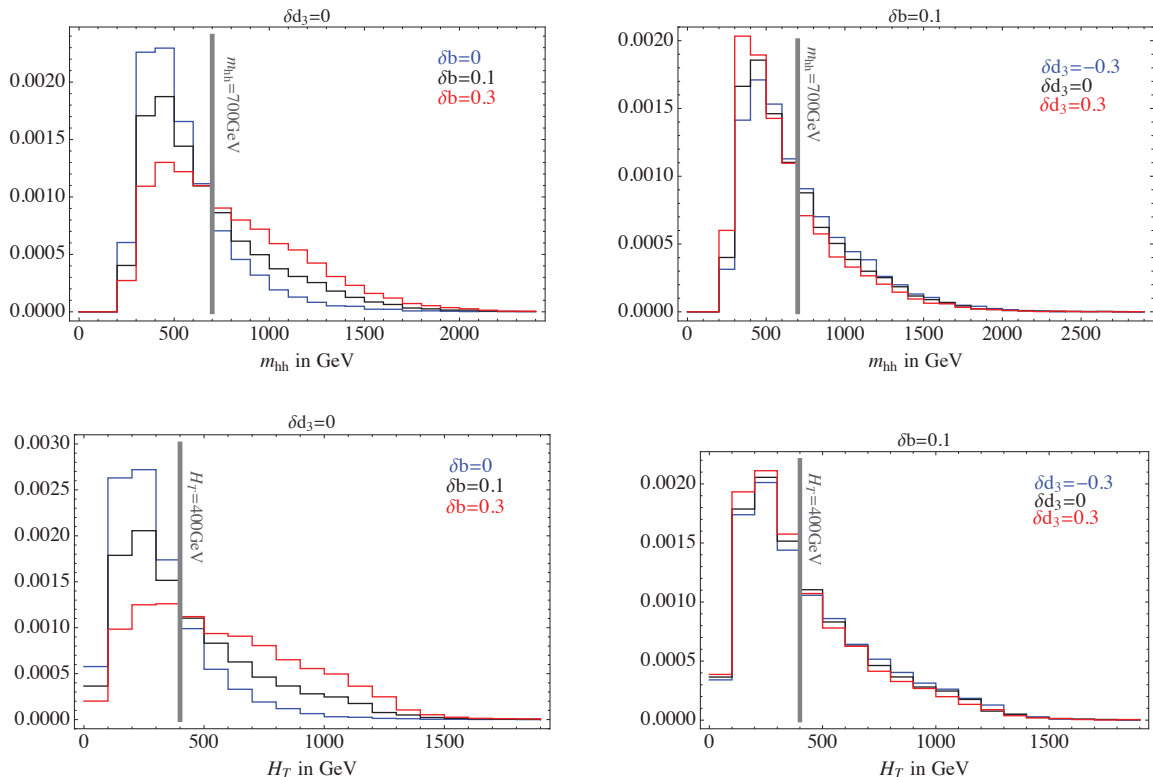


**Figure 2.3:** Normalised differential cross sections  $d\sigma/dm_{hh}$  and  $d\sigma/dH_T$  for  $e^+e^- \rightarrow \nu\bar{\nu}hh$  for CLIC at  $\sqrt{s} = 3$  TeV after applying generator-level identification cuts, for several values of  $\delta_b$  and  $\delta_{d_3}$ . The plot is taken from [22].

In the expression of the cross section of the double Higgs production via  $e^+e^- \rightarrow \nu\bar{\nu}hh$  in equation 2.48, the parameter  $a$ , which is proportional to  $g_{VVH}$ , enters as an overall factor. Figure 2.4 shows the comparison of cross sections as a function of the centre-of-mass energy, for different Higgs production modes. Up to a centre-of-mass energy of  $\sqrt{s} = 3$  TeV, the cross sections of the single Higgs production are two orders of magnitude larger than the cross sections of the double Higgs production. The cross section of  $e^+e^- \rightarrow \nu\bar{\nu}h$  channel is given by:

$$\sigma = \sigma_{SM}(1 + A\Delta a + B\Delta a^2), \quad (2.49)$$

where  $\Delta a \equiv 1 - a$  is the change in  $a$ , and  $A$  and  $B$  are two dimensionless coefficients. The measurement of the parameter  $a$ , using  $e^+e^- \rightarrow \nu\bar{\nu}h$  channel, would be performed before the measurement of the  $\delta_b$  and  $\delta_{d_3}$  for the double Higgs production.

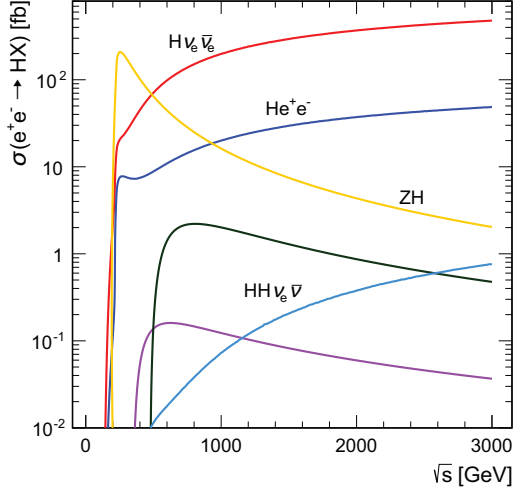


**Figure 2.4:** Cross sections as a function of centre-of-mass energy for Higgs production processes at an electron-positron collider for a Higgs mass of 126 GeV. The cross section values correspond to unpolarised beams and do not include the effect of beamstrahlung. The plot is taken from [24].

Therefore, for the purpose of measuring  $g_{VVH}$  and  $g_{HHH}$  via double Higgs production, it is sufficient to treat the parameter  $a$  as a known constant. Hence only a two-dimensional fit of the parameters  $\delta_b$  and  $\delta_{d_3}$  would be performed to extract values of  $\delta_b$  and  $\delta_{d_3}$ .

## 2.9. Tau pair polarisation correlations as a signature of Higgs boson

The tau lepton is a fundamental particle, with negative electric charge and a spin of  $\frac{1}{2}$ . It has the same fundamental interaction property as an electron, but a much larger mass. Unlike the stable electron, because the tau lepton is massive, it decays via the weak interaction with a mean decay lifetime of  $(290.3 \pm 0.5) \times 10^{-15}$  s. The tau lepton has many decay modes. The decay modes with branching ratio above 2% are listed in table 2.3.

Decay modes	Final states	Branching ratio
$e^- \bar{\nu}_e \nu_\tau$	$e^- \bar{\nu}_e \nu_\tau$	$17.83 \pm 0.04\%$
$\mu^- \bar{\nu}_\mu \nu_\tau$	$\mu^- \bar{\nu}_\mu \nu_\tau$	$17.41 \pm 0.04\%$
$\pi^- \nu_\tau$	$\pi^- \nu_\tau$	$10.83 \pm 0.06\%$
$\rho \nu_\tau$	$\pi^- \pi^0 \nu_\tau$	$25.52 \pm 0.09\%$
$a_1 \nu_\tau$	$\pi^- \pi^0 \pi^0 \nu_\tau$	$9.30 \pm 0.11\%$
$a_1 \nu_\tau$	$\pi^+ \pi^- \pi^- \nu_\tau$	$8.99 \pm 0.06\%$
$\pi^+ \pi^- \pi^- \pi^0 \nu_\tau$	$\pi^+ \pi^- \pi^- \pi^0 \nu_\tau$	$2.70 \pm 0.08\%$

**Table 2.3:** Decay modes, final state particles and branching ratios of the seven major  $\tau^-$  decays, taken from [6].

A scalar Higgs boson with spin-0 can decay to  $\tau_L^+ \tau_L^-$  or  $\tau_R^+ \tau_R^-$ , whereas a vector boson Z with spin-1 can decay to  $\tau_L^+ \tau_R^-$  or  $\tau_R^+ \tau_L^-$ , where L, R denotes the tau lepton helicity. Therefore, by studying the tau pair polarisation correlation from a boson decay, one can determine statistically if the parent boson is a scalar or a vector.

Tau pair polarisation correlations can be studied using various decay modes. Here reference [25] is followed and the  $\tau^- \rightarrow \pi^- \nu_\tau$  decay mode is used as the example. The Higgs and Z boson decay to a tau pair, where both tau leptons subsequently decay via  $\tau^- \rightarrow \pi^- \nu_\tau$ , can be represented as:

$$X \rightarrow \tau_\alpha^+ \tau_\beta^- \rightarrow \pi^+ \pi^- + \nu s, \quad (2.50)$$

where  $X$  is either H or Z, and  $\alpha, \beta$  are the tau lepton helicities, L or R. In the collinear limit where  $m_\tau^2/m_X^2 \ll 1$ , the appropriate kinematic variables are the energy fractions:

$$z = \frac{E_{\pi^-}}{E_{\tau^-}}, \quad (2.51)$$

$$\bar{z} = \frac{E_{\pi^+}}{E_{\tau^+}}. \quad (2.52)$$

For a single tau decay, the differential cross section distribution can be written as:

$$\frac{1}{\Gamma_\tau} \frac{d\Gamma}{dz} = Br(\tau^- \rightarrow \pi^- \nu_\tau) f(\tau_\alpha^- \rightarrow \pi^-; z), \quad (2.53)$$

where  $Br(\tau^- \rightarrow \pi^- \nu_\tau)$  is the branching fraction of  $\tau^- \rightarrow \pi^- \nu_\tau$  decay mode. The form  $f$  can be obtained by working out the matrix element from the Feynman diagram and integrating the square of the matrix element over the phase space [26]:

$$f(\tau_\alpha^- \rightarrow \pi^-; z) = 1 + P_\alpha(2z - 1), \quad (2.54)$$

where  $P_L = -1$  and  $P_R = +1$ . Hence for the tau pair decay, the differential cross section distribution is of the form:

$$\frac{d^2 N(X \rightarrow \tau^+ \tau^- \rightarrow \pi^+ \pi^- + \nu' s)}{dz d\bar{z}} = \left( Br(\tau^- \rightarrow \pi^- \nu_\tau) \right)^2 \sum_{\alpha, \beta} C_{\alpha\beta}^X f(\tau_\alpha^- \rightarrow \pi^-; z) f(\tau_\beta^+ \rightarrow \pi^+; \bar{z}), \quad (2.55)$$

where the only non-zero correlation coefficients  $C_{\alpha\beta}$  for the parity-conserving  $H \rightarrow \tau^+ \tau^-$  are:

$$C_{LL}^H = C_{RR}^H = \frac{1}{2}. \quad (2.56)$$

In contrast, the non-zero correlation coefficients for the  $Z \rightarrow \tau^+ \tau^-$  are:

$$C_{LR}^Z = \frac{1}{2}(1 - P_\tau), \quad C_{RL}^Z = \frac{1}{2}(1 + P_\tau), \quad (2.57)$$

where  $P_\tau$  is the mean non-zero tau polarisation of Z decays. The tau polarisation is not zero because the process  $Z \rightarrow \tau^+ \tau^-$  is not parity-conserving. In the SM:

$$P_\tau = \frac{-2va}{v^2 + a^2}, \quad (2.58)$$

where the parameter  $v = -\frac{1}{2} + \sin^2 \theta_W$  and  $a = -\frac{1}{2}$  are the respective vector and axial-vector  $Z\tau^+\tau^-$  couplings.

Figure 2.5 shows the resulting two-dimensional distributions of  $\bar{z} = \frac{E_{\pi^+}}{E_{\tau^+}}$  versus  $z = \frac{E_{\pi^-}}{E_{\tau^-}}$  for  $Z \rightarrow \tau^+ \tau^-$  and  $H \rightarrow \tau^+ \tau^-$  channels, where both tau leptons decay via  $\tau^- \rightarrow \pi^- \nu_\tau$ . The difference of the tau pair polarisation correlation between Z and H is clear. The energy distribution of the charged pion from  $Z \rightarrow \tau^+ \tau^-$  has the form of  $\bar{z} \sim z$ , whilst the distribution from  $H \rightarrow \tau^+ \tau^-$  has the form of  $\bar{z} \sim (1 - z)$ . Therefore, in  $Z \rightarrow \tau^+ \tau^-$  process, a high-energy  $\pi^\pm$  is likely to be associated with a high-energy  $\pi^\mp$ . In  $H \rightarrow \tau^+ \tau^-$  process, the opposite is favoured. If the tau pair decay from Higgs boson is observed, the decay can be recognised in the  $\tau^- \rightarrow \pi^- \nu_\tau$  mode as a high-energy  $\pi^\pm$  with a low-energy  $\pi^\mp$ . Hence, the tau decay product energy distribution can be a clean signature for  $H \rightarrow \tau^+ \tau^-$ .



**Figure 2.5:** Two-dimensional distribution of  $\bar{z} = E_{\pi^+}/E_{\tau^+}$  plotted against  $z = E_{\pi^-}/E_{\tau^-}$  for a)  $Z \rightarrow \tau^+ \tau^-$ , and b)  $H \rightarrow \tau^+ \tau^-$  channels, where both tau leptons decay via  $\tau^- \rightarrow \pi^- \nu_\tau$ , adapted from reference [26].



# Chapter 3.

## Detectors for Future Electron-Positron Linear Colliders

*'The great man is the one who does not lose his child's heart.'*

— Mencius, 372 BC - 289 BC

Two leading candidates for next generation electron-positron linear colliders are the International Linear Collider (ILC) [1], and the Compact Linear Collider (CLIC) [2]. This chapter provides an overview of the two colliders, followed by the physics programme at these colliders, the detectors requirements, the particle flow calorimetry, and the description of detectors for the ILC and the CLIC.

### 3.1. International Linear Collider

The ILC is a high-luminosity future electron-positron linear particle collider. The machine will be built in two stages. The first stage would have a centre-of-mass energy of 250/350 GeV. The second stage would have a centre-of-mass energy of 500 GeV with a possible upgrade to 1 TeV. A layout of the collider complex is shown in figure 3.1. Two detector concepts are developed for the ILC: the International Large Detector (ILD) [27], and the Silicon Detector (SiD) [28]. Both detectors are shown in figure 3.2.

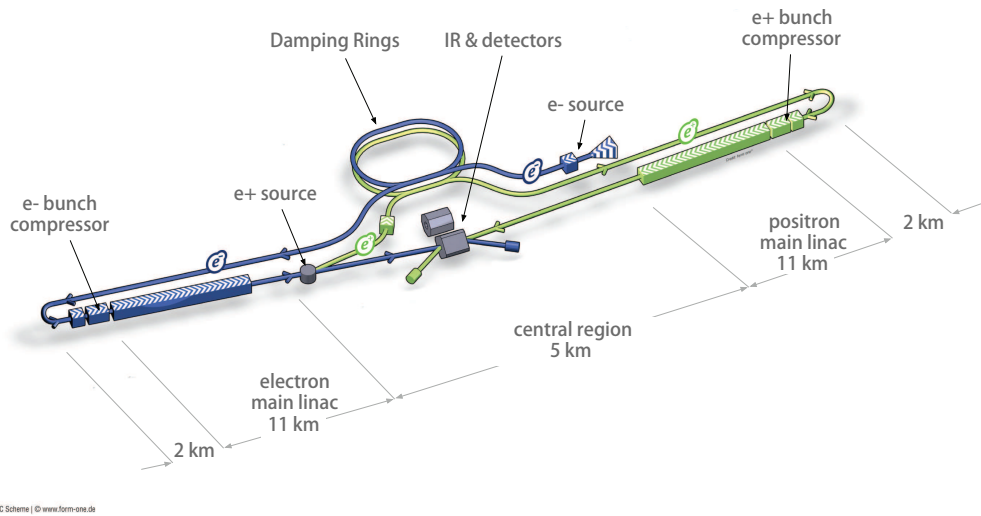


**Figure 3.1:** Schematic layout of the International Linear Collider, indicating all the major subsystems (not to scale), taken from [29].



**Figure 3.2:** a) the International Large Detector, and b) the Silicon Detector. Both detector concepts are developed for the International Linear Collider. Both figures are taken from [29].

### 3.2. Compact Linear Colliders

The CLIC is potential next-generation electron-positron linear particle collider at CERN [2]. The CLIC is designed to be built in three stages: first stage of a centre-of-mass energy of 380 GeV; second stage of a centre-of-mass energy of 1.4 TeV; and final stage of a centre-of-mass energy of 3 TeV. The layout of the CLIC complex at the final stage is shown in figure 3.3.

The ILC and the CLIC share some common features. Both colliders will be the linear colliders as oppose to the circular colliders, like the Large Hadron Collider (LHC). Detectors for both colliders will use the high granularity particle flow calorimetry [2, 29]. One major difference of two colliders is operating energies. Due to a higher centre-of-mass energy at the CLIC, there are significant beam related backgrounds. The  $e^+e^-$  incoherent pair background has a major influence on the design of the inner region of the detector and the forward region. The pile-up of  $3.2 \gamma\gamma \rightarrow \text{hadrons}$  events per bunch is also significant and needs to be removed for physics analyses. Another difference in the ILC and the CLIC is that the timing separation between bunches is much shorter at the CLIC. The CLIC beam contains 312 bunch trains with a train repetition rate of 50 Hz. The bunches are separated by 0.5 ns within each bunch train. The short timing separation between bunches suggests that the detector will integrate over a number of bunch crossings.



**Figure 3.3:** A layout of the Compact Linear Collider at the final stage of a centre-of-mass of energy of 3 TeV, taken from [30].

### 3.3. Physics at future linear colliders

The ILC and the CLIC share some common advantages over the current hadron collider, the LHC. Those advantages include: i) Events in the  $e^+e^-$  collider will be cleaner than those in the hadron collider. In the LHC, many proton-proton collisions per bunch crossing are expected [31], generating hundreds of particles from parton collisions. In the  $e^+e^-$  collider, the main source of background comes from photon-photon collisions [1, 2]. Depending on the operating energy and scheme, there will be a few of these collisions per bunch crossing. Particles produced from these collisions are mainly in the forward direction, which can be identified relatively easily. ii) Electroweak interactions in the  $e^+e^-$  collider will be democratic as the photon couples to all particles in and beyond Standard Model equally [6–9]. The production of pairs of all particles will be at a similar rate. In the LHC, the non-perturbative strong interaction is the main channel for the particle production. Not only a fraction of protons would collide, heavy particles has a lower production rate than light ones, as the parton distributions fall sharply for a composite object like a proton [32]. iii) Calculation in the  $e^+e^-$  collider requires less computational resources than it requires in the LHC. In the LHC, calculation of the cross section depends on quantum chromodynamics and the proton structure function, which have large systematic errors. In the  $e^+e^-$  collider, initial particles,  $e^+$  and  $e^-$ , can be treated as point-like particles, interacting through electroweak forces only. A high theoretical precision level of the electroweak interactions could be reached. iv) The physics in the  $e^+e^-$  collider can be studied in details. Without complicated underlying events, complete events can be reconstructed. Momenta of leptons and quarks can be calculated by kinematic fitting. Polarised beams of electrons and positrons with known initial and final polarisation states aslo could be used to aid the study.

The physics programme for the CLIC and the ILC, which is a driving force behind the detector design, share some common features. At a centre-of-mass energy of 250 GeV, the collider could operate as a Higgs factory, allowing measurements of precision Higgs couplings via channels like  $e^+e^- \rightarrow ZH$ . At a centre-of-mass energy of 350 GeV, the collider can continue to measure Higgs couplings, as well as to measure top quark mass and coupling via channels such as  $e^+e^- \rightarrow t\bar{t}$ . At a centre-of-mass energy of 1 TeV and beyond, the collider would be able to produce rare Higgs decays, allowing measurements of Higgs self-coupling and probing composite Higgs sector, and to search for supersymmetry particles.

### 3.4. Detector requirements

Many physics processes at a future linear collider can be characterised by multi-jet final states, often with charged leptons or missing momentum associated with neutrinos. The reconstruction of the invariant masses of two or more jets is critical for event reconstruction and event selection. At the Large Electron-Positron Collider (LEP), kinematic fitting [33] allowed precise invariant mass reconstruction. At a future collider, reconstruction invariant mass of multiple jets for final states with missing momentum will rely heavily on the intrinsic jet energy resolution of the detector.

One goal of jet energy resolution at a future linear collider is to be able to separate W and Z bosons, by reconstructing the invariant mass via quark-jets using the hadronic decay channel. The idealised reconstructed W and Z boson masses distributions of different assumed jet mass resolutions are shown in figure 3.4. As the invariant mass resolution is comparable to the gauge boson widths, i.e.  $\sigma_m/m \approx \Gamma_W/m_W \approx \Gamma_Z/m_Z$ , a separation of  $2.5\sigma$  in the masses distributions implies a jet energy resolution of 3.5% [34] for a range of jet energies from 50 GeV to 1 TeV.

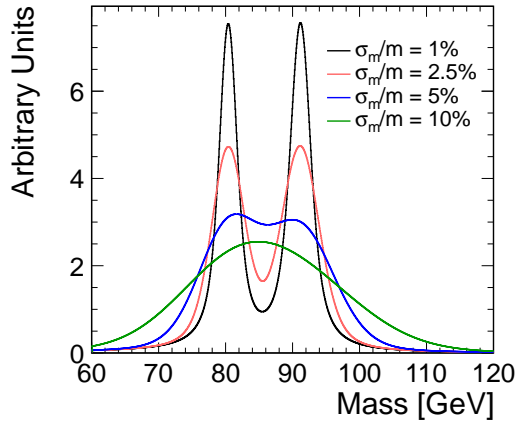


**Figure 3.4:** Ideal W/Z separation as a function of jet mass resolution obtained using a Gaussian smearing of Breit-Wigner distribution, taken from [2].

### 3.5. Particle Flow Calorimetry

A jet energy resolution of 3.5% is unlikely to be achieved with a traditional calorimeter design. Traditionally, jet energies are measured as a sum of energies deposited in the

electromagnetic (ECAL) and hadronic calorimeter (HCAL), giving a jet energy resolution of the form

$$\frac{\sigma_E}{E} = \frac{\alpha}{\sqrt{E(\text{GeV})}} \oplus \beta. \quad (3.1)$$

The stochastic term  $\alpha$  is typically greater than 60% [27, 35], and the constant term  $\beta$  is a few percent [27, 35]. To achieve a jet energy resolution of 3.5% or better, the stochastic term should be less than 30% with a small constant term, which is unlikely to be achieved by a traditional calorimeter.

In a typical jet, about 62% of the jet energy is from charged particles, 27% from photons, 10% from long-lived neutral hadrons, and 1.5% from neutrinos [36, 37]. In a traditional approach to calorimetry, the jet energy resolution is limited by the relative poor energy resolution of the hadronic calorimeters.

The particle flow approach to calorimetry improves the jet energy resolution by fully reconstructing all visible particles in the detector. The jet energy is the sum of energies of individual particles, where the energies of the charge particles are measured in the tracking detectors, and the energies of neutral particles are measured in calorimeters. Hence the hadronic calorimeter only measures about 10% of the jet energy, which would greatly improve the overall jet energy measurement.

As shown in table 3.1, assuming 30% of the jet energy (photon energy) is measured with  $\sigma_E/E = 15\%/\sqrt{E(\text{GeV})}$ , and 10% of the jet energy (hadron energy) is measured with  $\sigma_E/E = 55\%/\sqrt{E(\text{GeV})}$  [35], a jet energy of  $\sigma_E/E = 19\%/\sqrt{E(\text{GeV})}$  can be obtained. This satisfies the jet energy resolution requirement for separating W and Z bosons via their hadronic decays. In reality, this level of performance is unattainable due to incorrect association of energy deposits to particles. At jet energies beyond tens of GeVs, the “confusion” rather than the intrinsic detector performance limits the particle flow performance [34].

In the particle flow approach to calorimetry, the sum of calorimeter energies is replaced by a complex pattern-recognition problem, which is solved by the Particle Flow reconstruction Algorithm (PFA). Detailed simulations of the ILC and the CLIC detector concepts using the PandoraPFA [34, 38] particle flow reconstruction algorithms have demonstrated that a jet energy resolution of approximately 3% can be achieved for jet energies in the range of 100 GeV to 1 TeV.

Component	Detector	Energy fraction	Energy resolution	Jet energy resolution
Charged particles ( $\chi^+$ )	Tracker	$\sim 0.6E_j$	$10^{-4}E_{\chi^+}^2$	$< 3.6 \times 10^{-5}E_j^2$
Photons ( $\gamma$ )	ECAL	$\sim 0.3E_j$	$0.15\sqrt{E_\gamma}$	$0.08\sqrt{E_j}$
Neutral hadrons( $\chi^0$ )	HCAL	$\sim 0.1E_j$	$0.55\sqrt{E_{\chi^0}}$	$0.17\sqrt{E_j}$

**Table 3.1:** Contributions from the different particle components to the jet energy resolutions (all energies in GeV). The table lists the approximate fractions of charged particles, photons, and neutral hadrons in a jet of energy  $E_j$ , and the assumed single particle energy resolutions. The table is adapted from [34].

The particle flow calorimetry requires to fully reconstruct particles and to associate calorimeter hits to tracks in tracking detectors. This places stringent requirements on the calorimeter designs. The ECAL and the HCAL need to be highly granular for an excellent spatial resolution to correctly associate calorimeter hits to the inner detector tracks. The tracking system needs to have an excellent momentum resolution for the momentum measurements of the charged particles.

## 3.6. International Large Detector

Two detector concepts have been developed for the ILC. The motivation for two detectors is to have multiple independent measurements within one collider for cross-checking, complementary measurements, and competition between collaborations. The two detectors are both designed to be general purpose detectors. The Silicon Detector, SiD [28], is a compact detector with silicon tracking modules and a large magnetic field of 5 T. The other detector, the International Large Detector, ILD [27], is a larger detector with a time projection chamber as the main tracking unit.

The ILD detector concept has been optimised for particle flow techniques. Figure 3.5 shows the longitudinal cross section of top quadrant of the ILD detector concept. From the interaction point (IP) outwards, there are a tracking system comprising a large time projection chamber (TPC) augmented with silicon tungsten layers, highly granular electromagnetic calorimeters (ECAL) and hadronic calorimeters (HCAL), forward calorimeters (FCAL), magnetic coils, and muon chambers/iron yokes. The key parameters of the ILD are listed in table 3.2.

The section below describes the sub-systems of the ILD detector concept referred to as the ILD\_o1\_v05 option in MOKKA simulation [39] in the ILD technical design report [29].



**Figure 3.5:** The longitudinal cross section of top quadrant of the ILD, taken from [29]. From interaction point (IP) outwards, there are a tracking system comprising a large time projection chamber (TPC) augmented with silicon tungsten layer, highly granular electromagnetic calorimeters (ECAL) and hadronic calorimeters (HCAL), forward calorimeters (FCAL), magnetic coils, and muon chambers/iron yokes. The dimensions are in units of mm.

### 3.7. ILD sub-detectors

This section discusses the ILD sub-detectors. Starting with a discussion of the precision vertex detector and the tracking system, which are closest to the interaction point, the discussion moves onto the highly granular calorimeter system of the electromagnetic and

Component	ILD	CLIC_ILD
Tracker	TPC; Silicon	TPC; Silicon
Solenoid Field	3.5 T	4 T
Solenoid Field Bore	3.3 m	3.4 m
Solenoid Length	8.0 m	8.3 m
VTX Inner Radius	16 mm	31 mm
ECAL $r_{min}$	1.8 m	1.8 m
ECAL $\Delta r$	172 mm	172 mm
HCAL Absorber Barrel / Endcap	Fe / Fe	Fe / W
HCAL Interaction Length	$5.5 \lambda_I$	$7.5 \lambda_I$
Overall Height	14.0 m	14.0 m
Overall Length	13.2 m	12.8 m

**Table 3.2:** A comparison of key parameters of the ILD and CLIC\_ILD detector concepts. ECAL  $r_{min}$  is the smallest distance from the calorimeter to the main detector axis. The table is adapted from [2].

hadronic calorimeters. A discussion on solenoid, iron yoke and the muon system will be presented, followed by a discussion on the very forward calorimeters.

### 3.7.1. Vertex Detector

The pixel-vertex detector (VTX) needs to be close to the interaction point to reconstruct secondary vertices. As the TPC is the main tracking detector, the VTX mainly measures the impact parameter of tracks. Figure 3.6 shows the mechanical support structure of the vertex detector. The structure is of three, nearly cylindrical, concentric layers of double-sided ladders. Each ladder contains pixel sensors on both sides at 2 mm interval. This results in six measured impact positions for each charged particle traversing the detector. The first double layer is of the half length of the other two, to avoid the high occupancy region of direct low momentum hits from the incoherent pair background. The baseline geometry of the vertex detector can be found in table 3.3. The radii covered by the detector range from 16 mm to 60 mm.

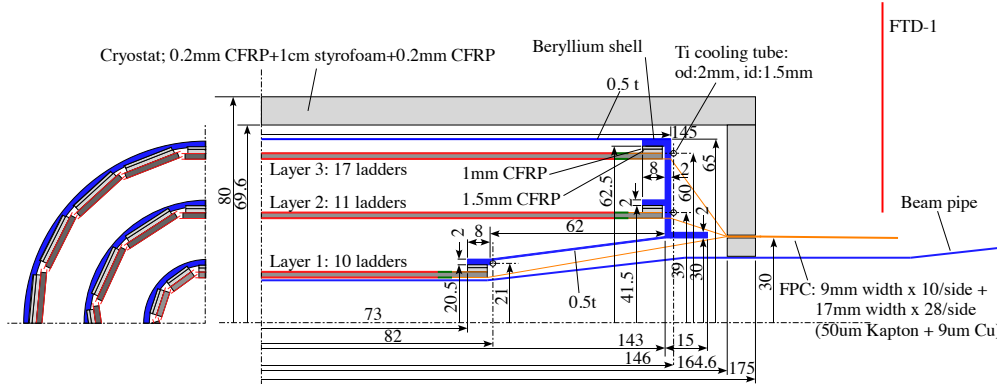


**Figure 3.6:** Mechanical support structure of ILD vertex detector, taken from [35].

	R	$ z $	$ \cos(\theta) $	$\sigma$	Readout time
Layer 1	16 mm	62.5 mm	0.97	$2.8 \mu\text{m}$	50 $\mu\text{s}$
Layer 2	18 mm	62.5 mm	0.96	$6 \mu\text{m}$	10 $\mu\text{s}$
Layer 3	37 mm	125 mm	0.96	$4 \mu\text{m}$	100 $\mu\text{s}$
Layer 4	39 mm	125 mm	0.95	$4 \mu\text{m}$	100 $\mu\text{s}$
Layer 5	58 mm	125 mm	0.91	$4 \mu\text{m}$	100 $\mu\text{s}$
Layer 6	60 mm	125 mm	0.90	$4 \mu\text{m}$	100 $\mu\text{s}$

**Table 3.3:** Key parameters for vertex detector in the ILC. The spatial resolution ( $\sigma$ ) and readout times are for the CMOS option. The table is adapted from [35].

### 3.7.2. Tracking Detectors

The hybrid tracking system consists of a large time projection chamber (TPC), a Silicon Inner Tracker (SIT), a Silicon External Tracker (SET) in the barrel region, a end cap tracking component (ETD) behind the endplate of the TPC, and a silicon forward tracker (ETD) in the forward region. A top quadrant view of the ILD silicon envelope system with the TPC is shown in figure 3.7. The SIT, SET, and ETD are made up of two single-sided strip layers tilted by a small angle. The ETD is a system of two silicon-pixel disks and five silicon-strip disks. The main parameters of the silicon system and the TPC can be found in table 3.4.

A TPC tracking detector has several advantages: a) tracks can be measured with a large number of three-dimensional ( $r, \phi, z$ ) spatial points. The continuous tracking allows precise reconstruction of tracks. b) The TPC uses a minimum amount of material, which minimises the effects due to the  $10^3$  beamstrahlung photons per bunch-crossing in the barrel region [40].

The silicon detector SIT and the SET in the barrel region provide spatial point measurements before and after the TPC. This helps to improve the overall momentum resolution by providing points to link the vertex detector with the TPC, and to extrapolate tracks from the TPC to the calorimeters. The ETD improves the low angle coverage of the tracking system, where the low angle is not covered by the TPC.

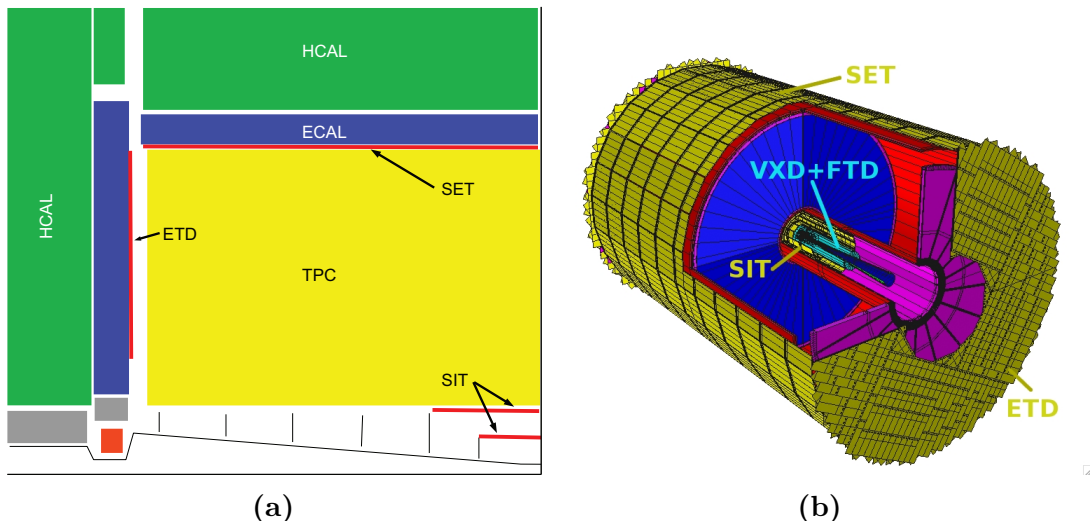


**Figure 3.7:** a) A top quadrant view of the ILD silicon envelope system, SIT, SET, ETD, and ETD, with TPC, ECAL, and HCAL, and b) a 3D detailed GEANT 4 simulation description of the silicon system as sketched in the quadrant view in a). Both plots are adapted from figures in [35].

	R	z	$\cos(\theta)$
SIT	153 mm	368 mm	0.910
SIT	300 mm	644 mm	0.902
SET	1811 mm	2350 mm	0.789
ETD	419-1822.7 mm	2420 mm	0.985-0.799
TPC	329-1808 mm	$\pm 2350$ mm	up to 0.98

**Table 3.4:** Main parameters of the central silicon systems (SIT, SET, and ETD) and the TPC. The table is adapted from [35].

### 3.7.3. Electromagnetic Calorimeter

The silicon-tungsten sampling electromagnetic calorimeters in the ILD consist of a nearly cylindrical barrel and two end cap systems, optimised for particle flow. The fine granular ECAL is located inside the HCAL. Figure 3.8a shows the position of the electromagnetic calorimeter in the ILD detector and the trapezoidal form of the modules. The ECAL measures photon energies and separates photons from other particles. The ECAL also hosts the first part of the hadronic showers and greatly assists the separation of hadronic showers.

The particle flow paradigm has a large impact on the ECAL design with many requirements. In addition to measuring and separating photons, the ECAL also needs to allow the reconstruction of detailed shower profiles to separate electromagnetic showers from hadronic showers, as approximately 50% of hadronic showers starts in the ECAL.

From test beam data and simulation studies [41–43], a sampling calorimeter with longitudinal and transverse segmentation below one Molière radius and below one radiation length at the front the calorimeter is needed. The most compact design is realised with tungsten as absorber material and silicon pad diodes as active material. A cross section of a ECAL layer is shown in figure 3.8. Tungsten is a dense material with a large ratio of interaction length to radiation length. A small radiation length will promote the start of the electromagnetic shower earlier in the calorimeter, whilst a large interaction length will reduce the fraction of hadronic showers starting in the ECAL.

The ECAL has 30 longitudinal layers, which is about 20 cm, providing about 24 radiation lengths. The first 20 layers use 2.1 mm thick absorber plates, which is twice finer sampling than the last 10 layers with 4.2 mm thick absorber plates.

The choice of thin silicon layers offers a great spatial resolution. The chosen size of 5.1 by 5.1 mm silicon pads provides enough segmentation to meet the requirements of the particle flow paradigm.

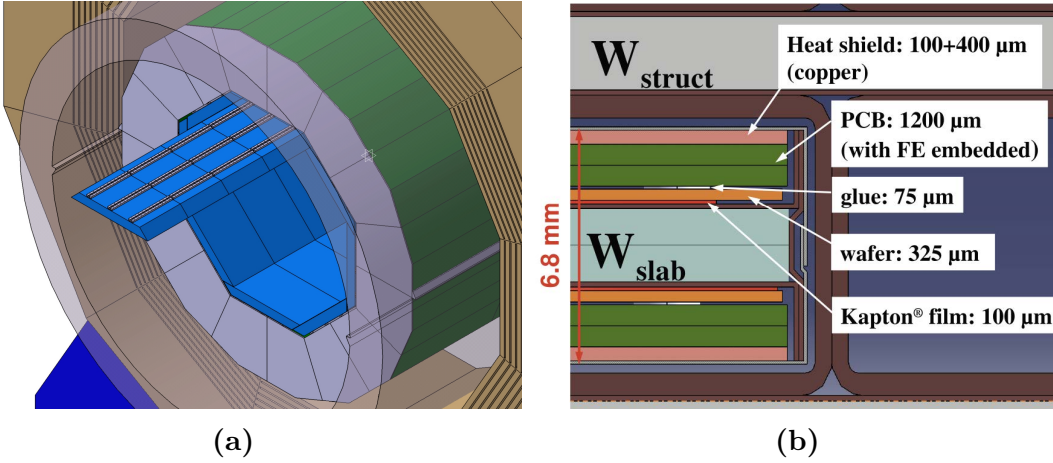


**Figure 3.8:** a) The electromagnetic calorimeter (in blue) within the ILD detector. b) A cross section through the electromagnetic calorimeter layers. Both plots are taken from [35].

### 3.7.4. Hadronic Calorimeter

The principal role of the HCAL is to separate neutral hadron showers from other particles, and to measure neutral hadron energies. The ILD HCAL is sampling calorimeter with steel absorber and scintillator tiles as active medium. The layout of the HCAL is 48 longitudinal layers with 3 by 3 cm scintillator tiles, using an analogue read out system. The layout of a technological prototype, the "EUDET prototype" [44] is shown in figure 3.9.

For the absorber material, stainless steel is chosen for mechanical and calorimetric reasons. Steel allows a self-supporting structure without auxiliary supports. At the same time, iron has a moderate ratio of hadronic interaction length ( $\lambda_I = 17$  cm) to electromagnetic radiation length ( $X_0 = 1.8$  cm), which allows a fine longitudinal sampling in  $X_0$  with a reasonable number of layers in a given total hadronic absorption length. The longitudinal system including the ECAL provides about 6 interaction lengths, which is sufficient to contain the hadronic showers.

The scintillator tiles provide both energy and position measurement. The transverse segmentation chosen by optimisation studies is about 3 by 3 cm<sup>2</sup>. This level of segmentation is sufficient to meet the requirement of the particle flow [35].

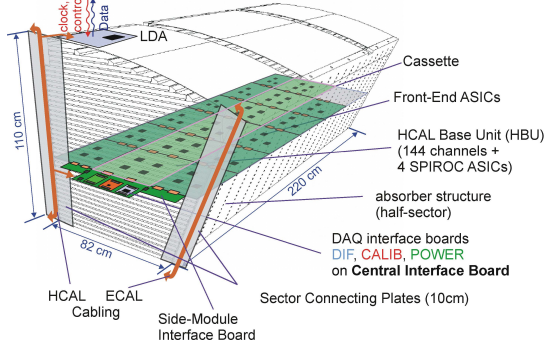


**Figure 3.9:** The schematic view of a CALICE analogue HCAL technological prototype module, taken from [29].

### 3.7.5. Solenoid, Yoke and Muon system

A large superconducting solenoid outside the calorimeters produces a nominal 3.5 T magnetic field. An iron yoke is instrumented with scintillator strips as active layers. The yoke returns the magnetic flux, and also acts as a muon detector and tail catcher calorimeter at the same time. The layout of the solenoid and the muon detector is shown in figure 3.10. The maximum magnetic field at 15 m radial distance from the detector is 50 Gauss to ensure safety [45]. A highly efficient muon detector is provided by the 3 by 3 cm scintillator strips. The first layer of the muon detector, also acting as a tail catcher calorimeter, catches the energy leakage from the HCAL and the ECAL. It has been shown that a 10% improvement of single particle energy resolution is possible with the tail catcher [46].

### 3.7.6. Very Forward Calorimeters

The forward region detectors provide luminosity measurements and forward coverage of calorimeters. A system of precision and radiation resistant calorimeters are required. Figure 3.11 shows the forward calorimeters of the ILD. The luminosity calorimeter (LumiCAL) counts Bhabha scattering to measure the luminosity to precision of 10<sup>-3</sup> at a 500 GeV centre-of-mass energy [47]. The beam calorimeter (BeamCAL), which is hit by many beamstrahlung pairs after each bunch crossing, extends the forward coverage. The

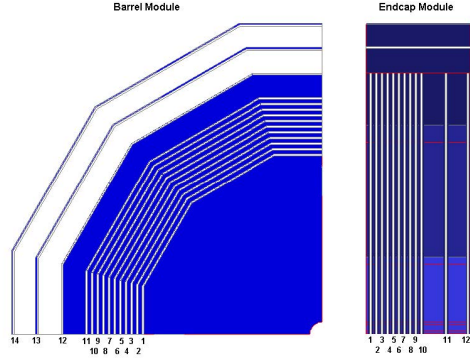


**Figure 3.10:** Sensitive layers of the ILD muon system, taken from [29].

BeamCAL also estimates a bunch-by-bunch luminosity. An additional hadron calorimeter at the forward region, LHCAL, extends the angular coverage of the HCAL to that of the LumiCAL. These forward region calorimeters also provide enough information for high-energy electron tagging [48], which aids event reconstruction at a high centre-of-mass energy. Table 3.5 lists the key parameters of the LumiCAL and the BeamCAL in the ILD.

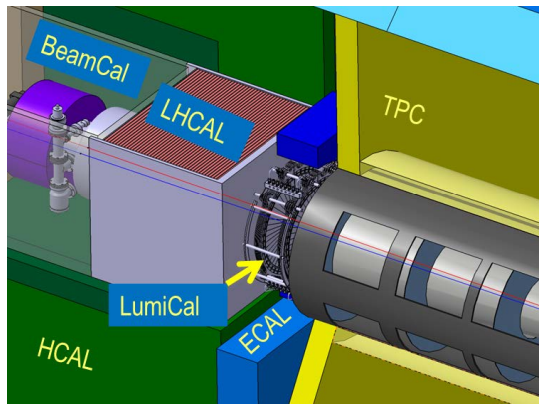


**Figure 3.11:** The forward calorimeters of the ILD, taken from [29]. The LumiCAL, the BeamCAL, and the LHCAL are the luminosity calorimeter, the beam calorimeter, and the forward hadronic calorimeter, respectively.

		ILD	CLIC_ILD
LumiCAL	geometrical acceptance (mrad)	31 - 77	38 - 110
	fiducial acceptance (mrad)	41 - 67	44 - 80
	z (start) (mm)	2450	2654
	number of layers (W + Si)	30	40
BeamCAL	geometrical acceptance (mrad)	5 - 40	10 - 40
	z (start) (mm)	3600	3281
	number of layers (W + sensor)	30	40
	graphite layer thickness (mm)	100	100

**Table 3.5:** Comparison of the key parameters of the LumiCAL and the BeamCAL at the ILD and the CLIC\_ILD. The table is adapted from [2].

## 3.8. Detector optimisation

### 3.8.1. Vertex detector optimisation

For the ILD vertex detector, figure 3.12 shows the impact parameter resolution as a function of the particle momentum for two different particle production angles from test beam results [35]. The curves with long dashes show the performance goal. The figure shows that the desired impact parameter resolution is achievable.

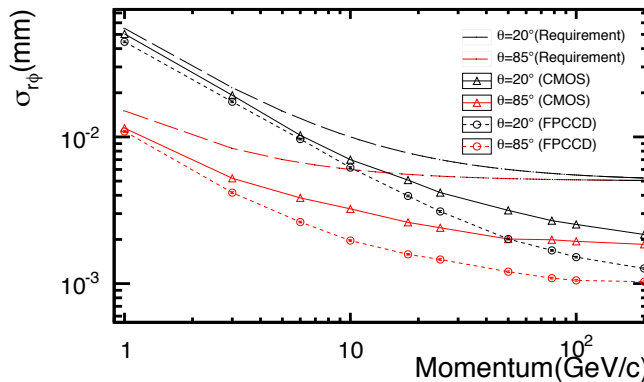


**Figure 3.12:** Impact parameter resolution of the ILD vertex detector for two different particle production angles ( $20^\circ$  and  $85^\circ$ ), assuming the baseline point resolution given in table 3.3 for CMOS option (solid line), and the FPCCD option (dotted line). The curves with long dashes show the performance goal. The figure is taken from [35].

### 3.8.2. Electromagnetic calorimeter optimisation

The optimisation of the ILD ECAL design as a function of the number of longitudinal layers is performed, whilst keeping other geometry constant. The metric for optimisation is the jet energy resolution, which defined as the root-mean-squared divided by the mean for the smallest width of distribution that contains 90% of entries, using  $e^+e^- \rightarrow Z'Z'$ , where  $Z' \rightarrow u\bar{u}/d\bar{d}/s\bar{s}$  sample at barrel region. The angular cut is to avoid the barrel/endcap overlap region. The light quark decay of the  $Z'$  is used as PandoraPFA does not attempt to recover missing momentum from semi-leptonic decay of heavy quarks. Using 90% of the entries is robust and focuses on the Gaussian part of the distribution. The total jet energy is sampled at 91, 200, 360 and 500 GeV.

Figure 3.13 shows the jet energy resolution for a single jet. For a 45 GeV jet, a degradation of 10% in the jet energy resolution is observed when the number of layers decreases from 30 to 20. The degradation in the jet energy resolution is significant for number of layers fewer than 20, although the impact is smaller for high energy jets. Therefore, 30 longitudinal layer is chosen for the ECAL.

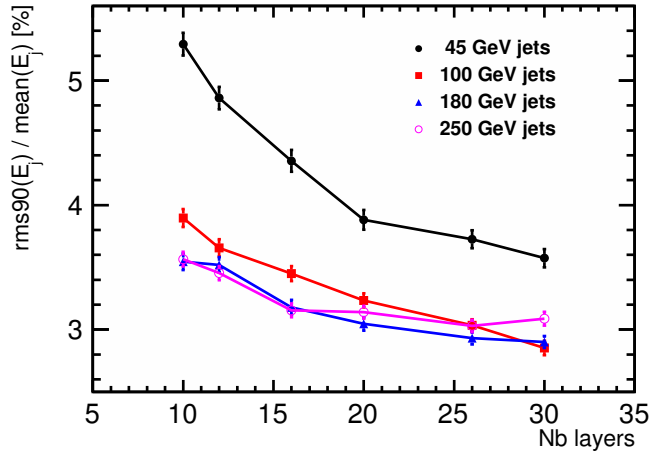


**Figure 3.13:** The single jet energy resolution as a function of the number of longitudinal ECAL layers, with different total jet energy using  $e^+e^- \rightarrow Z'Z'$ , where  $Z' \rightarrow u\bar{u}/d\bar{d}/s\bar{s}$  sample at barrel region, taken from [35].

### 3.8.3. Hadronic calorimeter optimisation

For the ILD HCAL design, the transverse cell sizes has been optimised for the best jet energy resolution. The jet energy resolutions as a function of HCAL scintillator square cell sizes for different jet energies are shown in figure 3.14. There is no substantial gain

in the jet energy resolution for cell sizes below 3 cm. However, the jet energy resolution degrades for cell sizes above 3 cm. Hence 3 by 3 cm scintillator cell size is chosen for the HCAL design.

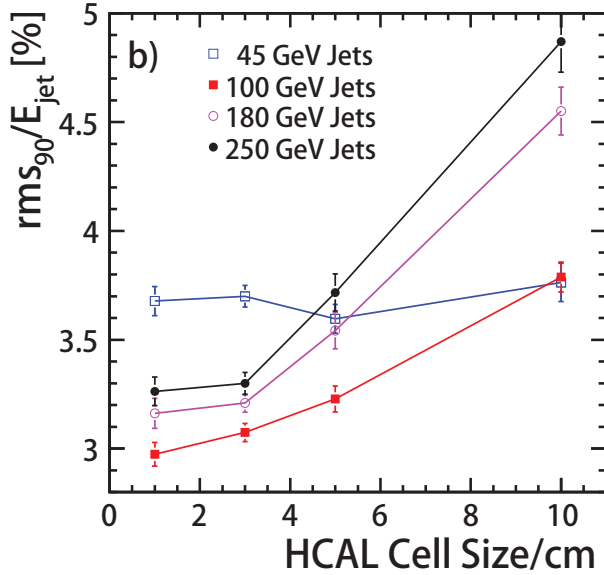


**Figure 3.14:** The single jet energy resolution as a function of the hadronic calorimeter scintillator cell sizes, with different total jet energy using  $e^+e^- \rightarrow Z'Z'$ , where  $Z' \rightarrow u\bar{u}/d\bar{d}/s\bar{s}$  sample at barrel region, taken from [29].

### 3.9. CLIC\_ILD

There are two detector concepts studied in the CLIC conceptual design report [2], the CLIC\_ILD and the CLIC\_SiD. The CLIC\_ILD detector concept is developed based on the ILD detector. Figure 3.15 shows the longitudinal cross section of the CLIC\_ILD detector. As the CLIC\_ILD is similar to the ILD, only the differences are highlighted here. A comparison of key parameters of the ILD and the CLIC\_ILD detector concepts is shown in table 3.2.

For the CLIC\_ILD vertex detector, the first layer is moved outwards by 15 mm due to a larger high occupancy region with a higher centre-of-mass energy. The detector is also required to provide time stamping at nanoseconds level, which needs different electronically components than those of the ILD.

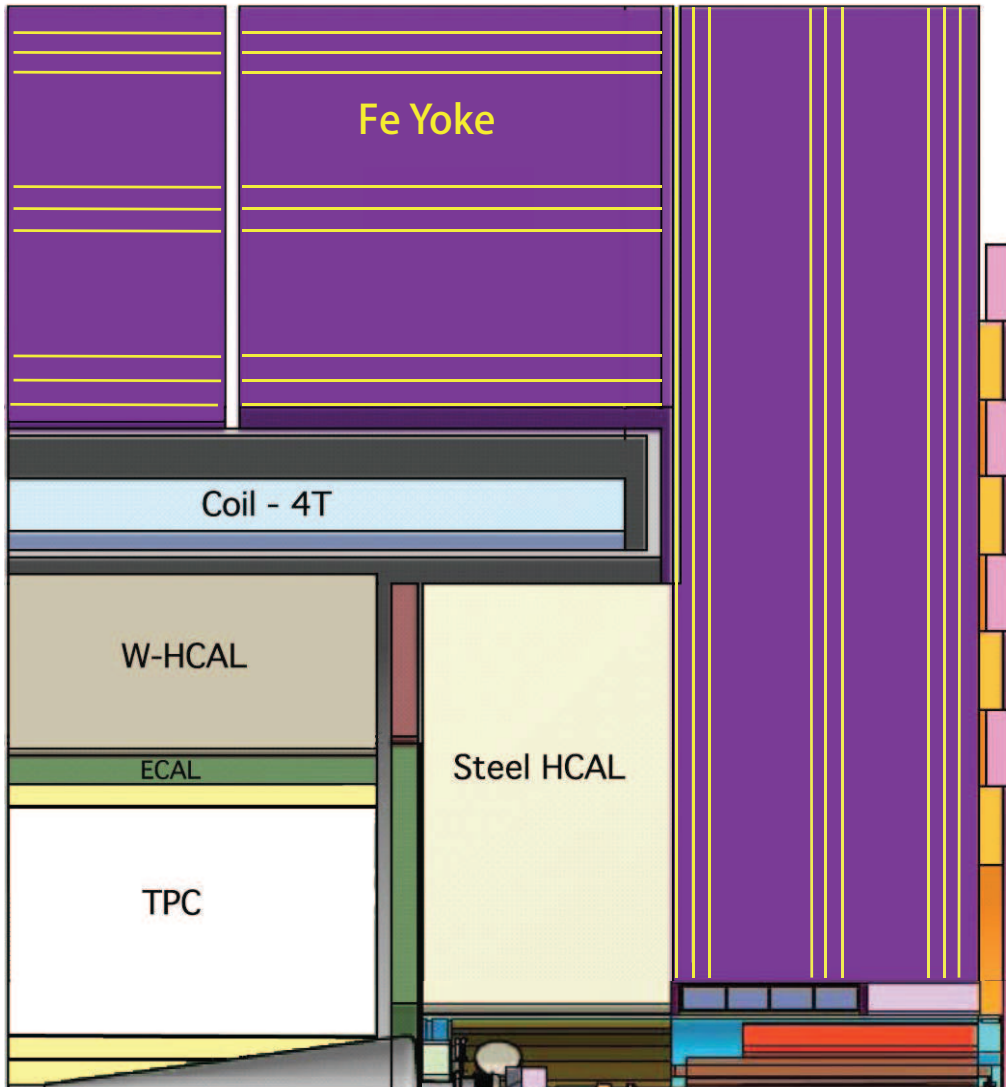


**Figure 3.15:** The longitudinal cross section of top quadrant the CLIC\_ILD, taken from and [2]. For both plots, from interaction point (IP) outwards, there is a tracking system comprising a large time projection chamber (TPC) augmented with silicon tungsten layer, highly granular electromagnetic calorimeters (ECAL) and hadronic calorimeters (HCAL), forward calorimeters (FCAL), magnetic coils, and muon chambers/iron yokes.

For the CLIC\_ILD tracking detector, the same silicon-TPC hybrid structure is used. At the CLIC, it is challenging to use a TPC to separate two tracks in high energy jets and to identify events in the collection of 312 bunch crossings in 156 ns. Hence the outer silicon tracking system is important to achieve a high momentum resolution at high centre-of-mass energy. The solid angle coverage of the tracking detector is  $12^\circ \lesssim \theta \lesssim 168^\circ$

For the CLIC\_ILD design, the same ECAL from the ILD is assumed, as the requirements of a CLIC detector are satisfied by the ECAL design at the ILD. The increased centre-of-mass energy results in extra energy leakage. The leakage is controlled by the HCAL. Only a small fraction of particles are affected by the leakage.

For the CLIC\_ILD HCAL, extra layers are added to contain the hadronic shower at a high centre-of-mass energy. The increased thickness is justified by the simulation studies [2], where the jet energy resolution degrades quickly for a thinner HCAL. To sustain the same inner bore radius of the ILC detector solenoids, a more dense material, tungsten, is chosen as the absorber material in the HCAL barrel.

The magnetic field is increased to 4 T for a better performance at a higher centre-of-mass energy. Due to the different magnetic field strength, the iron yoke thickness is therefore increased to 230 cm.

The CLIC\_ILD adopted a similar very forward calorimetry system as that of the ILD. The dimensions of the elements are changed due to a difference in the beam crossing angles (20 mrad for the CLIC and 14 mrad for the ILC). A comparison of the key parameters of the LumiCAL and the BeamCAL at the ILD and the CLIC\_ILD is shown in table 3.5.

# Chapter 4.

## Simulation, reconstruction, and analysis software for Future Electron-positron Linear Colliders

*'All the world's a stage, And all the men and women merely players;  
They have their exits and their entrances, And one man in his time plays  
many parts.'*

— William Shakespeare, 1564 - 1616

In previous chapters, overviews of the particle physics theory and the detectors of the future linear collider experiments have been provided. In this chapter, simulation, reconstruction and analysis software are discussed. Automated analysis is the only way to deal with the vast amount of data generated in high energy physics. Hence the software supporting the automated analysis are important. An analysis often consists of Monte Carlo event generation, event reconstruction, and using software to extract information of the event.

Simulation and reconstruction software of the ILC and the CLIC shares a common software framework. Therefore, the shared software is discussed first, and the CLIC specific issues are highlighted afterwards. The event reconstruction focuses on the PandoraPFA event reconstruction, which is the framework for the photon reconstruction algorithms in chapter 5. Afterwards analysis software is presented. The multivariate analysis is discussed in lengthy details due to its complexity.

## 4.1. Monte Carlo event generation

Monte Carlo (MC) event generation is often the first step for the simulated study. Most events used in this thesis are generated with the WHIZARD software [49, 50]. Some simple events used in this thesis are generated by writing the event manually in the HEPEVT format [51]. The PYTHIA software [52] is used to describe parton showering, hadronisation and fragmentation. The parameters for the PYTHIA are tuned to OPAL data from the Large Electron-Positron Collider (LEP) [53]. The TAUOLA software [54] is used to describe the tau lepton decay with correct spin correlations of the decay products. The Initial State Radiation (ISR) effect is simulated in the WHIZARD, with the ISR photons being collinear with the beam direction. The Final State Radiation (FSR) is simulated in the PYTHIA.

## 4.2. Event Simulation

For all the simulated events used in this thesis, the simulation software used to simulate the interaction of particles through the detector material is the GEANT4 software [55]. The detector geometry description is provided by the MOKKA software [39]. The QGSP\_BERT physics list is used to describe the hadronic shower decay in the detector.

## 4.3. Event Reconstruction

With simulated events (or real data in the future) as inputs, the next step is to reconstruct these events. The reconstruction software runs in the Marlin framework [56], as a part of the iLCSoft software package. The event reconstruction contains following steps: digitisation of simulated calorimeter hits, reconstruction of tracks in the tracking system (using pattern recognition algorithms), and particle flow objects (PFOs) reconstruction with PandoraPFA [34, 38]. Details of the event reconstruction can be found in [1, 2]. Here particle flow reconstruction via PandoraPFA will be discussed in details, as PandoraPFA provides the software framework for the photon reconstruction in chapter 5. The PandoraPFA event reconstruction is also used in the analyses in chapter 6 and chapter 7.

## 4.4. PandoraPFA event reconstruction

The traditional energy flow approach to calorimetry is unable to meet the mass and energy resolution requirements for future linear colliders. The particle flow approach to calorimetry with PandoraPFA has a proof-of-principle demonstration of its capability to reach the required jet energy resolution. The particle flow approach to calorimetry also puts stringent requirements on the detector design, which is described in section 3.4. By associating calorimeter hits to the tracks, around 60% of the jet energy from charged particles is measured by the tracking detector, which has a much better resolution than the calorimeter. Small cell sizes of the calorimeters are required to identify calorimeter hits from different particles. The traditional sum of calorimeter cell energies is hence replaced by particle flow reconstruction algorithms - a complex pattern recognition problem.

Developed with the ILD detector concept, PandoraPFA has been adapted to the CLIC condition and shows its ability to deliver required energy resolutions [2]. There are over 60 electron-positron linear collider specific reconstruction algorithms. Each algorithm aims to address a particular topological issue in the reconstruction. In the recent development, the core base codes for basic object and memory managements are factorised in the Pandora C++ Software Development Kit [57].

In the subsequent sections, the main steps in the PandoraPFA reconstructions are summarised below. The details of the PandoraPFA event reconstruction can be found in [34, 38, 57]. The inputs of PandoraPFA are digitised calorimeter hits and reconstructed tracks, with some detector geometry information to aid the reconstruction. The output are reconstructed particles with four-momenta, also known as the Particle Flow Objects (PFOs).

### 4.4.1. Track selection

Tracks from the inner tracking detectors are important inputs of the PandoraPFA reconstruction. These tracks are selected based on their topological properties, how likely they are from physical processes, and whether they are consistent with the tracker resolution. Only tracks passing the selection are used for the subsequent reconstruction.

Special topologies of tracks are identified, such as when a neutral particle decays or converts into a pair of charged tracks, leaving tracks of a “V0” shape. This is identified

by searching for a pair of tracks originated from a single point. Another topology is the “kinks” when a charged particle decays to a single charged particles with neutral particles. The last special topology are the “prongs” when a charged particle decays to multiple charged particles. This information about special topologies, along side with helical track fit (using last 50 reconstructed hits in the tracking detector) and the track projection to the front of the ECAL, is stored and passed onto the subsequent reconstruction.

#### **4.4.2. Calorimeter selection**

The other important inputs of the PandoraPFA reconstruction are the calorimeter hits from calorimeters. The properties of a calorimeter hit include its position, its layer in the calorimeter, and its energy response from the calorimeter digitiser.

Calorimeter hits are selected based on a series of criterion. The selected hits need to have energies above certain thresholds, measured in minimum ionising particle (MIP) equivalent or measured in directly converted energy. Only calorimeter hits that pass the selection are used in later steps.

Extra information about calorimeter hits are calculated, stored and used in later steps. The extra information includes the geometry information of the hit and likelihood of the hit originated from a minimum ionising particle (MIP).

Isolated hits, often originating from low energy neutrons in a hadronic shower, are difficult to associate to the correct hadronic shower. They are identified and not used during the clustering stage. However, these isolated hits participate in the reconstruction during the last step, particle flow object (PFO) creation, to contribute to the energy estimation.

#### **4.4.3. Particle Identification**

To improve the reconstruction of the charged particles, where calorimeter hits are associated to tracks, dedicated particle identification algorithms find calorimeter hits associated with muons and photons. These calorimeter hits are removed from the subsequent reconstruction. As fewer hits are left to be reconstructed, the reconstruction of charged particles is improved and the pattern recognition problem is simplified.

Identified muons and photons do not participate in the later clustering and re-clustering stages, but re-enter the reconstruction at the fragment removal stage (see section 4.4.8). See chapter 5 for details on the photon reconstruction related algorithms..

#### 4.4.4. Clustering

A cone-based clustering algorithm is used to group calorimeter hits into clusters. The output clusters are further processed, merged, or split based on their topological properties. Since the cone clustering algorithm is widely used in many other reconstruction algorithms in the PandoraPFA, it is necessary to introduce the cone based clustering algorithm, before discussing the rest of the PandoraPFA reconstruction.

There are two main types of clustering algorithms: cone-based algorithms and sequential combination algorithms. The main type of clustering algorithms used in the PandoraPFA is the cone based algorithms. Illustrated in figure 4.1, cone based clustering algorithm identifies a seed first, shown as the yellow dot. The algorithm then forms a cone to include hits that are within a specified opening angle to the seed. Afterwards the cone with the associated hits form the cluster.

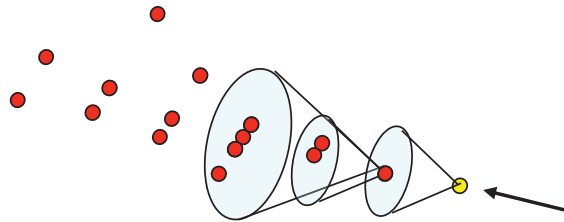


**Figure 4.1:** Illustration of the cone based clustering algorithm, taken from [58]

The cone-based clustering algorithm is preferred in PandoraPFA because the direction of the particle flow is largely unchanged from the originated particle, irrespective of the particle flow being an electromagnetic shower, QCD radiation, or hadronisation. Figure 4.2 shows the clustering algorithm used in the PandoraPFA. The seed for the cone clustering is typically the projection of a track to the front of the ECAL. A calorimeter hit can also be used as a seed. The initial cluster direction is taken as the direction of the seed. Afterwards, a cone with a specified opening angle and depth will be formed around the direction of the seed.

The building of the cone is iterated from the inner layer of the ECAL to the outer layer. At each layer, possible associations with calorimeters hits in previous layers and the same layer are made. If a calorimeter hit is not associated with the cone, the hit is used to seed a new cluster. The clustering algorithm produces basic working objects, clusters.

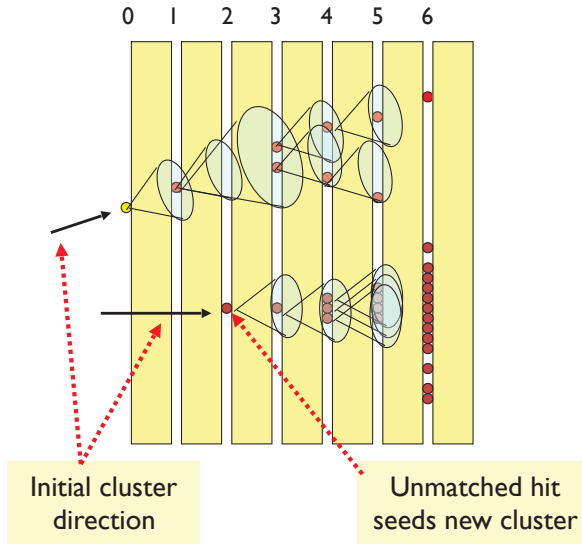


**Figure 4.2:** Illustration of the clustering algorithm used in the PandoraPFA, taken from [58]

#### 4.4.5. Topological cluster association

After the initial clustering, clusters are further refined using topological information of calorimeter hits in the calorimeters. This step is necessary because the initial clustering scheme tends to form small clusters. These small clusters are then merged based on clear topological signatures in this step. The merging signatures include combining track segments, connecting a track segment with gaps, connecting track segments to hadronic showers, and merging clusters when they are within close proximity. For example, association algorithms for looping track segments, back-scattered tracks from hadronic showers, and cone association are shown schematically in figure 4.3. In each case, the arrow indicates the tracks. The dark red dots represent the calorimeter hits in the associated cluster. The slightly fainter red dots represent the calorimeter hits in the neutral cluster. The black line represents the front of the ECAL.

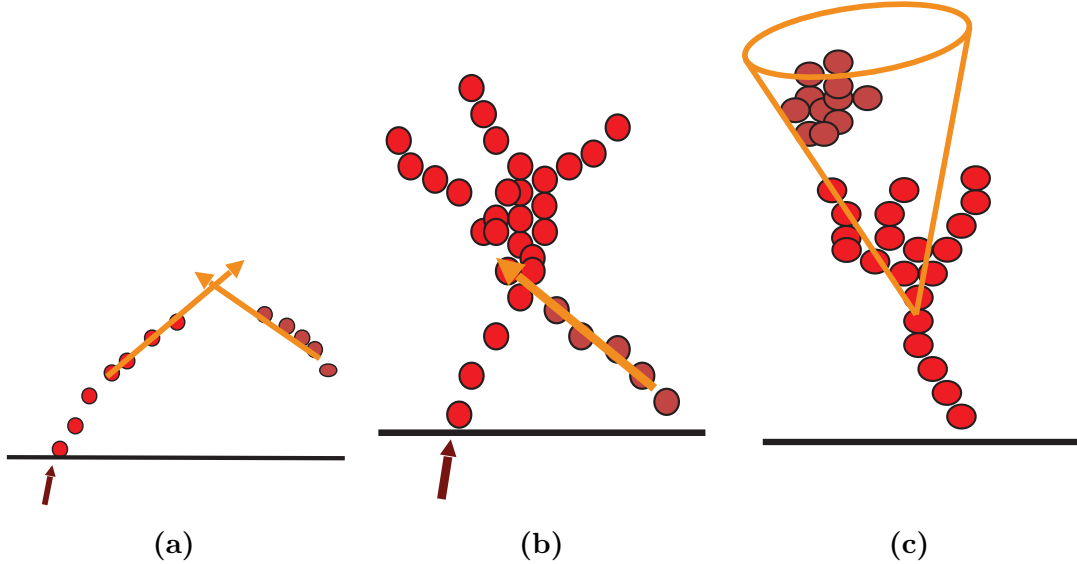


**Figure 4.3:** Examples of topological association in the PandoraPFA. Rules for a) looping track segments, b) back-scattered tracks from hadronic showers, c) and cone association are shown. In all plots, the arrow indicates the tracks. The dark red dots represent the calorimeter hits in the associated cluster. The slightly fainter red dots represent the calorimeter hits in the neutral cluster. The black line represents the front of the ECAL. Figures are taken from [58].

#### 4.4.6. Track-cluster association

Having refined the clusters in the calorimeter, the next step is to associate the clusters to the tracks obtained from the inner tracking detectors. The associations are made according to the proximity of the first layer of the cluster and the track projection to the front of the ECAL. The consistency between the track direction and the initial cluster direction, as well as a match between the track momentum and the cluster energy, are required.

#### 4.4.7. Re-clustering

The cluster association scheme described in the previous section works well for events with low-energy (less than 50 GeV) jets. For an environment with high-energy jets, electromagnetic and hadronic showers are boosted and are likely to overlap each other. Therefore, it is important to refine the track-cluster association based on the momentum and the energy information.

The re-clustering stage improves the compatibility of the cluster energy and the associated track momentum. It is performed on a statistical basis. If the cluster energy and the associated track momentum do not match, the cluster will be re-clustered either using the same clustering algorithm with different parameters, or different clustering algorithms. This re-clustering step creates many temporary clusters. Afterwards, out of many temporary clusters, the temporary cluster with the best track-momentum cluster-energy match is chosen, and the temporary cluster is associated with the track.

A schematic diagram of the re-clustering stage is shown in figure 4.4. In the figure, the black upright arrows indicate the tracks. The dark red dots represent the calorimeter hits in the associated cluster. The slightly fainter red dots represent the calorimeter hits in the neutral cluster. In this example, the initial cluster energy is less than the associated track momentum. The topological association algorithms did not add the natural cluster, as it would have formed a cluster with too much energy. The re-clustering scheme tries different cone clustering algorithms by splitting the neutral cluster so that the topological association could make a correct association.

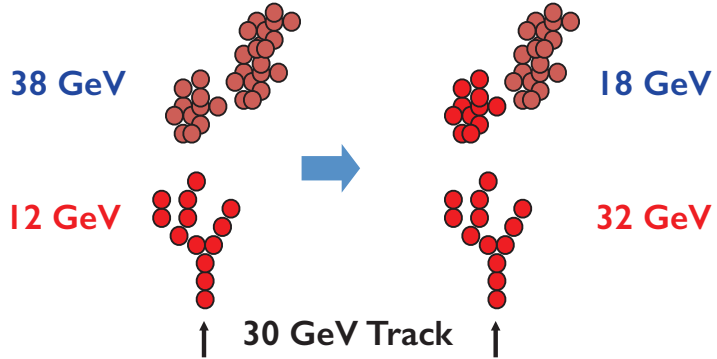


**Figure 4.4:** Illustration of the re-clustering algorithm in PandoraPFA, taken from [58]. The arrow indicates the tracks. The dark red dots represent the calorimeter hits in the associated cluster. The slightly fainter red dots represent the calorimeter hits in the neutral cluster. The initial cluster energy is less than the associated track momentum. The topological association algorithms did not add the natural cluster, as it would have formed a cluster with too much energy. The re-clustering algorithm tries different cone clustering algorithms to split the neutral cluster so that the topological association could make a correct association.

#### 4.4.8. Fragment removal

This stage of the PandoraPFA reconstruction will focus on merging low-energy clusters. These clusters are likely to be fragments of other particles. The merging criterion are

mostly based on the proximity of the fragment to the particle, and the energy comparison of the fragment to the particle. Algorithms dealing with photon fragment merging and photon splitting are described in details in chapter 5.

#### 4.4.9. Particle Flow Object Creation

The last stage of the reconstruction is the creation of the output objects, Particle Flow Objects (PFOs). The PFOs contain clusters and associated tracks. Simple, but effective, particle identification for electrons and muons are applied.

The output objects, PFOs, contain information on positions, four-momenta and associated quantities. These PFOs are heavily used in physics analyses. The electron, muon and photon identifications associated with the PFOs are also used in physics analyses, for example, the analyses in chapter 6 and in chapter 7.

### 4.5. The CLIC specific simulation and reconstruction issue

There are a few simulation and reconstruction issues specific to the CLIC, which affect the analysis in chapter 7. One issue is that the luminosity spectrum for interactions with photon from Beamstrahlung is different to the luminosity spectrum of electron-positron interactions. A solution is presented in section 4.5.1 to correct for the differences. Another issue is that there is a large amount of beam induced background in the CLIC environment, which needs to be suppressed before physics analyses. The background suppression is described in section 4.5.2. Lastly simulated masses of particles are given in section 4.5.3.

#### 4.5.1. Luminosity spectrum

The electron-photon interaction, where the photon is produced from initial state radiation via Beamstrahlung, has a different instantaneous luminosity than the electron-positron interaction. Hence, for the same time-frame, the total integrated luminosity of the electron-photon interaction is different to that of the electron-positron interaction. To correct for the difference in the luminosities, a simulated study [59] was performed with

the GUINEAPIG [60] and was simulated in the WHIZARD, to identify the ratio of the integrated luminosity of the electron-photon interaction to the electron-positron interaction. The results are summarised in table 4.1. For the physics analysis in chapter 7, event number for processes with initial-state photons from Beamstrahlung are corrected with the ratios in table 4.1.

Luminosity ratio	$\sqrt{s} = 1.4 \text{ TeV}$	$\sqrt{s} = 3 \text{ TeV}$
$L(e^+e^-) / L(e^+e^-)$	1	1
$L(e^\pm\gamma) / L(e^+e^-)$	0.75	0.79
$L(\gamma e^\pm) / L(e^+e^-)$	0.75	0.79
$L(\gamma\gamma) / L(e^+e^-)$	0.64	0.69

**Table 4.1:** Luminosity ratio for processes with initial-state photons from Beamstrahlung at the CLIC, at  $\sqrt{s} = 1.4 \text{ TeV}$  and  $3 \text{ TeV}$ . The table summarises results from [59].

### 4.5.2. Beam induced backgrounds

The other issue considered when using the CLIC\_IID detector concept is the beam induced background. At a high centre-of-mass energy, the background becomes important for the event reconstruction. Therefore, the beam induced background are considered in the simulation.

There are different types of the beam induced background. The  $\gamma\gamma \rightarrow \text{hadrons}$  is the dominant background in all calorimeters except inner part of the HCAL endcap. Hence another type of the background, the incoherent pairs, is ignored. Consequently, the  $\gamma\gamma \rightarrow \text{hadrons}$ , background, intergraded over 60 bunch crossing, is overlayed onto the reconstruction.

The hadronisation of  $\gamma\gamma \rightarrow \text{hadrons}$  background events are performed with the PYTHIA. The  $\gamma\gamma \rightarrow \text{hadrons}$  background events are superimposed on the physics process simulations to save computational resources. The choice of 60 bunch crossings is an estimate of the amount of background in the experiment condition [61].

The beam induced background deposits significant amounts of energies in the detector. It needs to be suppressed for physics analyses. Two software have been developed to suppress these background: a track selector and a PFO selector [38].

The track selector aims to remove poor quality and fake tracks that are more likely from the beam induced background. It places a simple track-quality cut and a time-of-arrival cut on tracks. If the arrival time of the track at the front of the ECAL, using the helical fit of the track, differs more than 50 ns from using a straight line fit, the track will be rejected.

The PFO selector discards PFOs that are originated from the beam induced background from the event reconstruction, based on the transverse momentum ( $p_T$ ) and time information of the PFOs. The PFOs from  $\gamma\gamma \rightarrow \text{hadrons}$  often have low  $p_T$  and have a range of time-of-arrivals. In contrast, the PFOs from physics processes have a range of  $p_T$ , and the time-of-arrivals are close to the bunch crossing time. By utilising the high spatial resolution from the high granular calorimeter, individual PFOs can be tracked and reconstructed.

The PFO selector uses different  $p_T$  and time-of-arrivals cuts for the central part of the detector and for the forward part of the detector. For the best performance, there are different cuts for different types of particles: photons, neutral PFOs, and charged PFOs. Three configurations of these cuts are developed: “loose”, “normal”, and “tight” selections. As the name suggested, “loose” selection corresponds to a looser cut of  $p_T$  and time-of-arrival, allows a larger value of  $p_T$  and time-of-arrival.

The optimal configuration depends on the centre-of-mass energy of the collision, and the physics process to study. Figure 4.5 shows the effect of the suppression of the background with the tight PFO selection. Reconstructed particles in a simulated  $e^+e^- \rightarrow HH \rightarrow t\bar{t}b\bar{b}$  event are integrated over a time window of 10 ns (100 ns in HCAL barrel) in the CLIC\_ILD detector model, with 60 bunch crossings of  $\gamma\gamma \rightarrow \text{hadrons}$  background overlaid in figure 4.5a. The effect of applying tight PFO section cuts is shown in figure 4.5b. The energy deposited in the detector by the background is reduced from 1.2 TeV to the level of 100 GeV.

#### 4.5.3. CLIC simulated particle masses

Another information used in the analysis with the CLIC detector concept is the simulated mass and width of quarks and bosons. These values are listed in table 4.2 and are used for generating Monte Carlo samples.

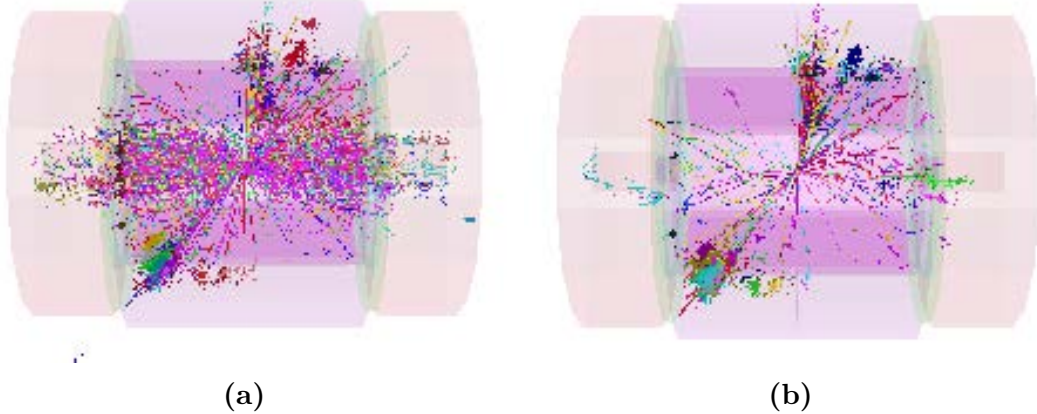


**Figure 4.5:** Reconstructed particles in a simulated  $e^+e^- \rightarrow HH \rightarrow t\bar{b}b\bar{t}$  are integrated over a time window of 10 ns (100 ns in HCAL barrel) event in the CLIC\_ILD detector model, with 60 bunch crossings of  $\gamma\gamma \rightarrow$  hadrons background overlaid in figure 4.5a. The effect of applying tight PFO section cuts is shown in figure 4.5b. The energy deposited in the detector by the background is reduced from 1.2 TeV to the level of 100 GeV. Figures are taken from [38].

Particle	Mass ( $GeV/c^2$ )	Width ( $GeV/c^2$ )
u, d, s quarks	0	0
c quark	0.54	0
b quark	2.9	0
t quark	174	1.37
W	80.45	2.071
Z	91.188	2.478

**Table 4.2:** The masses and widths of quarks and bosons used for generating samples. The H mass is specified for individual samples. The table is taken from [2].

## 4.6.

## 4.7. Analysis software

In the previous sections the automated reconstruction tools are described in details. This section is dedicated to the automated analysis software, which will be used in the analyses described in subsequent chapters.

### 4.7.1. Monte Carlo truth linker

It is extremely useful to be able to associate reconstructed objects to the Monte Carlo (MC) simulated particles, for algorithms development and event selection optimisation. The MC truth linker processor provides the link between a MC particle and a reconstructed calorimeter hit. From the link, the main MC particle, contributing to a reconstructed PFO or a group of PFOs (jet), can be determined.

### 4.7.2. Jet algorithms

For the linear collider, thanks to the high granular calorimeter and advanced PFA software, the starting point for analysis are individual Particle Flow Objects (PFOs), as well as individual tracks. Each of the PFOs encodes four-momentum and position information. At the same time, tracks would have momentum and position information. However, sometimes it is useful to group PFOs and tracks into jets, which are the results of hadronisation processes from high energy particles like quarks or gluons.

A jet is typically a visually obvious structure in an event display. The momentum and the direction of a jet tend to resemble the original particle. Despite the relative simplicity of identifying jets visually, it is a challenge for a pattern recognition program to identify jets effectively and efficiently. Early work on jet finding started in 1977 [62], where later development can be found in reviews [63–65]. This section is based on these reviews.

There are two large families of jet finding algorithm: cone based algorithms, and sequential combination algorithms. The cone based algorithms are briefly discussed in

section 4.4.4 in the context of the PandoraPFA reconstruction. Here the focus is on the sequential combination algorithms.

Sequential combination algorithms typically calculate a pair-wise distance metric between a seed and a particle. The particle with the smallest metric is combined into the jet with the seed. The distance metric will be updated after a combination. This procedure is repeated until some stopping criterion are satisfied. The different jet algorithms typically differ in the definitions of distance metrics and stopping criterion.

The chosen jet algorithm implementation for this thesis is the FastJet C++ software package [66, 67]. The implementation in the Marlin software package is called the MarlinFastJet. The package provides a range of jet finding algorithms. The notations in the subsequent discussion follow the convention in [66].

### 4.7.3. Longitudinally-invariant $k_t$ algorithm

Longitudinally-invariant  $k_t$  algorithm [68, 69] is one of the common sequential combination algorithms used in the pp collider experiments. There are two variants of the algorithm: inclusive and exclusive. In the inclusive variant, the symmetrical pair-wise distance metric between particle  $i$  and  $j$ ,  $d_{ij}$  or  $d_{ji}$ , and the beam distance,  $d_{iB}$ , are defined as

$$d_{ij} = d_{ji} = \min(p_{T_i}^2, p_{T_j}^2) \frac{\Delta R_{ij}^2}{R^2}, \quad (4.1)$$

$$d_{iB} = p_{T_i}^2, \quad (4.2)$$

where  $p_{T_i}$  is the transverse momentum of particle  $i$  with respect to the beam ( $z$ ) direction, and  $\Delta R_{ij}^2$  is the measurement of angular separation of particle  $i$  and  $j$ , defined as  $\Delta R_{ij}^2 = (y_i - y_j)^2 + (\phi_i - \phi_j)^2$ , where  $y_i = \frac{1}{2} \ln \frac{E_i + p_{zi}}{E_i - p_{zi}}$  and  $\phi_i$  are particle  $i$ 's rapidity and azimuthal angle.  $R$  is a free parameter, controlling the jet radius.

If  $d_{ij} < d_{iB}$ , particle  $i$  and  $j$  are merged. four-momentum of particle  $i$  is updated as the sum of the two particles. Otherwise if  $d_{ij} \geq d_{iB}$ , particle  $i$  is set to be a final jet. The above procedure is repeated until no particles are left.

The exclusive variant is similar to the inclusive variant. First difference is that when  $d_{iB} < d_{ij}$ , particle  $i$  forms part of the beam jet. The beam jet contains particles that are considered to be from the beam induced background. The beam jet is not used as a output. The second difference is that when both  $d_{ij}$  and  $d_{iB}$  are above some threshold,

$d_{cut}$ , the clustering will stop. In another word, the exclusive mode allows a specified number of jets to be found, where the  $d_{cut}$  is automatically determined. The inclusive mode, on the other hand, would find as many jets as the algorithm allows.

#### 4.7.4. Durham algorithm

The Durham algorithm [70], also known as  $e^+e^- k_t$  algorithm, is commonly used for the  $e^+e^-$  collider experiments. It only has one distance metric:

$$d_{ij} = 2 \min(E_i^2, E_j^2)(1 - \cos(\theta_{ij})), \quad (4.3)$$

where  $E_i$  is the energy of particle  $i$ ; and  $\theta_{ij}$  is the polar angle difference between particle  $i$  and  $j$ . The Durham algorithm can only be run at exclusive mode, which means that the clustering will stop when  $d_{ij}$  is above some threshold,  $d_{cut}$ .

Compared to the  $k_t$  algorithm, it uses energy instead of  $p_T$  in the distance metric, and it does not use the beam distance. This is because that for the  $e^+e^-$  collider at low centre-of-mass energies, the beam induced background is not significant.

#### 4.7.5. Jet algorithm for the CLIC

Although CLIC is a  $e^+e^-$  collider, the significant beam-induced background adds a large amount of energy. Therefore, traditional  $e^+e^-$  jet algorithms, like the Durham algorithm, are not suitable for the CLIC collision environment. Studies have shown that jet algorithms for the pp colliders give better performances for the CLIC [2, 71]. Therefore, longitudinal invariant  $k_t$  algorithm is often used in analyses with the CLIC environment.

#### 4.7.6. The $y$ parameter

The  $y$  parameter is a measure of the number of jets in an event. It describes the transition of the exclusive jet algorithm going from  $N$  clustered jets to  $N+1$  clustered jets. For example,  $y_{23}$  would be the  $d_{cut}$  value for a exclusive jet algorithm, above which the jet algorithm returns 2 jets, below which the jet algorithm returns 3 jets. Numerically the  $y$

parameter is often much smaller than 1. A typically way to convert the small number to a machine acceptable range is to take the negative logarithm of the number.

## 4.8. Multivariate Analysis

Multivariate analysis (MVA) has become increasingly important in high energy physics. MVA is typically used in the physics analysis to classify signal events from background events. The MVA can be viewed as an advanced tool for regression or classification. Compared to the traditional cut-based method, modern machine learning techniques offer much improvement to the data analysis. The implementation of the machine learning techniques used in this thesis are provided by TMVA [72].

A typical machine learning MVA can be used for classification or regression. Classification classifies events into one of several classes. Regression gives an output in a continuous range. The focus in this section is on the classification, as the MVA is often used to select one type of events from another type of events.

A typical machine learning MVA classification involves two classes, also known as signal and background. A machine learning model needs to be trained with training data. The model requires a set of discriminative variables, which separate the signal from background. The trained model will be applied onto the testing data for signal extraction. The response of the model is a classification with two-class outcome of signal or background.

This classification scheme can easily be extended to multiple classes, implemented in TMVA with the multiclass class. For example, The multiclass class is used in the tau decay mode classification in section 6.6 and in the flavour tagging classifier in section 7.5.

There should be three statistically independent samples for the MVA: one sample for the training; another sample for the validation, including optimisation and checking for overfitting; and the last sample for testing. However, due to technical reasons (TMVA only natively supports two samples), sometimes the same sample is used for the validation and the testing, which is an acceptable usage with samples of large data.

### 4.8.1. Optimisation and overfitting

One important concept with the MVA is the optimisation and the overfitting. The optimisation of the model refers to selecting the optimal free parameters of the model. One could build a complex model which fits the training samples very well, but it would not be optimal for another testing sample. A simple model is less prone to statistical fluctuation of samples, however, it might be too simple to achieve the optimal modeling. The former case is known as overfitting, or overtraining. The latter case is called underfitting, or undertraining. Another way to describe the difference in a simple and a complex model is that a simple model typically has a low variance but a high bias, whilst a complex model would often have a low bias but a high variance.

The optimal model is the one between overfitting and underfitting. In practice, this involves building the model with increasing complexities, and finding the point where overfitting occurs.

Figure 4.6 shows an example of the model efficiency as function of the model complexity. One definition for overfitting is when the efficiency of the signal selection in the training samples increases, but the efficiency in the testing sample decreases, with the increase of the model complexity. The example in figure 4.6 is chosen from the double Higgs analysis at  $\sqrt{s} = 3 \text{ TeV}$ , using the Boosted Decision Tree model. The efficiency of the signal selection is defined as the signal fraction when the background fraction is 1%, reported by the TMVA training process. In figure 4.6 , the depth of the tree, or the number of layers in the tree, reflects the complexity of the model. From a tree depth of two to six, the efficiency for both testing and training samples increases. From tree depth of six onwards, overfitting occurs. In this particular example, one should choose a tree depth fewer than seven to avoid overfitting.

### 4.8.2. Choice of models

The model to fit the data can be as simple as a cut-based model, a likelihood estimator, or a linear regression model. The model can also be as complicated as a non-linear tree, a non-linear neutral network, or a support vector machine. Regardless of the model complexity, the choice of the most optimal classifier is often data driven to match the nature of the sample. For example, a non-linear model is the best to model a non-linear response. The comparison between different models without individual optimisation is not rigorous. Nevertheless, as researchers in the machine learning suggested, the

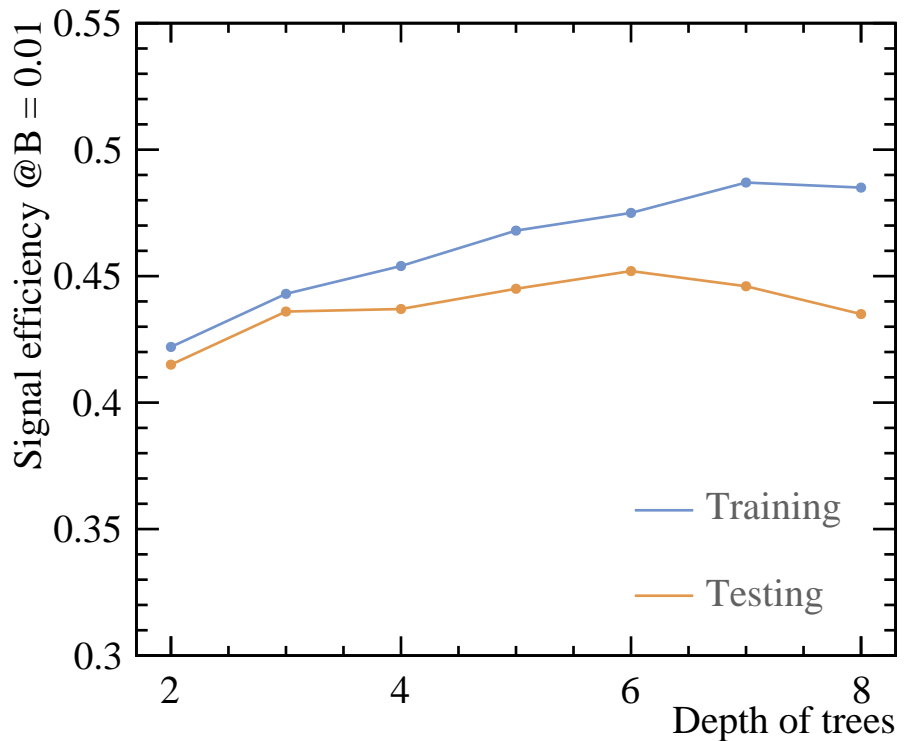


**Figure 4.6:** Example of model efficiency as function of the model complexity. Here the model is a boosted decision tree. The model parameter reflecting the model complexity is the depth of tree. The y-axis is the signal efficiency when the background efficiency is 1%. From the tree depth of six onwards, overfitting occurs.

boosted decision tree is probably the best out-of-the-box machine learning method. A neutral network model could potentially be better than the boosted decision tree model, but it requires more tuning, and it is less intuitive to interpret the neural network model. For these reasons, the boost decision tree model (BDT) is often the choice of machine learning model in high energy physics. And it is used in various physics analysis in this thesis. Before describing the BDT in detail, we will first visit some simpler models.

#### 4.8.3. Rectangular Cut model

The rectangular cut method, probably the most intuitive model, optimise cuts to maximise some pre-defined metrics. The metric could be the signal efficiency for a particular background efficiency. Alternatively, the metric can be the significance,  $\frac{S}{\sqrt{S+B}}$ , where  $S$  and  $B$  are signal and background numbers passing the rectangular cuts, respectively.

Discriminative variables give better separation power when they are gaussian-like and statistically independent. Therefore it is common to decorrelate the variables and gaussian transform them before using the rectangular cut MVA.

Because of its simplicity, the cut method is often performed manually, much more often at times pre-dating the spread of machine learning methods. It is still commonly used in the analyses in the pre-selection step before the MVA.

#### 4.8.4. Projective Likelihood model

The projective likelihood model with probability density estimators (PDE) is used in PandoraPFA for the photon ID, due to its simplicity and low requirement on computing resources. The PandoraPFA implementation is discussed in section 5.5.

The likelihood classifier calculates the probability density for each discriminative variable, for signal and background (hence PDE approach). The overall signal and background likelihood are defined as products of the individual probability density of each variable. The likelihood ratio,  $R$ , is then defined as the signal likelihood over signal plus background likelihood. TMVA implementation also fits an underlying function to the probability density.

Similarly to the rectangular cut method, the likelihood model works better with decorrelated, gaussian like variables.

#### 4.8.5. Decision Tree model

Before discussing boost decision tree (BDT), it is necessary to introduce the decision tree model. The decision tree is a non-linear tree based model. Its rather complex nature requires a careful explanation of many concepts.

The decision tree is a binary tree, where each node, the splitting point, uses a single discriminative variable to decide whether an event is signal-like (“goes down by a layer to the left”), or background-like (“goes down by a layer to the right”). At each node, samples are divided into signal-like and background-like sub-samples. The tree growing starts at the root node, and stops after certain criterion are met. The stopping criterion could be the minimum number of events in a node, the number of layers of the tree, or a minimum/maximum signal purity.

The training of the decision tree refers to the determination of the optimal cut at the node by minimising a metric. Assuming the probability of the cut producing the signal is  $p$ , three commonly used metrics for two-class classification are:

1. Misclassification error:  $1 - \max(p, 1-p)$ ,
2. Gini index:  $2p(1-p)$ ,
3. Cross-Entropy or deviance:  $-p \log p - (1-p) \log (1-p)$ .

The applying of a trained decision tree is performed by transversion the tree from the root node to the end node. The event is classified as signal or background, depending on whether it falls in the signal-like or background-like end node.

Figure 4.7 illustrates a simple example of a decision tree. The signal class is the PhD student and the background class is the undergraduate student. The depth of this imbalance binary tree is 2. A splitting node is represented by a diamond. The signal-like end node is represented by the red rectangle and the background-like end nodes are represented by blue rectangles. The tree is constructed with two possible cuts, “Party ends before 1am” and “Know where free pizza is”. The attribute of samples is listed in table 4.3 and table 4.4. The Gini index metric to determine the optimal cut. If the first cut is “Party ends before 1am”, the probability of the cut producing the signal,  $p$ , is  $\frac{10}{13}$ , as there are 10 PhD students and 3 undergraduate students who end part before 1 am. Gini index give  $2p(1-p) \simeq 0.36$ . If the first cut is “Know where free pizza is”,  $p = \frac{10}{15}$ , as there are 10 PhD students and 5 undergraduate students who know where the free pizza

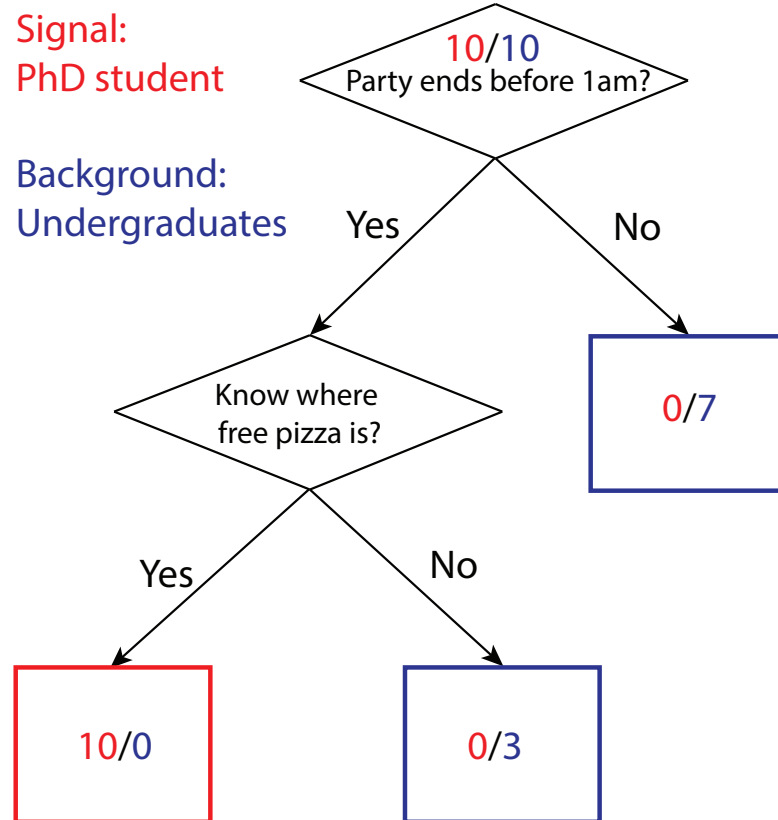


**Figure 4.7:** Example of a decision tree. Numbers in each node represent number of PhD student (red) and number of undergraduate student (blue) after each cut. Diamond boxes represent splitting nodes. Rectangular boxes represent end nodes. Blue boxes are background-like end nodes. Red boxes are signal-like end-nodes.

PhD student	Party ends before 1 am	Party ends after 1 am
Know where free pizza is	10	0
Not know where free pizza is	0	0

**Table 4.3:** The attribute of the PhD student class for the decision tree example shown in figure 4.7.

is located. Gini index is  $2p(1-p) \simeq 0.44$ . Therefore, by choosing the cut that minimise the Gini Index, the first cut is “Party ends before 1am”.

The simple tree in figure 4.7 is grown fully as each end node contains signal or background only. An example of applying the trained decision tree is provided: if there is a student who ends the party before 1 am and knows where a free pizza is located, then the student is classified as a PhD student.

Undergraduates	Party ends before 1 am	Party ends after 1 am
Know where free pizza is	0	5
Not know where free pizza is	3	2

**Table 4.4:** The attribute of the undergraduates class for the decision tree example shown in figure 4.7.

#### 4.8.6. To improve decision tree

The decision tree model has a low bias, but a high variance. This means it is very easy to construct a tree that fits the training data very well, but the tree would not be optimal for the testing sample. To overcome the instability of the decision tree, many methods have been developed. Some of the most successful ones are boosting, bagging, and random forest.

Boosting: it is a technique where the misclassified events receives a higher weight than the correctly classified events. Therefore, when the training is iterated, the misclassified events would receive higher and higher weights and be more likely to be classified correctly. The boosting is done at every iteration, which can be a few hundred or a few thousand times. This will create a “forest” of many trees. The final output could be a majority vote, by transversing the event to the end node for each tree in the forest.

Bagging: also known as boot-strap, it is a method that select a simple random sub-sets of the training sample, and apply the model. In this case, every boosting iteration takes a bagged sample, rather than the whole sample.

Random Forest: when a tree is grown, a randomly selected sub-set of discriminative variables are used to grow the tree. This method is known to reduce the variance of the tree.

#### 4.8.7. Boosted Decision Tree model

Boosted decision tree (BDT) contains a forest of decision trees , where each tree is iterated many times using a technique called boosting. By overcoming the instability of a single decision tree, BDT is often regarded as the best out-of-the-box machine learning method. There are two common boosting methods: adaptive boosting and gradient

boosting. The adaptive boosting, first introduced in [73], is discussed in further details, as it is simpler to understand than the gradient boosting.

The basic idea of adaptive boosting is that the tree making procedure focuses on events which are difficult to classify correctly. By assigning a weight to each event, after each tree growing iteration, the weights for misclassified events are gradually increased. Therefore misclassified events get more attention in the next iteration.

The adaptive boosting algorithm, adapted from [74], is outlined below:

- At the initialisation stage, event weight is initialised to  $w = 1/N$  for every event, for  $N$  total events.
- Iterate  $M$  times.  $M$  is the total number of trees. For iteration  $m$ :
  - Create a  $m^{th}$  tree with weighted samples.
  - Update  $m^{th}$  tree error function,  $err_m = \frac{\sum_{i=1}^N w_{i,m-1} B_{i,m}}{\sum_{i=1}^N w_{i,m-1}}$ .
  - Update  $m^{th}$  tree weight,  $\alpha_m = \log\left(\frac{1-err_m}{err_m}\right)$
  - Update  $i^{th}$  event weight,  $w_{i,m} = w_{i,m-1} e^{\alpha_m B_{i,m}}$ .
- The output,  $G(x)$ , for a testing event  $x$ , is a weighted vote from all  $M$  trees:

$$G(x) = \begin{cases} -1, & \text{if } \sum_{m=1}^M \alpha_m G_m(x) < 0, \\ 1, & \text{otherwise.} \end{cases} \quad (4.4)$$

The tree classifier output,  $G$ , is denoted as -1 or 1. One can think of -1 as background and 1 as signal. There are  $N$  events and  $M$  iterations (trees).  $B$  represents if a event is misclassified. For the  $i^{th}$  event in the  $m^{th}$  tree,  $B_{i,m} = 1$  if the event is misclassified and 0 if the event is correctly classified.  $w_{i,m}$  represent the event weight for  $i^{th}$  event in  $m^{th}$  tree.

In each iteration, if the  $i^{th}$  event is misclassified, the weight increases by a factor of  $(1 - err_m)/(err_m)$ . Otherwise, the event weight does not change.

The power of the adaptive boosting is to dramatically improve the performance of a weak classifier. A weak classifier is a classifier which is gives a predictive performance slightly better than a random guessing. A small decision tree would be a weak classifier.

By sequentially applying many weak classifier with weighted samples, the final “forest” is very robust with very good performance.

TMVA implementation of the BDT for the output is using a likelihood estimator, depending on how often an event is classified as signal in the forest. The likelihood number is later used to select signal from background.

#### **4.8.8. Optimisation of Boosted Decision Tree**

Many parameters of the BDT can be optimised. The most important parameter is the depth of a tree, which determines how many end nodes the tree has, or the degrees of freedom of the tree. The related parameter is the number of trees. Experience shows that using many small trees yields the best result.

The number of trees is another important parameter. Intuitively large number of trees leads to overfitting. However, it has been shown that a large number does not lead to overfitting [74]. Therefore there is a debate on the metric to determine the optimal number of trees.

The minimum number of events in a node, which is a stopping criteria for tree growing, affects the size of the tree. But it is less influential than the depth of the tree.

The boosting has two variants in TMVA implementation: adaptive boost and gradient boost.

The learning rate of the adaptive boost controls how fast the weight changes for events in each boosting iteration. Experience shows that a small learning rate ( $\sim 0.1$ ) with many trees works better than a large learning rate with fewer trees.

The shrinkage rate in the gradient boost is similar to the learning rate in the adaptive boost. The shrinkage rate controls how fast the weight changes for events in each boosting iteration. Again a small value ( $\sim 0.1$ ) is preferable.

The usual choice of the metric for the optimal cuts is either the Gini index or the cross-entropy. Typically the Gini index metric is chosen. The use of the Gini Index makes little differences to performances, comparing to the cross-entropy metric.

The number of bins per variable is a necessary parameter to make tree growing efficient, because discretely binned variables are faster to compute than continuous variables. This parameter, however, does not impact the performance much. But because

variables are binned, variables should be pre-processed before going into the model. For example, the variable should be limited to a sensible range to avoid the extreme values. The variable should also be transformed to obtain a more uniform distribution, if the original distribution is highly skewed.

For the end node, it can be determined as either signal-like or background-like, based on the majority of the training events in the end node. Numerically, it corresponds to 1/0. However, the end node could also use signal purity as the output, resulting in a continues spectrum of [0,1].

The bagging fraction determines the fraction of randomly selected samples used in each boosting iteration. By choosing a small value, samples between each boosting iteration are less correlated. Hence the overall performance improves.

The DoPreSelection flag allows the classifier to throw away phase spaces where there are only background events.

#### 4.8.9. Multiple classes

The above discussion assumes two classes - signal and background. The argument can be extended to multiple classes. There are two ways for the training multiple classes. “One versus one” scheme trains each class against each other class, and the overall likelihood is normalised. The second way to train these multiple classes is called “one versus all”, when each class is trained against all other classes.

Using a three-class example, A, B and C, “one versus one” scheme trains A against B; B against C; and C against A. Then the likelihood is normalised. “One versus all” scheme would train A against non-A; B against non-B; and C against non-C.

TMVA multiclass implementation uses the “one versus all” scheme. For each class, the multiclass classifier will train the class as the signal against all other classes as the background. This process is repeated for each class. The classifier output for a single event is a normalised response using all trained classifier, where the sum is one. The response of each class in an event can be treated as the likelihood. In the classicisation stage, the event is classified into a particular class if that class has the highest classifier output response.

The advantage of using the multiclass classifier instead of a two-class classifier for multiple classes is that the correlation between different classes are accounted for. The

classifier outputs are correctly adjusted for multiple classes. Hence one event can only be classified into one class. The issue with the multiclass is that powerful discriminative variables for each individual class need to enter the training stage simultaneously, resulting in a large number of variables in the multiclass classifier.

# Chapter 5.

## Photon Reconstruction in PandoraPFA

*‘When I walk along with two others, from at least one I will be able to learn.’*

— Confucius, 551 BC - 479 BC

Many aspects of the photon reconstruction are important. A good single photon energy resolution is necessary to reconstruct heavy particles using decay channels involving photons, such as  $\pi^0 \rightarrow \gamma\gamma$ . Another important aspect of the photon reconstruction is the photon separation resolution, which is the measure of minimum spatially closeness of two just resolved photons. The photon separation resolution is crucial for a photon counting experiment, where the number of the photon is used as a physics quantity. The most recent example of such a photon-counting experiemnt, benefited from this photon reconstruction, is the  $H \rightarrow \gamma\gamma$  simulation study at  $\sqrt{s} = 3$  TeV at the CLIC [75].

Having an efficient photon reconstruction in a dense jet environment also improves the overall event reconstruction. As the particle flow approach to the calorimetry aims to reconstruct each individual particle, by assigning correct calorimeter hits to photons, assigning the remaining hits to tracks for charged particles becomes an easier problem. Hence the correct track-cluster association can be achieved with fewer mistakes, and the jet energy resolution improves.

This chapter stats with a overview of the electromagnetic shower. It then discusses a number of photon reconstruction algorithms within the PandoraPFA framework, followed

by the performances of these algorithms. Part of this chapter has been published in a conference proceeding [76].

## 5.1. Electromagnetic shower

An electromagnetic (EM) shower refers to the pair production and bremsstrahlung when a high energy photon or electron passing though a thick absorber. The properties of the EM shower is used as the basis of forming photon candidates, photon ID test, and photon separation.

The pair production and bremsstrahlung generate many low energy photons and electrons, producing a shower-like structure. Two suitable length scales to describe the EM shower are the radiation length and the Molière radius. The radiation length of a material describes the longitudinal shower profile, defined as the mean distance travelled where an electron loses its energy by a factor of  $1/e$  via bremsstrahlung. It is also defined as the mean free path for pair production by a high energy photon [77]. The Molière radius of a material describes the transverse shower profile.

Figure 5.1 shows the simulated longitudinal electromagnetic shower profiles as a function of radiation length for electrons and photons. The mean EM longitudinal shower profile can be described by the following function [78] :

$$\frac{dE}{dt} = E_0 b \frac{(bt)^{a-1} e^{-bt}}{\Gamma(a)}, \quad (5.1)$$

where  $t$  is the number of radiation lengths; the parameter  $E_0$  is the shower energy; the parameter  $b$  varies slightly with material but it is sufficient to use  $b = 0.5$  for the purpose of photon reconstruction [6]; the parameter  $a$  is:

$$a = 1.25 + 0.5 \ln \left( \frac{E_0}{E_c} \right), \quad (5.2)$$

where  $E_c$  is the critical energy. The critical energy is defined as the energy at which the rate of losing energy by bremsstrahlung is the same as the rate of losing energy by ionisation [79]. The alternative definition is the energy at which the energy loss by ionisation per radiation length is the same of the particle energy [80]. This parametrisation of the EM longitudinal shower profile should only be used to describe an average behaviour of the EM shower, as the fluctuation is important.

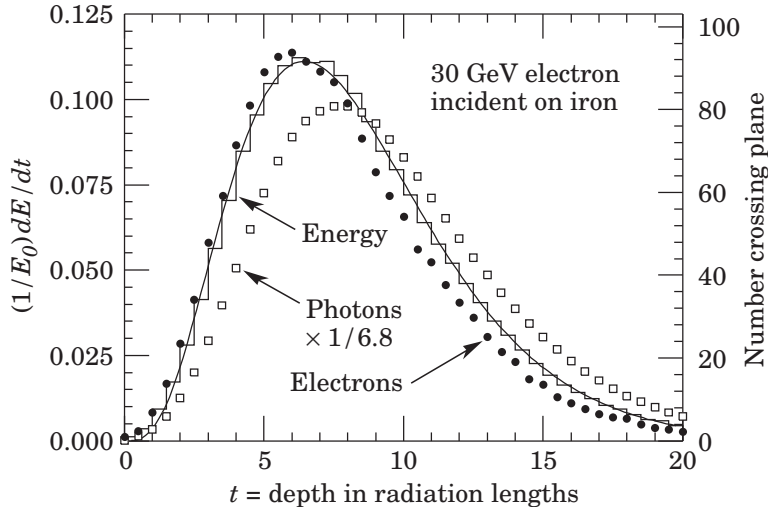


**Figure 5.1:** An EGS4 simulation of a 30 GeV electron-induced electromagnetic shower in iron. The histogram shows fractional energy deposition as a function of radiation lengths, and the curve is a gamma-function fit to the distribution. Circles and squares are the number of electrons and photons respectively with total energy greater than 1.5 MeV crossing planes with scale on right. Plot is taken from [6].

The transverse shower profile can be described as a narrow cone widening as the shower develops. 90% of the energy is contained in a fiducial cylinder with a radius of one Molière radius, along the direction of the shower. The dense shower core of the transverse profile allows the separation of two EM showers using a two-dimensional peak-finding algorithm, explained in a later section.

## 5.2. Overview of photon reconstruction in PandoraPFA

PandoraPFA is a multi-algorithm pattern-recognition software package for the event reconstruction and an implementation of the particle flow approach to calorimetry. A detailed discussion of the PandoraPFA and the main steps of the PandoraPFA event reconstruction can be found in section 4.4. The multi-algorithm approach of the PandoraPFA allows each algorithm to deal with a particular issue in the reconstruction.

Five algorithms are developed to tackle different issues in the photon reconstruction. The most important photon algorithm is the PHOTON RECONSTRUCTION algorithm. It reconstructs photons from calorimeter hits in the ECAL, including forming a photon

candidate and applying a photon ID test, with special treatments for photons close to charged particles.

Three algorithms remove photon fragments at a later stage in the reconstruction. Two photon fragment removal algorithms merge fragments in the ECAL, and one algorithm merges fragments in the HCAL. These algorithms improve the single photon energy resolution.

The last photon algorithm is a photon splitting algorithm. The algorithm separates accidentally merged photons, which helps photon separation resolution.

## 5.3. Photon Reconstruction algorithm

The PHOTON RECONSTRUCTION algorithm is a photon reconstruction algorithm at the early stage of the reconstruction. It corresponds to “Particle ID” stage of the PandoraPFA reconstruction chain. Main steps of the PHOTON RECONSTRUCTION algorithm, shown in figure 5.2, are: forming photon clusters; finding photon candidates; photon ID test; and optional fragment removals.

### 5.3.1. Form photon clusters

The inputs of the PHOTON RECONSTRUCTION algorithm are calorimeter hits in the ECAL that have not been used in previous algorithms. For example, muon reconstruction algorithms will form muons and remove calorimeter hits associated with muons from the reconstruction. The muon associated calorimeter hits are not used to form photons.

This step finds large potential photon clusters in the ECAL. The clusters are formed in a way such that a photon would not be split into two clusters, but one cluster may contain multiple photons. For simplicity, the algorithm opts to reuse the cone clustering algorithm provided inside PandoraPFA to find large clusters. Since the target for reconstruction is neutral photons, the cone cluster algorithm is set to use high-energy ECAL calorimeter hits as initial seeds, instead of using tracks as initial seeds.

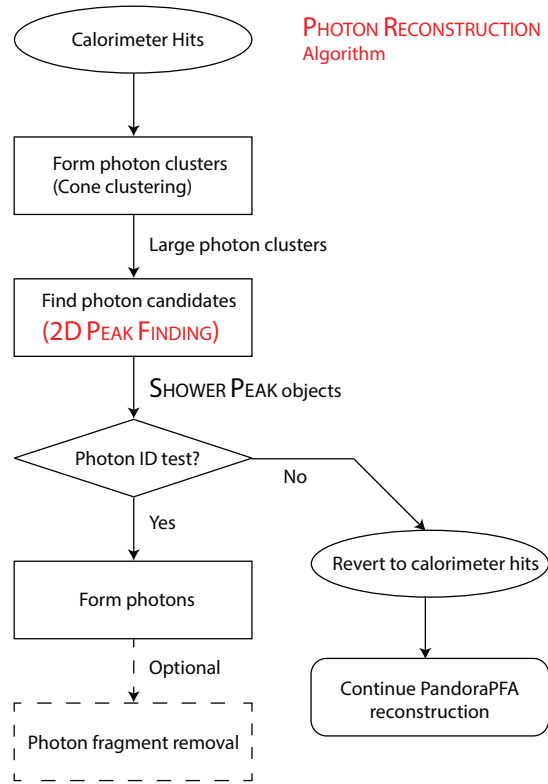


**Figure 5.2:** Main steps in the PHOTON RECONSTRUCTION algorithm.

### 5.3.2. Find photon candidates

The next stage is to refine large photon clusters into smaller photon candidates. Each photon candidate should contain calorimeter hits from one photon only.

The method for refining clusters is to split a three-dimensional cluster into several smaller clusters. The three-dimensional splitting problem is harder than a two-dimensional one. Therefore, a translation is needed to map the three-dimensional problem to a more manageable two-dimensional problem. This translation relies on the characteristic transverse EM shower profile, which is characterised by a narrow cone, widening while the shower develops. Along the direction of the shower, an EM shower can be modelled as a dense shower core with peripheral calorimeter hits around the core. When the energy deposition is projected on to a two-dimensional plane, an EM shower core would appear as a mountain-like structure in the plane. One example a large photon cluster projected onto a two-dimensional plane, where two EM showers are identified, is shown in Figure 5.3. Hence, by identifying a peak in the two-dimensional plane, an EM shower core is identified.

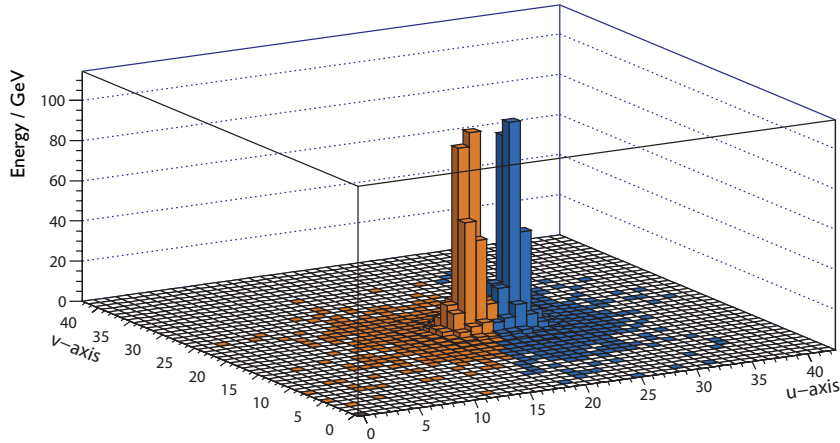


**Figure 5.3:** Two 500 GeV photons (yellow and blue) belonged to a large photon cluster, just resolved in a transverse plane orthogonal to the direction of the flight by projecting their energy depositions. The axes U and V are orthogonal axes in units of the ECAL cell sizes. The Z axis is the sum of the calorimeter hit energy.

A high-performance two-dimensional peak finding algorithm is the key to identify multiple photon candidates within a photon cluster. Due the complexity of the projection and the peak finding procedure, a peak-finding algorithm is developed, and discussed in section 5.4. The output of the two-dimensional peak-finding algorithm is a collection of SHOWER PEAK objects. Each SHOWER PEAK object corresponds to a photon candidate and associated calorimeter hits.

### 5.3.3. Photon ID test

This step applies the photon ID test on the SHOWER PEAK object. The photon ID test uses a multidimensional likelihood classifier, which is discussed in section 5.5. A set of variables, which exploit features of electromagnetic showers, are used. The response from the classifier determines if a SHOWER PEAK object is a photon. If it is a photon, the SHOWER PEAK object would be tagged as a photon and the SHOWER PEAK object does not participate in the subsequent event reconstruction. The identified photon reenters the event reconstruction at the fragment removal stage after the charged particle reconstruction. If SHOWER PEAK object is not a photon, the SHOWER PEAK object will be discarded. Associated calorimeter hits will be passed on to the next stage of the reconstruction.

### 5.3.4. Photon Fragment removal

The photon fragment removal algorithm merges small photon fragments to identified photons. The algorithm is optional as it is not used by the default setting of the event reconstruction. Since this algorithm shares the same logic as another fragment removal algorithm, two algorithms are discussed together in a later section 5.6.

This step marks the end of the photon reconstruction algorithm. The outputs are a collection of reconstructed photons, separated from non-photon calorimeter hits.

## 5.4. Two-dimensional peak-finding algorithm

As discussed in section 5.3.2, identifying photon candidates inside a cluster is translated to identifying peaks in a two-dimensional plane, with the two-dimensional peak-finding algorithm (2D PEAK FINDING algorithm). An example of two photons resolved in a two dimensional plane is shown in the figure 5.3. The 2D PEAK FINDING algorithm aims to correctly identify peak positions in a two-dimensional histogram and to associate calorimeter hits to identified peaks.

There are two variants of the 2D PEAK FINDING algorithm: the neutral cluster variant and the charged cluster variant. The base algorithm, the neutral cluster variant, treats all clusters as potential photon clusters. A flow chart of the main steps of the neutral cluster variant is shown in figure 5.4.

### 5.4.1. Initialise the two-dimensional histogram

This step initialises a two-dimensional (2D) histogram to host the projection of the energy deposition of the photon cluster. For the best resolving power between photons, the projection direction is chosen to be the direction of the cluster. Two axes of the two-dimensional histogram are chosen such that axes and the direction of the cluster form an orthogonal bases in the three-dimensional space.

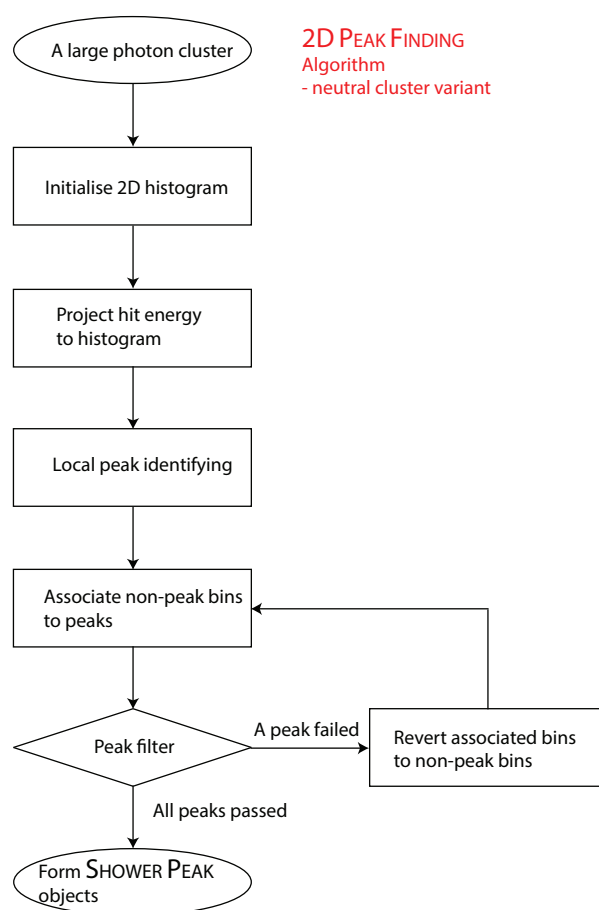


**Figure 5.4:** Main steps in the neutral cluster variant of 2D PEAK FINDING algorithm.

### 5.4.2. Project calorimeter hits to histogram

This step projects positions of the calorimeter hits associated with the photon cluster onto the 2D histogram initialised in the previous step. For a finite-sized 2D histogram, the projection is chosen such that the cluster centroid position is at the centre of the histogram. One bin size along either axes corresponds to one ECAL square cell length. The relative distance between the calorimeter hit position and the cluster centroid position is converted into a distance vector. The distance vector,  $\vec{s}_i$ , of a calorimeter hit  $i$  is obtained by:

$$\vec{s}_i = \frac{\vec{a}_i - \langle \vec{a} \rangle}{d_{cell}}, \quad (5.3)$$

where  $\vec{a}$  is the three-dimensional position of the hit  $i$ ;  $\langle \vec{a} \rangle$  is the centroid position of cluster  $a$ ; and  $d_{cell}$  is the ECAL square cell length. The distance vector is subsequently projected onto the histogram using the scalar product with the axes vectors.

The height of a bin in the 2D histogram is the sum of the energies associated with the calorimeter hits that fall in that particular bin. Each bin contains calorimeter hits that projected onto the bin.

### 5.4.3. Local peak identifying

This step identifies all local peaks in the 2D histogram. A local peak is defined as a bin where its height is above all eight neighbouring bins. The 2D histogram is scanned to identify all local peaks.

### 5.4.4. Associate non-peak bins to peaks

Having tagged all local peaks, this step associates non-peak bins to peaks based on the energy of the peak and the distance of the non-peak bin to the peak bin. The energy dependence is needed as the transverse EM shower width increases with the increase of the energy of the EM shower. The distance dependence is needed because the EM showers have dense shower cores. A non-peak bin should be associated to a high-energy peak bin that is close to the non-peak bin.

To associate non-peak bins to a peak bin, the peak bin is chosen by minimising the metric:

$$\min_i \frac{d_i}{\sqrt{E_i}} \quad (5.4)$$

where  $d_i$  is the Euclidean distance between a non-peak bin and a peak bin  $i$  on the 2D histogram, and  $E_i$  is the height of the peak bin  $i$ . The metric is iterated over all peak bins for each non-peak bin.

### 5.4.5. Peak filtering

The performance of the 2D PEAK FINDING algorithm is improved by peak filtering. In a two-dimensional histogram, such as the one in figure 5.3, major peaks most likely correspond to physical photons, while the minor peaks more likely come from fluctuations in the energy deposition. To select only the major peaks, every time after all non-peak bins are associated with peak bins, minor peaks with fewer than three bins associated (including the peak bin) are discarded. These discarded bins are re-associated with other peak bins. This iterative process stops when all peak bins have at least three bins associated.

The peak filtering step also allows bins with height below a critical value to not participate in the peak finding. The default value is set such that only non-empty bins are used.

The SHOWER PEAK object is created after peak filtering. One SHOWER PEAK object contains one peak bin and associated non-peak bins. The associated calorimeter hits within the bins are attached to the SHOWER PEAK object as well. If multiple peaks are identified in a cluster, multiple SHOWER PEAK objects are created as outputs.

This marks the end of the neutral clusters variant of the PHOTON RECONSTRUCTION algorithm, outlined in figure 5.4.

### 5.4.6. Candidate close to track projection

If a photon candidate is close to the projection of the track in the front of the ECAL, it is more likely that the candidate is a charged hadron. Misidentifying a charged hadron as a photon leads to significant degradation in reconstruction performance, because there will

be double counting of energy from the track and from the charged hadron misidentified as a photon. However, if a photon next to a charged hadron is carefully reconstructed, the overall reconstruction is improved.

This step aims to carefully identifies photon candidates next to charged hadrons, by using track information and features of EM showers. The important information is the electromagnetic shower typically starting in first few layers of the ECAL with direction of the EM shower largely unchanged.

Figure 5.5 shows the main steps in the full 2D PEAK FINDING algorithm, including the treatment to clusters close to tracks. The "Close to track" step determines if a cluster is close to a track. If a cluster is less than 3 mm from the closest track projection, it is treated as a potential charged cluster.

The "Create and iterate sub-clusters" step performs the following. The ECAL is sliced longitudinally. For example, the default three slices will result in three ECAL fiducial spaces, which cover spaces from the front of the ECAL to a third, two thirds, and the back of the ECAL, respectively. Three sub-clusters contained in each fiducial space are created. The neutral cluster variant of the 2D PEAK FINDING algorithm is then repeated for each sub-cluster, starting from the sub-cluster closest to the front of the ECAL, to the sub-cluster closest to the back of the ECAL.

The SHOWER PEAK objects created from each sub-cluster undergo the "SHOWER PEAK filter" step. Firstly all peaks and associated SHOWER PEAK objects from the first sub-cluster are preserved. Afterwards, peaks and associated SHOWER PEAK objects from subsequent sub-clusters are only preserved, if the peak bin position can be linked to a peak bin from the previous sub-cluster, allowing a shift in the peak bin position by no more than one neighbouring bin. The non-preserved peak and the associated SHOWER PEAK object are discarded. Furthermore, if a peak bin is within the eight neighbouring bins of the track projection, the peak is discarded. Only the peaks that are preserved in every sub-cluster through the iteration of "SHOWER PEAK filter" will form the final SHOWER PEAK objects.

#### 5.4.7. Inclusive mode

The two-dimensional histogram is iterated many times during the algorithm. The time complexity is  $O(n^2)$  for a  $n$  bins by  $n$  bins histogram (Default  $n = 41$ ). Therefore, for the purpose of speed, it is undesirable to have a large number of bins. Having a small

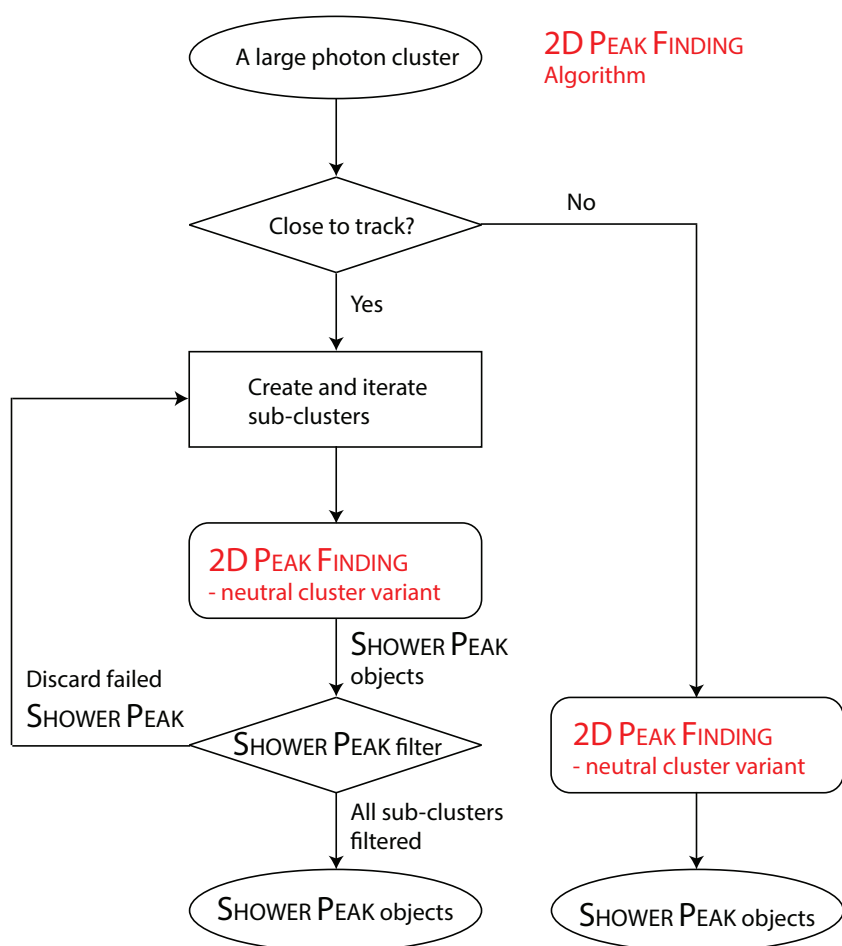


**Figure 5.5:** Main steps in the 2D PEAK FINDING algorithm, including the charged cluster variant.

finite-sized histogram speeds up the calculation. However, because of the finite size, only energy deposition projected onto the histogram would be considered for peak finding. Calorimeter hits projected outside the histogram would not be used when SHOWER PEAK objects are constructed. This behaviour is suitable if the algorithm is only interested in finding the EM shower cores, for example, the PHOTON RECONSTRUCTION algorithm. However, for photon splitting, all calorimeter hits should be used. Hence the inclusive mode of the 2D PEAK FINDING algorithm is developed, and allows energy deposition projected outside the histogram to be associated with identified peaks.

## 5.5. Likelihood classifier for photon ID

In section 5.3.3, the photon ID test in the photon reconstruction algorithm was outlined. This section describes the multidimensional likelihood classifier used in the photon ID test in details.

### 5.5.1. Variable used in the likelihood classifier

Variables exploit the differences between a characteristic electromagnetic shower and a hadronic shower, and the fact that a photon is more likely to be isolated from other showers and charged tracks. A full list of variables can be found in table 5.1.

Two variables exploit the longitudinal EM shower distribution: the variable  $t_0$  is the start layer from the longitudinal shower profile, shown in figure 5.6a; and  $\delta l$  is fractional difference of the observed shower profile to the expected EM shower profile [34]:

$$\delta l = \frac{1}{E_0} \sum_i |\Delta E_{obs}^i - \Delta E_{EM}^i|, \quad (5.5)$$

where  $\delta l$  is minimised as a function of the  $t_0$ . The  $\delta l$  distribution for photons and non-photons is shown in figure 5.6b. For a true photon,  $t_0$  and  $\delta l$  are expected to be small.

Three variables use information from the transverse EM shower: the variable  $\langle w \rangle$  is the energy weighted root-mean-squared distance of all bins in a SHOWER PEAK to its peak bin, shown in figure 5.6c. This is a measure of the transverse shower size; the variable  $\delta \langle w_{UV} \rangle$  is the smallest ratio of the two root-mean-squared distances of all bins

in a SHOWER PEAK to its peak bin in each of the U, V axis direction, a measure of the circularity of the transverse shower; the last variable,  $\delta E_{cluster}$ , is the ratio between the energy of the SHOWER PEAK object to the cluster energy. This is a measure of the dominance of a photon in a cluster.

The last variable used in the classifier,  $d$ , is the distance between the photon candidate and the closest track projection in the front of the ECAL. The SHOWER PEAK object is less likely to be a photon if it is close to a track. Its distribution for photons and non-photons is shown in figure 5.6d.

Categories	Variables
Longitudinal shower profile	$\delta l, t_0$
Transverse shower profile	$\langle w \rangle, \delta \langle w_{UV} \rangle, \delta E_{cluster}$
Distance to track	$d$

**Table 5.1:** List of variables for the likelihood based photon ID test.

### 5.5.2. Projective Likelihood classifier

Projective likelihood classifier with probability density estimators is used in PandoraPFA for the photon ID due to its low requirement on computing resources.

The probability distribution of each variable for photons and non-photons are obtained in the training stage. The distributions of these variables are normalised to probability distribution, stored in binned histograms. The classifier is improved by realising the variable distributions varies with photon energies. Thus the variables distributions are stored separately for different photon energy ranges. There are 8 energy ranges, obtained by binning the distribution of photon energies at 0.2, 0.5, 1, 1.5, 2.5, 5, 10, 20 GeV. The classifier training uses simulated 250 GeV  $Z'$  events, with  $Z' \rightarrow u\bar{u}/d\bar{d}/s\bar{s}$ . The 250 GeV jets allow the training of photon candidates with energies greater than 20 GeV.

After training, for a given photon candidate with the energy in the energy bin  $\alpha$ , the likelihood classifier output is given by

$$\text{Pid} = \frac{N_p^\alpha \prod_i^6 P_{i,p}^\alpha}{N_p^\alpha \prod_i^6 P_{i,p}^\alpha + N_{np}^\alpha \prod_i^6 P_{i,np}^\alpha} \quad (5.6)$$

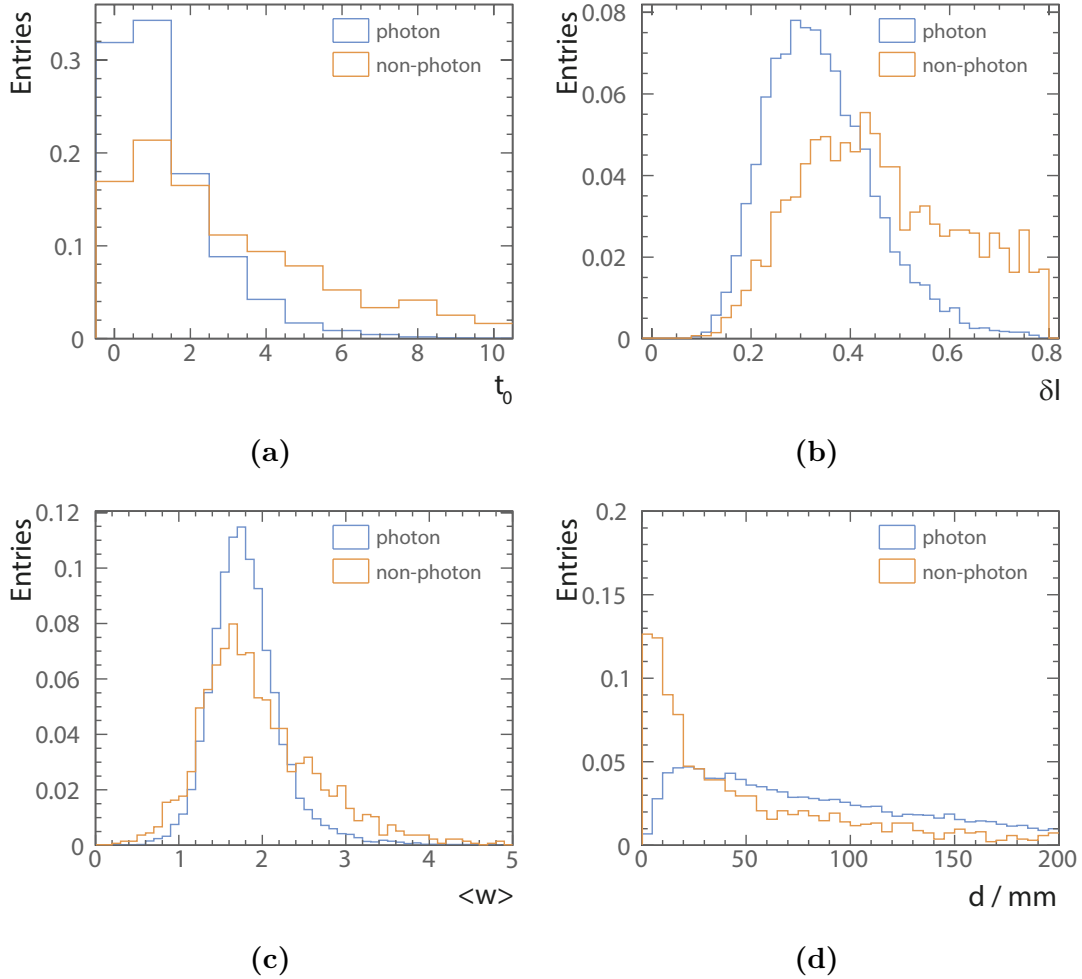


**Figure 5.6:** Distributions for a) the start layer from the longitudinal shower profile ( $t_0$ ), b) the fractional difference of the observed shower profile to the expected EM shower profile ( $\delta l$ ), c) the energy weighted root-mean-squared distance of all bins in a SHOWER PEAK to its peak bin ( $\langle w \rangle$ ), and d) the distance between the photon candidate and the closest track projection in the front of the ECAL ( $d$ ) are shown. All plots are normalised that the area under curve is 1. The particle ID is determined using the truth information. All plots are generated with simulated 250 GeV  $Z'$  events, where  $Z' \rightarrow u\bar{u}/d\bar{d}/s\bar{s}$ .

where  $P_{i,p}^\alpha$  and  $P_{i,np}^\alpha$  are the probability of the  $i^{th}$  variable of the photon candidate fallen in the  $i^{th}$  variable probability distribution of the photon and non-photons in the energy bin  $\alpha$ , respectively; the variables  $N_p^\alpha$  and  $N_{np}^\alpha$  are the number of photons and non-photons in the energy bin  $\alpha$  in the training sample, respectively.

During classification, a photon candidate passes the photon ID test if

$$\begin{cases} \text{PID} > 0.6, & \text{if } 0.2 < E < 0.5 \text{ GeV} \\ \text{PID} > 0.4, & \text{if } E \geq 0.5 \text{ GeV} \end{cases} \quad (5.7)$$

where  $E$  is the photon candidate energy. Two values of the cuts on PID reflect the different confidences level of the photon ID test with different candidate energies. The test is more cautious with low-energy candidates.

## 5.6. Photon fragment removal algorithm in the ECAL

During the reconstruction, it is possible that a core of the photon electromagnetic shower is identified as a photon (the main photon), but the outer part of the shower is reconstructed as a separate particle, and wrongly identified as a photon or a neural hadron. Figure 5.7 shows a typical creation of such a photon fragment. A fragment typically does not have the electromagnetic shower structure, and has much lower energy than a proper photon. If a photon-fragment pair is merged, the pair should be consistent with an one-particle profile.

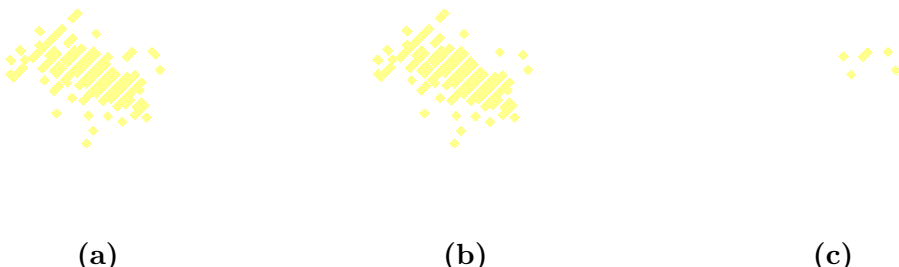


**Figure 5.7:** An event display of a typical 10 GeV photon shown in a), reconstructed into a main photon shown in b), and a photon fragment shown in c).

Photon fragment removal algorithms can exist at different places in the reconstruction: immediately after the PHOTON RECONSTRUCTION algorithm, or after the charged particle reconstruction. Since these algorithms share the same logics, they will be discussed together. The algorithm used after the charged particle reconstruction will be discussed here.

Spatially close photon and a potential fragment form a pair of particles (photon-fragment pair). Kinematic and topological properties of a photon-fragment pair are examined. The pair is merged when its properties pass a set of cuts, where cuts are developed by comparing true photon-fragment pairs and non photon-fragment pair. This merging test is iterated over all possible photon-fragment pairs. If multiple photon-fragment pairs with the same photon pass the merging test, the pair with closest distance metric,  $d$ , will be merged.

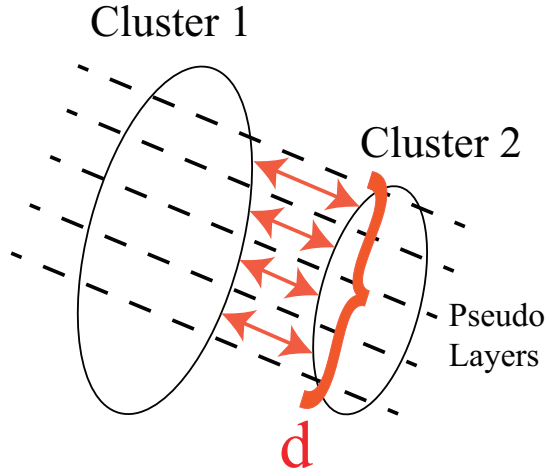
Depending on whether the fragment is reconstructed as a photon or a neutral hadron, the photon-fragment pairs is classified into photon-photon-fragment pairs and photon-neutral-hadron-fragment pairs, because they have different kinematic and topological distributions. The pairs are further classified into low energy and high energy pairs, depending on whether the fragment energy ( $E_p$ ) is above 1 GeV.

Table 5.2 lists cuts for merging photon-photon-fragment pairs and photon-neutral-hadron-fragment pairs for both low energy and high energy fragments: the variable  $d_c$  gives the distance between centroids of each PFO in the pair, which is a computationally quick but crude measurement; the variable  $d_h$  is the minimum distance between calorimeter hits of each PFO in the pair; the variable  $d$  is the mean energy weighted intra-layer distance between each PFO in the pair (see figure 5.8):

$$d = \frac{\sum_i^{layers} d_l^i E_f^i}{\sum_i^{layers} E_f^i} \quad (5.8)$$

where  $i$  indicates  $i^{th}$  pseudo-layer of the ECAL; the parameter  $d_l^i$  is the minimum distance between calorimeter hits of the pair in the  $i^{th}$  pseudo-layer; and  $E_f^i$  is the energy of the fragment in the  $i^{th}$  pseudo-layer. All three distance metrics should be small to merge a photon-fragment pair.

Other quantities used in the merging metric include  $E_m$  the main photon energy;  $E_f$ , the fragment energy;  $E_{p1}$  and  $E_{p2}$ , the energies of the two largest peaks and associated calorimeter hits respectively, found by the 2D PEAK FINDING algorithm, ordered by descending energy, using the pair as input;  $N_{calo}$ , the number of the ECAL hits in the



**Figure 5.8:** Illustration of distance metric,  $d$ .

fragment; and  $|\cos(\theta_Z)|$ , the absolute cosine of the polar angle of the main photon with respect to the beam direction.

Here each set of logics for merging fragments are discussed. Fragments passing either set of cuts will be merged. The values used in the cuts are listed in Tab:  
letab:photonFragRemovalCuts.

### 5.6.1. Transverse shower comparison cuts

One logic of merging is when the fragment is close to the main photon, and the fragment-photon pair looks like one photon in the two-dimensional energy deposition projection. The transverse shower comparison requires  $\frac{E_{p1}}{E_m+E_f} > 0.9$ , demanding most energy of the cluster contains in the first SHOWER PEAK object.

### 5.6.2. Low energy fragment cuts

The logic of merging is when the fragment has low energy and is close to the main photon. Hence  $d$  and  $E_p$  are both demanded to be small.

### 5.6.3. Small fragment cuts

Fragments that are close to the main photon and have very few number of associated calorimeter hits will be merged. The multiple cuts allow the merging of a fragment with fewer number of calorimeter hits with a slightly larger distance separation to the main photon, or a fragment with a slightly bigger number of calorimeter hits with a smaller distance separation to the main photon.

### 5.6.4. Small fragment forward region cuts

This set of logic is similar to the previous one, except that it only considers the fragment in the end cap region,  $|\cos(\theta_Z)| > 0.7$ .

### 5.6.5. Relative low energy fragment cuts

The merged fragment should be relatively low energetic. If the fragment is close to the photon, and it is relative low energy to the photon, then the fragment is merged to photon. The multiple cuts allow the merging of a fragment with a smaller fragment-to-photon energy ratio with a slightly larger distance separation to the main photon, or a fragment with a slightly bigger fragment-to-photon energy ratio with a smaller distance separation to the main photon.

Since all possible photon-fragment pairs are compared, this is a costly cooperation with  $O(n^2)$  time complexity for  $n$  particles. The speed is improved by considering only pairs with  $d < 80$  mm.

### 5.6.6. Photon fragment recovery algorithm after the Photon Reconstruction algorithm

The photon fragment removal algorithm immediately after the PHOTON RECONSTRUCTION algorithm shares the same logics as the stated above. The cuts for merging fragments are listed in table 5.3.

$E_f \leq 1 \text{ GeV}$	Photon-photon	Photon-neutral-hadron
transverse shower comparison, or	$d < 30 \text{ mm}; \frac{E_{p1}}{E_m + E_f} > 0.9;$ $\frac{E_{p2}}{E_f} < 0.5; E_{p1} > E_m$	-
low energy fragment, or	$d < 20 \text{ mm}; E_p < 0.4 \text{ GeV}$	$d < 20 \text{ mm}; d_c < 40 \text{ mm}$
small fragment 1, or	$d < 30 \text{ mm}; N_{calo} < 40;$ $d_c < 50 \text{ mm}$	$d < 50 \text{ mm}; N_{calo} < 10;$ $d_h < 50 \text{ mm}$
small fragment 2, or	$d < 50 \text{ mm}; N_{calo} < 20$	-
small fragment forward region, or	$N_{calo} < 40; d_c < 60 \text{ mm};$ $E_f < 0.6 \text{ GeV};$ $ \cos(\theta_Z)  > 0.7$	-
relative low energy fragment	$d < 40 \text{ mm}; d_h < 20 \text{ mm};$ $\frac{E_f}{E_m} < 0.01$	$d < 40 \text{ mm}; d_h < 15 \text{ mm};$ $\frac{E_f}{E_m} < 0.01$
$E_f > 1 \text{ GeV}$	Photon-photon	Photon-neutral-hadron
transverse shower comparison, or	$\frac{E_{p1}}{E_m + E_f} > 0.9; E_{p2} = 0 \text{ or}$ $(\frac{E_{p2}}{E_f} < 0.5, E_{p1} > E_m)$	$\frac{E_{p1}}{E_m + E_f} > 0.9; E_{p2} = 0 \text{ or}$ $(\frac{E_{p2}}{E_f} < 0.5, E_{p1} > E_m)$
relative low energy fragment 1, or	$d < 40 \text{ mm}; d_h < 20 \text{ mm};$ $\frac{E_f}{E_m} < 0.02$	$d < 40 \text{ mm}; d_h < 20 \text{ mm};$ $\frac{E_f}{E_m} < 0.02$
relative low energy fragment 2, or	-	$d < 40 \text{ mm}; d_h < 20 \text{ mm};$ $\frac{E_f}{E_m} < 0.1; E_f > 10 \text{ GeV}$
relative low energy fragment 3	-	$d < 20 \text{ mm}; d_h < 20 \text{ mm};$ $\frac{E_f}{E_m} < 0.2; E_f > 10 \text{ GeV}$

**Table 5.2:** The cuts for merging photon-photon-fragment pairs and photon-neutral-hadron-fragment pairs for both low energy and high energy fragments, after charged hadron reconstruction.  $d$ ,  $d_c$  and  $d_h$  are the mean energy weighted intra-layer distance of the pair, the distance between centroids, the minimum distance between calorimeter hits of the pair, respectively.  $E_m$  and  $E_f$  are the main photon energy and the fragment energy, respectively.  $E_{p1}$  and  $E_{p2}$  are the energies the two largest peaks, found by peak finding algorithm, ordered by descending energy, respectively.  $N_{calo}$  is the number of the calorimeter hits in the fragment.  $|\cos(\theta_Z)|$  is the absolute cosine of the polar angle, where beam direction is the z-axis.

$E_f \leq 1 \text{ GeV}$	Photon-photon	Photon-neutral-hadron
transverse shower comparison, or	$d < 20 \text{ mm}; \frac{E_{p1}}{E_m+E_f} > 0.9;$ $E_{p2} = 0 \text{ or } (\frac{E_{p2}}{E_f} < 0.5,$ $E_{p1} > E_m)$	$d < 20 \text{ mm}; \frac{E_{p1}}{E_m+E_f} > 0.9;$ $E_{p2} = 0 \text{ or } (\frac{E_{p2}}{E_f} < 0.5,$ $E_{p1} > E_m)$
low energy fragment, or small fragment 1, or	$d < 20 \text{ mm}; E_p < 0.2 \text{ GeV}$ $d < 30 \text{ mm}; N_{calo} < 20;$ $d_h < 13 \text{ mm}$	$d < 50 \text{ mm}; N_{calo} < 10;$ $d_h < 50 \text{ mm}$
small fragment 2, or	$d_c < 30 \text{ mm}; N_{calo} < 10;$ $d_h < 13 \text{ mm}$	-
relative low energy fragment	-	$d < 40 \text{ mm}; d_h < 15 \text{ mm};$ $\frac{E_f}{E_m} < 0.01$
$E_f > 1 \text{ GeV}$	Photon-photon	Photon-neutral-hadron
transverse shower comparison, or	$d < 20 \text{ mm}; \frac{E_{p1}}{E_m+E_f} > 0.9;$ $E_{p2} = 0 \text{ or } (\frac{E_{p2}}{E_f} < 0.5,$ $E_{p1} > E_m)$	$d < 20 \text{ mm}; \frac{E_{p1}}{E_m+E_f} > 0.9;$ $E_{p2} = 0 \text{ or } (\frac{E_{p2}}{E_f} < 0.5,$ $E_{p1} > E_m)$
relative low energy fragment	-	$d < 40 \text{ mm}; d_h < 20 \text{ mm};$ $\frac{E_f}{E_m} < 0.02$

**Table 5.3:** The cuts for merging photon-photon-fragment pairs and photon-neutral-hadron-fragment pairs for both low energy and high energy fragments, immediately after photon reconstruction.  $d$ ,  $d_c$  and  $d_h$  are the mean energy weighted intra-layer distance of the pair, the distance between centroids, the minimum distance between calorimeter hits of the pair, respectively.  $E_m$  and  $E_f$  are the main photon energy and the fragment energy, respectively.  $E_{p1}$  and  $E_{p2}$  are the energies the two largest peaks, found by peak finding algorithm, ordered by descending energy, respectively.  $N_{calo}$  is the number of the calorimeter hits in the fragment.

## 5.7. Photon fragment recovery algorithm in the HCAL

The previous section describes an effective algorithm to remove photon fragments in the ECAL that are peripheral to the electromagnetic shower core. There is another type of fragments originated from the leakage effect of the ECAL. When a high-energy EM shower is not fully contained in the ECAL, the shower deposits energy in the HCAL, which often forms a neutral hadron in the HCAL. An example of a 500 GeV photon reconstructed into a main photon in the ECAL (yellow) and a neutral hadron fragment in the HCAL (blue) is shown in figure 5.9. This section presents an algorithm to merge photon fragments in the HCAL. This photon fragment recovery algorithm is important when reconstructing high energy photons. For the ILD detector, this ECAL leakage effect appears when the photon energy is above 50 GeV.

Photon fragments in the HCAL are spatially close to the main photon. A fitted cone from the main photon, if extended to the HCAL, should contain most of the calorimeter hits of the fragment. These features allow a set of cuts developed to merge fragments in the HCAL, which are listed in table 5.4.



**Figure 5.9:** An event display of a typical 500 GeV photon, reconstructed into a main photon in the ECAL (yellow) and a neutral hadron fragment in the HCAL (blue).

This algorithm would collect photons in the ECAL and neutral hadrons in the HCAL as inputs. The algorithm then iterates over all pairs of reconstructed photons and neutral hadrons. For each pair, a set of variables are calculated and compared to a set of cuts. Photon-fragment pairs passing all the cuts will be merged.

### 5.7.1. Distance comparison cuts

Fragments in the HCAL should be spatially close to the main photon, measured by three metrics: the variable  $d_c^l$  is the distance between centroids of the last outer layer of the main photon and the first inner layer of the fragment; the variable  $d_{fit}^l$  is the distance between fitted directions using the last outer layer of the main photon and the first inner layer of the fragment; and  $d_{fit}$  is the distance between fitted directions using the main photon and the fragment. These three distances should be small for merging. The cut demands  $d_c^l \leq 173$  mm;  $d_{fit}^l \leq 100$  mm;  $d_{fit} \leq 100$  mm.

### 5.7.2. Projection comparison cuts

The direction of the fragment should be similar to the direction of the main photon. The variable  $r_f$  is the root-mean-squared energy weighted distance of a calorimeter hit in the fragment to the direction of the main photon. The cut requires  $r_f \leq 45$  mm.

### 5.7.3. Shower width comparison cuts

Another feature of the fragment and the main photon is that their shower widths should be similar. Variables  $w_m^l$  and  $w_f^l$  are the root-mean-squared widths of the last outer layer of the main photon in the ECAL, and the first inner layer of the fragment in the HCAL, respectively. The ratio  $\frac{w_f^l}{w_m^l}$  needs to be in the range of 0.3 to 5 for the merging. The generous upper bound is because the HCAL cell size is much larger than that of the cell size of the ECAL.

### 5.7.4. Cone comparison cuts

When a fitted cone from the main photon is extended to the HCAL, the cone should contain a significant amount of the fragment. The variable,  $\%N$ , the fraction of the calorimeter hits in the fragment in the extended fitted cone from the main photon comparing to the calorimeter hits in the fragment, has to be greater than 0.5 for merging.

### 5.7.5. Energy comparison cuts

The last criteria is the fragment should has a low energy relative to the main photon. The variables  $E_m$  and  $E_f$  are the main photon energy and the fragment energy, respectively. The ratio,  $\frac{E_f}{E_m}$ , has to be less than 0.1 for merging.

If multiple photon-fragment pairs pass the cuts with the same fragment, the pair with highest  $\%N$  will be merged.

This HCAL fragment removal algorithm occurs after the first pass of topological association in the reconstruction which connects tracks to clusters in the calorimeters.

High energy fragment recovery	Cuts
distance comparison	$d_c^l \leq 173 \text{ mm}; d_{fit}^l \leq 100 \text{ mm}; d_{fit} \leq 100 \text{ mm}$
projection comparison	$r_f \leq 45 \text{ mm}$
shower width comparison	$0.3 \leq \frac{w_f^l}{w_m^l} \leq 5$
cone comparison	$\%N \geq 0.5$
energy comparison	$\frac{E_f}{E_m} \leq 0.1$

**Table 5.4:** The cuts for merging high energy photon fragment in the HCAL to the main photon in the ECAL.  $d_c^l$  is the distance between centroids of the last outer layer of the main photon and the first inner layer of the fragment.  $d_{fit}^l$  is the distance between fitted directions using the last outer layer of the main photon and the first inner layer of the fragment.  $d_{fit}$  is the distance between fitted directions using the main photon and the fragment.  $w_m^l$  and  $w_f^l$  are the root-mean-squared width of the last outer layer of the main photon and the first inner layer of the fragment.  $r_f$  is the root-mean-squared energy weighted distance of a calorimeter hit in the fragment to the direction of the main photon.  $E_m$  and  $E_f$  are the main photon energy and the fragment energy.  $\%N$  is the fraction of the calorimeter hits in the fragment in the extended fitted cone of the main photon.

## 5.8. Photon splitting algorithm

Algorithms described above deal with forming photons from calorimeter hits in the ECAL, merging photon fragments in the ECAL and the HCAL. Another aspect in photon reconstruction is splitting accidentally merged photons. During the event reconstruction, it is possible that photons are accidentally merged if they are spatially close. Hence another algorithm at the end of the particle reconstruction addresses this issue and tries

to split merged photons. This algorithm focuses on energetic photons with energy greater than 10 GeV.

A merged photon should be consistent with topologies of a spatially closed photon pair. Extra care should be taken if the photon is close to a charged tracks.

Table 5.5 lists the cuts used in the algorithm. If an energetic photon is identified, the 2D PEAK FINDING algorithm will be used to identify EM showers in the photon using the transverse shower information. If energy of the photon is bigger than  $E_{c1}$  and the energy of the 2<sup>nd</sup> energetic EM shower is bigger than  $E_{c2}$ , the photon will be split according to the 2D PEAK FINDING results.

The values of  $E_{c1}$  and  $E_{c2}$  depends on if the photon is close to a charged track. The cut is more careful if the candidate is close to tracks. The number of nearby charged tracks is counted as number of tracks with the track projection on the front of the ECAL less than 100 mm to the photon position. If there is no nearby tracks, the  $E_{c1}$  is set to 10 GeV and  $E_{c2}$  is set to 1 GeV. If there is one nearby track, the  $E_{c1}$  is set to 10 GeV and  $E_{c2}$  is set to 5 GeV. If there is more than one nearby track, the  $E_{c1}$  is set to 20 GeV and  $E_{c2}$  is set to 10 GeV.

The constraint on  $N_p$ , the number of EM showers identified in the candidate, should be less than five, as one reconstructed photon is unlikely to be accidentally merged from more than four photons.

Photon splitting	Cuts
Cuts	$E > E_{c1}, E_{p2} > E_{c2}, N_p < 5$
$E_{c1}$ and $E_{c2}$ values	
0 charged tracks nearby	$E_{c1} = 10 \text{ GeV}, E_{c2} = 1 \text{ GeV}$
1 charged tracks nearby	$E_{c1} = 10 \text{ GeV}, E_{c2} = 5 \text{ GeV}$
> 1 charged tracks nearby	$E_{c1} = 20 \text{ GeV}, E_{c2} = 10 \text{ GeV}$

**Table 5.5:** The cuts for splitting photons, and the values for energy cut-off points.  $E$  is the photon energy.  $E_{p2}$  is energy if the second largest peak from the two dimensional peak finding.  $N_p$  is the number of peaks identified by the peak finding.  $E_{c1}$  and  $E_{c2}$  are the energy cut-off values, determined by the number of nearby charged PFOs.

## 5.9. Characterise the performance

The main photon reconstruction algorithm in section 5.3 improves the photon completeness and the photon pair resolution, due to the improved 2D PEAK FINDING algorithm in section 5.4. The fragment removal algorithms in section 5.6 and section 5.7 reduce the photon fragments in the ECAL and the HCAL. The photon splitting algorithm in section 5.8 exploits the 2D PEAK FINDING algorithms to separate photons using transverse shower information, which improves the photon separation resolution. Photon reconstruction improves single photon resolutions. It also improves jet energy resolution at a high centre-of-mass energy because of the high photon reconstruction completeness.

Three different versions of the PandoraPFA are used to characterise the performance.

- No stand-alone photon reconstruction algorithms
- With a stand-alone photon reconstruction algorithm from PandoraPFA version 1.
- With full photon related algorithms described above, incorporated in PandoraPFA version 3.

First the performance with the full algorithms is compared with no photon algorithms. The improvement from PandoraPFA version 1 to version 3 is shown. Afterwards, the individual photon algorithms are characterised, followed by characterisation of the performance of the photon reconstruction in PandoraPFA version 3.

## 5.10. Compare with no photon reconstruction

This section compares the performance with and without photon related algorithms photon pair and jet samples. The nominal ILD detector model is used. The single photon events were generated with an uniform distribution in the solid angle. The two-photon-per-event sample were generated with an uniform distribution in the solid angle of the first photon, and an uniform distribution in the solid angle between the pair for a range of the opening angles. Events are selected such that there is no early photon conversion in the tracking detector and the photon does not escape the detector. The events are further restricted to photon decaying in barrel and end cap region only, to avoid the barrel/endcap overlap region.

Figure 5.10 shows the photon reconstruction for two spatially close photons reconstructed with and without photon algorithms. Without the photon related algorithms, fragments are produced. The number of photons between 0 and 10 mm separation is around 1.5. The true photon number for that region should be 1, as it is extremely challenging to separate photons less than two cells apart. Without the photon related algorithms, photon separation resolution is much worse, as the number of photon appears to be flat between 0 to 30 mm separation. With the photon related algorithms, two photons start to be separated at 10 mm and fully separated at 20 mm separation. The number of reconstructed photon is 2 at 20 mm separation.

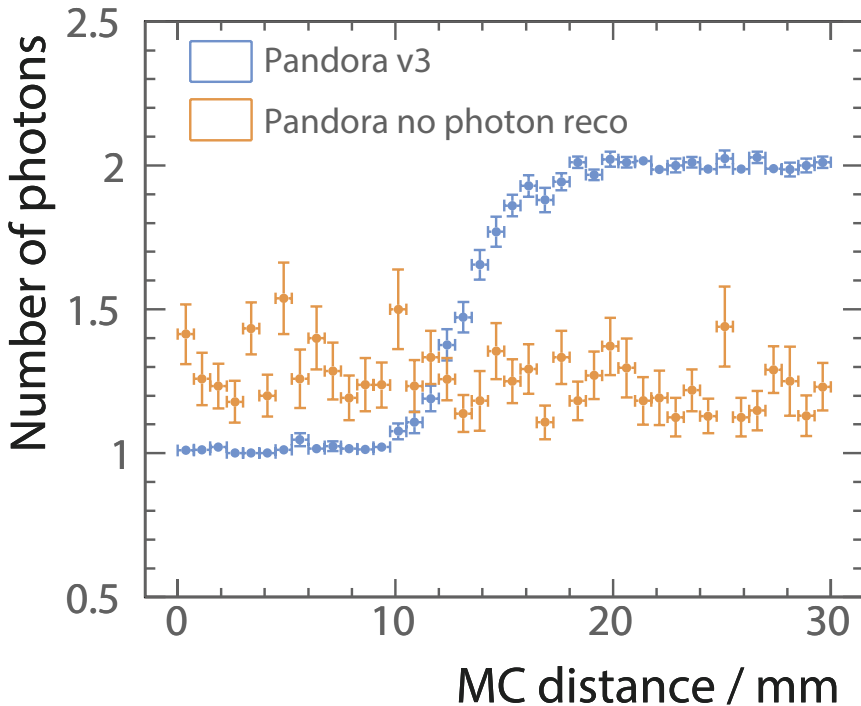


**Figure 5.10:** Average number of reconstructed photons using two-photon-per-event sample of 500 - 50 GeV without (orange) and with (blue) photon algorithms, as a function of the Monte Carlo distance separation between the photon pair.

The improvement in photon reconstruction leads to a considerable improvement in the jet energy resolution at a high energy. Jet energy resolution is defined as the root-mean-squared divided by the mean for the smallest width of distribution that contains 90% of entries, using  $e^+e^- \rightarrow Z'Z'$ , where  $Z' \rightarrow u\bar{u}/d\bar{d}/s\bar{s}$  sample at barrel region. The angular cut is to avoid the barrel/endcap overlap region. The light quark decay of the  $Z'$  is used as PandoraPFA does not attempt to recover missing momentum from semi-leptonic decay of heavy quarks. Using 90% of the entries is robust and focus on the Gaussian part of

the jet energy distribution. The total jet energy is sampled at the centre-of-mass energies of 91, 200, 360 and 500 GeV. As shown in figure 5.11, the jet energy resolutions are much better at 360 and 500 GeV with improved photon reconstruction. By identifying photons before reconstructing charged particles in a dense jet environment, the charged particle reconstruction is easier. However, at low energy, the reconstruction is worse with photon algorithms, because photon algorithms are optimised for high energies.

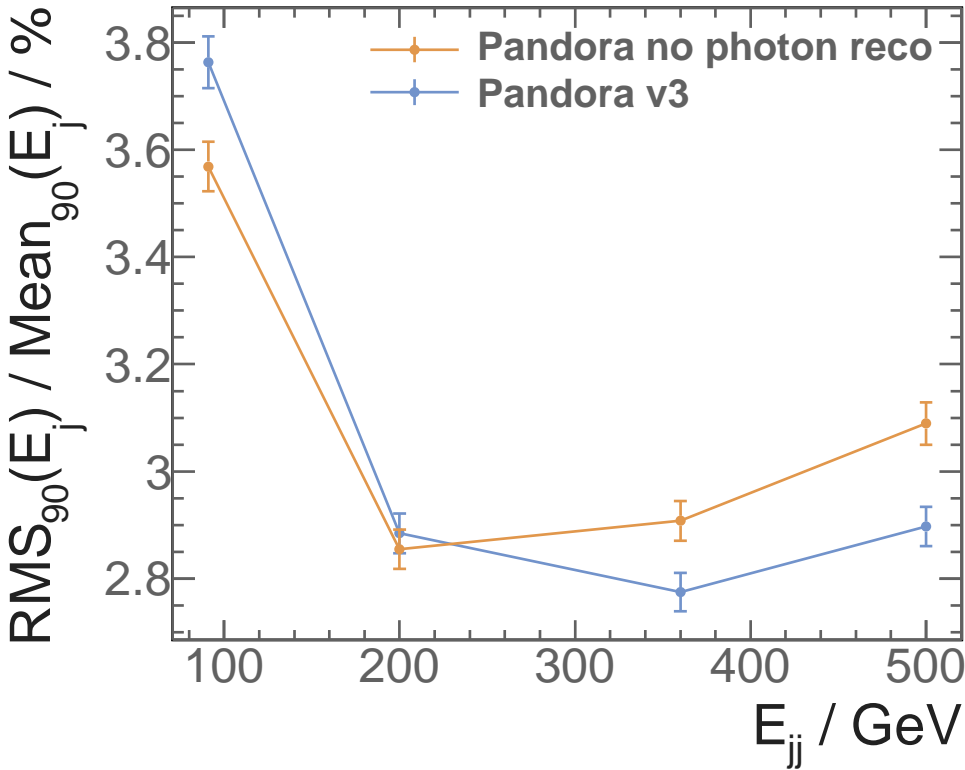


**Figure 5.11:** Jet energy resolution as a function of the total jet energy using  $e^+e^- \rightarrow Z'Z'$ , where  $Z' \rightarrow u\bar{u}/d\bar{d}/s\bar{s}$  sample at barrel region. The orange and bottom lines represent the reconstruction without and with photon algorithms, respectively.

To access the impact of photon algorithms on jet energy resolution, perfect photon reconstruction is used to compare the performances. The perfect photon reconstruction identifies photon by associating calorimeter hits using the truth information. Same  $e^+e^- \rightarrow Z'Z'$ , where  $Z' \rightarrow u\bar{u}/d\bar{d}/s\bar{s}$  samples are used. The photon confusion terms, which are defined as the quadrature differences of the jet energy resolution between a normal reconstruction and a perfect photon reconstruction, are listed in table 5.6. The photon confusion terms, except for  $\sqrt{s} = 91$  GeV, have been reduced to 0.9% with the photon algorithms.

Photon confusion	$\sqrt{s} = 91 \text{ GeV}$	200 GeV	360 GeV	500 GeV
PandoraPFA without photon algorithms	0.7%	0.9%	1.3%	1.4%
PandoraPFA with photon algorithms	1.4%	0.9%	0.9%	0.9%

**Table 5.6:** Photon confusion as a function of total jet energy in the  $e^+e^- \rightarrow Z'Z'$ , where  $Z' \rightarrow u\bar{u}/d\bar{d}/s\bar{s}$  samples for reconstruction with and without photon algorithms.

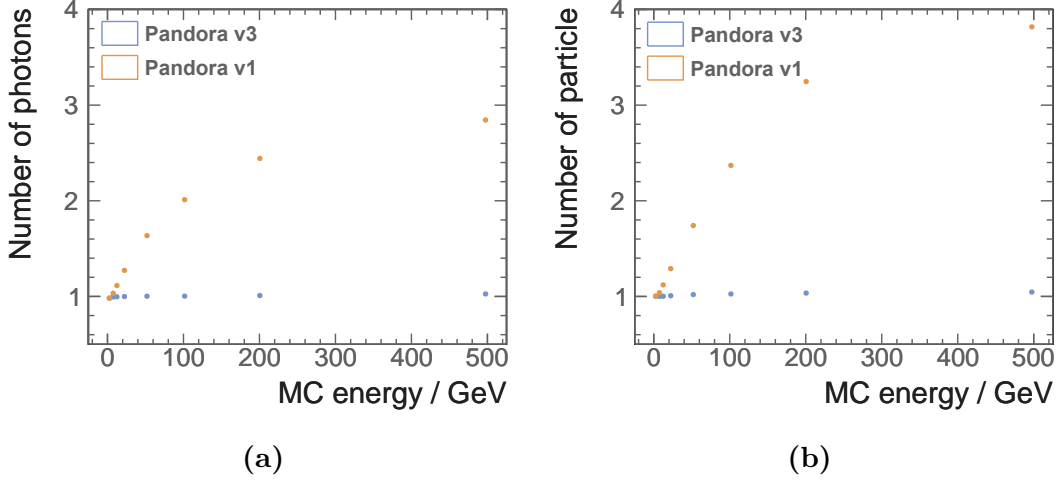
## 5.11. Compare with photon reconstruction in PandoraPFA version 1

This section reviews the performance improvement with the introduced algorithms, using single photon, photon pair and jet samples. There is a rudimentary photon reconstruction algorithm in PandoraPFA version 1. This section concentrates on the improvement of photon reconstruction from PandoraPFA version 1 to version 3.

Testing samples are generated in the same way as in the previous section. Figure 5.12a shows the reduction in fragments identified as photons, using a single-photon-per-event sample. For the PandoraPFA version 3, indicating as the blue dots on the plots, average number of photon stays below 1.05 even at 500 GeV (true value 1). Comparing with PandoraPFA version 1, for a 100 GeV photon sample, the average number of reconstructed photons is reduced to 1 from 2; for a 500 GeV photon sample, the number is reduced to 1.05 from 2.8.

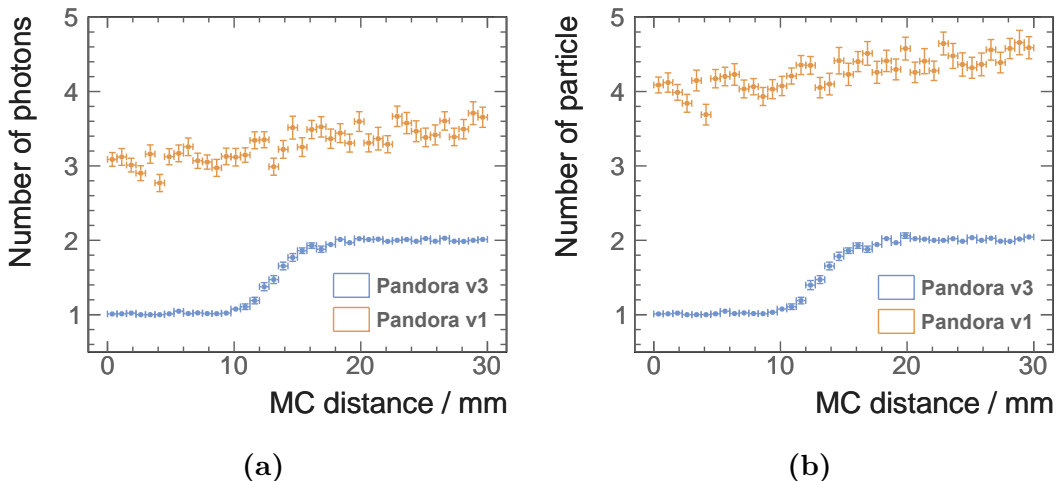
A similar improvement in the number of reconstructed particles is shown in figure 5.12b. The number of reconstructed particles counts the extra fragments identified as neutral hadrons. Comparing PandoraPFA version 3 with version 1, for a 100 GeV photon sample, the average number of reconstructed particles is reduced to 1 from 2.4; for a 500 GeV photon sample, the number is reduced to 1.05 from 3.8.

Figure 5.13 illustrates a reduction in the photon fragments and the neutral hadron fragments using a two-photon-per-event sample of 500 - 50 GeV. The figure shows the numbers of reconstructed photon and particles as a function of the Monte Carlo distance separation of the photon pair from 0 to 30 mm, which corresponds to approximately 6 ECAL square cell length of the default ILD detector model. In both figure 5.13a



**Figure 5.12:** Average number of reconstructed a) photons, and b) particles, as a function of their true energy using a single-photon-per-event sample. For both figures, the top orange and bottom blue dots are reconstructed with PandoraPFA version 1 and version 3, respectively. The photon reconstruction is changed in PandoraPFA version 2.

and figure 5.13b, the average numbers of photon and particle for reconstruction in PandoraPFA version 3 are below 2.05 at 30 mm apart, which is significantly better than the reconstruction in PandoraPFA version 1. For PandoraPFA version 3, two photons start to be resolved at 10 mm apart, and fully resolved at 20 mm apart.



**Figure 5.13:** Average number of reconstructed a) photons, and b) particles, as a function of the MC distance separation in the calorimeter, using two-photon-per-event sample of 500 - 50 GeV. For both figures, the top orange and bottom blue dots present the reconstruction with PandoraPFA version 1 and version 3, respectively. The photon reconstruction is changed in PandoraPFA version 2.

Another metric to reflect the improvement in photon reconstruction is the fraction of the fragment energy to the total energy. Shown in figure 5.14, using two-photon-per-event sample of 500 - 50 GeV, a reduction in fragment energy can be seen clearly going from PandoraPFA version 1 to version 3. With the improved photon reconstruction in PandoraPFA version 3, the average fragment energy fraction is below 0.1% up to 30 mm apart, whilst around 5% energy would be in fragments with PandoraPFA version 1.

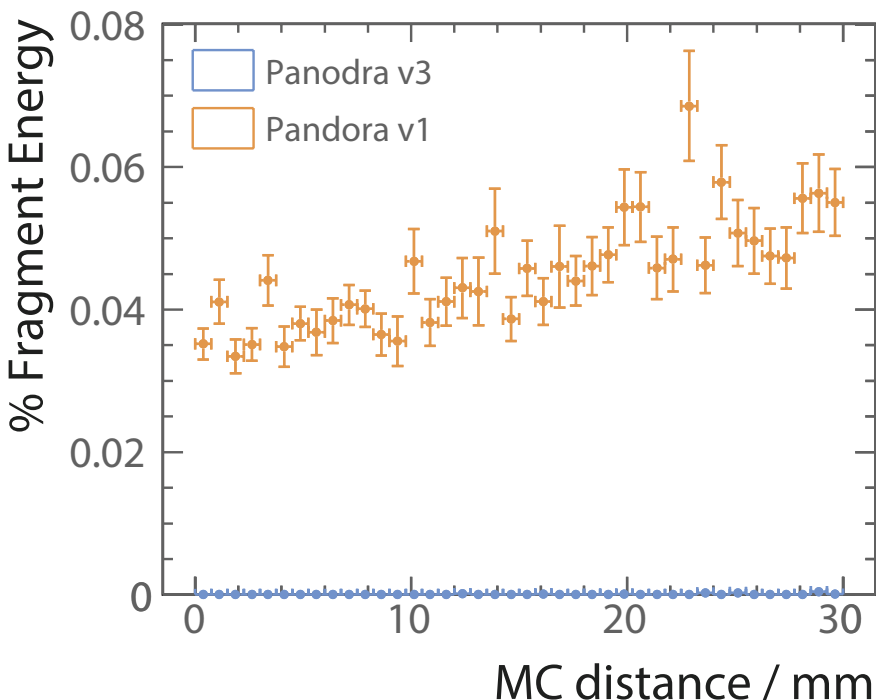


**Figure 5.14:** Average fraction of fragments energies to the total energy, as a function of the Monte Carlo distance separation in the calorimeter, using two-photon-per-event sample of 500 - 50 GeV. The top orange and bottom blue dots represent the reconstruction with PandoraPFA version 1 and version 3 respectively. The photon reconstruction is changed in PandoraPFA version 2.

The improvement in the completeness of the photon reconstruction, as shown in single photon and double photon reconstruction, leads to a small improvement in the jet energy resolution at high energy. The total jet energy is sampled at 91, 200, 360 and 500 GeV. Shown in figure 5.15, the jet energy resolutions are better at 360 and 500 GeV with improved photon reconstruction.

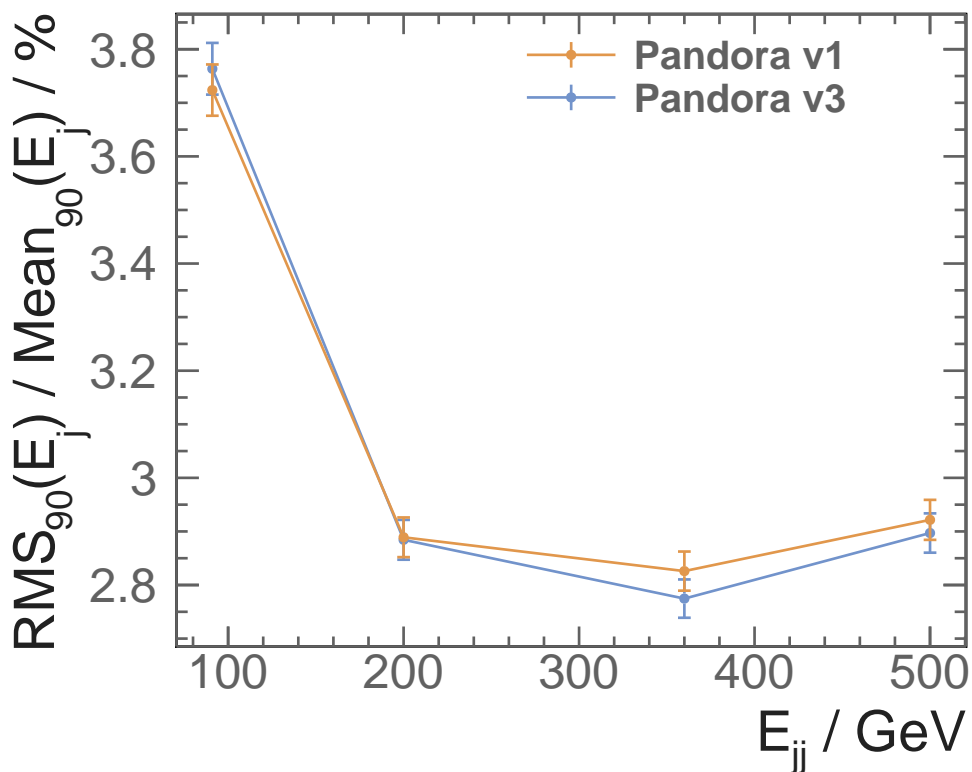


**Figure 5.15:** Jet energy resolution as a function of the total jet energy using  $Z' \rightarrow u\bar{u}/d\bar{d}/s\bar{s}$  sample at barrel region. The top orange and bottom blue dots represent the reconstruction with PandoraPFA version 1 and version 3. The photon reconstruction is changed in PandoraPFA version 2.

## 5.12. Understand photon reconstruction improvement

To show the incremental improvement of individual algorithm, the average number of particle for a high energy photon pair, 500 - 500 GeV is shown in figure 5.16. Blue, orange, green, and red dots represent full photon reconstruction, reconstructed with only fragment removal algorithms in the ECAL, reconstructed with fragment removal algorithms in the ECAL and the HCAL, and reconstructed with PandoraPFA version 1, respectively.

With fragment removal algorithm in the ECAL, the number of fragment is reduced significantly, comparing with photon reconstruction in PandoraPFA version 1. With the additional fragment removal in the HCAL, the number of fragments is reduced further. At 40 mm apart, with both fragment removal algorithms, there is less than 0.05 fragment per photon pair.

The introduction of the revised photon reconstruction and photon splitting improves the photon separation resolution. Photons pair starts to be resolved at 5 mm apart, and fully resolved at 15 mm apart, for a two-photon-per-event sample of 500 - 500 GeV.

## 5.13. Current photon reconstruction performance

In this section, the performance of the photon reconstruction as a function of photon energies will be described.

Single particle reconstruction and ID efficiency is demonstrated in figure 5.17. In single photon samples, an event can have an efficiency of 1 or 0, depending on whether the photon reconstructed corresponds to the MC truth photon. The single photon reconstruction efficiency is above 98% for photons above 2GeV and above 99.5% for photons above 100 GeV. The low efficiency in the first bin in figure 5.17a, from 0 to 0.25 GeV, is because photon reconstruction does not attempt to reconstruct photons below 0.2 GeV.

For two-photon-per-event samples, there are very few fragments. Shown in figure 5.18 for a two-photon-per-event sample of 500 - 500 GeV, the average numbers of photons and

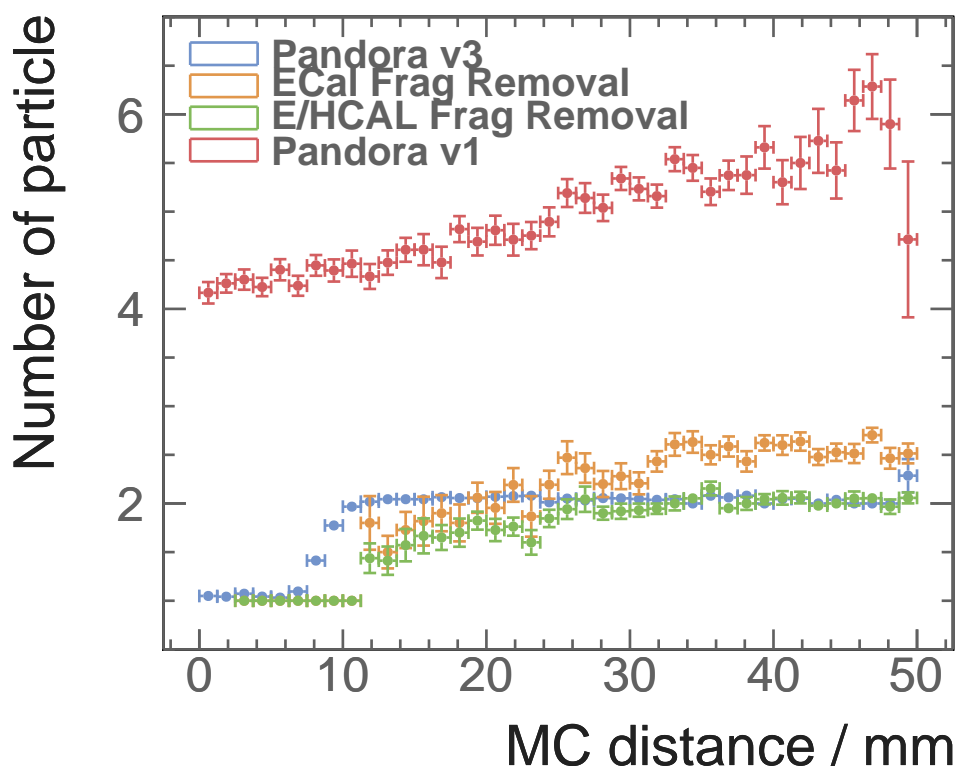


**Figure 5.16:** Average number of photons, as a function of the Monte Carlo distance separation between the photon pair in the calorimeter, using two-photon-per-event sample of 500 - 500 GeV. The blue, orange, green, and red dots represent the reconstruction with PandoraPFA version 3, with fragment removal in the ECAL, and with fragment removal in the ECAL and the HCAL, with PandoraPFA version 1, respectively. The photon reconstruction is changed in PandoraPFA version 2.

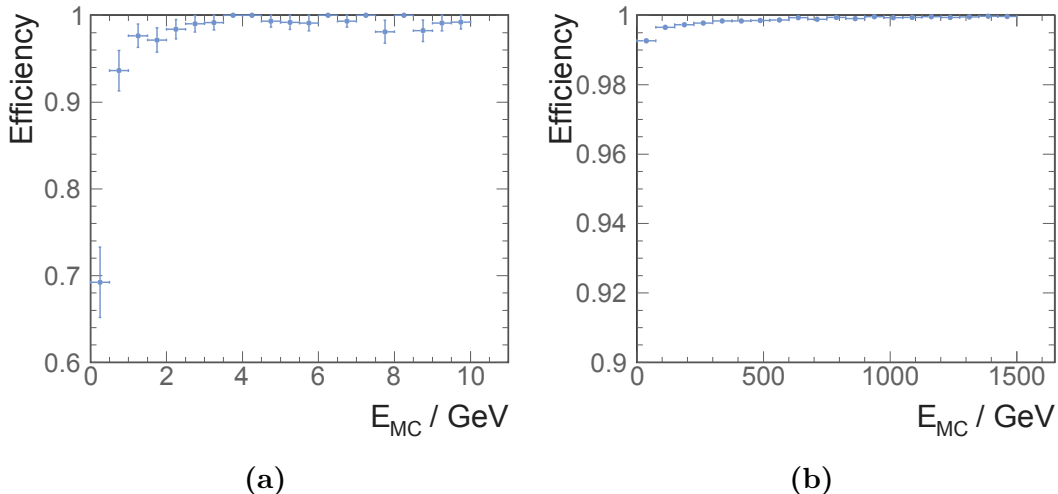


**Figure 5.17:** Single photon reconstruction efficiency as a function of true energies. a) the low energy region, and b) the high energy region.

particles beyond 20 mm apart are both less than 2.05, less than 1 fragment produced per 20 events.

The resolving power of a photon pair depends on energies of two photons. Figure 5.19 shows the average number of photon reconstructed for photon pairs of different energies. When the energies of two photons are similar, the resolving power is greater. This is because that the two photon showers have similar sizes, and the 2D PEAK FINDING algorithm can exploit the symmetry in the size of the EM showers. For example, 500 - 500 GeV photon pair and 10 - 10 GeV photon pair start to be resolved at 6 mm apart, which is about one ECAL cell length. Photon pairs with different energies, for example 500 - 50 GeV and 100 - 10 GeV pair, start to be resolved at 10 mm apart, which is about two ECAL cells length.

For an energetic photon, it is more difficult to remove fragments, but it is easier to identify the photon, because the electromagnetic shower core is more dominant than the peripherals. Therefore separating two energetic photons is easier than separating two low-energy photons. This can be seen in figure 5.19. At 20 mm apart, two photons in 500 - 500 GeV pair are fully resolved, whereas approximately only 60% of two photons in 10 - 10 GeV pair are resolved.

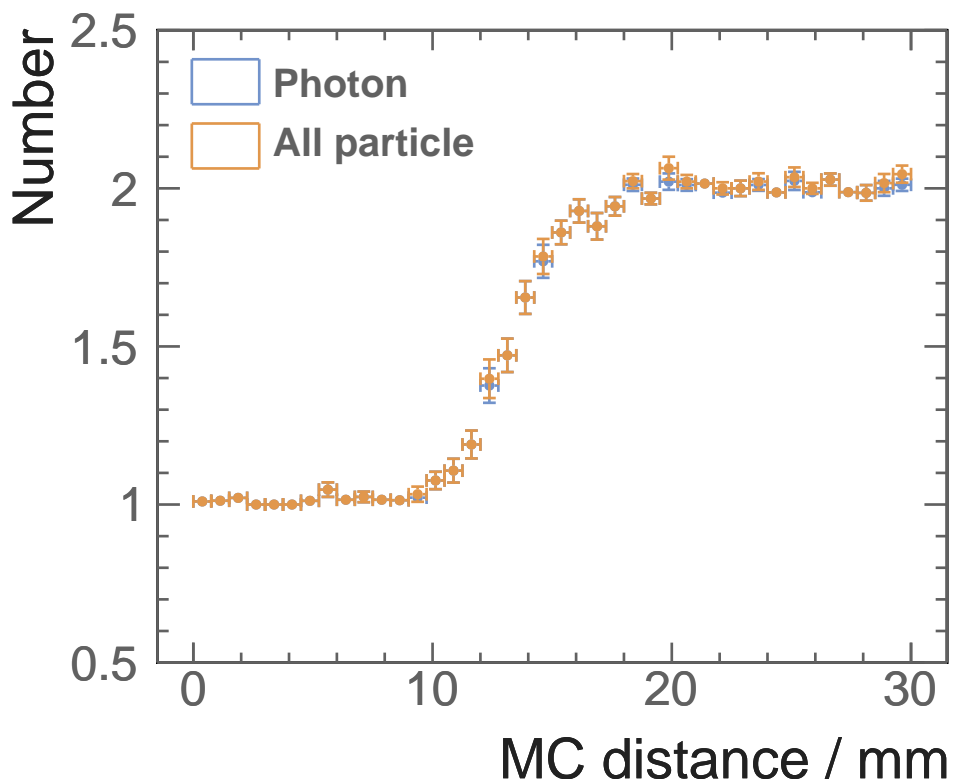


**Figure 5.18:** Average numbers of photon (blue) and particle (orange), as a function of the Monte Carlo distance separation between the photon pair, using two photons of 500 and 50 GeV per event sample.

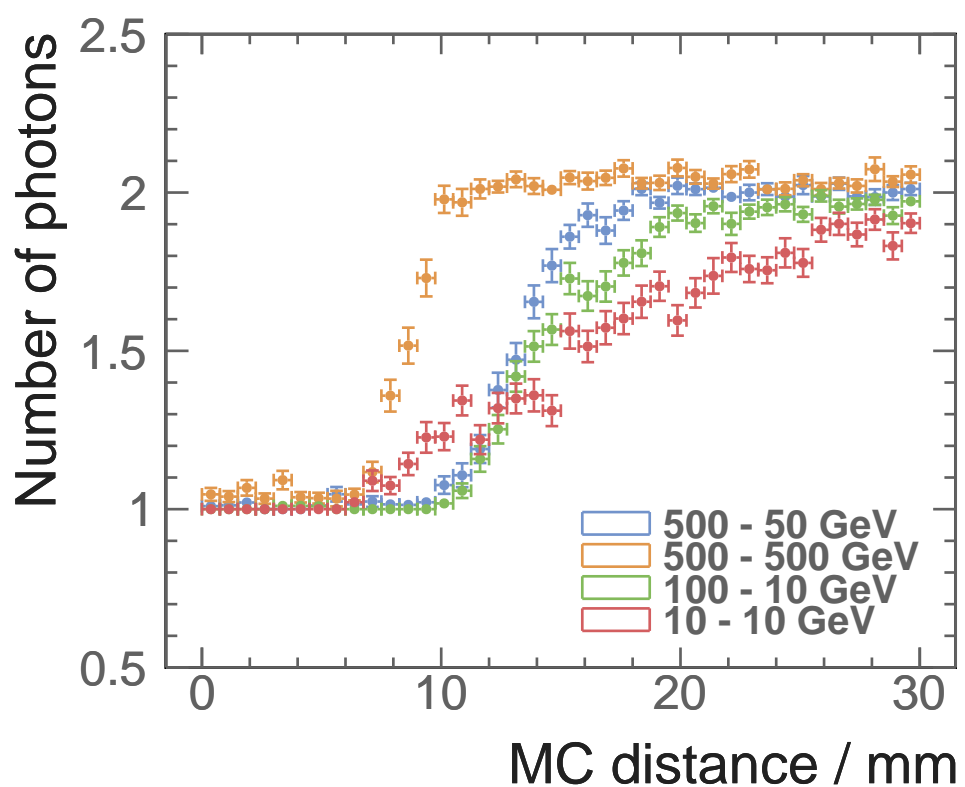


**Figure 5.19:** Average numbers of reconstructed photon for four different photon pairs: 500 - 50 GeV (blue), 500 - 500 GeV (orange), 100 - 10 GeV (green), and 10 - 10 GeV (red), as a function of the Monte Carlo distance separation between the photon pair.



# Chapter 6.

## Tau Lepton Decay Modes Classification

*'Give a man a fish and you feed him for a day; teach a man to fish and you feed him for a lifetime.'*

---

The tau lepton has been studied extensively in the past at the Large Electron Positron Collider (LEP) [81]. The tau lepton spin state, which can be derived from kinematic properties of tau decay products, can be used to measure the CP (the product of charge conjugation and parity symmetries) of the Higgs, via  $H \rightarrow \tau^+ \tau^-$  channel [82]. The polarisation correlation of the tau pairs can be used to infer the spin of the parent boson, differentiating  $H \rightarrow \tau^+ \tau^-$  from  $Z \rightarrow \tau^+ \tau^-$ .

The ability to identify tau decay mode can be also used as a benchmark for detector performance. Since tau lepton has a very short lifetime of 290 fs [83], only tau decay products can be detected with the tracking detectors and calorimeters. Therefore, the performances of the calorimetric and track systems determine the ability to reconstruct the tau lepton decay products and identify different tau decay modes.

The main challenge in the tau lepton decay modes classification is to reconstruct and separate spatially close photons. Many final states of the tau decay involves  $\pi^0$ , where  $\pi^0 \rightarrow \gamma\gamma$ . For some final states, the main difference in the topologies is the number of photons in the final state. At a high centre-of-mass energy, the decay products of the tau decay are often boosted. To reconstruct two photons from  $\pi^0$  decay as separate

entities requires good pattern recognition algorithms for photons and a fine ECAL spatial resolution. Hence the photon reconstruction dedicated in chapter 5 is used in this study to identify photons.

This chapter is organised as follows. Firstly, the choice of samples for the analysis will be discussed. The tau decay modes of interests are identified. The pre-selection cuts and variables used in the MVA classification are discussed. The performance of the tau decay mode classification will be given, followed by the ECAL optimisation study using the tau decay mode classification. Lastly, the tau decay mode classification is further used in a proof-of-principle analysis to demonstrate the ability to identify Higgs boson from Z boson using the tau pair decay channel.

## 6.1. Overview of the analysis

The analysis starts with defining the samples for study in section 6.2. Seven major tau lepton decay modes are chosen for the tau decay mode classification. The simulation and reconstruction of these tau lepton decays are described in section 6.3. Pre-selection of the events, discussed in section 6.4, are such that the reconstruction and detector effects, which do not vary with the ECAL cell sizes, are taken out of this analysis. After defining discriminative variables used in the MVA classification in section 6.5, the classification is performed with a multivariate classifier. Since the decay products of a tau need to be classified into one of the seven decay modes, a multiclass classification, presented in section 6.6, is used to allow simultaneous classification between multiple decay modes. Afterwards, the performance of the classification is described in section 6.7.

The classification of the tau lepton decay modes are then repeated for different energies of tau lepton decay to access the impact of the energy on the classification. The classification is also used to study the impact of the ECAL cell sizes on the classification performance, discussed in section 6.8. The classification is then utilised to demonstrate the ability to separate Higgs boson from Z boson using the tau pair decay channel in a proof-of-principle analysis, described in the section 6.9.

## 6.2. Samples for the analysis

The studied tau lepton decay channel for an electron-positron collider is  $e^+e^- \rightarrow \tau^+\tau^-$ , with a centre-of-mass energy of 100 GeV. An event display of  $e^+e^- \rightarrow \tau^+\tau^-$  interaction is shown in figure 6.1, simulated with the ILD detector model. The  $e^+e^- \rightarrow \tau^+\tau^-$  channel contains two tau leptons travelling in opposite directions. Since the tau decay mode classification is applied on a per tau lepton basis, the decay products of two taus in one event are divided into two collections for separate classification. Each collection of particles corresponds to the decay products of one tau lepton.

The principle thrust axis vector is used to separation particles into two collections. Two collections are obtained based on the sign of the scalar product between the principle thrust axis vector and the momentum vector of a particle. The principle thrust axis vector,  $\hat{t}$ , is chosen by maximising the classical event shape thrust [84],  $T$ :

$$T = \max_{\hat{t}} \frac{\sum_i |\hat{t} \cdot \vec{p}_i|}{\sum_i |\vec{p}_i|} \quad (6.1)$$

where  $\vec{p}_i$  is the momentum vector of the particle  $i$ ;  $\hat{t}$ , is the unit principle thrust axis vector; and index  $i$  is summed over all particles in an event. The principle thrust axis vector is the axis that most particle aligned to.

### 6.2.1. Tau lepton decay modes

Tau lepton decays into a number of final states. To study the predominant effect of the tau lepton decays, decay modes with branching ratio above 2% are classified. This results in seven tau lepton decay modes studied, which cover 92.58 % of total branching ratio of tau decay. Their branching ratios, along with decay modes and final states are shown in table 6.1.

## 6.3. Simulation and reconstruction

Two million  $e^+e^- \rightarrow \tau^+\tau^-$  events are simulated and reconstructed using the ILD detector model. As the study is aimed for optimisation study of the ECAL cell sizes, the beam

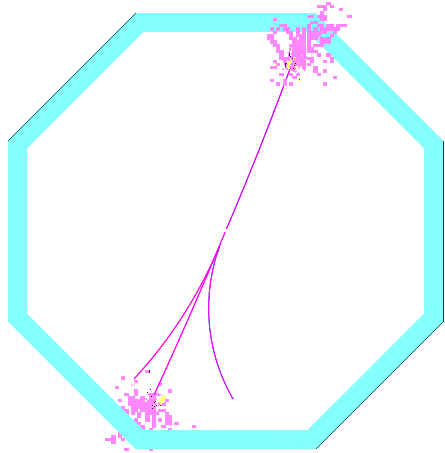


**Figure 6.1:** An example event display of a simulated  $e^+e^- \rightarrow \tau^+\tau^-$  event using the ILD detector model. The top half of the event is a tau lepton decaying into  $\pi^-\pi^0\nu_\tau$  final state and the bottom half of the event is a tau lepton decaying into  $\pi^+\pi^-\pi^-\pi^0\nu_\tau$  final state. The purple lines are the tracks left by  $\pi^\pm$  in the tracking detectors. The purple clusters are the calorimeter hits of  $\pi^\pm$ . And the yellow clusters are the calorimeter hits of photon from  $\pi^0 \rightarrow \gamma\gamma$ . The blue region is the transverse cross section of the ECAL barrel part along the beam line direction.

Decay modes	Detectable final states	Branching ratio
$e^-\bar{\nu}_e\nu_\tau$	$e^-$	$17.83 \pm 0.04\%$
$\mu^-\bar{\nu}_\mu\nu_\tau$	$\mu^-$	$17.41 \pm 0.04\%$
$\pi^-\nu_\tau$	$\pi^-$	$10.83 \pm 0.06\%$
$\rho\nu_\tau$	$\pi^-\pi^0$	$25.52 \pm 0.09\%$
$a_1\nu_\tau$	$\pi^-\pi^0\pi^0$	$9.30 \pm 0.11\%$
$a_1\nu_\tau$	$\pi^+\pi^-\pi^-$	$8.99 \pm 0.06\%$
$\pi^+\pi^-\pi^-\pi^0\nu_\tau$	$\pi^+\pi^-\pi^-\pi^0$	$2.70 \pm 0.08\%$

**Table 6.1:** Decay modes, detectable final state particles and branching ratios of the seven major  $\tau^-$  decays, taken from [6].  $\tau^+$  decays similarly to  $\tau^-$ .

specific effects that are not affected by the varying ECAL cell sizes are not simulated. These effects include the initial state radiation (ISR) and the beam induced background.

The software used for simulation and reconstruction is described in chapter 4. Events are reconstructed with iLCSoft version v01-17-07 [85] and PandoraPFA version 3 [57], where the photon reconstruction is discussed in chapter 5.

## 6.4. Event pre-selection

Pre-selection cuts select events using the truth information. Since the analysis is aimed for the optimisation of the ECAL cell sizes, these pre-selection cuts are such that effects not affected by the changing of the ECAL cell sizes are not considered in the analysis. These cuts allow the analysis to focus on the events with clear topologies. The pre-selection cuts are listed in table 6.2. The fraction of events passing each pre-selection cut for individual decay mode are listed in table 6.3.

One of the pre-selection cuts is to demand that the tau decay products do not have photons converted to electron pairs in the tracking detector, determined with the truth information. These discarded events would have fewer photons and more electrons than expected in the final states, which changes the topologies of the final states. Shown in table 6.3, only decay modes with photons in the final states are affected by this cut, as expected.

Another pre-selection cut requires the total energy of the non-neutrino tau decay products,  $E_{vis,MC}$ , to be greater than 5 GeV, based on the truth information. If most energy of a tau lepton is carried by neutrinos, non-neutrino decay products would have low energies and be difficult to be identified. Hence these events with low-energy non-neutrinos tau decay products are not used in the analysis. Decay modes with only one non-neutrino particle in the final states are mostly affected by this cut because more energies are carried by neutrinos, indicated in table 6.3.

The last pre-selection cut is to discard events with tau decay products depositing energies in the gap region between barrel and the end cap part of the calorimeter. As the reconstruction does not attempt to recover reconstruction in the gap region, there is a significant drop in the particle reconstruction efficiency in the gap region. The cut demands the absolute value of the polar angle of tau lepton, based on the truth information,  $|\theta_{Z,MC}|$ , is between 0.3 and 0.6 rad to be contained in the end cap region, or

is between 0.8 and 1.57 rad to be contained in the barrel region. All decay modes are affected almost equally by this cut, suggested by numbers in table 6.3.

Cuts	Values
Photon conversion in the tracking detector	No
Total energy of non-neutrino decay products	$E_{vis,MC} > 5 \text{ GeV}$
Polar angle acceptance	$0.6 >  \theta_{Z,MC}  > 0.3$ or $1.57 >  \theta_{Z,MC}  > 0.8$

**Table 6.2:** Pre-selection cuts for tau lepton decay modes classification.

Detectable final state	No photon conversion in the tracking detector	Total energy of non-neutrino decay products acceptance	Polar angle acceptance
$e^-$	100.0%	84.7%	66.2%
$\mu^-$	100.0%	85.2%	66.7%
$\pi^-$	100.0%	88.3%	60.9%
$\pi^-\pi^0$	77.1%	76.9%	61.9%
$\pi^-\pi^0\pi^0$	61.3%	61.2%	50.5%
$\pi^+\pi^-\pi^-$	100.0%	100.0%	78.0%
$\pi^+\pi^-\pi^-\pi^0$	77.0%	77.0%	61.8%

**Table 6.3:** The table shows the fraction of events passing successive cuts: no photon conversion in the tracking detector; total energy of non-neutrino decay products  $> 5 \text{ GeV}$ ; and  $0.6 > |\theta_{Z,MC}| > 0.3$  or  $1.57 > |\theta_{Z,MC}| > 0.8$ . All cuts are based on the truth information.

## 6.5. Variables used in the MVA

Having pre-selected events, variables are carefully developed for the multivariate analysis (MVA). The full list of the variables are shown in table 6.4. The distributions of the four most powerful variables for selected tau decay modes are shown in figure 6.2.

### 6.5.1. PFOs number variables

The most crucial variables are the number of PFOs of different types of particles. There are five PFOs number variables used in MVA event selection: the number of charged particles ( $N_{\chi^+}$ ); the number of muons ( $N_\mu$ ); the number of electrons ( $N_e$ ); the number of photons ( $N_\gamma$ ); and the number of charged pions ( $N_{\pi^-}$ ).

Figure 6.2a shows the distributions of the number of charged particles for selected tau decay modes. Over 98% one-prong final states have one track reconstructed, and around 95% three-prong final states have three tracks reconstructed. Figure 6.2b shows the distributions of the number of photons, which is powerful to distinguish final states with different numbers of  $\pi^0$  s.

### 6.5.2. Invariant mass variables

Five invariant mass variables participate the MVA classification: the invariant mass of all non-neutrino decay products ( $m_{vis}$ ); the invariant mass of all charged particles ( $m_{\chi^+}$ ); the invariant mass of all neutral particles ( $m_{\chi^0}$ ); the invariant mass of all photons ( $m_\gamma$ ); and the invariant mass of all charged pions ( $m_{\pi^-}$ ). Figure 6.2c shows the distributions of the invariant mass of all non-neutrino decay products for selected tau decay modes. Resonance structures can be seen for  $\rho$  and  $a_1$  decay modes in the figure.

### 6.5.3. Energy variables

Energy information helps to further separate different final states. Six energy variables are used in the MVA classification: the normalised total energy of all non-neutrino decay products ( $\tilde{E}_{vis}$ ); the normalised total energy of the charged particles ( $\tilde{E}_{\chi^+}$ ); the normalised total energy of the muons ( $\tilde{E}_\mu$ ); the normalised total energy of the electrons ( $\tilde{E}_e$ ); the normalised total energy of the photons ( $\tilde{E}_\gamma$ ); and the normalised total energy of the charged pions ( $\tilde{E}_{\pi^-}$ ). All variables are normalised with respect to the energy of the associated tau lepton.

### 6.5.4. Calorimetric information variables

Two calorimetric information variable are used in the MVA classification: the fraction of the energy deposited in the ECAL over the energy deposited in the calorimeters for all charge particles ( $\%E_{\chi^+}$ ) and the fraction of the energy deposited in the ECAL over the energy deposited in the calorimeters for all particles ( $\%E$ ). These two variables help to identify electrons and muons. For example, an electron deposits most energy in the ECAL, and a muon deposits 5% to 20% energy in the ECAL. The difference between two variables is that photons, which deposit most of their energy in the ECAL, do not participate in the calculation of  $\%E_{\chi^+}$ .

### 6.5.5. $\rho(\pi^-\pi^0)$ and $a_1(\pi^-\pi^0\pi^0)$ resonances reconstruction variables

$\rho(\pi^-\pi^0)$  and  $a_1(\pi^-\pi^0\pi^0)$  decay modes are identified further using their invariant mass resonance structure. For example,  $\rho(\pi^-\pi^0)$  decay mode contains a  $\pi^-$  and a  $\pi^0$  decaying into two photons. By selecting  $\pi^-$  and photons consistent with  $\rho$  mass,  $\rho(\pi^-\pi^0)$  decay mode could be identified. The  $\rho(\pi^-\pi^0)$  decay mode hypothesis test is performed by minimising a  $\chi^2$  function:

$$\chi^2 = \left( \frac{m_{tot} - m_{\rho}^{MC}}{\sigma_{\rho}^{MC}} \right)^2 + \left( \frac{m_{\gamma\gamma} - m_{\pi^0}^{MC}}{\sigma_{\pi^0}^{MC}} \right)^2, \quad (6.2)$$

where  $m_{\gamma\gamma}$  is the invariant mass of two photons;  $m_{tot}$  is the invariant mass of the two photons and one  $\pi^-$ ;  $m_{\rho}^{MC}$  and  $m_{\pi^0}^{MC}$  are true masses of  $\rho$  and  $\pi^0$ , respectively, taken from [6]; and  $\sigma_{\rho}^{MC}$  and  $m_{\pi^0}^{MC}$  are the half width of the invariant mass distribution of reconstructed  $\rho$  and  $\pi^0$ , respectively, obtained using the truth information. All combinations of photons and  $\pi^-$  are tested. Two variables obtained in this minimisation and used in the MVA classification are the invariant mass of the two photons in the fit,  $m_{\pi^0}(\rho)$ , and the invariant mass of the two photons and one  $\pi^-$ ,  $m_{\rho}$ .

Similarly,  $a_1(\pi^-\pi^0\pi^0)$  decay mode can be identified using an extended minimisation function:

$$\chi^2 = \left( \frac{m_{tot} - m_{a_1}^{MC}}{\sigma_{a_1}^{MC}} \right)^2 + \left( \frac{m_{\gamma 1 \gamma 2} - m_{\pi^0}^{MC}}{\sigma_{\pi^0}^{MC}} \right)^2 + \left( \frac{m_{\gamma 3 \gamma 4} - m_{\pi^0}^{MC}}{\sigma_{\pi^0}^{MC}} \right)^2, \quad (6.3)$$

where  $\rho$  has been replaced by  $a_1$  and other variables are defined in the same way as in the previous  $\chi^2$  function in equation 6.2. Two photon pairs and one  $\pi^-$  are needed for this minimisation. Both photon pairs are required to be consistent with the  $\pi^0 \rightarrow \gamma\gamma$ . Three variables obtained in this minimisation and used in the MVA classification are the invariant mass of the first two photons in the fit,  $m_{\pi^0}(a_1)$ ; the invariant mass of the last two photons in the fit,  $m_{\pi^0}^*(a_1)$ ; and the invariant mass of the four photons and one  $\pi^-$ ,  $m_{a_1}$ . The first photon pair is defined to have an invariant mass closer to the invariant mass of the  $\pi^0$  than the second photon pair. Figure 6.2d shows the distributions of the invariant mass of  $m_{a_1}$  under  $a_1(\pi^-\pi^0\pi^0)$  hypothesis test for selected tau decay modes. Only the distribution for  $a_1(\pi^-\pi^0\pi^0)$  decay mode has a resonance peak at  $a_1$  mass.

The  $\chi^2$  functions for both hypothesis test are adapted for events where the event reconstruction fails to reconstruct enough photons. Relevant terms are dropped from the expression if there are fewer photons reconstructed than required in the  $\chi^2$  functions.

### 6.5.6. Separate $e^-$ from $\pi^-$

The Particle ID obtained from PandoraPFA is used extensively to reconstruct variables used in the MVA classification. In particular PandoraPFA uses a wide range of information to determine the electron ID. However, extra variables are used in this analysis to help further identify electrons, which could be mistaken as  $\pi^-$  by PandoraPFA reconstruction.

An electron leaves a characteristic electromagnetic (EM) shower in the ECAL, whilst  $\pi^-$  doesn't. Variables characterising the EM shower help to identify  $e^-$ . Three variables are used in the MVA classification: the start layer of the longitudinal shower ( $t_0$ ); the fractional difference between observed and expected longitudinal shower profile describing the longitudinal EM shower ( $\delta l$ ); and  $\langle w \rangle$ , a measure of the EM shower transverse width. These variables are taken from the photon ID step in the photon reconstruction in PandoraPFA, described in section 5.5.

Another type of information to differentiate an EM shower from an early hadronic shower from a  $\pi^-$  is the calorimeter hit information. Two variables used in the MVA classification are: the average energy of a calorimeter hit ( $\bar{E}_{hit}$ ) and the average fraction of possible minimum ionising calorimeter hit for all particles (%MIP)

Last information used to separate  $e^-$  from  $\pi^-$  is the track-momentum-calorimeter-energy consistency check. The variable used in the MVA classification is the calorimeter energy divided by the track momentum for all particles ( $\Delta E/P$ ).

The variables used to separate  $e^-$  from  $\pi^-$  are obtained via a modified version of PandoraPFA.

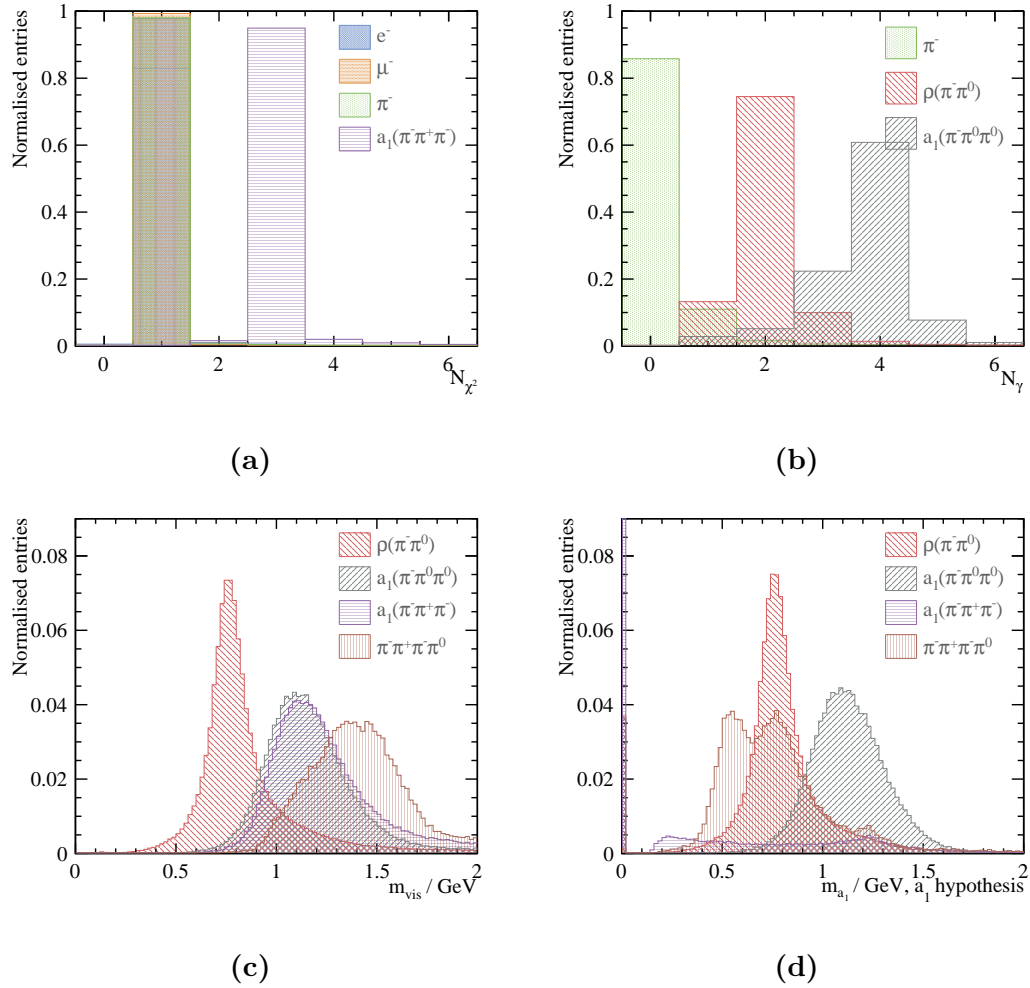


**Figure 6.2:** Distribution for a) the number of charged particle ( $N_{\chi^+}$ ); b) the number of photons ( $N_\gamma$ ); c) the invariant mass of all non-neutrino decay products ( $m_{vis}$ ); and d) the invariant mass of the  $a_1$ , reconstructed with  $a_1(\pi^-\pi^0\pi^0)$  hypothesis. Area under the curve for each decay mode is normalised to 1. Decay modes in all plots are selected using the truth information.

Category	Variable
PFOs number	$N_{\chi^+}, N_\mu, N_e, N_\gamma, N_{\pi^-}$
Invariant mass	$m_{vis}, m_{\chi^+}, m_{\chi^0}, m_\gamma, m_{\pi^-}$
Energy	$\tilde{E}_{vis}, \tilde{E}_{\chi^+}, \tilde{E}_\mu, \tilde{E}_e, \tilde{E}_\gamma, \tilde{E}_{\pi^-}$
Calorimetric info.	$\%E_{\chi^+}, \%E$
$\rho(\pi^-\pi^0)$ reconstruction	$m_{\pi^0}(\rho), m_\rho$
$a_1(\pi^-\pi^0\pi^0)$ reconstruction	$m_{\pi^0}(a_1), m_{\pi^0}^*(a_1), m_{a_1}$
EM shower profile	$\delta l, t_0, \langle w \rangle$
Calorimeter hit info.	$\bar{E}_{hit}, \%MIP$
Track info.	$\Delta E/P$

**Table 6.4:** Variables used in the MVA classification for the tau lepton decay mode classification.

## 6.6. Multivariate Analysis

For the multivariate analysis, the multiclass class of the TMVA package [86] was used to perform a multiclass classification, which classifies seven tau lepton decay final states simultaneously. The multiclass classifier is an extension of a standard two-class signal-background classifier. The discussion on multivariate analysis can be found in section 4.8. In particular, the multiclass classifier is discussed in section 4.8.9.

The multiclass classifier used is Boosted Decision Tree with Gradient boost (BDTG). The optimisation of the BDTG classifier followed the strategy in section 4.8.1. The optimised parameters are listed in table 6.5. An explanation of the variables can be found in section 4.8.8. Half of the randomly selected samples were used in the training process and the other half were used for testing.

## 6.7. Tau decay mode classification efficiency

The classification efficiencies for the seven tau decay modes are shown in table 6.6. Bold numbers show the correct classification probabilities.

For the  $e^-$  decay mode, 99.8% correct classification efficiency is achieved. For  $\mu^-$  decay mode, 99.5% correct classification efficiency is achieved, due to an effective track reconstruction and muon reconstruction algorithms in PandoraPFA.

Parameter	Value
Depth of tree	5
Number of trees	3000
Boosting	gradient boost
learning rate of the gradient boost	0.1
metric for the optimal cuts	Gini Index
bagging fraction	0.5
Number of bins per variables	100
End node output	yes/no

**Table 6.5:** Optimised parameters for the Boosted Decision Tree with Gradient boost multiclass classifier. See section 4.8.8 for a detailed explanation of variables.

For the  $\pi^-$  decay mode, 3.4% events were misclassified as  $\rho(\pi^-\pi^0)$  decay events. If the reconstruction is unable to reconstruct the photon pair from  $\pi^0$  decay in  $\rho(\pi^-\pi^0)$  decay mode, the  $\pi^-$  and  $\rho(\pi^-\pi^0)$  decay events would appear to similar and misclassification is caused. On the other hand, only 0.9% of  $\pi^-$  decay events are misclassified as  $e^-$  decay, due to variables dedicated to separation between  $e^-$  and  $\pi^-$ .

For the  $\rho(\pi^-\pi^0)$  decay mode, most misclassification comes from the confusion with  $a_1(\pi^-\pi^0\pi^0)$  decay mode. If the reconstruction is unable to resolve the all photon pair from  $\pi^0$  decay in  $\rho(\pi^-\pi^0)$  and  $a_1(\pi^-\pi^0\pi^0)$  decay mode, the two decay modes would have similar topologies.

For the  $a_1(\pi^-\pi^0\pi^0)$  decay mode, the correct classification rate is the lowest among seven decay modes, as the  $a_1(\pi^-\pi^0\pi^0)$  decay final state is the most challenging to reconstruct correctly: two photon pairs and one  $\pi^\pm$ . The 9.5% confusion with  $\rho(\pi^-\pi^0)$  is due to the same photon reconstruction failure issue. It should be noted that figure 6.2b suggests that 30% of  $a_1(\pi^-\pi^0\pi^0)$  events have fewer than four photons reconstructed, where the distribution overlaps with the distribution for  $\rho(\pi^-\pi^0)$  decay mode. The  $a_1(\pi^-\pi^0\pi^0)$  resonance reconstruction and the multiclass classifier reduce the confusion between two decay modes from 30% to 9.5%.

For the  $a_1(\pi^+\pi^-\pi^-)$  decay mode, the biggest source of misclassification is with  $\pi^+\pi^-\pi^-\pi^0$  decay mode. The biggest misclassification of  $\pi^+\pi^-\pi^-\pi^0$  decay mode is with  $a_1(\pi^+\pi^-\pi^-)$  decay mode.

Reco↓ Truth →	e <sup>-</sup>	μ <sup>-</sup>	π <sup>-</sup>	ρ(π <sup>-</sup> π <sup>0</sup> )	a <sub>1</sub> (π <sup>-</sup> π <sup>0</sup> π <sup>0</sup> )	a <sub>1</sub> (π <sup>+</sup> π <sup>-</sup> π <sup>-</sup> )	π <sup>+</sup> π <sup>-</sup> π <sup>-</sup> π <sup>0</sup>
e <sup>-</sup>	<b>99.7%</b>	-	0.9%	0.6%	0.4%	-	-
μ <sup>-</sup>	-	<b>99.5%</b>	0.6%	-	-	-	-
π <sup>-</sup>	-	0.3%	<b>94.0%</b>	0.8%	-	0.4%	-
ρ(π <sup>-</sup> π <sup>0</sup> )	-	-	3.4%	<b>93.6%</b>	9.5%	0.6%	2.3%
a <sub>1</sub> (π <sup>-</sup> π <sup>0</sup> π <sup>0</sup> )	-	-	-	4.5%	<b>89.7%</b>	-	0.6%
a <sub>1</sub> (π <sup>+</sup> π <sup>-</sup> π <sup>-</sup> )	-	-	0.9%	-	-	<b>96.8%</b>	6.4%
π <sup>+</sup> π <sup>-</sup> π <sup>-</sup> π <sup>0</sup>	-	-	-	0.3%	-	2.0%	<b>90.6%</b>

**Table 6.6:** Classification efficiency in percentage for seven tau decay modes using the nominal ILD detector model, using  $e^+e^- \rightarrow \tau^+\tau^-$  channel at  $\sqrt{s} = 100$  GeV. Bold numbers show the correct classification probabilities.  $\nu_\tau$  is not shown. - represents a number below 0.25%. Statistical uncertainties are less than 0.25%.

## 6.8. Electromagnetic calorimeter optimisation

In above sections, an analysis on tau decay mode classification is presented. Events used in the analysis were  $e^+e^- \rightarrow \tau^+\tau^-$  events at  $\sqrt{s} = 100$  GeV with the nominal ILD detector model. In this section, the analysis was repeated with varying ECAL square cell sizes at 3, 5, 7, 10, 15 and 20 mm, and at four centre-of-mass energies of 100, 200, 500, 1000 GeV. Other ECAL dimensions are kept the same as the ILD nominal detector. The multivariate classifier was trained for each ECAL cell size and each centre-of-mass energy. Because the electron and muon reconstruction mostly rely on the tracking system, which was not varied in this study, only the hadronic tau decay modes were investigated for the ECAL optimisation study. The correct classification efficiencies for tau hadronic decay final states as a function of the ECAL square cell sizes for different centre-of-mass energies are shown in figure 6.3.

As PandoraPFA is optimised for the nominal ILD detector, a re-optimisation is required when changing the ECAL square cell sizes. In particular, fragment removal algorithms have a large dependence on the ECAL cell sizes. For example, the PHOTON-FRAGMENTREMOVAL algorithm which merges photon fragments uses a distance metric that depends on the ECAL cell sizes. Table 6.7 shows the optimised distance metrics as a function of the ECAL square cell size. As cell sizes become larger, the distance cut for merging photons become larger, as expected.

ECAL square cell size	3 mm	5 mm	7 mm	10 mm	15 mm	20 mm
ClosestHitDistance	5 mm	10 mm	10 mm	10 mm	20 mm	20 mm

**Table 6.7:** Optimised parameters of PHOTONFRAGMENTREMOVAL algorithm as a function of the ECAL square cell size.

As the centre-of-mass energy increases, tau decay products are often boosted. It is increasingly difficult to separate tau decay products. For example, the photon pair from  $\pi^0$  decay becomes very challenging to separate at a high centre-of-mass energy. Therefore, the inability to separate photon pairs will degrade the classicisation performance.

An increase of the ECAL cell sizes has a similar effect of degrading the classicisation performance. The change in the ECAL cell size will change the transverse spatial resolution. Hence a large cell size will result in a low transverse spatial resolution, leading to inability to separate photon pairs. Consequently, a worse classification performance is expected for a larger ECAL cell size.

Supported by figure 6.3, tau decay mode correct classification efficiencies generally decrease with an increase of centre-of-mass energies and an increase of ECAL cell sizes, as expected. This trend is observed for almost all tau decay modes.

For the  $\rho(\pi^-\pi^0)$  decay mode, the efficiency for  $\sqrt{s} = 500 \text{ GeV}$  increases as the cell sizes increases. This is because the multivariate classifier optimises for the overall classification efficiency, which balances the decrease of the efficiency of one decay mode by the increase of the efficiency of another decay mode. In this case, the small increase in the efficiency for  $\rho(\pi^-\pi^0)$  at  $\sqrt{s} = 500 \text{ GeV}$  is compensated by the drastic decrease in the efficiency for  $a_1(\pi^-\pi^0\pi^0)$  at  $\sqrt{s} = 500 \text{ GeV}$ .

For the  $a_1(\pi^-\pi^0\pi^0)$  decay mode, the loss of efficiency with an increasing ECAL cell size and an increasing centre-of-mass energy is most significant comparing to other decay modes. With most number of particles in the final state, it is the most challenging decay channel to reconstruct and thus most sensitive to the change in cell sizes and centre-of-mass energies.

For the  $a_1(\pi^+\pi^-\pi^-)$  decay mode, the efficiencies are similar to that of the  $\pi^-$  decay mode. Both final states contain charged particles only. Therefore it is most sensitive to the tracking performance, which is not affected by the varying of the ECAL cell sizes.

For the  $\pi^+\pi^-\pi^-\pi^0$  decay mode, the decrease in efficiencies are more significant for  $\sqrt{s} = 500 \text{ GeV}$  and  $1000 \text{ GeV}$ .

The correct reconstruction efficiency of the tau leptonic decay is not used as a metric as they are similar across different ECAL cell sizes. This is because the  $e^\pm$  and  $\mu^\pm$  identifications mostly rely on the tracking system, which was not varied in this study. However the energy deposited in the calorimeter are also used for the association to the tracks. But the calorimeters have a small impact on the electron and muon identification.

### 6.8.1. Tau hadronic decay correct classification efficiency

There are two reasons to construct a single parameter for overall tau decay efficiency: firstly the multivariate classifier is trained to optimised to achieve the best the overall classification efficiency; secondly it is easier to compare the impact of different detector models and different centre-of-mass energies with a single parameter.

The constructed tau hadronic decay correct classification efficiency,  $\varepsilon_{had}$ , is a weighted correct classification efficiency for five hadronic decay modes:

$$\varepsilon_{had} = \frac{\sum_i^5 Br_i \varepsilon_i}{\sum_i^5 Br_i}, \quad (6.4)$$

where  $Br_i$  is the branching fraction of the hadronic decay mode  $i$  after the pre-selection cuts;  $\varepsilon_i$  is the correct reconstruction efficiency of the decay mode  $i$ ; and index  $i$  is summed over five tau hadronic decay modes.

Figure 6.4 shows  $\varepsilon_{had}$  as a function of ECAL cell sizes with increasing centre-of-mass energies. The general trend for the  $\varepsilon_{had}$  is that  $\varepsilon_{had}$  decreases with the increase of centre-of-mass energies and the increase of ECAL cell sizes, because it is increasingly difficult to reconstruct photons with boosted particles and lower ECAL transverse spatial resolutions.

At  $\sqrt{s} = 100 \text{ GeV}$ , the  $\varepsilon_{had}$  decreases from 94% at 3 mm cell size, to 91% at 20 mm cell size. The decrease is approximately linear to the increase in the cell size. The decrease in  $\varepsilon_{had}$  is greater at  $\sqrt{s} = 200 \text{ GeV}$ , where  $\varepsilon_{had}$  declined from 94% at 3 mm cell size, to 86% for a ECAL cell size of 20 mm. Most significant decrease in the  $\varepsilon_{had}$  occurs at  $\sqrt{s} = 500 \text{ GeV}$ , where the  $\varepsilon_{had}$  decreases from 92% at 3 mm cell size, to 78% at 20 mm cell size. At  $\sqrt{s} = 1000 \text{ GeV}$ , the  $\varepsilon_{had}$  drops from 85% at 3 mm cell size, to 75% at 20 mm cell size.

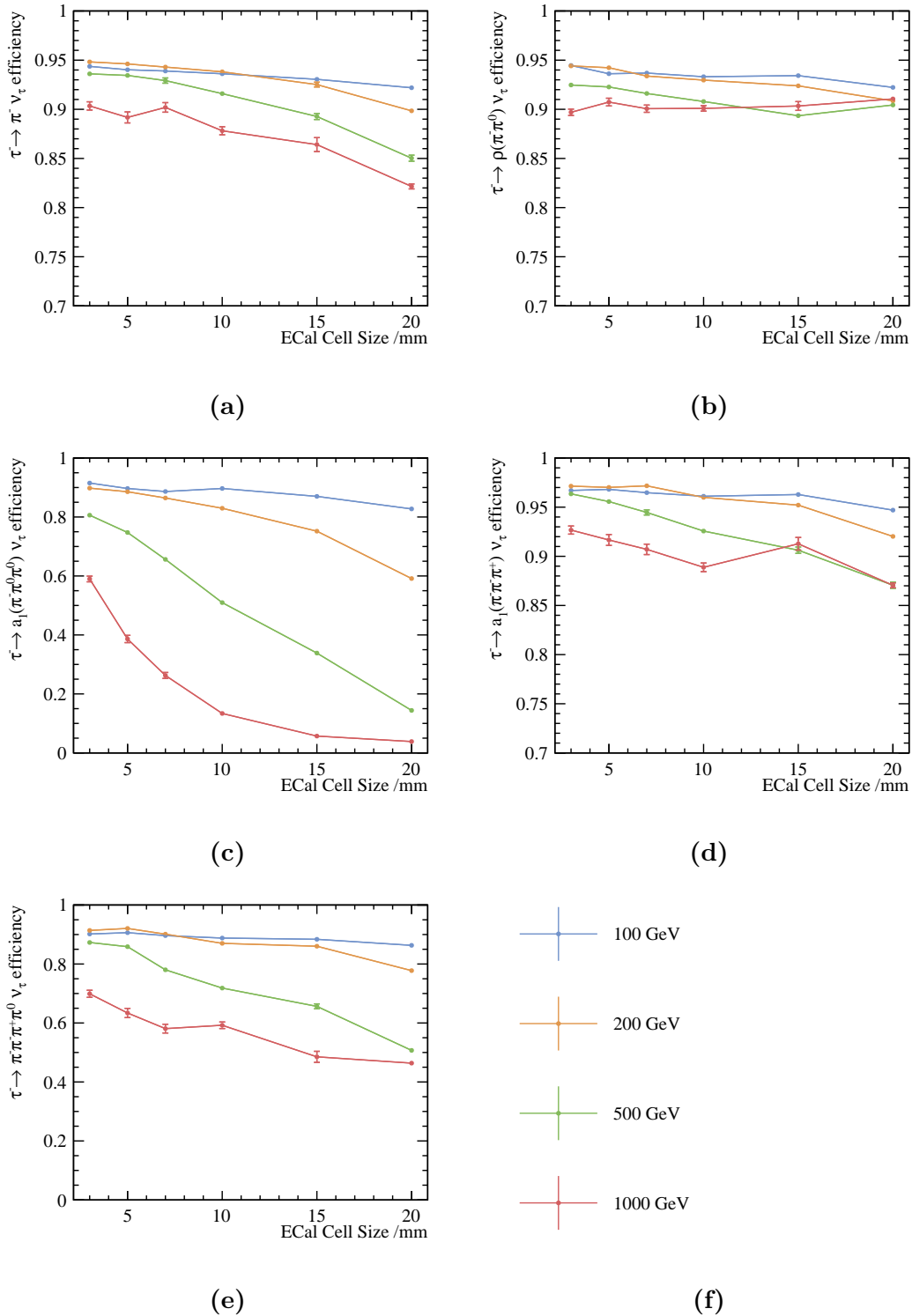


**Figure 6.3:** The correct classification efficiencies for tau hadronic decay final states as a function of the ECAL square cell sizes for a)  $\pi^-$  decay mode, b)  $\rho(\pi^-\pi^0)$  decay mode, c)  $a_1(\pi^-\pi^0\pi^0)$  decay mode, d)  $a_1(\pi^+\pi^-\pi^-)$  decay mode, and e)  $\pi^+\pi^-\pi^-\pi^0$  decay mode. The legend is shown in f). All plots are produced using the ILD detector model with  $\sqrt{s} = 100, 200, 500$  and  $1000$  GeV.

The increase in ECAL cell sizes has a larger impact on tau decay classification at high centre-of-mass energies. With decay products being spatially close at high centre-of-mass energies, it is more beneficial to have a smaller ECAL cell size to reconstruct individual particle.

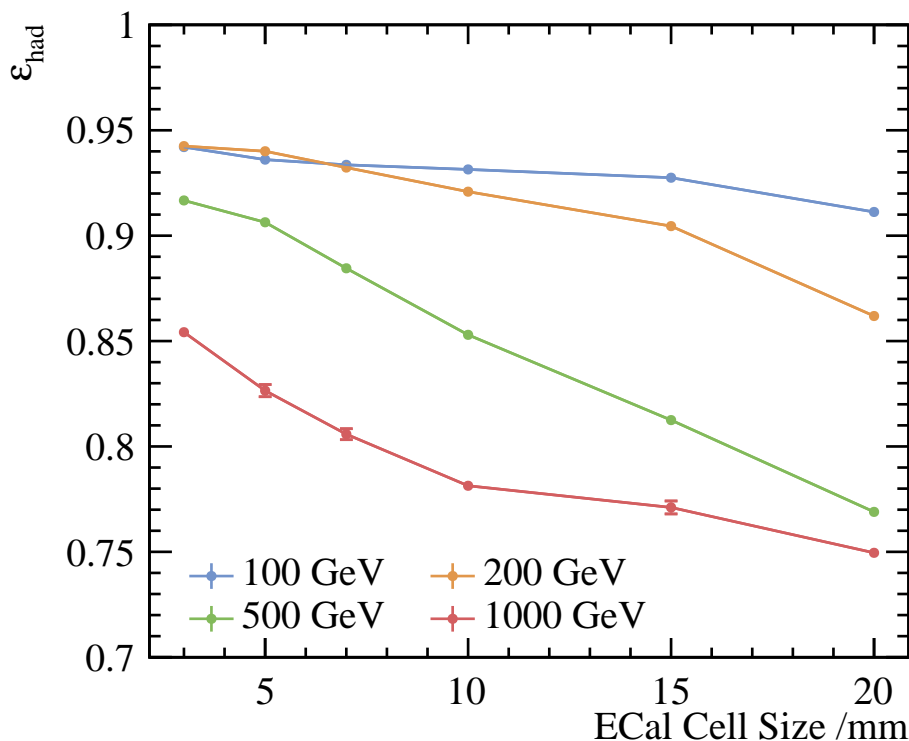


**Figure 6.4:** The tau hadronic decay efficiency,  $\varepsilon_{had}$ , as a function of the ECAL cell sizes with different centre-of-mass energies using the ILD detector model. The blue, orange, green and red lines represent the efficiencies at  $\sqrt{s} = 100, 200, 500$  and  $1000\text{ GeV}$  respectively.

## 6.9. Tau pair polarisation correlations as a signature of Higgs boson

Many BSM theories predict the  $H\tau^+\tau^-$  coupling would dominate the Higgs boson to leptons couplings [87]. Therefore, if an experiment observes an excess of tau pair decay events, it could be an indication of the Higgs boson. Here, this section follows the

theoretical discussion in section 2.9 to present a proof-of-principle analysis using tau pair polarisation correlation as a signature of Higgs boson.

Comparing  $H \rightarrow \tau^+ \tau^-$  and  $Z \rightarrow \tau^+ \tau^-$ , the difference in the spin of the bosons reflects in the different polarisation correlation of the tau pair. By extracting the polarisation correlations of the tau pair, the parent boson can be identified.

The subsequent sections discuss the ability to reconstruct the polarisation correlation of the tau pair with  $Z \rightarrow \tau^+ \tau^-$  channel, where both  $\tau^- \rightarrow \pi^- \nu_\tau$ . The analysis starts with the event pre-selection, followed by identifying the tau decay products in the events. Afterwards, the tau decay mode classification is used to identify  $\tau^- \rightarrow \pi^- \nu_\tau$  decays. Lastly the tau pair polarisation correlation is presented and compared to the correlation distribution obtained with Monte Carlo simulation.

### 6.9.1. Event pre-selection

The channel to study is  $e^+ e^- \rightarrow ZZ$ , where one Z decays hadronically and the other Z decays to a tau lepton pair. The samples were generated at  $\sqrt{s} = 350$  GeV without ISR contribution for this proof-of-principle study.

The same seven tau decay modes in section 6.2 are studied. The  $\tau^- \rightarrow \pi^- \nu_\tau$  decay mode is selected for the proof-of-principle analysis of H/Z separation with tau pair decay channel.

The event pre-selection is similar to that in section 6.4. The cut on the total energy of non-neutrino decay products is not used, because a large fraction of  $Z \rightarrow \tau^+ \tau^-$  events, where  $\tau^- \rightarrow \pi^- \nu_\tau$ , has two low-energy charged pions. Therefore, the cut on the energy of non-neutrino decay products would throw away many events.

### 6.9.2. Find tau decay products

The final state of the selected channel,  $e^+ e^- \rightarrow ZZ \rightarrow \tau^+ \tau^- qq$ , contains two tau leptons and two quark jets. Therefore, tau decay products can either be found by direct tau lepton searching, or by using jet algorithms to find tau decay products as jets. If a tau lepton decays into a few particles, then the direct tau searching would work better. If a tau lepton decays into many particles, finding tau decay products as a jet has a better

performance, as jet clustering works better with more particles. Hence, two approaches are combined to find the best tau pair.

### 6.9.2.1. Direct tau searching

Tau finder processer, ISOLATEDTAUIDENTIFER, is a modified version of the one in section 7.3.2.2. The basic idea is to find tau decay products consistent with tau decay topologies, and requires the tau decay products to be isolated from the rest of the particles. Parameters chosen are set to find as many tau candidates as possible.

Table 6.8 lists all the cuts used in the ISOLATEDTAUIDENTIFER. Particles with transverse momentum ( $p_T$ ) less than 0.5 GeV are not considered. A seed particle is chosen and a search cone is formed around the seed, which requires one or three tracks with the invariant mass of all particles inside the search cone less than 3 GeV. The maximum search cone opening angle ( $\theta_S$ ) is  $\cos^{-1}(0.99)$ . The isolation criteria states that the opening angle between the search cone and the 2<sup>nd</sup> closest track ( $\theta_{cone,2^{nd}X^+}$ ) is larger than 0.6 rad. If the criteria is satisfied, the search cone with the tau seed is identified as a tau lepton.

Modified ISOLATEDTAUIDENTIFER	Selection
Veto low $p_T$	$p_T < 0.5 \text{ GeV}$
Seed particle	$p_T > 1 \text{ GeV}$
Maximum search cone opening angle	$\theta_S \leq \cos^{-1}(0.99)$
Tau candidate rejection	$N_{X^+} \neq 1 \text{ or } 3; m_{PFO} > 3 \text{ GeV}$
Isolation	$\theta_{cone,2^{nd}X^+} > 0.6 \text{ rad}$

**Table 6.8:** Optimised parameters of the modified ISOLATEDTAUIDENTIFER.

### 6.9.2.2. Jet clustering

Tau hadronically decay products can be also identified as a small jet. The Durham algorithm, also known as the  $e^+e^- k_t$  algorithm, was used to form jets (see section 4.7.4). The jet algorithm runs in the exclusive mode to find four jets for  $e^+e^- \rightarrow ZZ \rightarrow \tau^+\tau^-qq$  channel.

### 6.9.2.3. Select tau candidates

The best tau pair candidates are further selected using kinematic constraints. In  $e^+e^- \rightarrow ZZ$  events, the energy of the Z is half of the centre-of-mass energy. The invariant mass of two quarks from Z should be close to Z mass. Therefore, the minimisation function utilising kinematic constraints is:

$$\chi^2 = \frac{(m_{qq} - m_Z)^2}{\sigma_{m_{qq}}^2} + \frac{(E_{qq} - \frac{\sqrt{s}}{2})^2}{\sigma_{E_{qq}}^2}, \quad (6.5)$$

where  $\sqrt{s}$  is the centre-of-mass energy;  $m_Z$  is the mass of Z from reference [6];  $\sigma_{m_{qq}}$  and  $\sigma_{E_{qq}}$  are the reconstructed mass resolution and energy resolution of the  $Z \rightarrow qq$ , respectively;  $m_{qq}$  and  $E_{qq}$  are defined differently for the direct tau searching and the jet clustering method; and the minimisation is iterated over all tau pairs from direct tau searching method or over all jets from jet clustering method. For the direct tau searching method,  $m_{qq}$  and  $E_{qq}$  are obtained from the recoil momenta against two tau candidates, assuming collisions happening at  $\sqrt{s}$ :  $m_{qq}$  is the invariant mass of the recoil momenta, and  $E_{qq}$  is the energy of the recoil momenta. For the jet clustering method,  $m_{qq}$  and  $E_{qq}$  are defined as the total invariant mass and energy of two jets.

The  $\chi^2$  minimiser is repeated for the direct tau searching method and the jet clustering method. Each method selects a best tau pair candidate with the smallest  $\chi^2$ . Hence two tau pair candidates are obtained. To find the best overall tau pair candidate, a set of conditions is used. If the best tau pair candidate from both methods satisfies the kinematic constraint:

$$\left| m_{qq} - m_Z \right| < \sigma_{m_{qq}}, \quad \left| E_{qq} - \frac{\sqrt{s}}{2} \right| < \sigma_{E_{qq}}, \quad (6.6)$$

the tau pair candidate with smallest  $\chi^2$  is selected. Otherwise, if only one tau pair candidate satisfies the constraint in equation 6.6, that candidate is chosen. If none of the candidates satisfies the constraint, and if one jet from the jet clustering is close to the beam pipe and there are exactly two tau candidates from ISOLATEDTAUIDENTIFIER, then these two tau candidates are chosen. This is because if one jet is close to the beam pipe, it is likely that some particles close to the jet are undetected, which leads to a failure in the kinematic constraint or the jet reconstruction. Lastly, if all conditions above are not satisfied, two smallest jets by the number of PFOs are chosen to be the best tau pair candidate.

### 6.9.3. Boost tau decay products to Z decay rest frame

The previous section describes the method to identify the tau pair decay products. To use the tau decay mode classifier, it is necessary to know the tau lepton energy. For the channel  $Z \rightarrow \tau^+ \tau^-$ , the energy of the tau lepton can only be obtained in  $Z\tau^+\tau^-$  decay rest frame, which is half of the Z energy in the  $Z\tau^+\tau^-$  rest frame. Hence the tau decay products need to be boosted to the Z decay rest frame for the calculation of the variables used in the MVA classification. The boosting requires the four-momentum of the Z.

The four-momentum of the Z decaying to tau pair is calculated from the recoil momenta of non tau-decay-products:

$$p_{\tau\tau}^\mu = \begin{pmatrix} \sqrt{s} \\ \sqrt{s} \times \sin(\theta_{beam}) \\ 0 \\ 0 \end{pmatrix} - \sum_i^{non-\tau} p_i^\mu, \quad (6.7)$$

where  $\theta_{beam}$  is the beam crossing angle;  $\sqrt{s}$  is the centre-of-mass energy;  $p_i^\mu$  is the four-momentum vector of the particle  $i$ ;  $p_{\tau\tau}^\mu$  is the four-momentum vector of the Z, where  $Z \rightarrow \tau^+ \tau^-$ ; and index  $i$  is summed over all non-tau-decay-product PFOs. Extra kinematic constraint fixes the energy of the  $p_{\tau\tau}^\mu$  to be half of  $\sqrt{s}$ :

$$p_{\tau\tau,correct}^\mu \equiv p_{\tau\tau}^\mu \times \frac{\frac{1}{2}\sqrt{s}}{E_{\tau\tau}}, \quad (6.8)$$

where  $E_{\tau\tau}$  is the energy of the vector  $p_{\tau\tau}^\mu$  and other variables are defined in the same way as in the previous equation.  $p_{\tau\tau,correct}^\mu$  is then treated as the four-momentum vector of Z, where  $Z \rightarrow \tau^+ \tau^-$ . Tau decay products are boosted to the Z decay rest frame accordingly. The calculation of the variables used in the MVA classifier are then performed in the  $Z \rightarrow q\bar{q}$  decay rest frame.

### 6.9.4. Variables used in the MVA

Variables used in the MVA classifier are a subset of the ones used in the previous analysis. Variables regarding EM shower profiles, calorimeter hit information and track information

are not used (the last three rows in table 6.4) as the information was not available in the standard version of PandoraPFA used in this analysis.

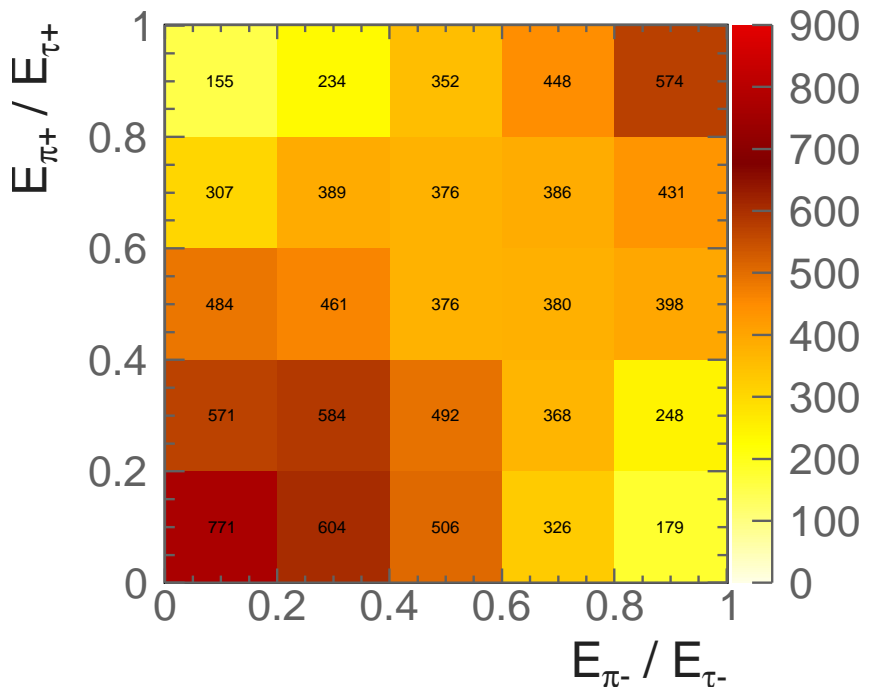
### 6.9.5. Multivariate analysis

Half of the randomly selected sample is used to train the multivariate classifier, which follows the procedure in section 6.6. The same classifier as in the previous analysis is used. In the classifier applying stage,  $\tau^- \rightarrow \pi^- \nu_\tau$  decay mode is selected with an additional criteria that there is at least one  $\pi^\pm$  among the tau decay products.

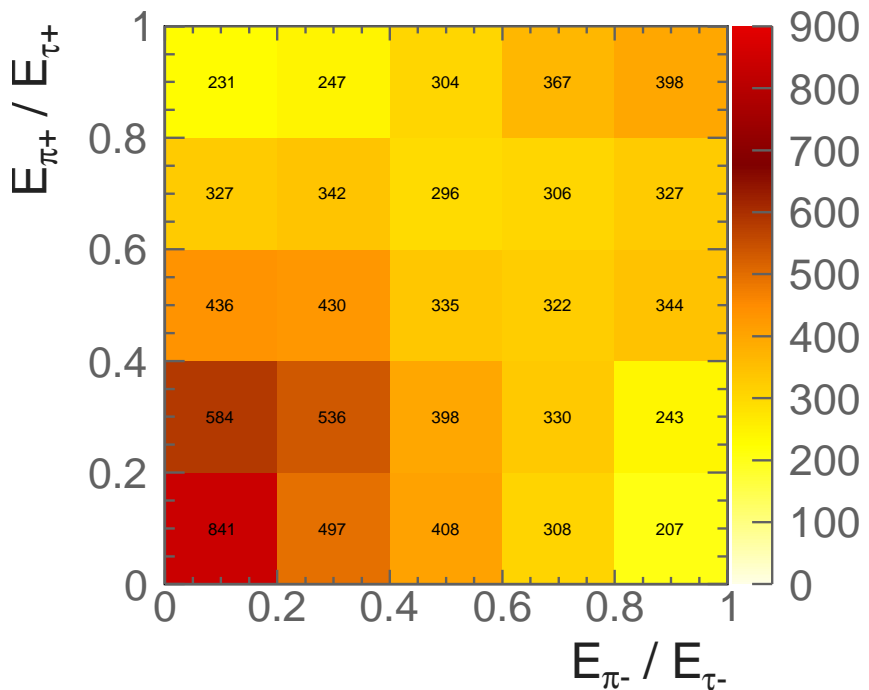
### 6.9.6. Result

Figure 6.5 shows the two-dimensional plot of tau pair polarisation correlations from Z decay, using  $\tau^- \rightarrow \pi^- \nu_\tau$  decay mode, with  $e^+ e^- \rightarrow ZZ$  channel where one Z decays to a tau pair and the other Z decays hadronically. The energy fractions of the tau decay product to the tau lepton are the appropriate kinematic variables, motivated in the theoretical discussion in section 2.9. Figure 6.5a shows the distribution obtained with the Monte Carlo particles. Figure 6.5b shows the distribution using full detector simulation. Dark regions along the diagonal can be seen in both the distribution for the full detector simulation and the distribution for the Monte Carlo simulation. In the  $Z \rightarrow \tau^+ \tau^-$  decays, an energetic  $\pi^+$  is likely to be associated with an energetic  $\pi^-$  and a low-energy  $\pi^+$  is likely to be associated with a low-energy  $\pi^-$ . This trend is shown in both the distribution produced with the Monte Carlo particles and with the full detector simulation. Comparing the two figures in Figure 6.5, some events in the top right quadrant, resembling both  $\pi^\pm$  being energetic, are not reconstructed correctly. This is due to the incorrect finding of the tau pair decay products (section 6.9.2).

This proof-of-principle analysis shows the tau polarisation correlations with  $Z \rightarrow \tau^+ \tau^-$  decay where  $\tau^- \rightarrow \pi^- \nu_\tau$  can be observed with ILD detector model. With a similar study of  $H \rightarrow \tau^+ \tau^-$ , the tau polarisation correlations can be used to separate Higgs boson from Z boson, and to identify Higgs boson in an experiment that observes the breaking of the lepton universality by favouring tau pair events.



(a) Monte Carlo particles



(b) Simulated and reconstructed particles

**Figure 6.5:** Two-dimensional histograms of  $E_{\pi^+}/E_{\tau^+}$  as a function of  $E_{\pi^-}/E_{\tau^-}$  obtained with  $Z \rightarrow \tau^+\tau^-$  channel, selecting  $\tau^- \rightarrow \pi^-\nu_\tau$  decay mode for both taus, for a) Monte Carlo particles, and b) simulated and reconstructed particles.



# Chapter 7.

## Double Higgs Boson Production Analysis

*'The supreme art of war is to subdue the enemy without fighting.'*

— Sun Tzu, 544 BC - 496 BC

Having discovered a Higgs-like particle the LHC in 2012 [3, 4], it became crucial to understand the interaction between the Higgs and other particles, and to determine whether it is the Standard Model Higgs. A number of Higgs theories beyond the Standard Model may be tested via the double Higgs production in an electron-positron collider [13, 14]. The study of double Higgs production would prevail the measurement of the Higgs trilinear self coupling,  $g_{H\bar{H}H}$ , and the quartic coupling,  $g_{WW\bar{H}H}$ . The precision for the measurement of  $g_{H\bar{H}H}$  achievable by the Compact Linear Collider (CLIC), is superior to that at the LHC and the HL-LHC [22].

In  $e^+e^-$  collisions, there are two main challenges with the study the double Higgs production,  $e^+e^- \rightarrow HH\nu_e\bar{\nu}_e$ . Firstly, the process has a small cross section; 0.149 fb at  $\sqrt{s} = 1.4$  TeV and 0.588 fb at  $\sqrt{s} = 3$  TeV. The other challenge is that at high centre-of-mass energies, events are often boosted. Consequently, many final-state particles are in the forward region of the detector, where the reconstruction performance is inferior to the barrel region. In addition, particles can escape detection, causing a degradation in the event reconstruction performance.

In this chapter, a full CLIC\_ILD detector simulation study has been performed for the double Higgs production channel,  $e^+e^- \rightarrow HH\nu_e\bar{\nu}_e$ , via  $W^+W^-$  fusion. Event

generation and simulation will be discussed first. An overview of the analysis, including lepton finding and jet reconstruction, is presented, followed by an optimised multivariate analysis to distinguish signal from background processes. The optimised event selection is used to derive an estimate of the uncertainty on  $g_{HHH}$  and  $g_{WWHH}$  measurements at the CLIC. Part of this analysis has been published in [24].

## 7.1. Analysis Strategy Overview

The study of double Higgs production via  $W^+W^-$  fusion can probe the Higgs trilinear self coupling,  $g_{HHH}$ , and quartic coupling,  $g_{WWHH}$ . Leading-order Feynman diagrams for double Higgs production via  $W^+W^-$  fusion are shown in figure 7.1. The diagram shown in figure 7.1a contains the triple Higgs vertex, which is sensitive to the Higgs trilinear self coupling  $g_{HHH}$ . The diagram in the figure 7.1b is sensitive to the quartic coupling  $g_{WWHH}$ . Figures 7.1c and 7.1d show the Feynman diagrams for irreducible background processes in the study of  $g_{HHH}$  and  $g_{WWHH}$ .

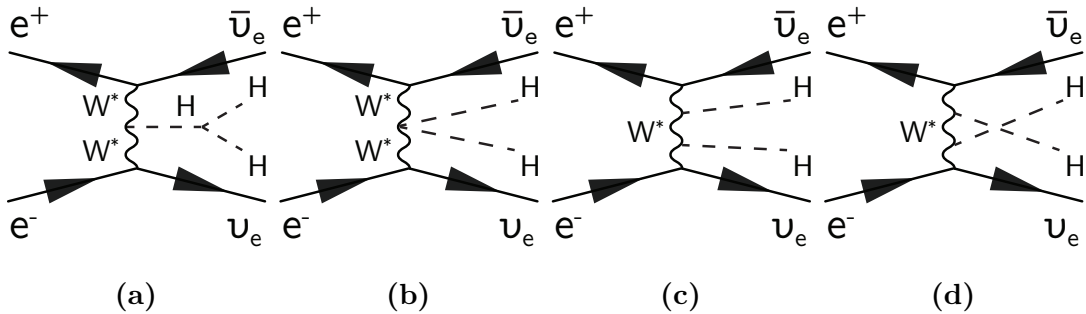


**Figure 7.1:** The main Feynman diagrams for the leading-order  $e^+e^- \rightarrow HH\nu_e\bar{\nu}_e$  processes at CLIC.

Double Higgs production can be also proceeded via  $e^+e^- \rightarrow ZHH$ , where the  $Z$  decays to  $\nu\bar{\nu}$ . The  $ZHH$  channel has been studied in  $e^+e^-$  collisions  $\sqrt{s} = 500$  GeV [29]. However, for the CLIC energies of  $\sqrt{s} = 1.4$  TeV and 3 TeV, its contribution to the  $HH\nu\bar{\nu}$  final state is small compared to that of the  $W^+W^-$  fusion, and it can be neglected.

The two Higgs in the  $e^+e^- \rightarrow HH\nu_e\bar{\nu}_e$  decay to a range of particles. Hence double Higgs production has several distinct final-state topologies. The sub-channel with the largest cross section,  $HH \rightarrow b\bar{b}b\bar{b}$ , has been studied by collaborators at CERN. In this chapter, the  $HH \rightarrow b\bar{b}W^+W^-$  sub-channel is investigated. Firstly, the  $HH \rightarrow b\bar{b}W^+W^-$  sub-channel is studied for fully hadronic decays of the  $W^+W^-$ ; fully hadronic  $W^+W^-$

decays have the largest branching fraction and the lack of neutrinos in the final states allows each W to be reconstructed. The semi-leptonic final state of the  $W^+W^-$  system in  $HH \rightarrow b\bar{b}W^+W^-$  is also studied. Here the presence of the neutrino in the final state makes it difficult to reconstruct the two Higgs bosons.

The process,  $HH\nu_e\bar{\nu}_e \rightarrow b\bar{b}W^+W^-\nu_e\bar{\nu}_e \rightarrow b\bar{b}qqqq\nu_e\bar{\nu}_e$ , results in a six quark final state with missing momentum. The high number of quarks requires an efficient jet reconstruction and a jet pairing algorithm to select the signal events. The two b quarks in the final state can be identified statistically with b jet tagging.

The chapter is organised as follows. Firstly, suitable signal and background channels are identified. Events with isolated high-energy leptons are discarded. Vertex information is used to identify b quark jets, in return to help to select signal events. The particles are clustered into jets and afterwards, the jets are used as inputs for pre-selection and multivariate analysis.

The event reconstruction was first performed for  $\sqrt{s} = 1.4$  TeV and then  $\sqrt{s} = 3$  TeV, using the Marlin framework and reconstruction package in iLCSoft v01-16. More details on the reconstruction software can be found in chapter 4.

## 7.2. Monte Carlo sample generation

A full list of generated samples with their cross sections can be found in table 7.1. All samples were generated with the CLIC\_ILD detector model.

At high centre-of-mass energies, in addition to considering electron-electron interactions, electron-photon and photon-photon interactions are important as their interactions become significant. These photons are produced due to the high electric field generated by the colliding beams. Processes involving real photons from beamsstrahlung (BS) and “quasi-real” photons are generated separately. For the “quasi-real” photon initiated processes, the Equivalent Photon Approximation (EPA) has been used [88].

Background processes with multiple quarks and missing momentum in the final states are challenging to reject, as the topologies are similar to that of the signal events. Two example background processes are  $e^+e^- \rightarrow qqqq\nu\bar{\nu}$  and  $e^\pm\gamma \rightarrow \nu qqqq$ . For the same reason, single Higgs boson production, such as  $e^+e^- \rightarrow qqH\nu\bar{\nu}$ , has a similar final state to the signal events and is also difficult to reject.

Some processes are not considered in this analysis because they either have very different event topologies to the signal, or they have very small cross sections. For example,  $e^\pm\gamma \rightarrow qqH\ell$  is neglected as the cross section is very small, even at  $\sqrt{s} = 3\text{ TeV}$ .

The background processes are generated according to the final states fermions and usually correspond to the contributions from multiple Feynman diagrams. These diagrams are already accounted for in the generated samples for explicit Higgs production. Therefore, to separate Higgs production from other processes, all background processes are generated with a Higgs boson mass of 14 TeV to ensure a negligible Higgs contribution. Processes involving Higgs production are simulated with a Higgs boson mass of 126 GeV.

The cross section of the signal,  $HH \rightarrow b\bar{b}W^+W^-$ , is scaled according to values listed in [89], as the values are more updated than the default Higgs branching ratios in the generator software.

The simulation and reconstruction chain is described in chapter 4. For some background processes, events are generated requiring that the invariant mass of the total momenta of all quarks is above 50 GeV or 120 GeV. This restricts the event generation to the region of phase space that could be populated by the signal processes.

Finally, the beam induced background,  $\gamma\gamma \rightarrow \text{hadrons}$ , is simulated and overlayed on all events. Details can be found in section 4.5.2.

## 7.3. Lepton identification

For the signal channel,  $HH \rightarrow b\bar{b}W^+W^- \rightarrow b\bar{b}qqqq$ , there is no primary lepton in the final state, whilst many background processes, such as  $qqqq\ell\nu$ , contain primary leptons in final states. Hence, efficiently rejecting events with primary leptons is an important step in the event selection. Primary leptons deposit energies in the tracking detector. The impact parameter to the interaction point of the fitted track of the primary lepton is typically small. At the same time, the primary leptons often have energies above 10 GeV and are isolated from other particles. High-energy electrons and muons are stable enough to deposit energies in the calorimeters. However, tau leptons are short lived with a typical decay lifetime of 290 fs [83]. They decay before reaching the vertex detector. Therefore, only the decay products of the tau leptons can be reconstructed.

Channel $\sqrt{s} = 1.4 \text{ TeV}$	$\sigma / \text{fb}$
$e^+e^- \rightarrow HH\nu_e\bar{\nu}_e$	0.149
$e^+e^- \rightarrow HH\nu_e\bar{\nu}_e \rightarrow b\bar{b}W^+W^-_{\text{hadronic}}$	0.018
$e^+e^- \rightarrow HH\nu_e\bar{\nu}_e \rightarrow b\bar{b}b\bar{b}\nu_e\bar{\nu}_e$	0.047
$e^+e^- \rightarrow HH \rightarrow \text{others}$	0.085
$e^+e^- \rightarrow q\bar{q}H\nu\bar{\nu}$	0.86
$e^+e^- \rightarrow c\bar{c}H\nu\bar{\nu}$	0.36
$e^+e^- \rightarrow b\bar{b}H\nu\bar{\nu}$	0.31
$e^+e^- \rightarrow qqqq$	1245.1
$e^+e^- \rightarrow qqqq\ell\ell$	62.1*
$e^+e^- \rightarrow qqqq\ell\nu$	110.4*
$e^+e^- \rightarrow qqqq\nu\bar{\nu}$	23.2*
$e^+e^- \rightarrow qq$	4009.5
$e^+e^- \rightarrow qq\ell\nu$	4309.7
$e^+e^- \rightarrow qq\ell\ell$	2725.8
$e^+e^- \rightarrow qq\nu\nu$	787.7
$e^\pm\gamma(\text{BS}) \rightarrow e^\pm qqqq$	2317
$e^\pm\gamma(\text{EPA}) \rightarrow e^\pm qqqq$	574
$e^\pm\gamma(\text{BS}) \rightarrow \nu qqqq$	159.1†
$e^\pm\gamma(\text{EPA}) \rightarrow \nu qqqq$	34.7†
$e^\pm\gamma(\text{BS}) \rightarrow qqH\nu$	31.5*
$e^\pm\gamma(\text{EPA}) \rightarrow qqH\nu$	6.78*
$\gamma(\text{BS})\gamma(\text{BS}) \rightarrow qqqq$	21406.2*
$\gamma(\text{BS})\gamma(\text{EPA}) \rightarrow qqqq$	4018.7*
$\gamma(\text{EPA})\gamma(\text{BS}) \rightarrow qqqq$	4034.8*
$\gamma(\text{EPA})\gamma(\text{EPA}) \rightarrow qqqq$	753.0*

**Table 7.1:** List of signal and background samples used in the double Higgs analysis with the corresponding cross sections at  $\sqrt{s} = 1.4 \text{ TeV}$ .  $q$  can be  $u$ ,  $d$ ,  $s$ ,  $b$  or  $t$ . Unless specified,  $q$ ,  $\ell$  and  $\nu$  represent either particles or the corresponding anti-particles.  $\gamma$  (BS) represents a real photon from beamstrahlung (BS).  $\gamma$  (EPA) represents a “quasi-real” photon, simulated with the Equivalent Photon Approximation. For processes labeled with \* and †, events are generated with the invariant mass of the total momenta of all quarks above 50 and 120 GeV, respectively.

### 7.3.1. Electron and muon identification

Two approaches to electron and muon identification were utilised, which are described below. The performance is summarised in table 7.6.

#### 7.3.1.1. IsolatedLeptonFinder

An optimised version of the existing ISOLATEDLEPTONFINDER reconstruction package is used. This algorithm identifies high energy electrons and muons that are isolated from other particles. The algorithm parameters were optimised by the collaborator using the  $\text{HH} \rightarrow b\bar{b}b\bar{b}$  as the signal channel and the  $e^+e^- \rightarrow qqqq\ell\nu$  as the background channel, as the background channels are the same for this analysis with  $\text{HH} \rightarrow b\bar{b}W^+W^-$  channel.

Optimal values of the parameters of the ISOLATEDLEPTONFINDER are listed in table 7.2:  $E$  is the energy of the lepton;  $E_{ECAL}$  is the energy of the lepton deposited in the ECAL;  $E_{cone}$  is the total energy within a cone of an opening angle of  $\cos^{-1}(0.995)$  around the lepton; and the impact parameters,  $d_0$ ,  $z_0$ , and  $r_0$  are the closest Euclidean distance of the fitted track of the primary lepton to the interaction point in  $x$ - $y$  plane, in  $z$  direction, and in  $x$ - $y$ - $z$  three dimensional space, respectively.

ISOLATEDLEPTONFINDER	Selection
High Energy	$E > 15 \text{ GeV}$
$e^\pm$ ID	$\frac{E_{ECAL}}{E} > 0.9$
$\mu^\pm$ ID	$0.25 > \frac{E_{ECAL}}{E} > 0.05$
Primary Track	$d_0 < 0.02 \text{ mm}; z_0 < 0.03 \text{ mm}; r_0 < 0.04 \text{ mm}$
Isolation	$E_{cone}^2 \leqslant 5.7 \text{ GeV} \times E - 50 \text{ GeV}^2$

**Table 7.2:** Optimised parameters for the ISOLATEDLEPTONFINDER processor.

#### 7.3.1.2. IsolatedLeptonIdentifier

A complimentary electron finder, ISOLATEDLEPTONIDENTIFIER, was developed to further identify isolated electrons and muons. Compared to the ISOLATEDLEPTONFINDER, the main difference is that the ISOLATEDLEPTONIDENTIFIER utilises particle ID information provided by the PandoraPFA reconstruction to identify leptons.

Table 7.3 lists the selection cuts for ISOLATEDLEPTONIDENTIFIER. The variables in the ISOLATEDLEPTONFINDER and the ISOLATEDLEPTONIDENTIFIER are defined in the same way. In addition:  $p_T$  is the transverse momentum;  $E_{cone1}$  and  $E_{cone2}$  are the total energy of PFOs within a cone around the lepton of an opening angle of  $\cos^{-1}(0.995)$  and  $\cos^{-1}(0.99)$  respectively.

The algorithm uses two sets of cuts to identify isolated leptons. If a PFO passes either set of cuts, it will be identified by the processor. The first set of cuts uses the particle ID information from PandoraPFA, demanding a PandoraPFA electron or muon with high energy above 10 GeV and  $r_0 < 0.015$  mm. Afterwards, the lepton should either have  $p_T > 40$  GeV, or  $E \geq 23\text{ GeV}^{\frac{1}{2}} \times \sqrt{E_{cone1}} + 5$  GeV. Figure 7.2a and 7.2b show the distributions of the  $p_T$  of identified electrons after  $E$  and  $r_0$  cuts, for  $\text{HH} \rightarrow b\bar{b}W^+W^- \rightarrow b\bar{b}qqqq$  signal channel and  $e^+e^- \rightarrow qqqq\ell\nu$  background channel respectively. A cut of  $p_T > 40$  GeV preserves most signal events. Figure 7.2c and 7.2d show the distributions of the  $23\text{ GeV}^{\frac{1}{2}} \times \sqrt{E_{cone1}} + 5$  GeV as a function of  $E$  of identified electrons after  $E$  and  $r_0$  cuts, for  $\text{HH} \rightarrow b\bar{b}W^+W^- \rightarrow b\bar{b}qqqq$  signal channel and  $e^+e^- \rightarrow qqqq\ell\nu$  background channel respectively. A cut along the two-dimensional histogram would discard background events and leave signal events intact.

The second set of cuts is similar to the first set of cuts. Apart of the differences in the values of the cuts, lepton ID in the second set cuts is determined using the fraction of the energy deposited in the ECAL as a function of the total energy,  $\frac{E_{ECAL}}{E}$ : if  $\frac{E_{ECAL}}{E} > 0.95$  then the PFO is an electron; and if  $0.2 > \frac{E_{ECAL}}{E} > 0.05$  then the PFO is a muon.

### 7.3.2. Tau lepton identification

The tau lepton has a short lifetime and decays before reaching the vertex detector and can only be identified through the reconstruction of its decay products. The leptonic decay of tau lepton can be identified using the isolated lepton finder processors described above. Therefore in this section, tau identification will focus on the hadronic decay modes.

The existing TAUFINDER [90] reconstruction package has been optimised. In addition, a package, ISOLATEDTAUIDENTIFIER, was developed to provide additional tau lepton identification.

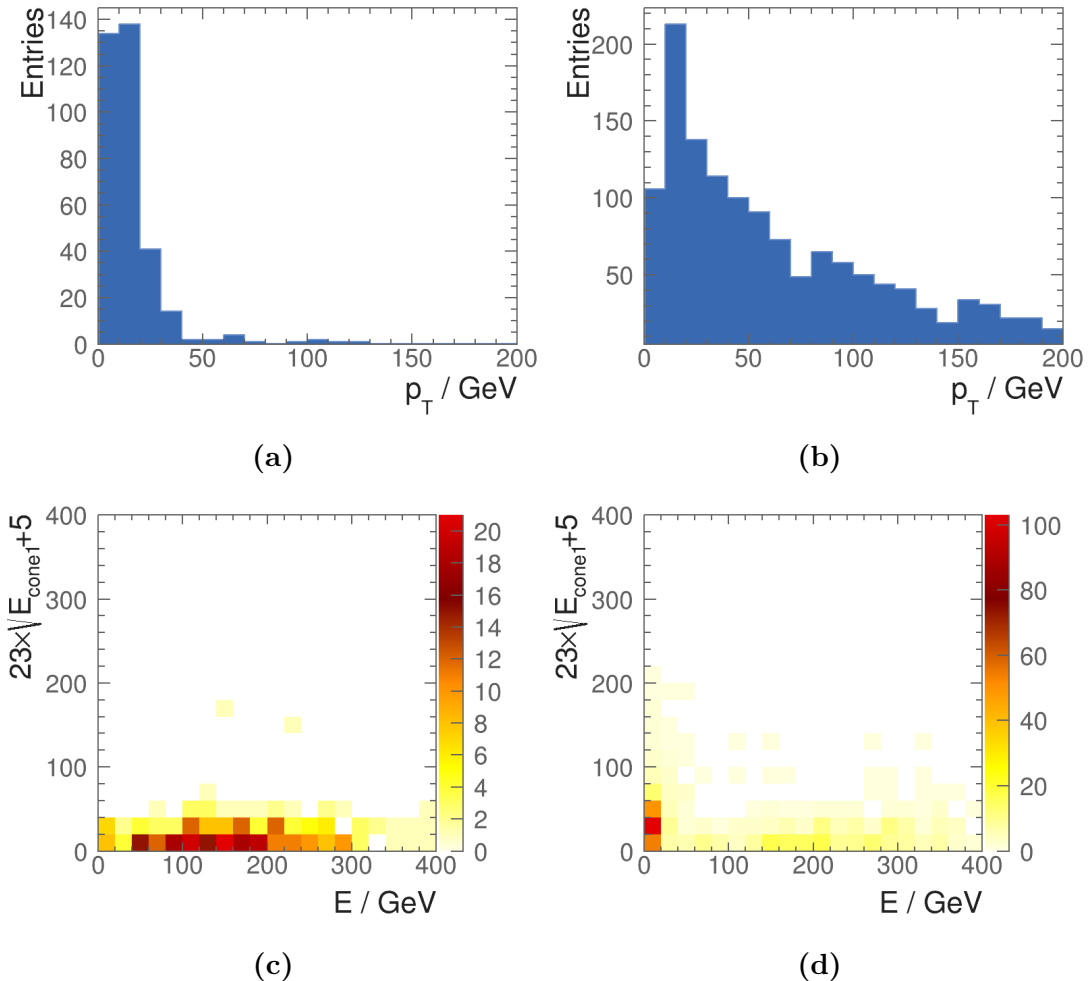


**Figure 7.2:** Distributions shown for  $p_T$  of identified electrons after  $E$  and  $r_0$  cuts, for a)  $\text{HH} \rightarrow b\bar{b}W^+W^- \rightarrow b\bar{b}\text{qqqq}$  signal channel; and b)  $e^+e^- \rightarrow \text{qqqq}\ell\nu$  background channel. Distributions shown for  $23\text{ GeV}^{\frac{1}{2}} \times \sqrt{E_{cone1}} + 5$  GeV as a function of  $E$  after  $E$  and  $r_0$  cuts, for c)  $\text{HH} \rightarrow b\bar{b}W^+W^- \rightarrow b\bar{b}\text{qqqq}$  signal channel; and d)  $e^+e^- \rightarrow \text{qqqq}\ell\nu$  background channel.

ISOLATEDLEPTONIDENTIFIER	Selection
High Energy	$E > 10 \text{ GeV}$
$e^\pm$ ID	PandoraPFA reconstructed; $\frac{E_{ECAL}}{E} > 0.95$
$\mu^\pm$ ID	PandoraPFA reconstructed
Primary Track	$r_0 < 0.015 \text{ mm}$
a) High Transverse Momentum, or	$p_T > 40 \text{ GeV}$
b) Isolation	$E \geq 23 \text{ GeV}^{\frac{1}{2}} \times \sqrt{E_{cone1}} + 5 \text{ GeV}$
High Energy	$E > 10 \text{ GeV}$
$e^\pm$ ID	$\frac{E_{ECAL}}{E} > 0.95$
$\mu^\pm$ ID	$0.2 > \frac{E_{ECAL}}{E} > 0.05$
Primary Track	$r_0 < 0.5 \text{ mm}$
a) High Transverse Momentum, or	$p_T > 40 \text{ GeV}$
b) Isolation	$E \geq 28 \text{ GeV}^{\frac{1}{2}} \times \sqrt{E_{cone2}} + 30 \text{ GeV}$

**Table 7.3:** Optimised parameters for the ISOLATEDLEPTONIDENTIFIER processor. A PFO needs to pass either set of cuts to be identified as a isolated electron or muon. Within a set of cuts, the PFO needs to satisfy either condition a) or b).

### 7.3.2.1. TauFinder

The TAUFINDER works by identifying tau lepton decay products, and requiring the decay products to be isolated from other PFOs. To find the decay products, the algorithm starts with the highest energy track as a seed for the cone clustering algorithm. A cone with opening angle 0.03 rad with respect to the seed is formed. The PFOs within the cone are required to be consistent with the signature of a tau hadronic decay: no more than 3 charged particles in the cone; invariant mass of all PFOs in the cone less than 2 GeV; and few than 10 PFOs in the cone. The cone is also required to be isolated from other particles. To reduce fake rate, PFOs with low momentum (less than 1 GeV) are not used in tau finding, as they more likely come from  $\gamma\gamma \rightarrow \text{hadrons}$  background. The identified tau lepton and associated decay products are then not used in further tau finding. This tau lepton finding procedure iterates with other high-energy tracks as seeds.

The optimised parameters are listed in table 7.4. The optimisation is performed by the collaborator using  $\text{HH} \rightarrow b\bar{b}b\bar{b}$  signal channel and the  $e^+e^- \rightarrow qqqq\ell\nu$  background channel, by scanning the parameters to obtain a good background rejection rate with lowest signal rejection rate. Variables are defined in the same way as in previous sections. In addition:  $\theta_Z$  is the polar angle with respect to the beam axis;  $N_{X^+}$  and  $N_{tau}$  are the

number of charged particles and the number of PFOs in the tau cone respectively;  $m_{tau}$  is the invariant mass of the sum of the PFOs in the tau candidate; and  $E_{cone}$  is the total energy of PFOs within a cone of an opening angle between 0.03 and 0.33 rad around tau seed track.

TAUFINDER	Selection
Veto $\gamma\gamma \rightarrow$ hadrons	$p_T < 1 \text{ GeV}$
Seed particle	$p_T > 10 \text{ GeV}$
Tau candidate cone opening angle	0.03 rad
Tau candidate rejection	$N_{X^+} > 3; N_{tau} > 10; m_{tau} > 2 \text{ GeV}$
Isolation	$E_{cone} < 3 \text{ GeV}$

**Table 7.4:** Optimised parameters for the TAUFINDER processor.

### 7.3.2.2. IsolatedTauIdentifier

The ISOLATED TAU IDENTIFIER works in a similar way to the TAUFINDER. It identifies high momentum particles as tau seeds. Particles are iteratively added to a cone in the order of the ascending opening angle to the seed. The cone is called search cone, which contains candidate tau decay products. After each particle addition, the temporary search cone is then considered as a temporary tau candidate and tested for isolation and consistency with a tau hadronic decay signature. The temporary tau candidate only needs to pass one of the isolation conditions to be identified as a tau candidate. There are multiple isolation conditions for tau 1-prong decay and 3-prong decay, reflecting different topologies of tau decay final states. The isolation criterion typically demand few particles around the search cone and the total  $p_T$  in the search cone to be greater than a threshold.

The iterative particle addition procedure stops when the cone opening angle is larger than a threshold. If multiple temporary tau candidates of the same tau seed pass the selection, the one with smallest opening angle is chosen to form the final tau candidate. To reduce the fake rate from  $\gamma\gamma \rightarrow$  hadrons background, particles with energies less than 1 GeV are not considered.

Figure 7.3 show the isolation criterion of tau candidate for  $\text{HH} \rightarrow b\bar{b}W^+W^- \rightarrow b\bar{b}qqqq$  signal channel (blue) and  $e^+e^- \rightarrow qqqq\ell\nu$  background channel (orange). Figure 7.3a shows the isolation criteria 1, where the cut at  $p_{Tcone} \geq 10 \text{ GeV}$  selects more tau candidates

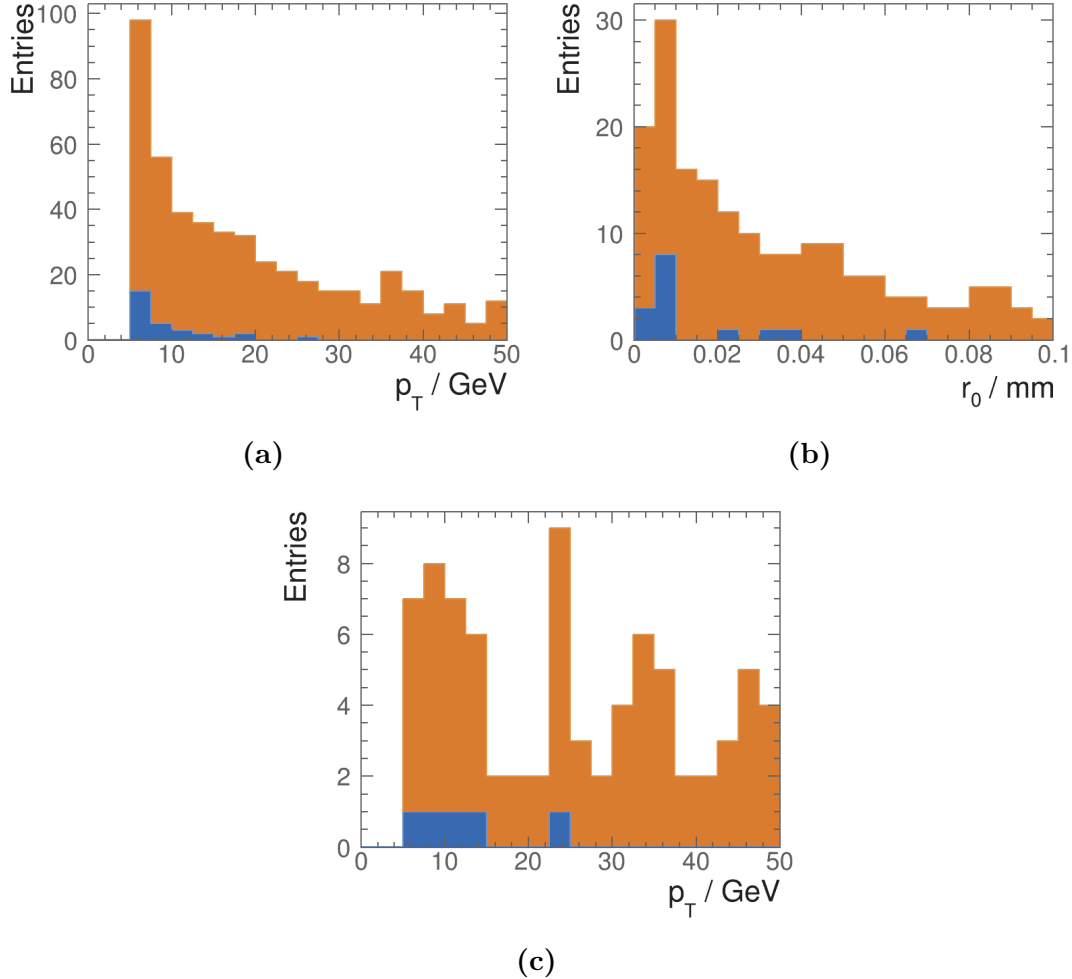


**Figure 7.3:** Distributions to show isolation criterion. a) Distribution of  $p_{Tcone}$  for isolation criteria 1 after  $N_{cone1} = 0$ ; b) distribution of  $r_0$  for isolation criteria 2 after  $N_{X^+} = 1$ ,  $N_{cone1} = 1$ ; and c) distribution of  $p_{Tcone}$  for isolation criteria 3 after  $N_{X^+} = 3$ ,  $N_{cone1} = 1$ ,  $\theta_S < \cos^{-1}(0.9995)$ .

in background events than in the signal events. Similarly, in figure 7.3b, the cut at  $r_0 > 0.01$  mm, and in figure 7.3c, the cut at  $p_{Tcone} \geq 10$  GeV select more tau candidates in background events.

Table 7.4 lists the optimised parameters for ISOLATEDTAUIDENTIFIER. Variables are defined in the same way as those in previous sections In addition,  $\theta_S$  is the opening angle of the search cone in rad; *cone1* and *cone2* are defined as a cone around the tau seed of an opening angle of  $\cos^{-1}(0.95)$ , and  $\cos^{-1}(0.99)$  respectively.

ISOLATEDTAUIDENTIFIER	Selection
Veto $\gamma\gamma \rightarrow \text{hadrons}$	$E < 1 \text{ GeV}$
Seed particle	$p_T > 5 \text{ GeV}$
Maximum search cone opening angle	$\theta_S \leq \cos^{-1}(0.999) \text{ GeV}$
Tau candidate rejection	$N_{X^+} \neq 1, 3; m_{PFO} > 3 \text{ GeV}$
Isolation 1 or	$N_{cone1} = 0; p_{Tcone} \geq 10 \text{ GeV}$
Isolation 2 or	$N_{X^+} = 1; N_{cone1} = 1; r_0 > 0.01 \text{ mm}$
Isolation 3 or	$N_{X^+} = 3; N_{cone1} = 1; p_{Tcone} \geq 10 \text{ GeV}; \theta_S < \cos^{-1}(0.9995)$
Isolation 4 or	$N_{X^+} = 1; N_{cone2} = 0; r_0 > 0.01 \text{ mm}; p_{Tcone} \geq 10 \text{ GeV}$
Isolation 5	$N_{X^+} = 3; N_{cone2} = 0; p_{Tcone} \geq 10 \text{ GeV}; \theta_S < \cos^{-1}(0.9995)$

**Table 7.5:** Optimised parameters of ISOLATEDTAUIDENTIFIER processor

Relative to the TAUFINDER algorithm, the main difference is that the ISOLATEDTAUIDENTIFIER adopts an iterative approach to build up a tau candidate, which allows a dynamic tau search cone size. The ISOLATEDTAUIDENTIFIER also has smaller cut values on the minimum  $p_T$  and invariant mass of the tau candidate, but stricter isolation criterions.

### 7.3.3. Very forward electron identification

At the high centre-of-mass energy of CLIC, particles produced are often highly boosted. Because of this, it is important to identify leptons in the forward calorimeters to aid the signal selection. In particular, photon-electron interactions, can have energetic primary electrons in the forward calorimeters, the LumiCAL and/or the BeamCAL.

Because of the large background in the forward region, it is challenging to identify primary leptons. In the Monte Carlo production, particles including the primary leptons and beam induced background in the forward calorimeters are not simulated, due to the high demand on the computational resources. Instead, studies have been performed with particles simulated in the forward calorimeters to understand the primary lepton identification efficiencies [48, 91, 92]. The studied primary lepton identification efficiencies are then parameterised as a function of lepton energies. The parametrisation approach is adopted in this analysis.

Figure 7.4a shows the primary electron identification efficiencies in the BeamCAL as a function of polar angle for a 500 GeV electron. An external processor [91] has developed

to parameterise the primary electron identification efficiencies in the BeamCAL at  $\sqrt{s} = 3\text{ TeV}$  as a function of electron energy and the polar angle. The full simulation study to obtain the primary electron identification efficiencies in the BeamCAL assumes a background integrated over 40 bunch crossings. The same primary electron identification efficiency is assumed for  $\sqrt{s} = 1.4\text{ TeV}$  and  $\sqrt{s} = 3\text{ TeV}$ . In the analysis for  $\sqrt{s} = 1.4\text{ TeV}$ , the momenta of the electron is scaled down by a ratio of the centre-of-mass energy to use the external processor.

Figure 7.4b shows the primary electron identification efficiencies in the LumiCAL as a function of electron energy for a polar angle  $\theta = 50\text{ mrad}$ . The efficiency is obtained from a full simulation study [92], assuming a background integrated over 100 bunch crossings. In this analysis, the primary electron identification efficiency is assumed to be parasitised as a function of electron energy by the curve in figure 7.4b. The polar angle dependency of the efficiency is not considered, due to the lack of study. The primary electron identification efficiency curve in figure 7.4b takes the functional form of:

$$\varepsilon = \begin{cases} 0, & \text{if } E < 50\text{ GeV}, \\ 0.99 \times \frac{\text{erf}(E/\text{GeV} - 100) + 1}{2}, & \text{otherwise,} \end{cases} \quad (7.1)$$

where  $E$  is the energy of the electron and  $\text{erf}$  is the error function.

Due to lack of tracking ability in the forward region, electrons and photons can not be differentiated. Therefore, both photons and electrons are identifier in the forward calorimeters. Events with identified high-energy electrons and/or photons in the BeamCAL and/or LumiCAL are rejected.

### 7.3.4. Lepton identification performance

The performances of the different lepton finding processors for signal events and the selected background processes are shown in table 7.6 for  $\sqrt{s} = 1.4\text{ TeV}$ . Numbers in the table represent the fractions of events where no leptons are identified by the individual lepton finder. ISOLATEDLEPTONIDENTIFIER and ISOLATEDTAUIDENTIFIER reject more background events than the ISOLATEDLEPTONFINDER and TAUFINDER. By combining the processors, 86.6% of the signal events remain and 16.8% of the  $e^+e^- \rightarrow qqqq\ell\nu$  events survive after rejecting events where leptons are identified.

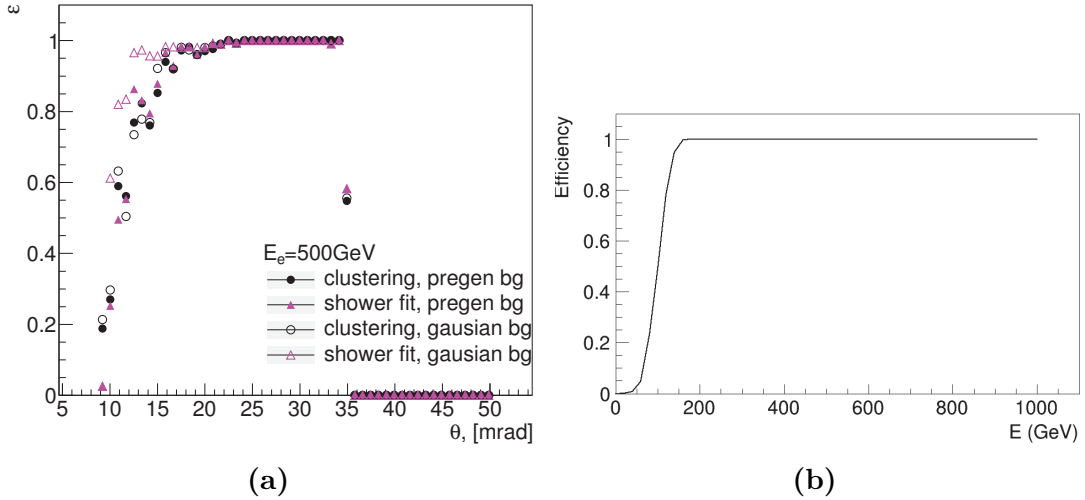


**Figure 7.4:** a) shows the 500 GeV electron identification efficiency in the BeamCAL as a function of polar angles, with different methods to model backgrounds: pregenerated and Gaussian, and two methods to identify electrons: clustering algorithm and shower fitting algorithm, obtained from a full simulation study in [91]. b) shows the electron tagging efficiency in the LumiCAL as a function of the electron energy, for a polar angle  $\theta = 50$  mrad, obtained from a full simulation study in [92].

Efficiency (1.4 TeV)	Signal	$e^+e^- \rightarrow qqqq\ell\nu$	$e^-\gamma(BS) \rightarrow e^-qqqq$
ISOLATEDLEPTONFINDER	99.3%	50.3%	87.3%
ISOLATEDLEPTONIDENTIFIER	99.1%	39.9%	83.7%
TAUFINDER	97.5%	52.3%	90.4%
ISOLATEDTAUIDENTIFIER	89.7%	38.5%	78.5%
Forward Finder Processors	98.9%	95.1%	53.6%
Combined	86.6%	16.8%	30.8%

**Table 7.6:** The performances of the lepton finding algorithms for the signal events and selected background events at  $\sqrt{s} = 1.4$  TeV. Numbers represent the fractions of events where no leptons are identified by the individual lepton finder.

The forward lepton finders are most effective at rejecting background events with primary leptons in the forward region. Table 7.6 shows the performance of the processors for signal events and the  $e^-\gamma(BS) \rightarrow e^-qqqq$  background events. Only 1% of signal events are rejected, but 47.4% of the  $e^-\gamma(BS) \rightarrow e^-qqqq$  background events are rejected. Table 7.9 list the number of events surviving lepton rejection for signal and all background channels.

Efficiency (3 TeV)	Signal	$e^+e^- \rightarrow qqqq\ell\nu$	$e^-\gamma(\text{BS}) \rightarrow e^-qqqq$
ISOLATEDLEPTONFINDER	99.5%	66.8%	88.8%
ISOLATEDLEPTONIDENTIFER	99.0%	52.5%	82.2%
TAUFINDER	97.7%	79.5%	76.7%
ISOLATEDTAUIDENTIFER	86.3%	60.3%	92.6%
Forward Finder Processors	95.9%	80.7%	55.4%
Combined	81.0%	23.3%	33.4%

**Table 7.7:** The performances of the lepton finding algorithms for the signal events and selected background events at  $\sqrt{s} = 3$  TeV. Numbers represent the fractions of events where no leptons are identified by the individual lepton finder.

The lepton finding processors were optimised with events at  $\sqrt{s} = 1.4$  TeV. It was found that the same set of parameters is also effective for  $\sqrt{s} = 3$  TeV. The performances of the lepton finders at  $\sqrt{s} = 3$  TeV are shown in table 7.7.

When comparing the lepton finding performances at  $\sqrt{s} = 1.4$  TeV and  $\sqrt{s} = 3$  TeV, the performance for  $\sqrt{s} = 1.4$  TeV is better. This is because at  $\sqrt{s} = 3$  TeV, particles tend to be boosted more and the spatial separation between particles is smaller due to the higher multiplicities. Consequently particles are less isolated from each other. The higher centre-of-mass energy also affects the performance of the forward lepton finder. Whilst at  $\sqrt{s} = 1.4$  TeV, the forward finder only rejects 5% of the  $e^+e^- \rightarrow qqqq\ell\nu$  background events and 1% of the signal events, at  $\sqrt{s} = 3$  TeV it rejects 19% of events from the same background process and 4% of the signal events, as more leptons are boosted into the forward region.

## 7.4. Jet reconstruction

The signal channel,  $HH \rightarrow b\bar{b}W^+W^- \rightarrow b\bar{b}qqqq$ , is a six-quark final state, which will result in multiple reconstructed jets. The pairing of jets to form the H,  $W^+$  and  $W^-$  in the event is an essential part of the event reconstruction. In this section, the optimisation of the jet reconstruction is discussed.

### 7.4.1. Jet reconstruction optimisation

Jet reconstruction algorithms cluster particles into jets. For this analysis, longitudinal invariant  $k_t$  jet algorithm is chosen for the jet clustering, as discussed in section 4.7.2. The free parameter for  $k_t$  algorithm is the  $R$  parameter, which controls the radius of the jet. The jet clustering will also depend on the centre-of-mass energy of the event. This is particularly important at the CLIC because of the large beam induced background from relative low  $p_T$  particles. Hence a suitable level of background suppression needs to be chosen, which is incorporated in the choice of the PFO collection.

The use of the  $k_t$  jet algorithm in exclusive modes allows some particles to be clustered into beam jet, which is not used in the subsequent event reconstruction.

The value of the  $R$  parameter and the PFO collection are chosen to optimise the invariant mass and mass resolution of H and W. To choose the optimal parameters,  $\text{HH} \rightarrow b\bar{b}W^+W^- \rightarrow b\bar{b}\text{qqqq}$  events are processed through  $k_t$  jet algorithm in the 6-jet exclusive mode. The six jets are paired using the MC truth information by examining the decay chain of MC particles. Four invariant mass distributions are obtained: two Higgs masses ( $m_{H_{bb}}$  and  $m_{H_{WW^*}}$ ) and two W masses ( $m_W$  and  $m_{W^*}$ ). Here  $W^*$  indicates the off-mass-shell W boson. The MC paring is old used to optimised the choice of parameters. It is not used in the subsequent analysis.

Three invariant mass distributions are considered:  $m_{H_{bb}}$ ,  $m_{H_{WW^*}}$ , and  $m_W$ . The optimal jet reconstruction should produce sharp mass peaks around the simulated particle masses. For example, figure 7.5 shows the  $m_{H_{bb}}$  invariant mass distribution for  $R = 1.3$  using the loose PFO collection for samples at  $\sqrt{s} = 3\text{ TeV}$ . An analytical functional form is fitted to describe the shape. The fitting function is a Gaussian-like function. Additional parameters are used in the fitting function to describe the tails of the distribution. The fitting function takes the form of

$$f(m) = A \exp \left\{ -\frac{(m - \mu)^2}{g} \right\}, \quad (7.2)$$

$$g = \begin{cases} 2\sigma_L + \alpha_L(m - \mu), & \text{if } m < \mu, \\ 2\sigma_R + \alpha_R(m - \mu), & \text{if } m \geq \mu, \end{cases} \quad (7.3)$$

where:  $\mu$  is the fitted mass peak position;  $\sigma_L$  and  $\sigma_R$  allow for an asymmetrical width of the distribution;  $\alpha_L$  and  $\alpha_R$  account for a constant tail of the distribution; and  $A$  is a normalisation factor.

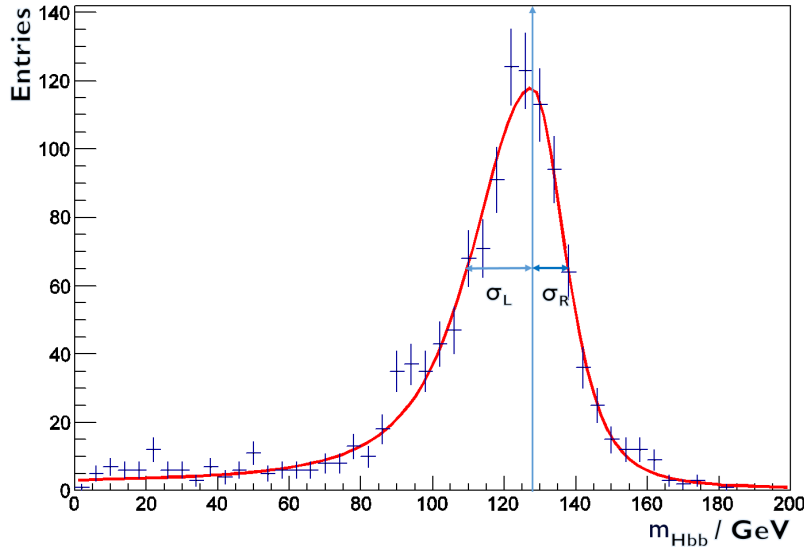


**Figure 7.5:** A typical example of the reconstructed  $m_{H_{bb}}$  mass distribution for  $R = 1.3$  using loose PFO collection for  $HH \rightarrow b\bar{b}W^+W^- \rightarrow b\bar{b}qqqq$  samples at  $\sqrt{s} = 3$  TeV. The fitting function is superimposed in red. The arrow shows the fitted peak position.

To parameterise the performance of different jet algorithm settings, the overall relative width is used, defined as  $(\sigma_L + \sigma_R) / M$ . A smaller width indicates a better mass resolution. The fitted  $H_{bb}$ ,  $H_{WW^*}$ , and  $W$  masses are studied for  $R$  values between 0.5 and 1.3, and with the three possible PFO collections: loose, normal, and tight.

Figure 7.6 shows the variation of the mass peak position and its relative width as a function of  $R$  and PFO collections, for  $m_{H_{bb}}$ ,  $m_{H_{WW^*}}$ , and  $m_W$ . The mass peak position,  $\mu$ , increases as  $R$  increases. This is because more particles are included in jets with increasing jet radius. For the relative width, the values for  $H_{bb}$  increase with increasing jet radius, but the values for  $H_{WW^*}$  decrease with increasing jet radius. This is due to a compensating effect; the invariant mass for  $H_{WW^*}$  is formed from four jets, which prefers a large jet radius, whereas the invariant mass for  $H_{bb}$  is obtained from two jets, which favours a small jet radius.

The choice of PFO collection impacts number of PFOs in the event. The loose PFO selection has the most PFOs in the event and, therefore, the largest invariant mass and worst mass resolution.

Based on the results summarised in figure 7.6 for this analysis, it was decided to use  $R = 0.7$  with the selected PFO collection. This choice gives good fitted mass peak positions for  $H_{bb}$ ,  $H_{WW^*}$  and  $W$ . The extracted fitted parameters of optimal jet reconstructions are summarised in table 7.8.

Fitted jet parameters	$\sqrt{s} = 1.4 \text{ TeV}$	$\sqrt{s} = 3 \text{ TeV}$
$\mu_{H_{bb}}$	$122.3 \pm 0.2$	$119.1 \pm 0.3$
$\sigma_{L,H_{bb}}$	$15.2 \pm 0.2$	$15.0 \pm 0.3$
$\sigma_{R,H_{bb}}$	$7.55 \pm 0.16$	$8.4 \pm 0.2$
$\mu_{H_{WW^*}}$	$125.7 \pm 0.2$	$123.0 \pm 0.3$
$\sigma_{L,H_{WW^*}}$	$29.4 \pm 0.3$	$36.6 \pm 0.6$
$\sigma_{R,H_{WW^*}}$	$7.18 \pm 0.17$	$7.4 \pm 0.2$
$\mu_W$	$80.5 \pm 0.2$	$78.1 \pm 0.3$
$\sigma_{L,W}$	$16.2 \pm 0.3$	$13.1 \pm 0.4$
$\sigma_{R,W}$	$9.03 \pm 0.16$	$9.5 \pm 0.2$

**Table 7.8:** The fitted mass parameters for  $\sqrt{s} = 1.4 \text{ TeV}$  analysis:  $R = 0.7$  using the selected PFO collection, and for  $\sqrt{s} = 3 \text{ TeV}$  analysis:  $R = 0.7$  using the tight selected PFO collection.

A separate jet reconstruction optimisation is performed for  $\sqrt{s} = 3 \text{ TeV}$  analysis. Figure 7.7 shows the variation of fitted mass peak positions and the relative mass resolutions for  $H_{bb}$ ,  $H_{WW^*}$ , and  $W$  as function of  $R$  and PFO collections. The relative mass resolution of  $W$  boson quickly degrades with increasing  $R$ . The fitted mass peak positions also increases more rapidly with the increase of  $R$ , compared with the fitted positions at  $\sqrt{s} = 1.4 \text{ TeV}$ . This is because at a higher centre-of-mass energy, more beam induced background particles are produced. The background particles, if included in the jets, will increase the invariant masses of the fitted physical bosons. Based on this study,  $R = 0.7$  with the tight selected PFO collection was chosen for the  $\sqrt{s} = 3 \text{ TeV}$  analysis. With chosen parameters, the better relative mass resolutions compensate for the invariant masses being slightly smaller than simulated values. The extracted fitted parameters of optimal jet reconstructions at  $\sqrt{s} = 3 \text{ TeV}$  are summarised in table 7.8.

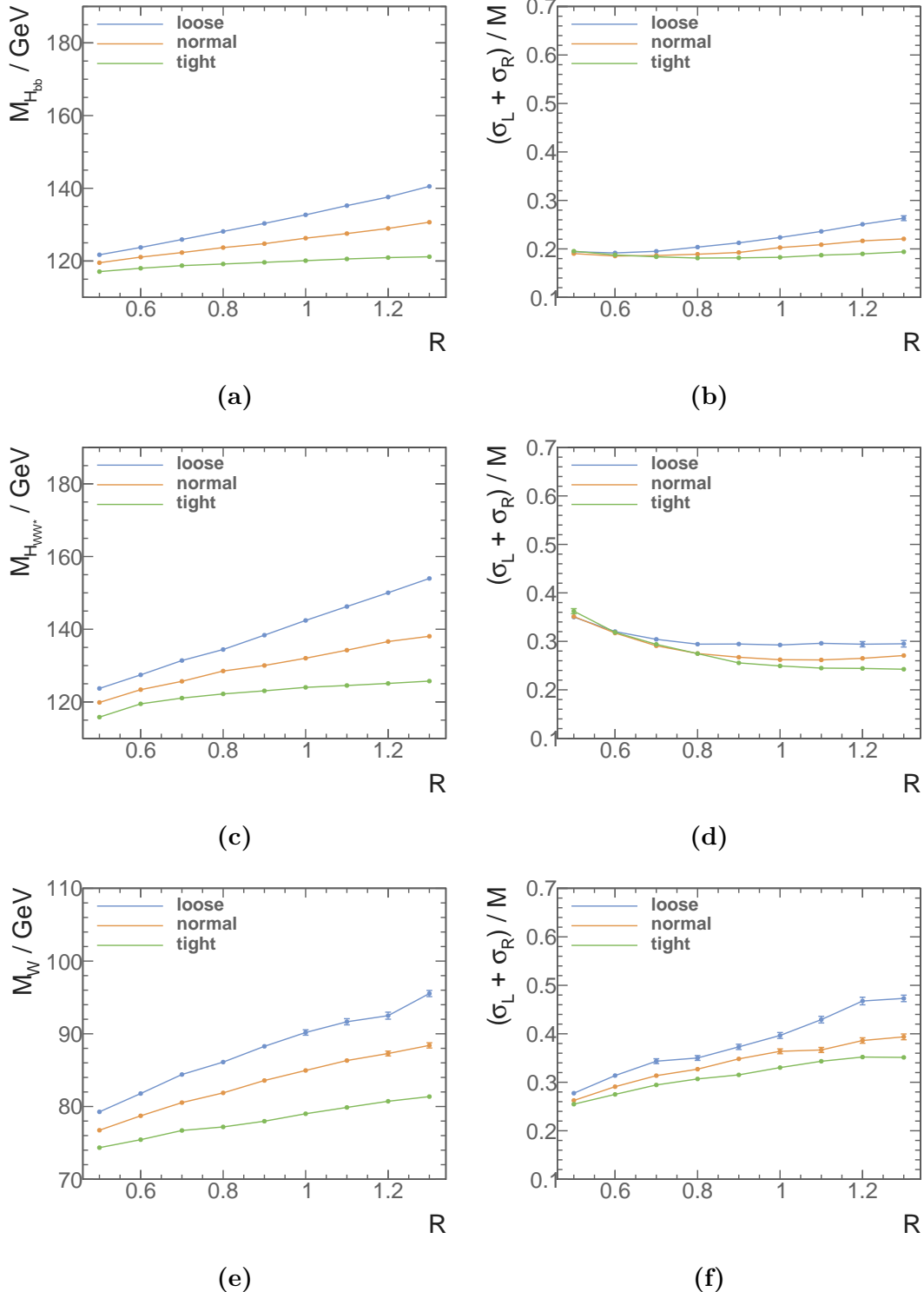


**Figure 7.6:** Distributions of a) fitted mass peak positions for  $H_{bb}$ , b) relative mass peak width for  $H_{bb}$ , c) fitted mass peak positions for  $H_{WW^*}$ , and f) relative mass peak width for  $H_{WW^*}$ , e) fitted mass peak positions for  $W$ , b) relative mass peak width for  $W$ . All plots show the variation of the fitted masses and mass resolutions as a function of  $R$  for loose, normal, and tight selected PFO collections at  $\sqrt{s} = 1.4 \text{ TeV}$ , using  $\text{HH} \rightarrow b\bar{b}W^+W^- \rightarrow b\bar{b}qqqq$ .

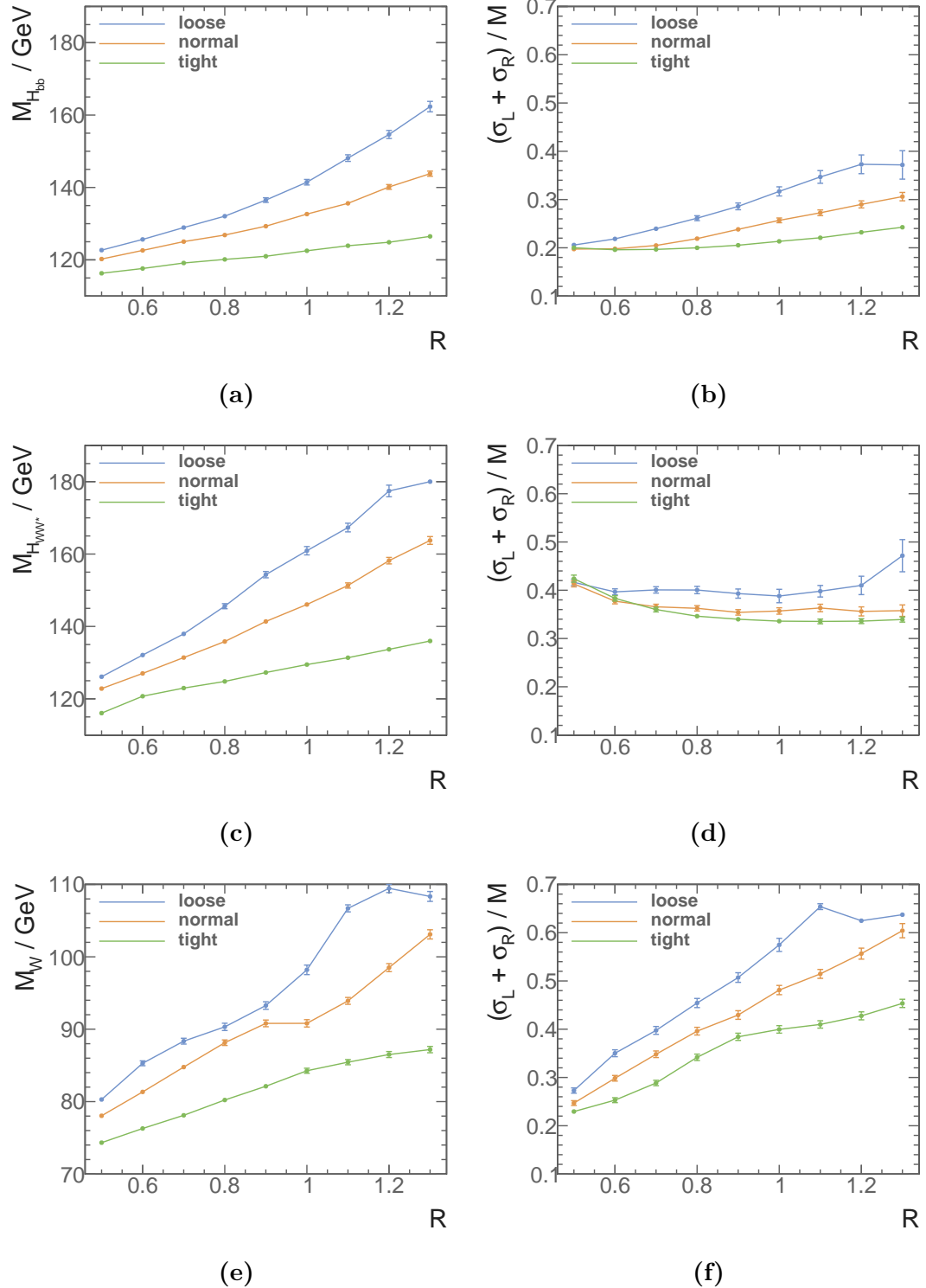


**Figure 7.7:** Distributions of a) fitted mass peak positions of  $H_{bb}$ , b) relative mass peak widths of  $H_{bb}$ , c) fitted mass peak positions of  $H_{WW^*}$ , d) relative mass peak widths of  $H_{WW^*}$ , e) fitted mass peak positions of  $W$ , and f) relative mass peak widths of  $W$ . All plots show the variation of fitted masses and mass resolutions as a function of  $R$  for loose, normal, and tight selected PFO collections at  $\sqrt{s} = 3 \text{ TeV}$ , using  $\text{HH} \rightarrow b\bar{b}W^+W^- \rightarrow b\bar{b}\text{qqqq}$  channel.

## 7.5. Jet flavour tagging

As the signal channel,  $\text{HH} \rightarrow b\bar{b}W^+W^- \rightarrow b\bar{b}\text{qqqq}$ , contains two b quarks in the final state, identifying jets originated from b quarks is an important part of the event selection.

The flavour tagging processor, LCFIPlus [93] is used. The processor is based on the LCFIVertex package [94], which was used in the simulation studies for the ILC Letter of Intent [27, 95] and the CLIC Concept Design Report [2].

After the previous jet clustering step, PFOs, which are not in the beam jet, are used as inputs for the flavour tagging. The flavour tagging algorithm identifies vertices, then re-cluster PFOs into jets. Lastly, the algorithm decides if a jet is a b jet or a c jet.

The vertex finding algorithms perform vertex fitting and identify primary and secondary vertices. There are two vertex refining algorithm. First algorithm rejects the topology of a neutral particle that decays into pairs of charged particles, which can be mistaken as the decay of b or c quarks. The second algorithm is performed after the re-clustering step to reconstruct more secondary vertices, with additional information from the jet clustering.

The jet re-clustering algorithm is a modified Durham algorithm, with additional constraint of the secondary vertices and the muons, which are identified from semi-leptonic decay of the quarks, falling into the same jet as the quarks. This ensures the topology of the jet remains consistent with the hadronic decays of heavy quarks.

Having obtained re-cluster jets, the next step is the flavour tagging, which uses a multivariate classifier to determine if a jet is from b quark or c quark. LCFIPlus uses the Boosted Decision Tree MVA multiclass classifier as implemented in the TMVA software package [72]. There are four categories for classification: jets with zero, one, two properly reconstructed vertices, or a single-track pseudo-vertex. A jet can be classified into one of three classes: a b jet, a c jet, or a light flavour quark jet (u, d or s).

The MVA multiclass classifier was trained with  $e^+e^- \rightarrow Z\nu\nu$  event at  $\sqrt{s} = 1.4 \text{ TeV}$ , where Z decays to  $b\bar{b}$ ,  $c\bar{c}$ , or  $u\bar{u}/d\bar{d}/s\bar{s}$ . The training sample contains missing momentum, which is similar to the signal sample. The training sample only has two quarks in the final states, which reduces the error in jet clustering and provides a good ground truth for training. The MVA classification efficiency with the training samples is shown in figure 7.8a.

Having trained the MVA classifier, the MVA classifier is applied to the samples. Under the signal hypothesis, the re-cluster algorithm is set to find six jets. The normalised distribution of the highest b-jet tag value for the  $\text{HH} \rightarrow b\bar{b}W^+W^- \rightarrow b\bar{b}\text{qqqq}$  sample is shown in figure 7.9.

For the  $\sqrt{s} = 3$  TeV analysis, the MVA classifier is re-trained with  $e^+e^- \rightarrow Z\nu\bar{\nu}$  event at  $\sqrt{s} = 3$  TeV. The performance of the flavour tagging with training samples is shown in figure 7.8b. The performance at  $\sqrt{s} = 3$  TeV is slightly worse than at  $\sqrt{s} = 1.4$  TeV, because at the higher centre-of-mass energy, jets are more collimated and more difficult to separate.

Compared to the performance at  $\sqrt{s} = 1.4$  TeV, the performance is slightly worse, because at a high centre-of-mass energy, particles are more collimated and more difficult to separate. Therefore, the vertex identification and the flavour tagging performance are worse.

F

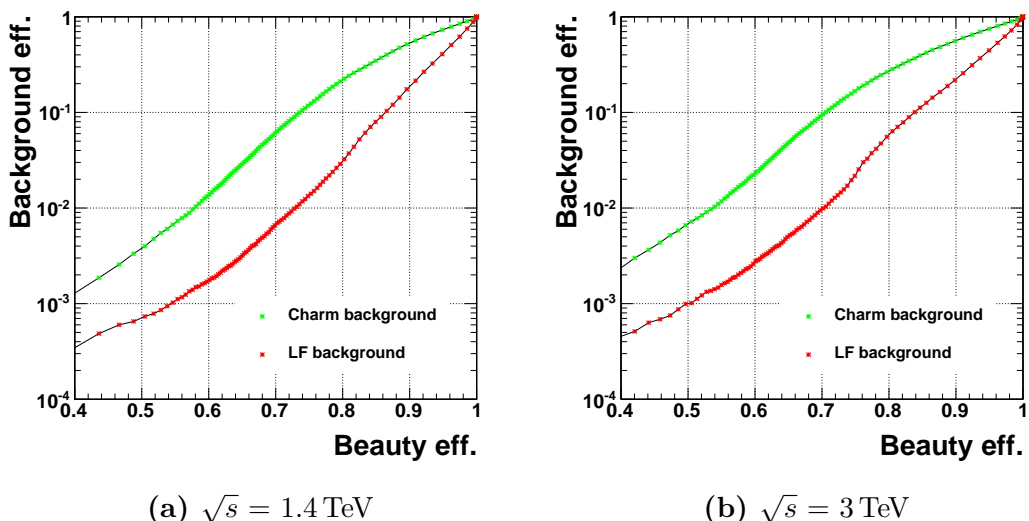


**Figure 7.8:** Performance of b-jet tagging with  $e^+e^- \rightarrow Z\nu\bar{\nu}$  samples, where  $Z$  decays to  $b\bar{b}$ ,  $c\bar{c}$ , or  $u\bar{u}/d\bar{d}/s\bar{s}$  at a)  $\sqrt{s} = 1.4$  TeV, and b)  $\sqrt{s} = 3$  TeV.

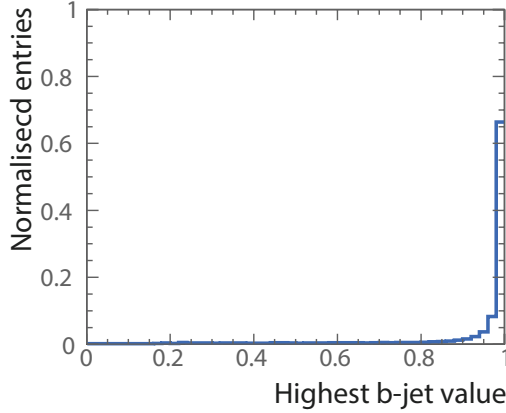


**Figure 7.9:** The distribution of the highest b-jet value for the  $\text{HH} \rightarrow b\bar{b}W^+W^- \rightarrow b\bar{b}\text{qqqq}$  events at  $\sqrt{s} = 1.4 \text{ TeV}$ . Area under the curve is normalised to 1.

### 7.5.1. Mutually exclusive cuts for $\text{HH} \rightarrow b\bar{b}W^+W^-$ and $\text{HH} \rightarrow b\bar{b}b\bar{b}$

The two  $e^+e^- \rightarrow \text{HH}\nu_e\bar{\nu}_e$  final states with the largest branching fractions are  $\text{HH} \rightarrow b\bar{b}b\bar{b}$  (31.5%) and  $\text{HH} \rightarrow b\bar{b}W^+W^-$  (25.9%). These two final states have different topologies and are subject of two analysis strategies. The  $\text{HH} \rightarrow b\bar{b}W^+W^-$  final state is the subject of this thesis. The study of the  $\text{HH} \rightarrow b\bar{b}b\bar{b}$  final state is the subject of an independent analysis. Because the results of the two studies are subsequently combined, a set of cuts are designed to separate samples, for both signal and background events, into two mutually exclusive sets for two independent analyses. This ensures there are no correlations between two analyses.

The most distinctive difference between the  $\text{HH} \rightarrow b\bar{b}W^+W^-$  and  $\text{HH} \rightarrow b\bar{b}b\bar{b}$  sub-channels is the different jet multiplicity and the different number of b-jets in the final state. Consequently variables relating to the number of b-jets and total number of jets are suitable for separating the two sub-channels.

Figure 7.10 shows the sum of b-jet tag values, when the event is clustered into four jets, as a function of  $-\log(y_{34})$  for the hadronic  $W^+W^-$  decay in  $\text{HH} \rightarrow b\bar{b}W^+W^-$  and  $\text{HH} \rightarrow b\bar{b}b\bar{b}$ . As expected, the two sub-channels can be clearly separated in this two dimensional phase space. A rectangular cut can be used to separate the phase space into two spaces, denoted as  $S$  and  $\neg S$ . The hadronic  $W^+W^-$  decay in  $\text{HH} \rightarrow b\bar{b}W^+W^-$  events should be contained in  $S$ , and the  $\text{HH} \rightarrow b\bar{b}b\bar{b}$  events should be contained in  $\neg S$ .

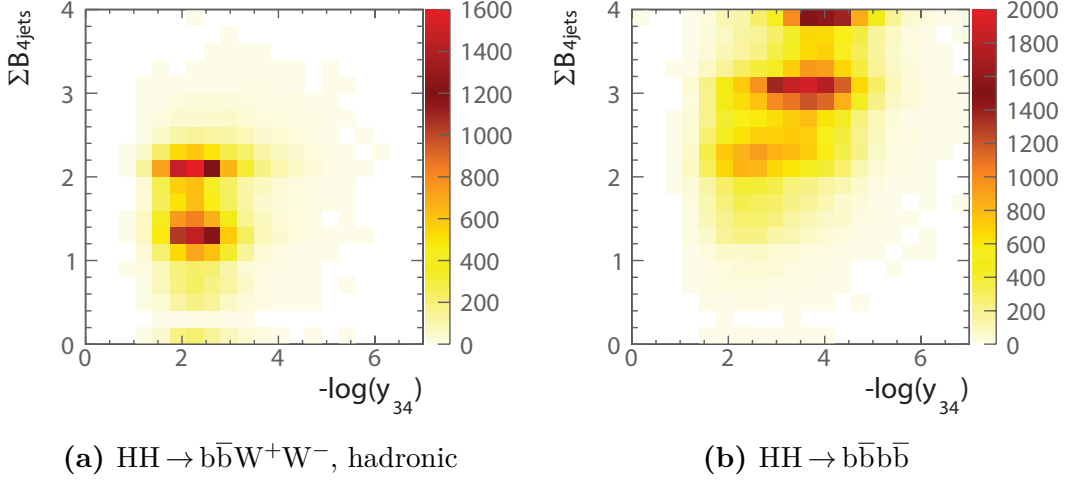


**Figure 7.10:** The two-dimensional distribution of sum of b-jet tag values against  $-\log(y_{34})$ . The plots show a) hadronic  $W^+W^-$  decay of  $\text{HH} \rightarrow b\bar{b}W^+W^-$ , and b)  $\text{HH} \rightarrow b\bar{b}b\bar{b}$  events at  $\sqrt{s} = 1.4$  TeV. The sum of b-jet tag values is calculated for the case where events are clustered into four jets.

The optimal cuts are chosen such that they maximise:

$$\varepsilon = \frac{N_{\text{HH} \rightarrow b\bar{b}W^+W^-, \text{hadronic}} \in S}{N_{\text{HH} \rightarrow b\bar{b}W^+W^-, \text{hadronic}}} \times \frac{N_{\text{HH} \rightarrow b\bar{b}b\bar{b}} \in \neg S}{N_{\text{HH} \rightarrow b\bar{b}b\bar{b}}}, \quad (7.4)$$

where  $N \in S$  indicates number of events in the phase space  $S$ .

Several combinations of pairs of variables were considered. In each case, the product of the fraction of the sub-channel events in each space,  $\varepsilon$  was maximised. This procedure identified  $\Sigma B_{4\text{jets}} < 2.3$ ,  $-\log(y_{34}) < 3.7$  as the best choice with 86% of the hadronic  $W^+W^-$  decay in  $\text{HH} \rightarrow b\bar{b}W^+W^-$  events are in  $S$  and 78% of the  $\text{HH} \rightarrow b\bar{b}b\bar{b}$  events are in  $\neg S$ . The full list of fraction of events after passing mutually exclusive cuts for individual background processes are listed in table 7.9.

## 7.6. Jet pairing

Events are reconstructed assuming the  $\text{HH} \rightarrow b\bar{b}W^+W^-$  signal topology. The six jets are obtained from the jet re-clustering step in the LCFIPlus processor. The next step is to group jets according to signal event topology. Jets are paired up such that there are two jets for  $H \rightarrow b\bar{b}$ , two jets for hadronic decay of a  $W$ , and two jets for hadronic decay of a  $W^*$ . In addition, the two  $W$ s should be from the  $H$  boson decay.

Six jets are associated to  $H_{bb}$ ,  $W$  and  $W^*$ . There are 90 possible permutations for associating six jets to  $H_{bb}$ ,  $W$  and  $W^*$ . The best permutation is obtained by minimising a  $\chi^2$  quantity representing the consistency of the hypothesis with the signal topology:

$$\chi^2 = \left( \frac{m_{ij} - \mu_{H_{bb}}}{\sigma'_{H_{bb}}} \right)^2 + \left( \frac{m_{klmn} - \mu_{H_{WW^*}}}{\sigma'_{H_{WW^*}}} \right)^2 + \left( \frac{m_{kl} - \mu_W}{\sigma'_W} \right)^2, \quad (7.5)$$

where the indices represent the six jets. The parameter  $\mu$  and  $\sigma'$  are the expected peak and (asymmetric) width of the reconstructed mass distributions given in table 7.8, defined as:

$$\sigma'_{H_{bb}} = \begin{cases} \sigma_{L,H_{bb}}, & \text{if } m_{ij} < \mu_{H_{bb}}, \\ \sigma_{R,H_{bb}}, & \text{otherwise,} \end{cases} \quad \text{etc.} \quad (7.6)$$

A jet pairing is only considered when at least one of the jets associated to the  $H_{bb}$  decay has a b-jet tag  $> 0.2$ . Of these combinations of jets, the jet pairing giving smallest  $\chi^2$  is selected. Figure 7.11 shows the normalised distribution of  $m_{H_{bb}}$  after jet pairing, for the signal channel,  $HH \rightarrow b\bar{b}W^+W^-$  and the sum of all background channels. For the signal channel, the distribution peaks around the expected mass of  $m_{H_{bb}}$ . Around 1% of signal events have no solutions for the jet pairing, as no jet has a b-jet tag  $> 0.2$ . These events are no longer considered in the analysis. The full list of fraction of events surviving after this jet pairing selection are listed in table 7.9 for signal  $HH \rightarrow b\bar{b}W^+W^-$  and all background channels.

## 7.7. Pre-selection

After the association of jets to candidate bosons are made under hypothesis that an event is signal, kinematic and topological variables can be calculated. A set of pre-selection cuts are placed to discard the phase space dominated by background events. Cuts on  $p_T$ , b-jet tag, and invariant mass of the double Higgs system are used.

Since both Higgs bosons are on mass shell, the invariant mass of the double Higgs system is large. Consequently, a cut on  $m_{HH} > 150$  GeV, as shown in Figure 7.12, removes a small amount of signal events, but discards lots of background events, especially  $\gamma\gamma \rightarrow qqqq$  events.

$\sqrt{s} = 1.4 \text{ TeV}$	N	Lepton evto	$b\bar{b}W^+W^- / b\bar{b}W^+W^-$ separation	Valid jet Pairing
$e^+e^- \rightarrow HH\nu_e\bar{\nu}_e \rightarrow b\bar{b}W^+W^- \nu_e\bar{\nu}_e$ , hadronic	27.9	89.7%	79.1%	78.3%
$e^+e^- \rightarrow HH\nu_e\bar{\nu}_e \rightarrow b\bar{b}b\bar{b}\nu_e\bar{\nu}_e$	67.6	90.8%	18.0%	18.0%
$e^+e^- \rightarrow HH\nu_e\bar{\nu}_e \rightarrow \text{other}$	128.0	40.8%	35.8%	31.2%
$e^+e^- \rightarrow q\bar{q}H\nu\bar{\nu}$	1290	72.8%	69.7%	57.7%
$e^+e^- \rightarrow c\bar{c}H\nu\bar{\nu}$	540	74.7%	59.8%	52.7%
$e^+e^- \rightarrow b\bar{b}H\nu\bar{\nu}$	465	74.3%	32.2%	31.8%
$e^+e^- \rightarrow qqqq$	1867650	79.9%	64.0%	38.6%
$e^+e^- \rightarrow qqqq\ell\ell$	93150	8.9%	8.2%	4.7%
$e^+e^- \rightarrow qqqq\ell\nu$	165600	16.5%	14.6%	13.3%
$e^+e^- \rightarrow qqqq\nu\bar{\nu}$	34800	87.6%	82.0%	46.8%
$e^+e^- \rightarrow qq$	6014250	81.0%	57.8%	39.0%
$e^+e^- \rightarrow qq\ell\nu$	6464550	22.5%	17.0%	10.5%
$e^+e^- \rightarrow qq\ell\ell$	4088700	19.4%	18.6%	12.4%
$e^+e^- \rightarrow qq\nu\nu$	1181550	91.8%	74.0%	47.3%
$e^\pm\gamma(\text{BS}) \rightarrow e^\pm qqqq$	2606625	34.2%	33.5%	22.9%
$e^\pm\gamma(\text{EPA}) \rightarrow e^\pm qqqq$	861000.0	16.4%	15.8%	10.7%
$e^\pm\gamma(\text{BS}) \rightarrow \nu qqqq$	178987.5	85.6%	81.3%	54.4%
$e^\pm\gamma(\text{EPA}) \rightarrow \nu qqqq$	52050	44.5%	42.0%	27.4%
$e^\pm\gamma(\text{BS}) \rightarrow qqH\nu$	35437.5	70.7%	65.0%	55.4%
$e^\pm\gamma(\text{EPA}) \rightarrow qqH\nu$	10170	37.0%	33.8%	28.8%
$\gamma(\text{BS})\gamma(\text{BS}) \rightarrow qqqq$	2054951.5	85.6%	81.3%	54.0%
$\gamma(\text{BS})\gamma(\text{EPA}) \rightarrow qqqq$	4521037.5	49.6%	48.5%	32.9%
$\gamma(\text{EPA})\gamma(\text{BS}) \rightarrow qqqq$	4539150	49.6%	48.5%	32.9%
$\gamma(\text{EPA})\gamma(\text{EPA}) \rightarrow qqqq$	1129500	31.0%	30.1%	20.5%

**Table 7.9:** The table show the expected number of events, before cuts and after successive cuts: the lepton veto,  $HH \rightarrow b\bar{b}W^+W^- / HH \rightarrow b\bar{b}b\bar{b}$  separation, and valid jet pairing, for the signal and background events at  $\sqrt{s} = 1.4 \text{ TeV}$ , assuming an integrated luminosity of  $1500 \text{ fb}^{-1}$ .  $q$  can be  $u, d, s, b$  or  $t$ . Unless specified,  $q, \ell$  and  $\nu$  represent either particles or the corresponding anti-particles.

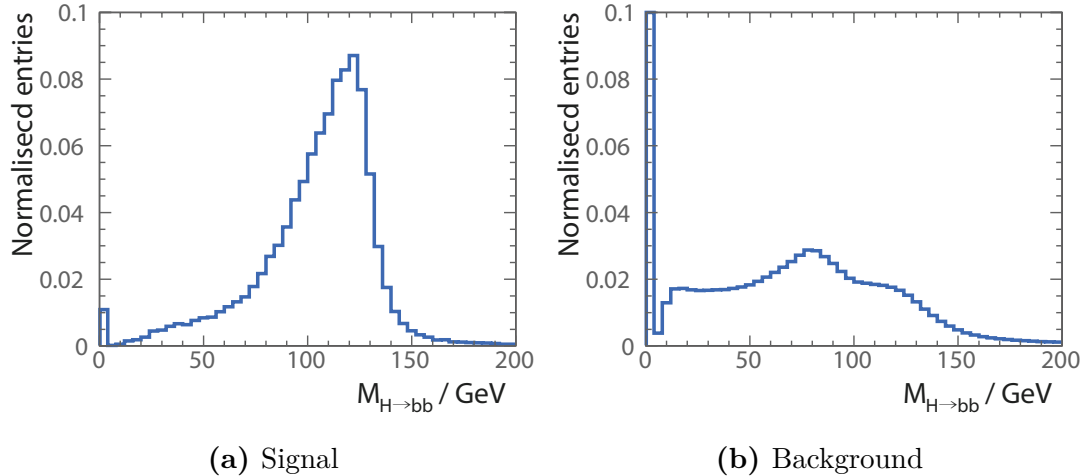


**Figure 7.11:** The distribution of  $m_{H_{bb}}$  for a) the signal channel, hadronic  $W^+W^-$  decay of  $HH \rightarrow b\bar{b}W^+W^-$ , and b) the sum of all background channels normalised to the respective cross sections. The area under the curve is normalised to 1. All plots are shown for  $\sqrt{s} = 1.4 \text{ TeV}$ .

Many background events do not have b-quark jets in the final state. Therefore, by requiring the second highest b-jet tag value greater than 0.2, as shown in Figure 7.13, background events with no b-jets in final states are removed.

The signal final states have neutrinos and hence missing momentum in the events. Therefore, the transverse momentum of the two Higgs system is non zero. A cut of  $p_T > 30 \text{ GeV}$ , as shown in figure 7.14, is extremely effective against background channels with no neutrinos in the final state.

The full list of fraction of events after each pre-selection cut can be found in table 7.10.

## 7.8. MVA variables

Having extracted information about leptons, b-jets, and jet pairing, a number of variables are used to differentiate the signal and the background events. These variables are the basis of the subsequent MVA event selection. The variables used are listed in table 7.11. The distributions of the four most power discriminators are show in figure 7.15.

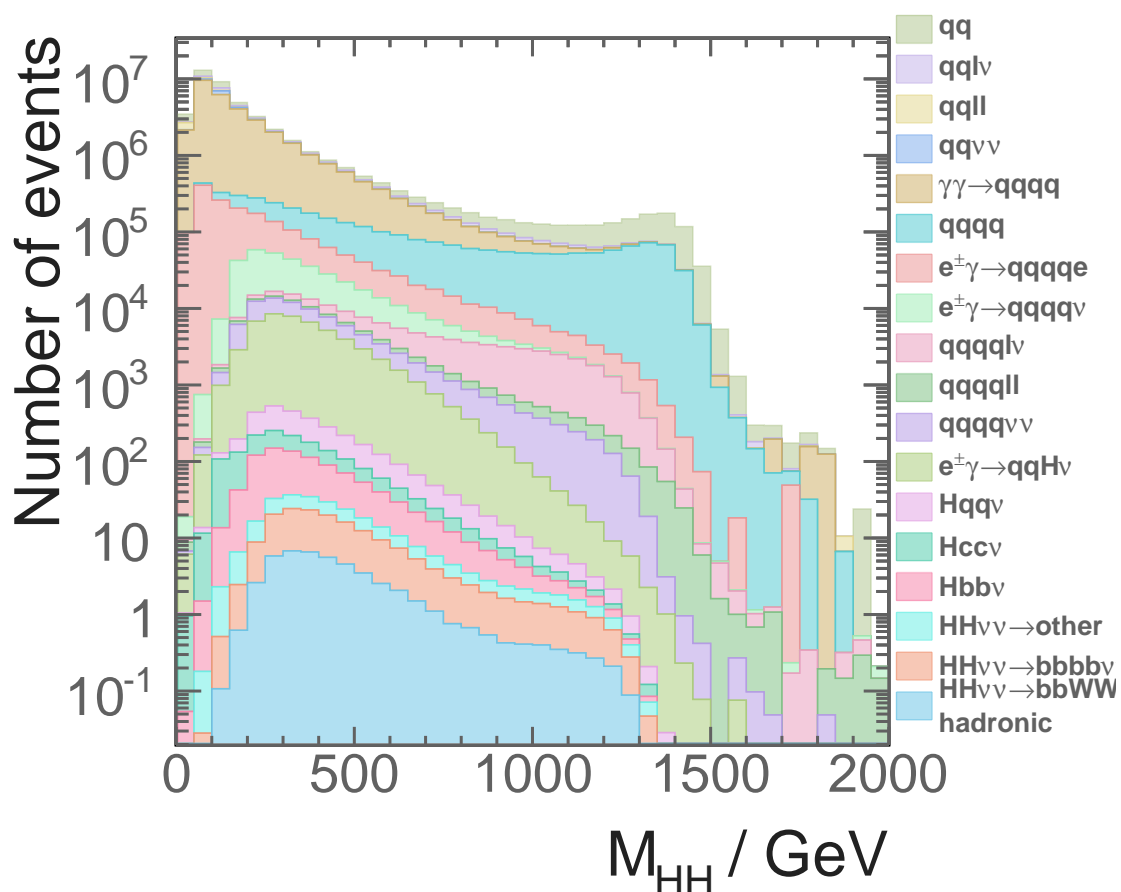


**Figure 7.12:** Distributions of the invariant mass of the two Higgs system for  $\sqrt{s} = 1.4 \text{ TeV}$ , assuming an intergraded luminosity of  $1500 \text{ fb}^{-1}$ .

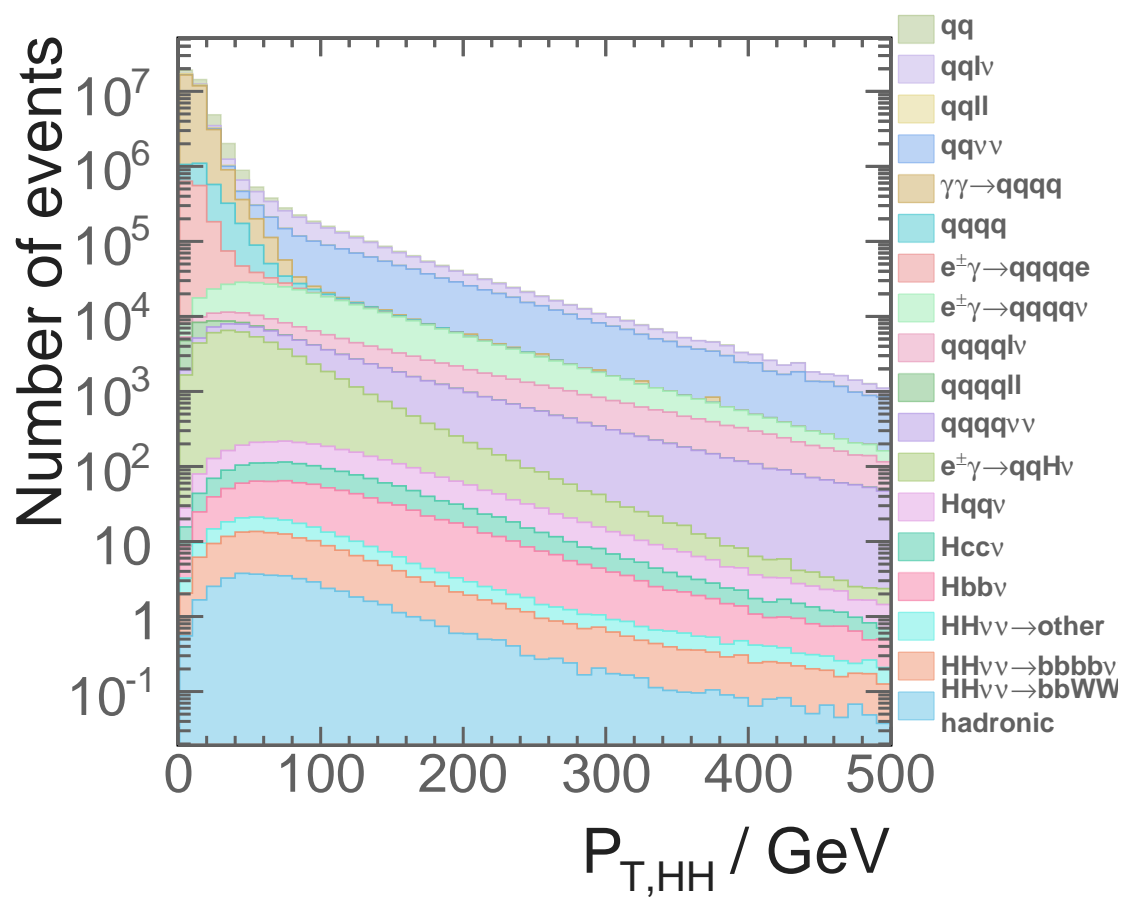


**Figure 7.13:** Distributions of the second highest b-jet tag value for  $\sqrt{s} = 1.4$  TeV, assuming an intergraded luminosity of  $1500 \text{ fb}^{-1}$ .

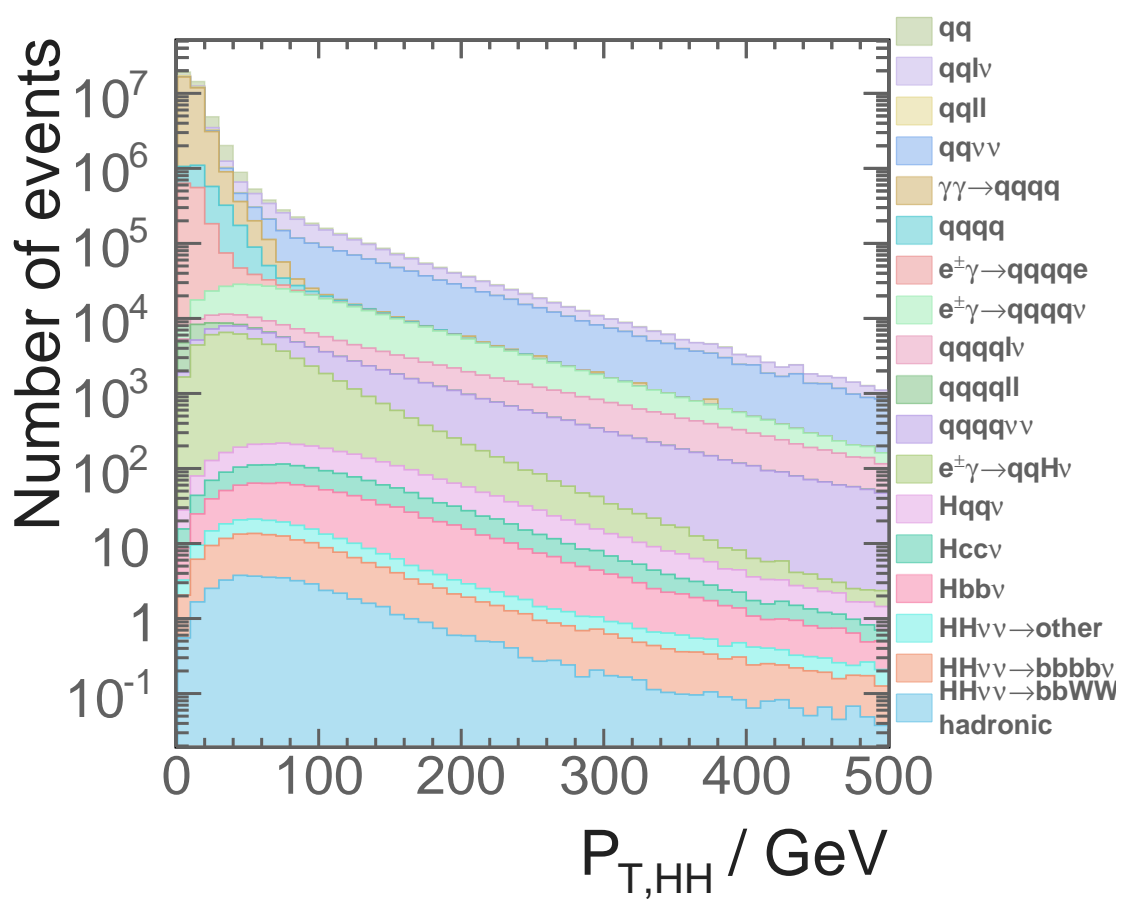


**Figure 7.14:** Distributions of the transverse momentum of the two Higgs system for  $\sqrt{s} = 1.4 \text{ TeV}$ , assuming an intergraded luminosity of  $1500 \text{ fb}^{-1}$ .

Channel	$m_{HH} > 150 \text{ GeV}$	$B_2 > 0.2$	$p_T > 30 \text{ GeV}$
$e^+e^- \rightarrow HH\nu_e\bar{\nu}_e \rightarrow b\bar{b}W^+W^-\nu_e\bar{\nu}_e$ , hadronic	78.1%	66.3%	59.7%
$e^+e^- \rightarrow HH\nu_e\bar{\nu}_e \rightarrow b\bar{b}b\bar{b}\nu_e\bar{\nu}_e$	17.8%	17.4%	15.4%
$e^+e^- \rightarrow HH\nu_e\bar{\nu}_e \rightarrow \text{other}$	30.5%	23.0%	20.5%
$e^+e^- \rightarrow q\bar{q}H\nu\bar{\nu}$	56.8%	42.3%	39.5%
$e^+e^- \rightarrow c\bar{c}H\nu\bar{\nu}$	44.8%	34.1%	31.7%
$e^+e^- \rightarrow b\bar{b}H\nu\bar{\nu}$	30.7%	27.0%	25.2%
$e^+e^- \rightarrow qq\bar{q}\bar{q}$	36.1%	13.2%	3.4%
$e^+e^- \rightarrow qqqq\ell\ell$	4.7%	1.5%	0.3%
$e^+e^- \rightarrow qqqq\ell\nu$	13.2%	10.7%	9.8%
$e^+e^- \rightarrow qqqq\nu\bar{\nu}$	46.1%	17.7%	16.6%
$e^+e^- \rightarrow qq$	8.1%	3.7%	0.8%
$e^+e^- \rightarrow q\bar{q}\ell\nu$	3.1%	1.2%	0.9%
$e^+e^- \rightarrow q\bar{q}\ell\ell$	0.7%	0.4%	0.1%
$e^+e^- \rightarrow qq\nu\nu$	9%	4.3%	4.0%
$e^\pm\gamma(\text{BS}) \rightarrow e^\pm qqqq$	10.1%	4.1%	0.4%
$e^\pm\gamma(\text{EPA}) \rightarrow e^\pm qqqq$	5.1%	2.0%	0.3%
$e^\pm\gamma(\text{BS}) \rightarrow \nu qqqq$	53.0%	28.0%	25.1%
$e^-\gamma(\text{EPA}) \rightarrow \nu qqqq$	26.7%	13.8%	12.5%
$e^\pm\gamma(\text{BS}) \rightarrow qqH\nu$	54.3%	40.3%	30.6%
$e^-\gamma(\text{EPA}) \rightarrow qqH\nu$	28.2%	20.9%	16.1%
$\gamma(\text{BS})\gamma(\text{BS}) \rightarrow qqqq$	23.1%	9.2%	0.3%
$\gamma(\text{BS})\gamma(\text{EPA}) \rightarrow qqqq$	13.6%	5.4%	0.4%
$\gamma(\text{EPA})\gamma(\text{BS}) \rightarrow qqqq$	13.6%	5.4%	0.3%
$\gamma(\text{EPA})\gamma(\text{EPA}) \rightarrow qqqq$	8.6%	3.5%	0.3%

**Table 7.10:** The table shows the expected number of events after successive cuts: invariant mass of the two Higgs system  $> 150 \text{ GeV}$ , the second highest b-jet tag value  $> 0.2$ , and the transverse momentum of the two Higgs system  $> 30 \text{ GeV}$ . All cuts include the lepton veto,  $HH \rightarrow b\bar{b}W^+W^-/HH \rightarrow b\bar{b}b\bar{b}$  separation, and valid jet pairing. The table shows for the signal and background events at  $\sqrt{s} = 1.4 \text{ TeV}$ , assuming an integrated luminosity of  $1500 \text{ fb}^{-1}$ .  $q$  can be  $u, d, s, b$  or  $t$ . Unless specified,  $q, \ell$  and  $\nu$  represent either particles or the corresponding anti-particles.

### 7.8.1. Invariant mass variables

Four invariant masses are used in the MVA event selection: the invariant mass of  $H_{bb}$  ( $m_{H_{bb}}$ ), the invariant mass of  $H_{WW^*}$  ( $m_{H_{WW^*}}$ ), the invariant mass of  $W$  ( $m_W$ ), and the invariant mass of the double Higgs system ( $m_{HH}$ ).

After the jet pairing under the hypothesis of the signal events, the distributions of the invariant mass of the physical bosons of the signal events have peaks around the expect masses, where the distributions of the background events do not have such resonance structure. Shown in the figure 7.15a, the distributions of the invariant mass of the  $H_{bb}$  is different to the distributions of the background events. Similarly, the distributions of the invariant mass of the  $H_{WW^*}$ , shown in figure 7.15b have a different peak position to the distributions of the background events. The invariant mass of the double Higgs system in the signal events is large due to the presence of two on-mass-shell Higgs bosons, which is also different to the distribution of the background events

### 7.8.2. Energy and momentum variables

Six energy and momentum variables participate in the MVA event selection: the energy of the off-mass-shell  $W$  ( $E_{W^*}$ ), the energy of the missing momenta ( $E_{mis}$ ), the transverse momentum of  $H_{bb}$  ( $p_{TH_{bb}}$ ), the transverse momentum of  $H_{WW^*}$  ( $p_{TH_{WW^*}}$ ), the transverse momentum of  $W$  ( $p_{TW}$ ), and the transverse momentum of the double Higgs system ( $p_{THH}$ ).

For the off-mass-shell  $W$ , the energy is used instead of the invariant mass, as invariant mass distribution of  $W^*$  does not have a resonance structure. The energy of the missing momenta is powerful against background events with no neutrinos in the final states. The missing momenta is calculated by assuming the collision at  $\sqrt{s}$  and a beam crossing angle of 20 mrad. Other momentum variables correspond to the same physical bosons or the double Higgs system used in the invariant mass variables, for the same reason that the distributions of these momentum variables are different for the signal events and the background events.

### 7.8.3. Lab-frame angle variables

Four lab-frame angle variables are in the MVA event selection: the pseudorapidity of the missing momenta ( $\eta_{mis}$ ), the acollinearity of the two jets associated with  $H_{bb}$  ( $A_{H_{bb}}$ ), the acollinearity of the two jets associated with  $H_{WW^*}$  ( $A_{H_{WW^*}}$ ), and the acollinearity of the two Higgs bosons ( $A_{HH}$ ).

The pseudorapidity of the missing momenta is used, instead of the polar angle, because the forward polar angles are transformed to a larger range in the pseudorapidity. The pseudorapidity of the missing momenta is defined as

$$\eta_{mis} \equiv -\ln \left[ \tan \left( \frac{\theta_{mis}}{2} \right) \right], \quad (7.7)$$

where  $\theta_{mis}$  is the polar angle of the missing momenta measured in a spherical polar coordinate system.

Acollinearity is a measures the angle between the two momenta. The definition for the acollinearity for momenta  $i$  and momenta  $j$  is

$$A_{ij} = \pi - \cos^{-1} (\hat{\mathbf{p}}_i \cdot \hat{\mathbf{p}}_j), \quad (7.8)$$

where  $\hat{\mathbf{p}}_i$  is the unit momentum three-vector of momenta  $i$ . The distribution of the  $A_{H_{bb}}$ , shown in figure 7.15c, peaks at the value of 0 or  $\pi$  for many background events, which are not the same as the signal events. For the same reason, the distributions of  $A_{H_{WW^*}}$  and  $A_{HH}$  are different for the signal and the background events.

### 7.8.4. Boosted-frame angle variables

The MVA event selection also uses five boosted-frame angle variables: the angle between two jets associated with  $H_{bb}$  in the  $H_{bb}$  decay rest frame ( $\cos(\theta_{H_{bb}}^*)$ ), the angle between two W associated with  $H_{WW^*}$  in the  $H_{WW^*}$  decay rest frame ( $\cos(\theta_{H_{WW^*}}^*)$ ), the angle between two jets associated with W in the W decay rest frame ( $\cos(\theta_W^*)$ ), the angle between two jets associated with  $W^*$  in the  $W^*$  decay rest frame ( $\cos(\theta_{W^*}^*)$ ), and the angle between two Higgs bosons in two Higgs bosons decay rest frame ( $\cos(\theta_{HH}^*)$ ).

These variables are some of the most powerful variables. For example,  $\cos(\theta_{H_{bb}}^*)$  for the signal events has a uniform distribution, shown in figure 7.15d, as it is equally

likely for two quarks to decay in any open angle in the  $H_{bb}$  decay rest frame. For the background events, by pairing jets under the signal event hypothesis,  $\cos(\theta_{H_{bb}}^*)$  does not have a flat distribution. The  $\cos(\theta_{H_{bb}}^*)$  distribution for the background events peaks at 1.

### 7.8.5. Event shape variables

Five event shapes variables are used in the MVA event selection: the absolute value of the sphericity ( $|\mathbf{S}|$ ), the negative logarithm of  $y_{23}$  ( $-\ln(y_{23})$ ), the negative logarithm of  $y_{34}$  ( $-\ln(y_{34})$ ), the negative logarithm of  $y_{45}$  ( $-\ln(y_{45})$ ), the negative logarithm of  $y_{56}$  ( $-\ln(y_{56})$ )).

The sphericity,  $\mathbf{S}$ , is a measurement of the spherically symmetry of the event, which will be different for the signal and background events. The sphericity is derived from the sphericity tensor [96]. The sphericity tensor is defined as

$$\mathbf{S}^{\alpha\beta} = \frac{\sum_i p_i^\alpha p_i^\beta}{\sum_i |\vec{p}_i|^2}, \quad (7.9)$$

where  $\vec{p}_i$  is the momentum vector of the particle  $i$ ; index  $i$  is summed over all particles in the event; and  $\alpha$  and  $\beta$  refer to the x, y, z coordinate axis. Eigenvalues of  $\mathbf{S}$  tensor, denoted with  $\lambda_1, \lambda_2, \lambda_3$ , can be found via diagonalisation of the matrix  $\mathbf{S}$ . The normalisation condition requires  $\lambda_1 \geq \lambda_2 \geq \lambda_3$  and  $\lambda_1 + \lambda_2 + \lambda_3 = 1$ . Sphericity,  $S$ , is defined in terms of  $\lambda$ ,

$$\mathbf{S} = \frac{3}{2}(\lambda_1 + \lambda_2). \quad (7.10)$$

$\mathbf{S}$ , is 0 for a perfect pencil-like back-to-back two-jet event, and 1 for a perfect spherically symmetric event.

### 7.8.6. b and c tag variables

Six b-jet and c-jet tag variables are used in the MVA event selection: the highest b-jet tag value of the two jets associated with  $H_{bb}$  ( $B_{1,H_{bb}}$ ), the lowest b-jet tag value of the two jets associated with  $H_{bb}$  ( $B_{2,H_{bb}}$ ), the highest b-jet tag value of the two jets associated with  $W$  ( $B_{1,W}$ ), the highest b-jet tag value of the two jets associated with  $W^*$  ( $B_{1,W^*}$ ),

Category	Variable
Invariant mass	$m_{H_{bb}}, m_{H_{WW^*}}, m_W, m_{HH}$
Energy and momentum	$E_{W^*}, E_{mis}, p_{TH_{bb}}, p_{TH_{WW^*}}, p_{TW}, p_{THH}$
Lab-frame angles	$\eta_{mis}, A_{H_{bb}}, A_W, A_{HH}$
Boosted-frame angles	$\cos(\theta_{H_{bb}}^*), \cos(\theta_{H_{WW^*}}^*), \cos(\theta_W^*), \cos(\theta_{W^*}^*), \cos(\theta_{HH}^*)$
Event shape	$ \mathbf{S} , -\ln(y_{23}), -\ln(y_{34}), -\ln(y_{45}), -\ln(y_{56})$
b and c tag	$B_{1,H_{bb}}, B_{2,H_{bb}}, B_{1,W}, B_{1,W^*}, C_{1,H_{bb}}, C_{1,W}$
PFOs number	$N_{H_{bb}}, N_{H_{WW^*}}, N_W, N_{W^*}$

**Table 7.11:** Variables used in the MVA event selection for  $\sqrt{s} = 1.4$  TeV

the highest c-jet tag value of the two jets associated with  $H_{bb}$  ( $C_{1,H_{bb}}$ ), and the highest c-jet tag value of the two jets associated with  $W$  ( $C_{1,W}$ ).

As mentioned in the flavour tagging section, these b-jet and c-jet tag variables are useful to separate the signal events from the background events which do not have b-quark jets in the final states.

### 7.8.7. PFOs number variables

The last four variables used in the MVA event selection are the PFOs number variables: the number of PFOs associated with  $H_{bb}$  ( $N_{H_{bb}}$ ), the number of PFOs associated with  $H_{WW^*}$  ( $N_{H_{WW^*}}$ ), the number of PFOs associated with  $W$  ( $N_W$ ), the number of PFOs associated with  $W^*$  ( $N_{W^*}$ ). These variables are effective to differentiate the signal events from the background events with fewer than six quarks in final states.

An optimal set of 32 variables are chosen for the best MVA performance, whilst no strong ( $> 80\%$ ) pair-wise correlation exists between any two variables.

### 7.8.8. Cuts to aid the MVA

A set of cuts reduce the range of invariant masses variables in order to increase the effectiveness of the MVA event selection. Occasionally, extreme values of the invariant masses variables skew the distributions. Therefore by limiting the range of the variables,

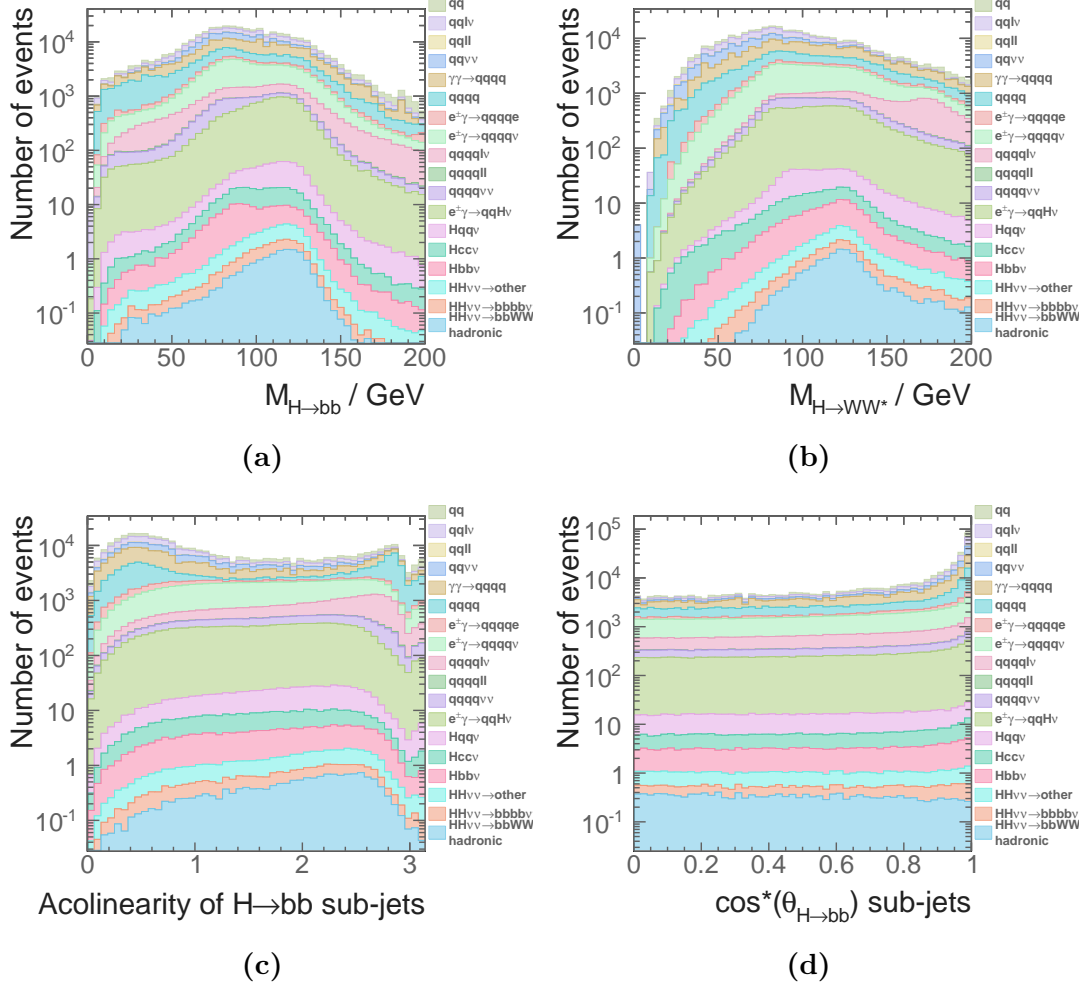


**Figure 7.15:** Distributions of the four variables with highest discriminating power: a) the invariant mass of  $H_{bb}$ , b) the invariant mas of  $H_{WW^*}$ , c) the acolinearity of the two jets associated with  $H_{bb}$ , and d) the opening angles of the two jets associated with  $H_{bb}$  in the decay rest frame of the  $H_{bb}$ . All plots assumes an intergraded luminosity of  $1500 \text{ fb}^{-1}$  at  $\sqrt{s} = 1.4 \text{ TeV}$  after all pre-selection cuts applied before the MVA.

the MVA classifier could focus on the phase spaces with high event densities. The cuts require the invariant mass of the  $H_{bb} < 500 \text{ GeV}$ , the invariant mass of the  $H_{WW^*} < 800 \text{ GeV}$ , the invariant mass of the  $W < 200 \text{ GeV}$ , and the invariant mass of the double Higgs system  $< 1400 \text{ GeV}$ .

## 7.9. Multivariate analysis

After gathering information and applying pre-selection cuts, signal events are selected using the multivariate analysis (MVA) with Boosted Decision Tree classifier (BDT), as implemented in the TMVA [72]. The parameters for boosted decision tree were optimised and checked for overtraining, following the strategy outlined in section 4.8. Half of the events were used for training, and the other half used for testing and classifier optimisation. The optimised parameters are listed in table 7.12.

After dividing all events into a training set and a testing set, in the training stage of the MVA classifier, the training signal events are the hadronic  $W^+W^-$  decay of the  $HH \rightarrow b\bar{b}W^+W^-$  events in the training set. The training background events are all events without double higgs production in the training set. However, for the extraction of the  $g_{HHH}$  and  $g_{WWHH}$ , all events with double higgs production are sensitive to the couplings. Therefore, at the applying stage of the MVA classifier, all events in the testing set are used.

## 7.10. Signal selection results

Number of events passed the MVA event selection at  $\sqrt{s} = 1.4 \text{ TeV}$ , assuming a luminosity of  $1500 \text{ fb}^{-1}$  are listed in table 7.13 for individual channels. A few background channels have non-zero events after the MVA event selection.  $e^+e^- \rightarrow q\bar{q}H\nu\bar{\nu}$  events are difficult to discard because its topology, one Higgs plus neutrino, is very similar to the signal event topology. Similarly,  $e^+e^- \rightarrow qqqq\ell\nu$  events can be confused with the signal events when the lepton is undetected in the forward region, or the energy of the lepton is too low to be tagged.  $e^+e^- \rightarrow qqqq\nu\bar{\nu}$  events can also have a similar topology to the signal events. Other background channels that are not discarded after the MVA are the electron-photon and photon interactions with the same final states as the channels above.

Parameter	Value
Depth of tree	4
Number of trees	4000
The minimum number of events in a node	0.25% of the total events
Boosting	adaptive boost
Learning rate of the adaptive boost	0.5
Metric for the optimal cuts	Gini Index
Bagging fraction	0.5
Number of bins per variables	40
End node output	$x \in [0, 1]$
Do-PreSelection	yes

**Table 7.12:** Optimised parameters for the boosted decision tree classifier used in the MVA event selection. See section 4.8.8 for detailed explanations of variables.

Before interpreting the result for analysis at  $\sqrt{s} = 1.4$  TeV, the analyses at  $\sqrt{s} = 3$  TeV and the semi-leptonic channel of  $e^+e^- \rightarrow HH\nu_e\bar{\nu}_e \rightarrow b\bar{b}W^+W^-\nu_e\bar{\nu}_e$  are presented.

## 7.11. $\sqrt{s} = 3$ TeV analysis

The hadronic  $W^+W^-$  decay of the  $e^+e^- \rightarrow HH\nu_e\bar{\nu}_e \rightarrow b\bar{b}W^+W^-\nu\bar{\nu}$  at  $\sqrt{s} = 3$  TeV analysis follows the same strategy as the analysis at  $\sqrt{s} = 1.4$  TeV. Lepton finding, jet pairing and flavouring tagging have been discussed in previous sections. The differences, which have not been mentioned, will be highlighted in this section.

Cross sections of used samples are listed in table 7.14. The mutually exclusive cuts to separate events into two independent sets are almost identical to the cuts used in the  $\sqrt{s} = 1.4$  TeV analysis. Figure 7.16 shows the sum of b-jet tag values, when the event is clustered into four jets, as a function of  $-\log(y_{34})$  for the hadronic  $W^+W^-$  decay in  $HH \rightarrow b\bar{b}W^+W^-$  and  $HH \rightarrow b\bar{b}b\bar{b}$  sub-channels. The optimised cuts are  $\sum B_{4jets} < 2.3$ ,  $-\log(y_{34}) < 3.6$ . The selection efficiencies of evens after lepton veto, the mutually exclusive cuts and the jet pairing for individual channel are shown in table A.1.

The pre-selection cuts at  $\sqrt{s} = 3$  TeV use the same cut on  $m_{HH}$ . The cut on b-jet tag is different because the performance of flavour tagging is worse at  $\sqrt{s} = 3$  TeV in

$\sqrt{s} = 1.4 \text{ TeV}$	N	$\varepsilon_{presel}$	$\varepsilon_{MVA}$	$N_{MVA}$
$e^+e^- \rightarrow HH\nu_e\bar{\nu}_e \rightarrow b\bar{b}W^+W^-\nu_e\bar{\nu}_e$ , hadronic	27.9	59.8%	8.2%	1.29
$e^+e^- \rightarrow HH\nu_e\bar{\nu}_e \rightarrow b\bar{b}b\bar{b}\nu_e\bar{\nu}_e$	67.6	15.4%	0.5%	0.05
$e^+e^- \rightarrow HH\nu_e\bar{\nu}_e \rightarrow \text{other}$	128.0	20.4%	1.7%	0.45
$e^+e^- \rightarrow q\bar{q}H\nu\bar{\nu}$	1290	39.5%	0.05%	0.29
$e^+e^- \rightarrow c\bar{c}H\nu\bar{\nu}$	540	31.6%	0.1%	0.16
$e^+e^- \rightarrow b\bar{b}H\nu\bar{\nu}$	465	24.7%	0.3%	0.37
$e^+e^- \rightarrow qqqq$	1867650	3.3%	-	-
$e^+e^- \rightarrow qq\bar{q}\ell\bar{\ell}$	93150	0.3%	-	-
$e^+e^- \rightarrow qq\bar{q}\ell\nu$	165600	9.8%	0.01%	2.06
$e^+e^- \rightarrow qq\bar{q}\nu\bar{\nu}$	34800	16.5%	0.002%	0.10
$e^+e^- \rightarrow qq$	6014250	0.8%	-	-
$e^+e^- \rightarrow q\bar{q}\ell\nu$	6464550	0.9%	-	-
$e^+e^- \rightarrow q\bar{q}\ell\bar{\ell}$	4088700	0.08%	-	-
$e^+e^- \rightarrow q\bar{q}\nu\bar{\nu}$	1181550	4.0%	-	-
$e^\pm\gamma(BS) \rightarrow e^\pm qqqq$	2606625	0.3%	-	-
$e^\pm\gamma(EPA) \rightarrow e^\pm qqqq$	861000	0.3%	-	-
$e^\pm\gamma(BS) \rightarrow \nu qqqq$	178987.5	25.7%	0.005%	2.05
$e^\pm\gamma(EPA) \rightarrow \nu qqqq$	52050	12.5%	0.004%	0.27
$e^\pm\gamma(BS) \rightarrow q\bar{q}H\nu$	35437.5	30.7%	0.02%	2.16
$e^\pm\gamma(EPA) \rightarrow q\bar{q}H\nu$	10170.0	16.1%	0.06%	0.95
$\gamma(BS)\gamma(BS) \rightarrow qqqq$	2054951.5	0.2%	-	-
$\gamma(BS)\gamma(EPA) \rightarrow qqqq$	4521037.5	0.4%	-	-
$\gamma(EPA)\gamma(BS) \rightarrow qqqq$	4539150.0	0.3%	-	-
$\gamma(EPA)\gamma(EPA) \rightarrow qqqq$	1129500.0	0.3%	-	-

**Table 7.13:** List of signal and background events with selection efficiency and number of events at  $\sqrt{s} = 1.4 \text{ TeV}$ , assuming a luminosity of  $1500 \text{ fb}^{-1}$ . The number of events (N), the selection efficiencies of pre-selection cuts ( $\varepsilon_{presel}$ ), the selection efficiencies of MVA after pre-selection cuts ( $\varepsilon_{MVA}$ ), and the number of events after MVA ( $N_{MVA}$ ) are shown. - represents a number less than 0.01. q can be u, d, s, b or t.

Channel	$\sigma(\sqrt{s} = 3 \text{ TeV}) / \text{fb}$
$e^+e^- \rightarrow HH\nu_e\bar{\nu}_e$	0.588
$e^+e^- \rightarrow HH\nu_e\bar{\nu}_e \rightarrow b\bar{b}W^+W^-$ , hadronic	0.07
$e^+e^- \rightarrow HH\nu_e\bar{\nu}_e \rightarrow b\bar{b}b\bar{b}\nu_e\bar{\nu}_e$	0.19
$e^+e^- \rightarrow HH \rightarrow \text{others}$	0.34
$e^+e^- \rightarrow q\bar{q}H\nu\bar{\nu}$	3.06
$e^+e^- \rightarrow c\bar{c}H\nu\bar{\nu}$	1.15
$e^+e^- \rightarrow b\bar{b}H\nu\bar{\nu}$	1.78
$e^+e^- \rightarrow qqqq$	546.5*
$e^+e^- \rightarrow qqqq\ell\ell$	169.3*
$e^+e^- \rightarrow qqqq\ell\nu$	106.6*
$e^+e^- \rightarrow qqqq\nu\bar{\nu}$	71.5*
$e^+e^- \rightarrow qq$	2948.9
$e^+e^- \rightarrow qq\ell\nu$	5561.1
$e^+e^- \rightarrow qq\ell\ell$	3319.6
$e^+e^- \rightarrow qq\nu\nu$	1317.5
$e^\pm\gamma(\text{BS}) \rightarrow e^\pm qqqq$	2536.3*
$e^\pm\gamma(\text{EPA}) \rightarrow e^\pm qqqq$	575.7*
$e^\pm\gamma(\text{BS}) \rightarrow \nu qqqq$	524.8*
$e^\pm\gamma(\text{EPA}) \rightarrow \nu qqqq$	108.4*
$e^\pm\gamma(\text{BS}) \rightarrow qqH\nu$	117.1*
$e^\pm\gamma(\text{EPA}) \rightarrow qqH\nu$	22.4*
$\gamma(\text{BS})\gamma(\text{BS}) \rightarrow qqqq$	13050.3*
$\gamma(\text{BS})\gamma(\text{EPA}) \rightarrow qqqq$	2420.6*
$\gamma(\text{EPA})\gamma(\text{BS}) \rightarrow qqqq$	2423.1*
$\gamma(\text{EPA})\gamma(\text{EPA}) \rightarrow qqqq$	402.7*

**Table 7.14:** List of signal and background samples used in the double Higgs analysis with the corresponding cross sections at  $\sqrt{s} = 3 \text{ TeV}$ .  $q$  can be  $u, d, s, b$  or  $t$ . Unless specified,  $q, \ell$  and  $\nu$  represent either particles or the corresponding anti-particles.  $\gamma$  (BS) represents a real photon from beamstrahlung (BS).  $\gamma$  (EPA) represents a “quasi-real” photon, simulated with the Equivalent Photon Approximation. For processes labelled with \*, events are generated with the invariant mass of the total momenta of all quarks above 50 GeV.

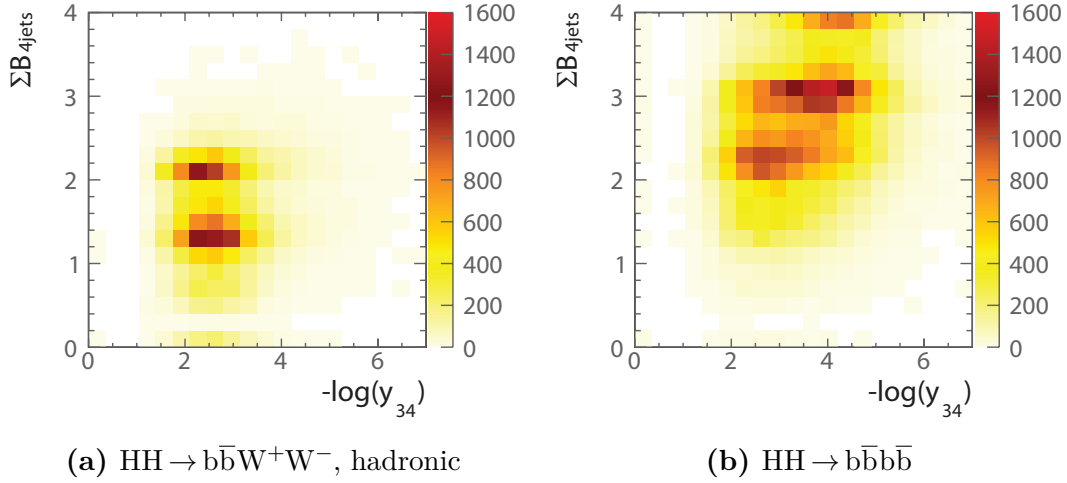


**Figure 7.16:** The two-dimensional distribution of sum of b-jet tag values against  $-\log(y_{34})$ . The plots show a) a) hadronic  $W^+W^-$  decay of  $\text{HH} \rightarrow b\bar{b}W^+W^-$ , and b)  $\text{HH} \rightarrow b\bar{b}b\bar{b}$  events at  $\sqrt{s} = 3$  TeV. The sum of b-jet tag values is calculated for the case where events are clustered into four jets.

comparison to the performance at  $\sqrt{s} = 1.4$  TeV. Figure 7.18 shows the distribution of the highest b-jet tag value, where the cut above 0.7 helps to reduce background events with no b-jet in final states. Figure 7.17 shows the distribution of the invariant mass of the two Higgs system, where the cut above 150 GeV is effective against samples with two-quark final states. The fraction of events passing each pre-selection cut for individual channel are listed in table A.2.

The cuts to aid the MVA at  $\sqrt{s} = 3$  TeV are largely the same as the ones at  $\sqrt{s} = 1.4$  TeV, apart from the difference on the cut of the invariant mass of HH due to a higher  $\sqrt{s}$ . The cuts are the invariant mass of the  $H_{bb} < 500$  GeV, the invariant mass of the  $H_{WW^*} < 800$  GeV, the invariant mass of the  $W < 200$  GeV, and the invariant mass of the double Higgs system  $< 3000$  GeV.

The same set of variables are used in the MVA as in the analysis at  $\sqrt{s} = 1.4$  TeV. The optimised parameters for the Boosted Decision Tree classifier are the same. The efficiencies of the MVA event selections and the number of events after the MVA event selection are listed in table 7.15. Background channels that are dominant after the MVA event selection are almost identical to those at  $\sqrt{s} = 1.4$  TeV. Hence see section 7.10 for discussion.

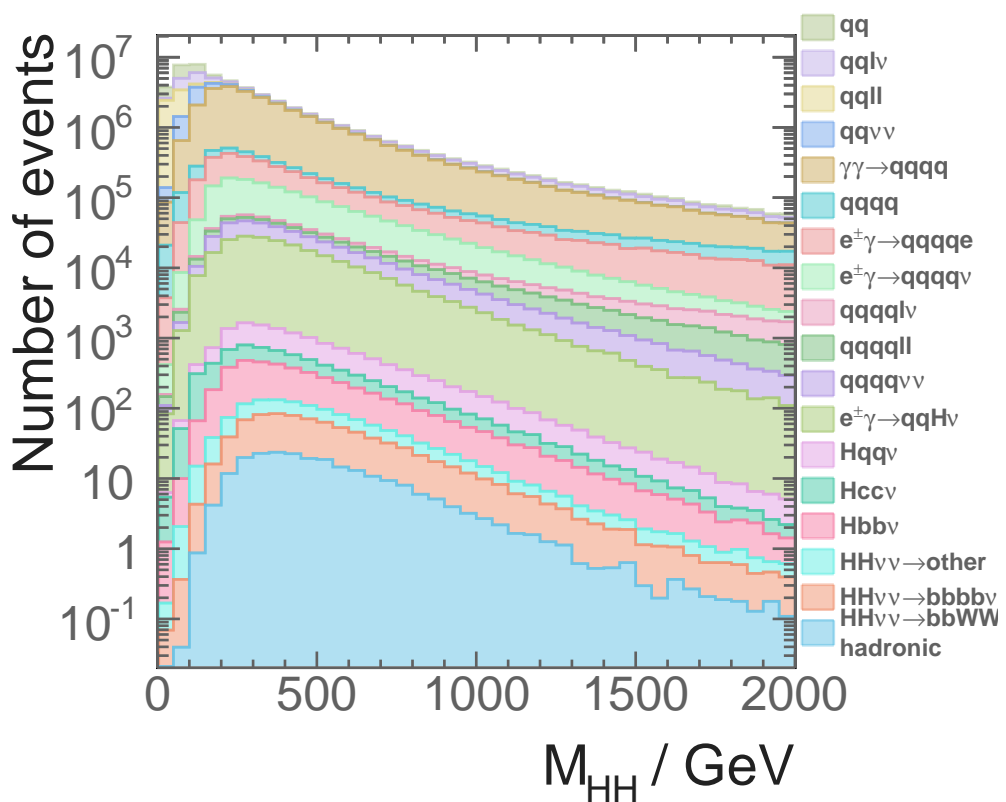


**Figure 7.17:** Distributions of the invariant mass of the two Higgs system for  $\sqrt{s} = 3 \text{ TeV}$ , assuming an intergraded luminosity of  $2000 \text{ fb}^{-1}$ .

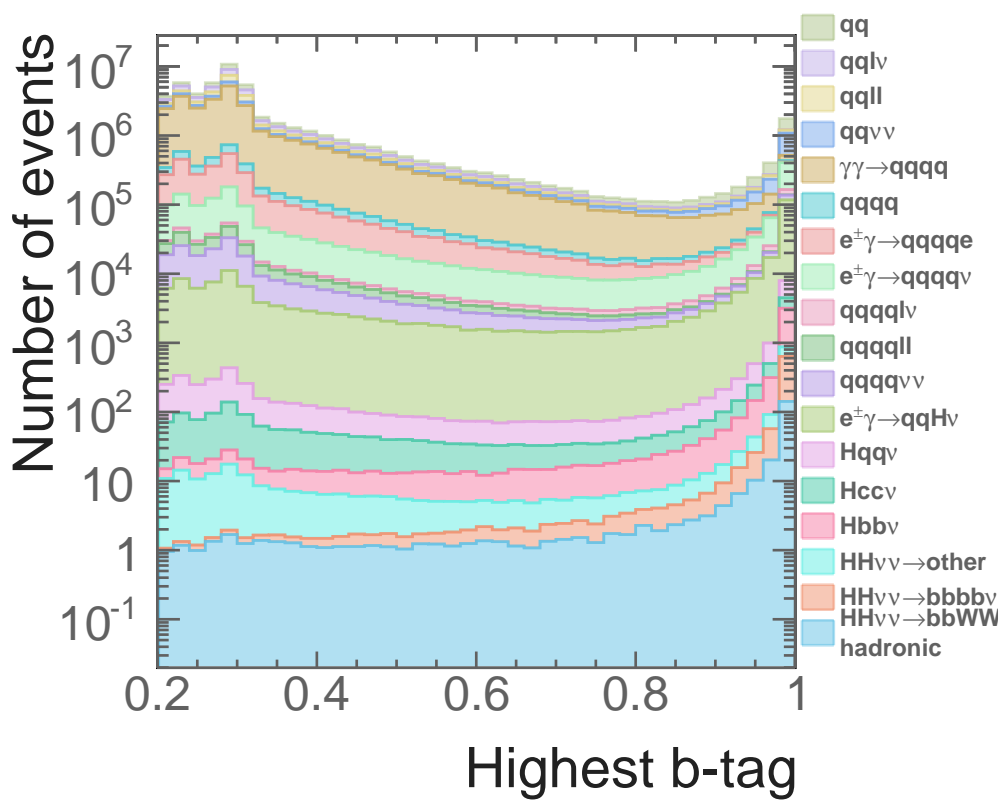


**Figure 7.18:** Distributions of the highest b-jet tag value for  $\sqrt{s} = 3$  TeV, assuming an integrated luminosity of  $2000 \text{ fb}^{-1}$ .

$\sqrt{s} = 3 \text{ TeV}$	N	$\varepsilon_{\text{presel}}$	$\varepsilon_{\text{MVA}}$	$N_{\text{MVA}}$
$e^+e^- \rightarrow HH\nu_e\bar{\nu}_e \rightarrow b\bar{b}W^+W^-\nu_e\bar{\nu}_e, \text{ hadronic}$	146.0	61.7%	11.6%	9.89
$e^+e^- \rightarrow HH\nu_e\bar{\nu}_e \rightarrow b\bar{b}b\bar{b}\nu_e\bar{\nu}_e$	355.0	18.8%	1.5%	1.05
$e^+e^- \rightarrow HH\nu_e\bar{\nu}_e \rightarrow \text{other}$	675.0	20.0%	3.6%	4.51
$e^+e^- \rightarrow q\bar{q}H\nu\bar{\nu}$	6120	36.0%	0.4%	9.42
$e^+e^- \rightarrow c\bar{c}H\nu\bar{\nu}$	2300	26.3%	0.5%	3.13
$e^+e^- \rightarrow b\bar{b}H\nu\bar{\nu}$	3560	25.8%	1.2%	6.82
$e^+e^- \rightarrow qqqq$	1093000	1.4%	0.01%	1.43
$e^+e^- \rightarrow qqqq\ell\ell$	338600	0.6%	-	-
$e^+e^- \rightarrow qqqq\ell\nu$	213200	7.3%	0.05%	8.35
$e^+e^- \rightarrow qqqq\nu\bar{\nu}$	143000	9.0%	0.05%	6.35
$e^+e^- \rightarrow qq$	5897800	1.4%	-	-
$e^+e^- \rightarrow qq\ell\nu$	11121800	0.1%	-	-
$e^+e^- \rightarrow qq\ell\ell$	6639200	0.4%	-	-
$e^+e^- \rightarrow qq\nu\nu$	2635000	3.1%	-	-
$e^\pm\gamma(\text{BS}) \rightarrow e^\pm qqqq$	4007354	0.7%	-	-
$e^\pm\gamma(\text{EPA}) \rightarrow e^\pm qqqq$	1151200	0.4%	-	-
$e^\pm\gamma(\text{BS}) \rightarrow \nu qqqq$	829184	16.4%	0.04%	61.0
$e^\pm\gamma(\text{EPA}) \rightarrow \nu qqqq$	216800	7.6%	0.04%	6.0
$e^\pm\gamma(\text{BS}) \rightarrow qqH\nu$	185018	30.2%	0.2%	121.7
$e^\pm\gamma(\text{EPA}) \rightarrow qqH\nu$	46800.0	15.3%	0.2%	18.1
$\gamma(\text{BS})\gamma(\text{BS}) \rightarrow qqqq$	18009414	1.6%	-	-
$\gamma(\text{BS})\gamma(\text{EPA}) \rightarrow qqqq$	3824548	1.0%	-	-
$\gamma(\text{EPA})\gamma(\text{BS}) \rightarrow qqqq$	3828498	1.0%	-	-
$\gamma(\text{EPA})\gamma(\text{EPA}) \rightarrow qqqq$	805400	0.6%	-	-

**Table 7.15:** List of signal and background events with selection efficiency and number of events at  $\sqrt{s} = 3 \text{ TeV}$ , assuming a luminosity of  $2000 \text{ fb}^{-1}$ . The number of events (N), the selection efficiencies of pre-selection cuts ( $\varepsilon_{\text{presel}}$ ), the selection efficiencies of MVA after pre-selection cuts ( $\varepsilon_{\text{MVA}}$ ), and the number of events after MVA ( $N_{\text{MVA}}$ ) are shown. - represents a number less than 0.01. q can be u, d, s, b or t. Unless specified, q,  $\ell$  and  $\nu$  represent either particles or the corresponding anti-particles.  $\gamma$  (BS) represents a real photon from beamstrahlung (BS).  $\gamma$  (EPA) represents a “quasi-real” photon, simulated with the Equivalent Photon Approximation.

## 7.12. Semi-leptonic decay at $\sqrt{s} = 3 \text{ TeV}$ analysis

The final analysis is the semi-leptonic  $W^+W^-$  decay of  $e^+e^- \rightarrow HH\nu_e\bar{\nu}_e \rightarrow b\bar{b}W^+W^-\nu\bar{\nu}$  at  $\sqrt{s} = 3 \text{ TeV}$ . The semi-leptonic decay analysis at  $\sqrt{s} = 1.4 \text{ TeV}$  was also performed. However there are not enough signal events to have a meaningful discussion for the analysis at  $\sqrt{s} = 1.4 \text{ TeV}$ . Hence, only the semi-leptonic decay analysis at  $\sqrt{s} = 3 \text{ TeV}$  is presented.

The strategy of the semi-leptonic decay analysis is very similar to the hadronic decay analysis. The main difference are that there is one lepton in the final state and the final state has four quarks instead of six.  $H_{bb}$  and  $W$  can not be reconstructed due to the leptonic decay of one of the  $W$ . Hence, the signal events are selected when there is one identified lepton using the same lepton finding processors. The jet reconstruction parameters are the same as hadronic decay analysis at the  $\sqrt{s} = 3 \text{ TeV}$ . There are no mutually exclusive cuts since there is no semi-leptonic analysis in the  $HH \rightarrow b\bar{b}b\bar{b}$  analysis.

The pre-selection cuts are similar to the cuts in the hadronic analysis. The invariant mass of the double Higgs system is required to be above 150 GeV. The highest b-jet tag value is higher than 0.2. The transverse momentum of the double Higgs system is higher than 30 GeV.

Variables used in the MVA classifier, listed in table 7.16, belong to a reduced set of the variables used in the hadronic decay analysis, as  $H_{bb}$  and  $W$  can not be reconstructed in the semi-hadronic decay analysis. For the same reason, the cuts to aid the MVA are reduced to the invariant mass of  $H_{bb} < 500 \text{ GeV}$  and the invariant mass of the double Higgs system  $< 3000 \text{ GeV}$ .

Figure 7.17 lists the selection efficiency and number of events after the MVA event selection for individual channel at  $\sqrt{s} = 3 \text{ TeV}$ , assuming a luminosity of  $2000 \text{ fb}^{-1}$ . Almost all background channels are non-zero after the MVA event selection. Nevertheless, dominant background channels are almost identical to the hadronic decay analysis at  $\sqrt{s} = 3 \text{ TeV}$ . Hence discussion of the MVA event selection is provided in section 7.10.

Category	Variable
Invariant mass	$m_{H_{bb}}, m_W, m_{HH}$
Energy and momentum	$E_{mis}, p_{TH_{bb}}, p_{TW}, p_{THH}$
Lab-frame angles	$\theta_{mis}, A_{H_{bb}}, A_W, A_{HH}$
Boosted-frame frames	$\cos(\theta_{H_{bb}}^*), \cos(\theta_{HH}^*)$
Event shape	$ S , -\ln(y_{23}), -\ln(y_{34}), -\ln(y_{45}), -\ln(y_{56})$
b and c tag	$B_{1,H_{bb}}, B_{2,H_{bb}}, B_{1,W}, C_{1,H_{bb}}, C_{1,W}$
PFOs number	$N_{H_{bb}}, N_W$

**Table 7.16:** Variables used in the MVA event selection for the semi-leptonic  $W^+W^-$  decay of  $HH \rightarrow b\bar{b}W^+W^-$  analysis at  $\sqrt{s} = 3$  TeV.

## 7.13. Result interpretation

The results of analyses at the  $\sqrt{s} = 1.4$  TeV and  $\sqrt{s} = 3$  TeV are summarised in table 7.18. For the hadronic  $W^+W^-$  decay of  $HH \rightarrow b\bar{b}W^+W^-$  analyses at  $\sqrt{s} = 1.4$  TeV and  $\sqrt{s} = 3$  TeV, numbers of the signal events passing the MVA event selection are 1.79 and 15.45, respectively; the numbers of background events passing the MVA event selection are 8.41 and 242.28, respectively. For the semi-leptonic  $W^+W^-$  decay of  $HH \rightarrow b\bar{b}W^+W^-$  analyses  $\sqrt{s} = 3$  TeV, the number of the signal events passing the MVA event selection is 31.24, whilst the numbers of background events passing the MVA event selection is 3612.39.

The expected uncertainty on the measurement of the cross sections, which is roughly  $\sqrt{N_S + N_B}/N_S$  at  $\sqrt{s} = 1.4$  TeV and 3 TeV, are:

$$\frac{\Delta [\sigma(HH\nu_e\bar{\nu}_e)]}{\sigma(HH\nu_e\bar{\nu}_e)} = \begin{cases} 179\%, & \text{at } \sqrt{s} = 1.4 \text{ TeV,} \\ 92\%, & \text{at } \sqrt{s} = 3 \text{ TeV,} \end{cases} \quad (7.11)$$

where  $N_S$  is the number of  $e^+e^- \rightarrow HH\nu_e\bar{\nu}_e$  events passing the MVA event selection and  $N_B$  is the number of background events passing the MVA event selection. The result at  $\sqrt{s} = 3$  TeV combines both the hadronic and semi-leptonic decay sub-channels.

As previously stated, the double Higgs production cross section is sensitive to the Higgs trilinear self coupling  $g_{HHH}$ . The relative uncertainty on the coupling can be related

$\sqrt{s} = 3 \text{ TeV}$	N	$\varepsilon_{\text{presel}}$	$\varepsilon_{\text{MVA}}$	$N_{\text{MVA}}$
$e^+e^- \rightarrow HH\nu_e\bar{\nu}_e \rightarrow b\bar{b}W^+W^-\nu_e\bar{\nu}_e, \text{ semi-leptonic}$	96.8	44.6%	21.9%	13.11
$e^+e^- \rightarrow HH\nu_e\bar{\nu}_e \rightarrow b\bar{b}b\bar{b}\nu_e\bar{\nu}_e$	355.0	13.3%	10.9%	5.38
$e^+e^- \rightarrow HH\nu_e\bar{\nu}_e \rightarrow \text{other}$	724.2	13.1%	13.6%	12.75
$e^+e^- \rightarrow q\bar{q}H\nu\bar{\nu}$	6120	7.4%	13.7%	62.63
$e^+e^- \rightarrow c\bar{c}H\nu\bar{\nu}$	2300	6.3%	12.1%	17.10
$e^+e^- \rightarrow b\bar{b}H\nu\bar{\nu}$	3560	15.9%	5.1%	18.03
$e^+e^- \rightarrow qqqq$	1093000	0.6%	0.2%	15.04
$e^+e^- \rightarrow qqqq\ell\ell$	338600	1.0%	0.06%	1.85
$e^+e^- \rightarrow qqqq\ell\nu$	213200	27.6%	0.5%	270.33
$e^+e^- \rightarrow qqqq\nu\bar{\nu}$	143000	1.9%	1.6%	43.78
$e^+e^- \rightarrow qq$	5897800	0.4%	0.3%	60.82
$e^+e^- \rightarrow qq\ell\nu$	11121800	0.3%	0.08%	21.24
$e^+e^- \rightarrow qq\ell\ell$	6639200	0.6%	0.2%	84.14
$e^+e^- \rightarrow qq\nu\nu$	2635000	0.4%	0.9%	92.55
$e^\pm\gamma(\text{BS}) \rightarrow e^\pm qqqq$	4007354	1.2%	-	-
$e^\pm\gamma(\text{EPA}) \rightarrow e^\pm qqqq$	1151200	1.1%	-	-
$e^\pm\gamma(\text{BS}) \rightarrow \nu qqqq$	829184	3.6%	1.5%	452.45
$e^\pm\gamma(\text{EPA}) \rightarrow \nu qqqq$	216800	11.0%	0.9%	200.65
$e^\pm\gamma(\text{BS}) \rightarrow qqH\nu$	185018	7.9%	10.4%	1521.93
$e^-\gamma(\text{EPA}) \rightarrow qqH\nu$	46800	22.8%	7.1%	750.85
$\gamma(\text{BS})\gamma(\text{BS}) \rightarrow qqqq$	18009414	0.4%	-	-
$\gamma(\text{BS})\gamma(\text{EPA}) \rightarrow qqqq$	3824548	1.0%	-	-
$\gamma(\text{EPA})\gamma(\text{BS}) \rightarrow qqqq$	3828498	1.0%	0.08%	28.85
$\gamma(\text{EPA})\gamma(\text{EPA}) \rightarrow qqqq$	805400	1.1%	-	-

semi-leptonic  $W^+W^-$  decay of  $HH \rightarrow b\bar{b}W^+W^-$

**Table 7.17:** List of signal and background events with selection efficiency and number of events at  $\sqrt{s} = 3 \text{ TeV}$  for semi-leptonic  $W^+W^-$  decay of  $HH \rightarrow b\bar{b}W^+W^-$  analysis, assuming a luminosity of  $2000 \text{ fb}^{-1}$ . The number of events (N), the selection efficiencies of pre-selection cuts ( $\varepsilon_{\text{presel}}$ ), the selection efficiencies of MVA after pre-selection cuts ( $\varepsilon_{\text{MVA}}$ ), and the number of events after MVA ( $N_{\text{MVA}}$ ) are shown. - represents a number less than 0.01. q can be u, d, s, b or t. Unless specified, q,  $\ell$  and  $\nu$  represent either particles or the corresponding anti-particles.  $\gamma$  (BS) represents a real photon from beamstrahlung (BS).  $\gamma$  (EPA) represents a “quasi-real” photon, simulated with the Equivalent Photon Approximation.

Channel	$N_S$	$N_B$	$N_S/\sqrt{N_S + N_B}$
HH $\rightarrow b\bar{b}W^+W^-$ , hadronic, $\sqrt{s} = 1.4 \text{ TeV}$	1.79	8.41	0.56
HH $\rightarrow b\bar{b}W^+W^-$ , hadronic, $\sqrt{s} = 3 \text{ TeV}$	15.45	242.28	0.96
HH $\rightarrow b\bar{b}W^+W^-$ , semi-leptonic, $\sqrt{s} = 3 \text{ TeV}$	31.24	3612.39	0.52

**Table 7.18:** Number of signal and background events, and significance after MVA for all HH  $\rightarrow b\bar{b}W^+W^-$  analyses.

to the uncertainty on the coupling via:

$$\frac{\Delta g_{\text{HHH}}}{g_{\text{HHH}}} \approx \kappa \cdot \frac{\Delta [\sigma (\text{HH}\nu_e\bar{\nu}_e)]}{\sigma (\text{HH}\nu_e\bar{\nu}_e)}, \quad (7.12)$$

$\kappa$  can be extracted by varying the  $g_{\text{HHH}}$  and parameterising the cross section. Figure 7.19 shows the cross sections as a function of the coupling at generator level for  $\sqrt{s} = 1.4 \text{ TeV}$  and  $\sqrt{s} = 3 \text{ TeV}$  [24]. The negative gradient indicates that the Feynman diagram that is sensitive to the  $g_{\text{HHH}}$  experiences destructive interferences with other SM Feynman diagrams. At the SM  $g_{\text{HHH}}$  value, the  $\kappa$  is 1.22 and 1.47 at  $\sqrt{s} = 1.4 \text{ TeV}$  and 3 TeV respectively.

The uncertainty on measurement of the Higgs trilinear self coupling,  $g_{\text{HHH}}$ , from  $e^+e^- \rightarrow \text{HH}\nu_e\bar{\nu}_e \rightarrow b\bar{b}W^+W^-\nu_e\bar{\nu}_e$  analysis is obtained via equation 7.12:

$$\frac{\Delta g_{\text{HHH}}}{g_{\text{HHH}}} = \begin{cases} 218\%, & \text{at } \sqrt{s} = 1.4 \text{ TeV}, \\ 135\%, & \text{at } \sqrt{s} = 3 \text{ TeV}. \end{cases} \quad (7.13)$$

Since the Feynman diagrams for the double Higgs boson productions include t-channel WW-fusion, the cross section can be enhanced by using polarised electron beam. For  $P(e^-) = 80\%$ , the uncertainty of  $g_{\text{HHH}}$  via equation 7.12 becomes:

$$\frac{\Delta g_{\text{HHH}}}{g_{\text{HHH}}} = \begin{cases} 163\%, & \text{at } \sqrt{s} = 1.4 \text{ TeV}, \\ 97\%, & \text{at } \sqrt{s} = 3 \text{ TeV}. \end{cases} \quad (7.14)$$

When both  $\sqrt{s}$  are combined, the statistical precision on  $\lambda$  increases to 99% for the unpolarised beam, and 87% for the polarised beam with  $P(e^-) = 80\%$ .

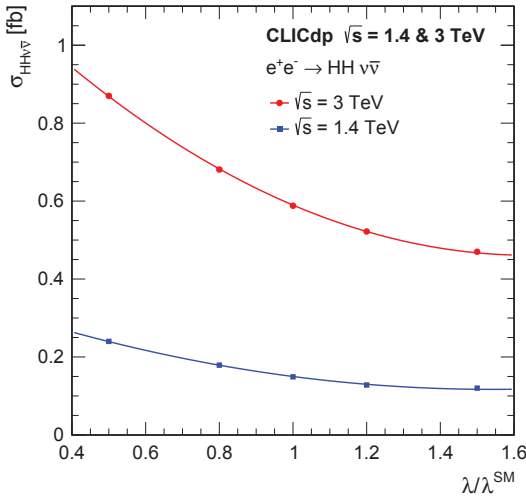


**Figure 7.19:** Cross section for the  $e^+e^- \rightarrow HH\nu_e\bar{\nu}_e$  process as a function of the ratio  $\lambda/\lambda_{SM}$  at  $\sqrt{s} = 1.4 \text{ TeV}$  and  $3 \text{ TeV}$ , taken from [24]. Here  $\lambda$  is the Higgs trilinear self coupling,  $g_{HHH}$ .

## 7.14. Combined results

When  $HH \rightarrow b\bar{b}W^+W^-$  and  $HH \rightarrow b\bar{b}b\bar{b}$  sub-channels are combined, the expected precisions on the cross sections are:

$$\frac{\Delta [\sigma(HH\nu_e\bar{\nu}_e)]}{\sigma(HH\nu_e\bar{\nu}_e)} = \begin{cases} 44\%, & \text{at } \sqrt{s} = 1.4 \text{ TeV}, \\ 20\%, & \text{at } \sqrt{s} = 3 \text{ TeV}, \end{cases} \quad (7.15)$$

This translates to the uncertainty on the Higgs trilinear self coupling  $g_{HHH}$ , via equation 7.12, without electron polarisation:

$$\frac{\Delta g_{HHH}}{g_{HHH}} = \begin{cases} 54\%, & \text{at } \sqrt{s} = 1.4 \text{ TeV}, \\ 29\%, & \text{at } \sqrt{s} = 3 \text{ TeV}. \end{cases} \quad (7.16)$$

## 7.15. Simultaneous couplings extraction

As stated in the beginning of the chapter the study of the double Higgs production via  $W^+W^-$  fusion can probe the Higgs trilinear self coupling,  $g_{HHH}$  and quartic coupling,  $g_{WWHH}$ . Therefore, a simultaneous extraction on the coupling uncertainty can be performed by extending the method in the previous sections. Once a relationship between

$g_{\text{HHH}}$ ,  $g_{\text{WWHH}}$  and difference in kinematic variable distributions is established, a contour of the uncertainty of the measurements of  $g_{\text{HHH}}$  and  $g_{\text{WWHH}}$  in two-dimensional phase space can be obtained.

This two dimensional template fitting is performed at  $\sqrt{s} = 3 \text{ TeV}$ , as the precision at  $\sqrt{s} = 1.4 \text{ TeV}$  is too low to support such a fitting. The integrated luminosity is assumed to be  $3000 \text{ fb}^{-1}$  to reflect the updated CLIC running scenario.

The normalised cross section of the  $e^+e^- \rightarrow HH\nu_e\bar{\nu}_e$  as a function of  $g_{\text{HHH}}$  and  $g_{\text{WWHH}}$  is shown in figure 7.20. The SM cross section is normalised to 1. Around the SM coupling value, the cross section increases with the decrease of  $g_{\text{HHH}}$  and with the increase of  $g_{\text{WWHH}}$ . Hence the cross sections along the anti-diagonal are nearly constant, which would be difficult to precisely determine the statistical uncertainty on the coupling measurements.

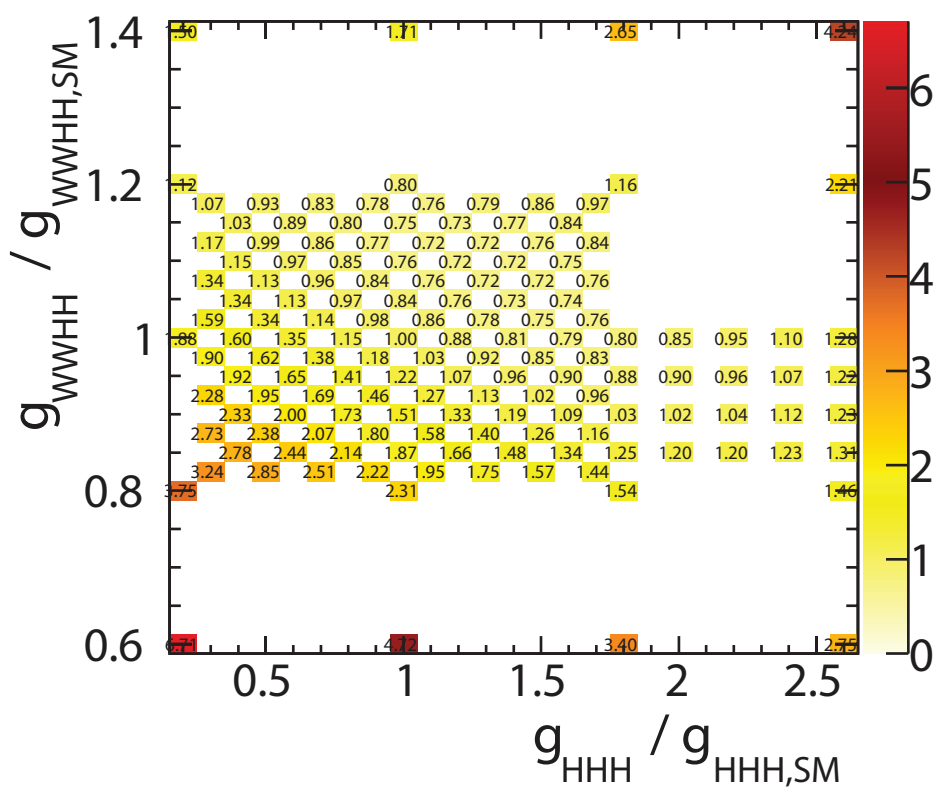
To determine the uncertainty on the coupling measurements, the variables proposed in the generator-level study in section 2.8 are used: the invariant mass of the two Higgs system,  $m_{\text{HH}}$ , and the scalar sum of the two Higgs transverse momentum,  $H_T$ .

Simulated events with non-SM couplings are generated and reconstructed. These events went through the analysis chain discussed in this chapter with the same cuts and the same MVA classifier. Figure 7.21 shows the signal significance of the double Higgs events with hadronic  $W^+W^-$  decay of  $HH \rightarrow b\bar{b}W^+W^-$  sub-channel as a function of  $g_{\text{HHH}}$  and  $g_{\text{WWHH}}$ .

The selected events are divided into 8 kinematic bins. Two bins in  $H_T$  are obtained by dividing the  $H_T$  distribution at 200 GeV. Four bins in  $m_{\text{HH}}$  are obtained by dividing the  $m_{\text{HH}}$  distribution at 400, 560, and 720 GeV. A  $\chi^2$  function is constructed to access the difference of the  $m_{\text{HH}}$  and  $H_T$  distributions for non-SM coupling comparing to SM coupling sample, defined as:

$$\chi^2 = \sum_i^{bins} \frac{(N_i - N_{i,observed})^2}{N_i}, \quad (7.17)$$

where  $N_i$  is the number of event expected in a kinematic bin  $i$  for a non-SM coupling sample; and  $N_{i,observed}$  is the number of event observed in a kinematic bin  $i$ . Here the observed set is the SM coupling sample. The expression is summed over all kinematic bins. By construction, the SM coupling point has a  $\chi^2$  of 0. Figure 7.22 shows the  $\chi^2$  as a function of  $g_{\text{HHH}}$  and  $g_{\text{WWHH}}$  for two sub-channels; hadronic  $W^+W^-$  decay of



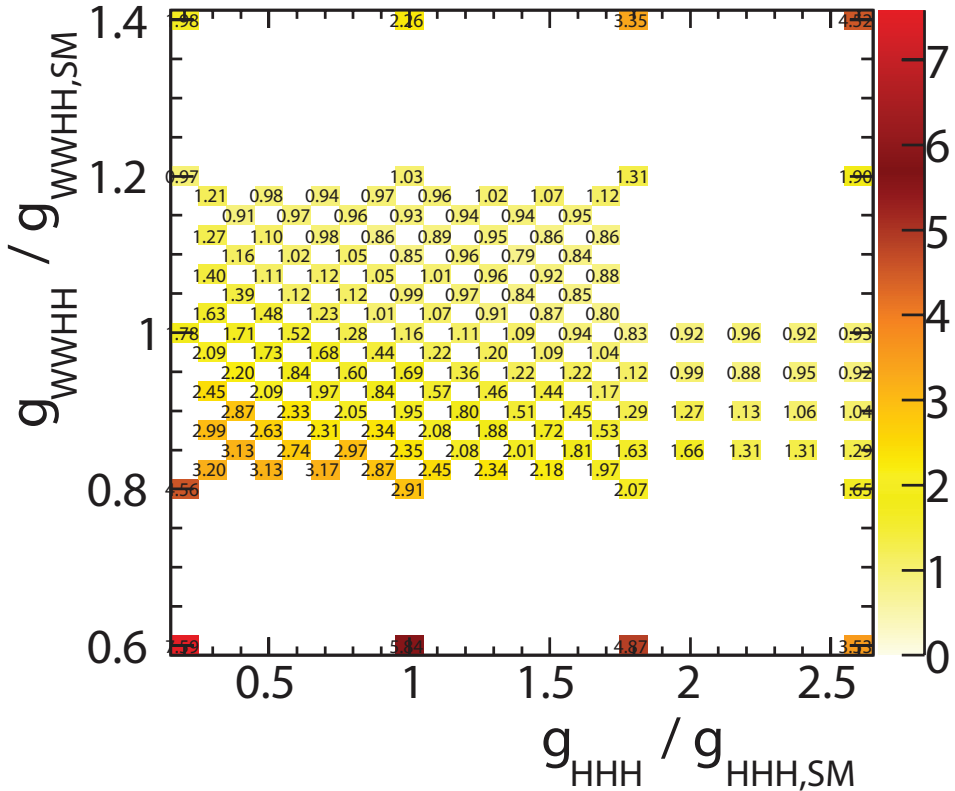


**Figure 7.21:** The significance for the  $e^+e^- \rightarrow HH\nu_e\bar{\nu}_e$  process as a function of the  $g_{HHH}/g_{HHH,SM}$  and  $g_{WWHH}/g_{WWHH,SM}$  at  $\sqrt{s} = 3$  TeV, using sub-channel hadronic  $W^+W^-$  decay of  $HH \rightarrow b\bar{b}W^+W^-$ , assuming an integrated luminosity of  $3000 \text{ fb}^{-1}$ .

$HH \rightarrow b\bar{b}W^+W^-$  and  $HH \rightarrow b\bar{b}b\bar{b}$ . The  $\chi^2$  values for the  $HH \rightarrow b\bar{b}b\bar{b}$  sub-channel are larger as the  $HH \rightarrow b\bar{b}b\bar{b}$  is more sensitive to the couplings.

Two sub-channels, hadronic  $W^+W^-$  decay of  $HH \rightarrow b\bar{b}W^+W^-$  and  $HH \rightarrow b\bar{b}b\bar{b}$ , are combined to increase the statistical precision on the coupling measurements. To avoid statistical fluctuations in the sample, a toy MC experiment is performed. The SM coupling samples are treated as a data template set. 100000 data sets are generated by fluctuating the event number in each kinematic bin in the data template set according to Poisson distribution. The  $\chi^2$  is performed and summed using these generated data sets as the observed data. The summed  $\chi^2$  is then averaged over the number of data sets (100000) and normalised such that the  $\chi^2$  at the SM coupling is 0. Since only the difference between the non-SM and SM  $\chi^2$  is used for the coupling measurements, the normalisation does not affect the measurements and helps to ease the visualisation. Figure 7.23 shows the normalised  $\chi^2$  after averaging over the toy MC experiments as

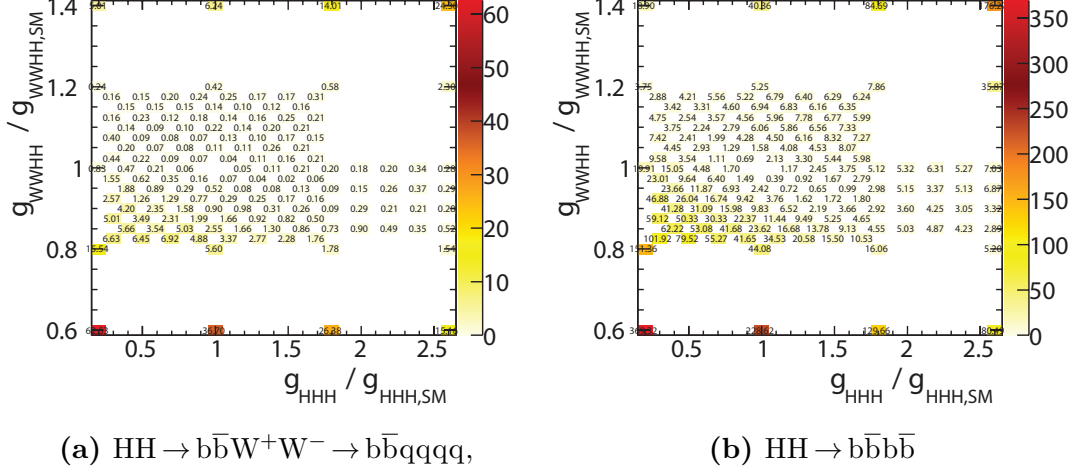


**Figure 7.22:** The  $\chi^2$  for the  $e^+e^- \rightarrow HH\nu_e\bar{\nu}_e$  process as a function of the  $g_{\text{HHH}}/g_{\text{HHH},\text{SM}}$  and  $g_{\text{WWHH}}/g_{\text{WWHH},\text{SM}}$  at  $\sqrt{s} = 3 \text{ TeV}$ , using a) hadronic  $W^+W^-$  decay of  $\text{HH} \rightarrow b\bar{b}W^+W^-$ , b) and  $\text{HH} \rightarrow b\bar{b}b\bar{b}$  sub-channel, assuming an integrated luminosity of  $3000 \text{ fb}^{-1}$ .

a function of  $g_{\text{HHH}}/g_{\text{HHH},\text{SM}}$  and  $g_{\text{WWHH}}/g_{\text{WWHH},\text{SM}}$ . The  $\chi^2$  changes slowly along the anti-diagonal which is similar to the cross section plot.

Since there are two couplings in this  $\chi^2$  surface, the degree of freedom for this fit is 2. A contour of 68% confidence ( $\chi^2 = 2.3$ ) can be drawn by interpolating between points on the surface. Figure 7.24 shows the contour. The counter can be sliced one dimensionally to extract the uncertainty of the measurements of one coupling for a given value of the other coupling. For example:

$$\frac{\Delta g_{\text{WWHH}}}{g_{\text{WWHH}}} \simeq 4.9\% \text{ for } g_{\text{HHH}} = g_{\text{HHH},\text{SM}} \quad (7.18)$$

$$\frac{\Delta g_{\text{HHH}}}{g_{\text{HHH}}} \simeq 29\% \text{ for } g_{\text{WWHH}} = g_{\text{WWHH},\text{SM}} \quad (7.19)$$

The statistical precisions on  $g_{\text{WWHH}}$  and  $g_{\text{HHH}}$  are much better at the CLIC than at the current LHC or at the high luminosity upgraded LHC [21].

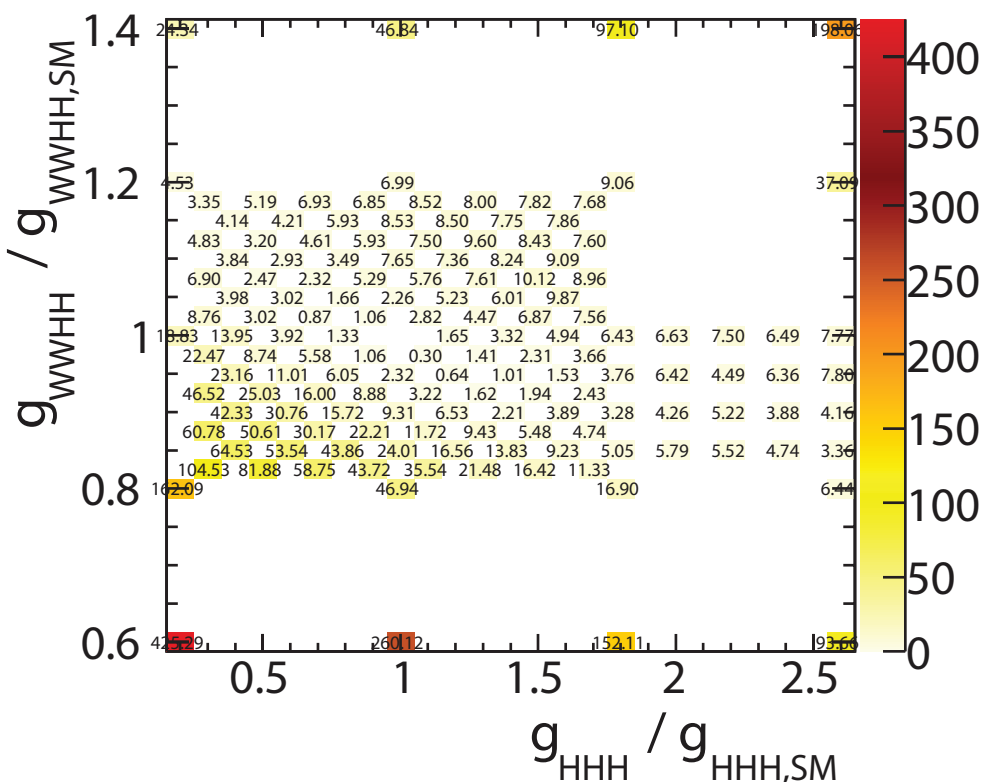


**Figure 7.23:** Normalised  $\chi^2$ , after averaging the toy MC experiments, as a function of  $g_{\text{HHH}}/g_{\text{HHH,SM}}$  and  $g_{\text{WWWH}}/g_{\text{WWWH,SM}}$ , combining hadronic decay  $\text{HH} \rightarrow b\bar{b}W^+W^-$  and  $\text{HH} \rightarrow b\bar{b}b\bar{b}$  sub-channels, assuming an integrated luminosity of  $3000 \text{ fb}^{-1}$ .

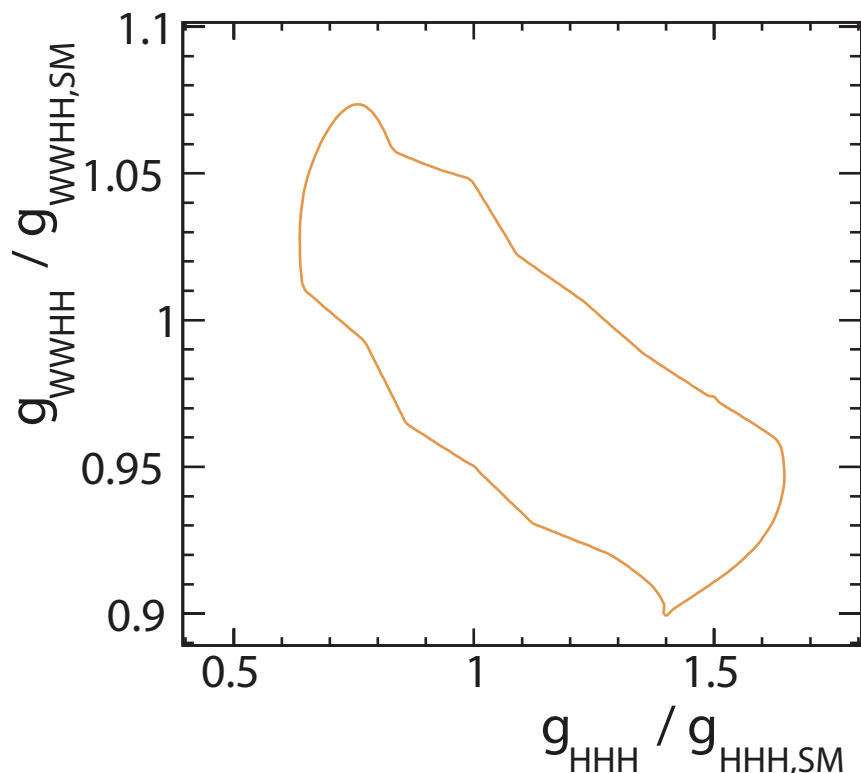


**Figure 7.24:** Contour plot of 68% confidence ( $\chi^2 = 2.3$ ) , after averaging the toy MC experiments, as a function of  $g_{H\bar{H}H} / g_{H\bar{H}H,SM}$  and  $g_{WW\bar{W}\bar{H}} / g_{WW\bar{W}\bar{H},SM}$ , combining hadronic  $W^+W^-$  decay of  $H\bar{H} \rightarrow b\bar{b}W^+W^-$  and  $H\bar{H} \rightarrow b\bar{b}b\bar{b}$  sub-channels, assuming an integrated luminosity of  $3000 \text{ fb}^{-1}$ .



# Chapter 8.

## Summary

*'If you know the enemy and know yourself, you need not fear the result of a hundred battles.'*

— Sun Tzu, 544 BC - 496 BC

This chapter summarises key results presented in analyses in previous chapters. In chapter 5, a set of photon reconstruction algorithms developed in PandoraPFA are presented. The photon fragments produced during the event reconstruction have been greatly reduced. The photon separation power and the jet energy resolution have improved, as a result of a better photon reconstruction.

For the single photon reconstruction, the efficiency is above 98% for photons with energies above 2GeV, and above 99.5% for photons with energies above 100 GeV. For the photon fragment reduction using a 500 - 50 GeV photons pair sample, the average number of photons and particles beyond 20 mm apart are both less than 2.05, where the true value is 2. For the photon separation power, 500 - 500 GeV photon pair and 10 - 10 GeV photon pair start to be resolved at 6 mm apart, which is about 1 ECAL cell. For photon pairs with different energies, for example 500 - 50 GeV pair and 100 - 10 GeV pair, start to be resolved at 10 mm apart, which is about 2 ECAL cells. At 20 mm apart, two photons in 500 - 500 GeV pair are fully resolved, where approximately 60% of two photons in 10 - 10 GeV pair are resolved.

In chapter 6, a high classification rate of the tau lepton seven major decay modes is achieved. The classification is applied to different ECAL cell sizes with different centre-of-mass energies. The tau hadronic decay correct classification efficiency,  $\varepsilon_{had}$ , is

used as the performance metric. At  $\sqrt{s} = 100 \text{ GeV}$ , the  $\varepsilon_{had}$  decreases from 94% at 3 mm cell size, to 91% at 20 mm cell size. Most significant decrease in the  $\varepsilon_{had}$  occurs at  $\sqrt{s} = 500 \text{ GeV}$ , where the  $\varepsilon_{had}$  decreases from 92% at 3 mm cell size, to 78% at 20 mm cell size. The increase in ECAL cell sizes has a larger impact in tau decay classification at high centre-of-mass energies. With decay products spatially close at high centre-of-mass energies, it is more beneficial to have a smaller ECAL cell size to reconstruct individual particle.

With the developed tau decay mode classification, a proof-of-principle analysis shows the tau pair polarisation correlations with  $Z \rightarrow \tau^+ \tau^-$  decay where  $\tau^- \rightarrow \pi^- \nu_\tau$  can be observed with ILD detector model. A good match of the tau pair polarisation correlations between the reconstruction and the Monte Carlo simulation is also achieved. With a similar study of  $H \rightarrow \tau^+ \tau^-$ , the tau polarisation correlations can be used to as a signature to identify Higgs boson from Z boson.

In chapter 7, the analyses of the  $e^+ e^- \rightarrow HH\nu_e \bar{\nu}_e \rightarrow b\bar{b}W^+W^-\nu_e \bar{\nu}_e$  channel for the Compact Linear Collider at  $\sqrt{s} = 1.4 \text{ TeV}$  and  $\sqrt{s} = 3 \text{ TeV}$  are performed. The significance of the signal events are 0.56 and 1.09, assuming an integrated luminosity of  $1500 fb^{-1}$  and  $2000 fb^{-1}$ , for  $\sqrt{s} = 1.4 \text{ TeV}$  and  $\sqrt{s} = 3 \text{ TeV}$  respectively. The uncertainty on measurement of the Higgs trilinear self coupling,  $g_{HHH}$ , from  $e^+ e^- \rightarrow HH\nu_e \bar{\nu}_e \rightarrow b\bar{b}W^+W^-\nu_e \bar{\nu}_e$  analysis is obtained:

$$\frac{\Delta g_{HHH}}{g_{HHH}} = \begin{cases} 218\%, & \text{at } \sqrt{s} = 1.4 \text{ TeV}, \\ 135\%, & \text{at } \sqrt{s} = 3 \text{ TeV}. \end{cases} \quad (8.1)$$

When analysis at both  $HH \rightarrow b\bar{b}W^+W^-$  and  $HH \rightarrow b\bar{b}b\bar{b}$  sub-channels are combined at  $\sqrt{s} = 3 \text{ TeV}$  to improve the measurement, the simultaneous extraction of the uncertainty on the measurement of the  $g_{HHH}$  and  $g_{WWHH}$  yields:

$$\frac{\Delta g_{WWHH}}{g_{WWHH}} \simeq 4.9\% \text{ for } g_{HHH} = g_{HHH,SM} \quad (8.2)$$

$$\frac{\Delta g_{HHH}}{g_{HHH}} \simeq 29\% \text{ for } g_{WWHH} = g_{WWHH,SM} \quad (8.3)$$

## Appendix A.

# Double Higgs Boson Production Analysis

*'I was an adventurer like you, then I took an arrow in the knee.'*

— The town guard, Skyrim, 2011

Here are extra tables and plots for the chapter 7.

### A.1. Hadronic decay at $\sqrt{s} = 3 \text{ TeV}$ analysis

$\sqrt{s} = 3 \text{ TeV}$	N	Lepton evto	$b\bar{b}W^+W^- / b\bar{b}W^+W^-$ separation	Valid jet Pairing
$e^+e^- \rightarrow HH\nu_e\bar{\nu}_e \rightarrow b\bar{b}W^+W^-\nu_e\bar{\nu}_e$ , hadronic	146.0	80.9%	72.8%	72.1%
$e^+e^- \rightarrow HH\nu_e\bar{\nu}_e \rightarrow b\bar{b}b\bar{b}\nu_e\bar{\nu}_e$	355.0	83.5%	20.5%	20.5%
$e^+e^- \rightarrow HH\nu_e\bar{\nu}_e \rightarrow \text{other}$	675.0	40.1%	34.3%	20.5%
$e^+e^- \rightarrow q\bar{q}H\nu\bar{\nu}$	6120	67.7%	61.9%	61.9%
$e^+e^- \rightarrow c\bar{c}H\nu\bar{\nu}$	2300	69.1%	53.0%	48.8%
$e^+e^- \rightarrow b\bar{b}H\nu\bar{\nu}$	3560	70.1%	30.9%	30.6%
$e^+e^- \rightarrow qqqq$	1093000	62.4%	44.9%	34.9%
$e^+e^- \rightarrow qqqq\ell\ell$	338600	21.4%	19.6%	13.3%
$e^+e^- \rightarrow qqqq\ell\nu$	213200	23.3%	19.5%	16.3%
$e^+e^- \rightarrow qqqq\nu\bar{\nu}$	143000	80.7%	71.4%	50.7%
$e^+e^- \rightarrow qq$	5897800	72.9%	63.9%	55.4%
$e^+e^- \rightarrow qq\ell\nu$	11121800	34.0%	24.7%	20.5%
$e^+e^- \rightarrow qq\ell\ell$	6639200	43.1%	41.7%	37.0%
$e^+e^- \rightarrow qq\nu\nu$	2635000	84.6%	63.8%	53.2%
$e^\pm\gamma(\text{BS}) \rightarrow e^\pm qqqq$	4007354	31.0%	28.2%	21.1%
$e^\pm\gamma(\text{EPA}) \rightarrow e^\pm qqqq$	1151200	15.9%	14.5%	10.9%
$e^\pm\gamma(\text{BS}) \rightarrow \nu qqqq$	829184	78.3%	68.8%	53.3%
$e^\pm\gamma(\text{EPA}) \rightarrow \nu qqqq$	216800	39.6%	35.0%	26.9%
$e^\pm\gamma(\text{BS}) \rightarrow qqH\nu$	185018.0	64.0%	55.4%	49.8%
$e^\pm\gamma(\text{EPA}) \rightarrow qqH\nu$	46800	32.9%	28.8%	25.9%
$\gamma(\text{BS})\gamma(\text{BS}) \rightarrow qqqq$	18009414	71.6%	65.5%	49.4%
$\gamma(\text{BS})\gamma(\text{EPA}) \rightarrow qqqq$	3824548	44.3%	40.6%	30.6%
$\gamma(\text{EPA})\gamma(\text{BS}) \rightarrow qqqq$	3828498	44.3%	40.7%	30.7%
$\gamma(\text{EPA})\gamma(\text{EPA}) \rightarrow qqqq$	805400	29.0%	26.7%	20.1%

**Table A.1:** The table shows the expected number of events, before cuts and after successive cuts: the lepton veto,  $HH \rightarrow b\bar{b}W^+W^- / HH \rightarrow bbbb$  separation, and valid jet pairing, for the signal and background events at  $\sqrt{s} = 3 \text{ TeV}$ , assuming an integrated luminosity of  $2000 \text{ fb}^{-1}$ . q can be u, d, s, b or t. Unless specified, q,  $\ell$  and  $\nu$  represent either particles or the corresponding anti-particles.

Channel	$m_{\text{HH}} > 150 \text{ GeV}$	$B_1 > 0.7$
$e^+e^- \rightarrow HH\nu_e\bar{\nu}_e \rightarrow b\bar{b}W^+W^-\nu_e\bar{\nu}_e$ , hadronic	71.7%	61.8%
$e^+e^- \rightarrow HH\nu_e\bar{\nu}_e \rightarrow b\bar{b}b\bar{b}\nu_e\bar{\nu}_e$	20.2%	18.8%
$e^+e^- \rightarrow HH\nu_e\bar{\nu}_e \rightarrow \text{other}$	30.2%	20.0%
$e^+e^- \rightarrow q\bar{q}H\nu\bar{\nu}$	53.1%	36.0%
$e^+e^- \rightarrow c\bar{c}H\nu\bar{\nu}$	43.8%	26.3%
$e^+e^- \rightarrow b\bar{b}H\nu\bar{\nu}$	29.6%	25.9%
$e^+e^- \rightarrow qqqq$	26.5%	1.7%
$e^+e^- \rightarrow qqqq\ell\ell$	12.8%	0.7%
$e^+e^- \rightarrow qqqq\ell\nu$	16.0%	7.9%
$e^+e^- \rightarrow qqqq\nu\bar{\nu}$	49.7%	9.0%
$e^+e^- \rightarrow qq$	8.3%	1.4%
$e^+e^- \rightarrow qq\ell\nu$	6.0%	0.1%
$e^+e^- \rightarrow qq\ell\ell$	1.9%	0.4%
$e^+e^- \rightarrow qq\nu\nu$	16.6%	3.1%
$e^\pm\gamma(\text{BS}) \rightarrow e^\pm qqqq$	19.4%	0.7%
$e^\pm\gamma(\text{EPA}) \rightarrow e^\pm qqqq$	9.9%	0.4%
$e^\pm\gamma(\text{BS}) \rightarrow \nu qqqq$	51.3%	16.4%
$e^\pm\gamma(\text{EPA}) \rightarrow \nu qqqq$	26.0%	7.7%
$e^\pm\gamma(\text{BS}) \rightarrow qqH\nu$	47.9%	30.3%
$e^-\gamma(\text{EPA}) \rightarrow qqH\nu$	25.0%	15.8%
$\gamma(\text{BS})\gamma(\text{BS}) \rightarrow qqqq$	44.5%	1.7%
$\gamma(\text{BS})\gamma(\text{EPA}) \rightarrow qqqq$	27.4%	1.0%
$\gamma(\text{EPA})\gamma(\text{BS}) \rightarrow qqqq$	27.5%	1.0%
$\gamma(\text{EPA})\gamma(\text{EPA}) \rightarrow qqqq$	18.0%	0.7%

**Table A.2:** The table shows the expected number of events after successive cuts: invariant mass of the two Higgs system  $> 150 \text{ GeV}$ , and the highest b-jet tag value  $> 0.7$ . All cuts include the lepton veto,  $HH \rightarrow b\bar{b}W^+W^- / HH \rightarrow b\bar{b}b\bar{b}$  separation, and valid jet pairing. The table shows for the signal and background events at  $\sqrt{s} = 3 \text{ TeV}$ , assuming an integrated luminosity of  $2000 \text{ fb}^{-1}$ .  $q$  can be  $u, d, s, b$  or  $t$ . Unless specified,  $q, \ell$  and  $\nu$  represent either particles or the corresponding anti-particles.



# Colophon

This thesis was made in L<sup>A</sup>T<sub>E</sub>X 2 <sub>$\varepsilon$</sub>  using the “hepthesis” class [97].



# Bibliography

- [1] J. Brau *et al.*, (2007).
- [2] L. Linssen, A. Miyamoto, M. Stanitzki, and H. Weerts, (2012), 1202.5940.
- [3] ATLAS Collaboration, G. Aad *et al.*, Phys.Lett. **B716**, 1 (2012), 1207.7214.
- [4] CMS Collaboration, S. Chatrchyan *et al.*, Phys.Lett. **B716**, 30 (2012), 1207.7235.
- [5] CLIC Detector and Physics Study, H. Abramowicz *et al.*, Physics at the CLIC e+e- Linear Collider – Input to the Snowmass process 2013, in *Proceedings, 2013 Community Summer Study on the Future of U.S. Particle Physics: Snowmass on the Mississippi (CSS2013): Minneapolis, MN, USA, July 29-August 6, 2013*, 2013, 1307.5288.
- [6] C. Patrignani and P. D. Group, Chinese Physics C **40**, 100001 (2016).
- [7] M. Thomson, *Modern particle physics* (Cambridge University Press, New York, 2013).
- [8] D. Tong, Lectures on quantum field theory, 2006.
- [9] B. Gripaios, Lectures on gauge field theory, 2017.
- [10] SLD Electroweak Group, DELPHI, ALEPH, SLD, SLD Heavy Flavour Group, OPAL, LEP Electroweak Working Group, L3, S. Schael *et al.*, Phys. Rept. **427**, 257 (2006), hep-ex/0509008.
- [11] D0, S. Abachi *et al.*, Phys. Rev. Lett. **74**, 2632 (1995), hep-ex/9503003.
- [12] DONUT, K. Kodama *et al.*, Phys. Lett. **B504**, 218 (2001), hep-ex/0012035.
- [13] D. B. Kaplan and H. Georgi, Phys. Lett. **B136**, 183 (1984).
- [14] W. D. Goldberger, B. Grinstein, and W. Skiba, Phys. Rev. Lett. **100**, 111802 (2008), 0708.1463.

- [15] M. Peskin and D. Schroeder, *An Introduction to Quantum Field Theory*Advanced book classics (Avalon Publishing, 1995).
- [16] Y. Nambu, Phys. Rev. **117**, 648 (1960).
- [17] J. Goldstone, Nuovo Cim. **19**, 154 (1961).
- [18] S. Weinberg, Phys. Rev. Lett. **19**, 1264 (1967).
- [19] D. Rainwater, Searching for the Higgs boson, in *Proceedings of Theoretical Advanced Study Institute in Elementary Particle Physics : Exploring New Frontiers Using Colliders and Neutrinos (TASI 2006): Boulder, Colorado, June 4-30, 2006*, pp. 435–536, 2007, hep-ph/0702124.
- [20] G. F. Giudice, C. Grojean, A. Pomarol, and R. Rattazzi, JHEP **06**, 045 (2007), hep-ph/0703164.
- [21] R. Contino, C. Grojean, M. Moretti, F. Piccinini, and R. Rattazzi, JHEP **05**, 089 (2010), 1002.1011.
- [22] R. Contino, C. Grojean, D. Pappadopulo, R. Rattazzi, and A. Thamm, JHEP **02**, 006 (2014), 1309.7038.
- [23] V. Barger, T. Han, P. Langacker, B. McElrath, and P. Zerwas, Phys. Rev. **D67**, 115001 (2003), hep-ph/0301097.
- [24] H. Abramowicz *et al.*, (2016), 1608.07538.
- [25] B. K. Bullock, K. Hagiwara, and A. D. Martin, Phys. Lett. **B273**, 501 (1991).
- [26] Y.-S. Tsai, Phys. Rev. **D4**, 2821 (1971), [Erratum: Phys. Rev.D13,771(1976)].
- [27] Linear Collider ILD Concept Group -, T. Abe *et al.*, (2010), 1006.3396.
- [28] SiD, H. Aihara *et al.*, (2010).
- [29] H. Baer *et al.*, (2013), 1306.6352.
- [30] M. Aicheler *et al.*, (2012).
- [31] O. S. Bruning *et al.*, (2004).
- [32] R. Placakyte, Parton Distribution Functions, in *Proceedings, 31st International Conference on Physics in collisions (PIC 2011): Vancouver, Canada, August 28-September 1, 2011*, 2011, 1111.5452.

- [33] M. Thomson, Eur. Phys. J. **C33**, S689 (2004).
- [34] M. Thomson, Nucl.Instrum.Meth. **A611**, 25 (2009), 0907.3577.
- [35] H. Abramowicz *et al.*, (2013), 1306.6329.
- [36] I. G. Knowles and G. D. Lafferty, J. Phys. **G23**, 731 (1997), hep-ph/9705217.
- [37] M. Green, *Electron-Positron Physics at the Z*Studies in high energy physics, cosmology, and gravitation (Taylor & Francis, 1998).
- [38] J. S. Marshall, A. Míznnich, and M. A. Thomson, Nucl. Instrum. Meth. **A700**, 153 (2013), 1209.4039.
- [39] P. Mora de Freitas and H. Videau, p. 623 (2002).
- [40] A. Vogel, *Beam-induced backgrounds in detectors at the ILC*, PhD thesis, Hamburg U., 2008.
- [41] CALICE, M. Ramilli, J. Phys. Conf. Ser. **404**, 012050 (2012).
- [42] C. Adloff *et al.*, Nucl. Instrum. Meth. **A608**, 372 (2009).
- [43] CALICE, C. Adloff *et al.*, JINST **9**, P01004 (2014), 1311.3505.
- [44] CALICE, C. Adloff, (2011), 1105.0511.
- [45] B. Parker *et al.*, (2009).
- [46] CALICE, JINST **7**, P04015 (2012), 1201.1653.
- [47] C. Grah and A. Sapronov, Journal of Instrumentation **3**, P10004 (2008).
- [48] A. Sailer, *Radiation and Background Levels in a CLIC Detector Due to Beam-beam Effects: Optimisation of Detector Geometries and Technologies* (Humboldt Universität zu Berlin, Mathematisch-Naturwissenschaftliche Fakultät I, 2012).
- [49] W. Kilian, T. Ohl, and J. Reuter, European Physical Journal C **71** (2011).
- [50] M. Moretti, T. Ohl, and J. Reuter, p. 1981 (2001), hep-ph/0102195.
- [51] G. Altarelli, R. Kleiss, and C. Verzegnassi, editors, *Z PHYSICS AT LEP-1. PROCEEDINGS, WORKSHOP, GENEVA, SWITZERLAND, SEPTEMBER 4-5, 1989. VOL. 3: EVENT GENERATORS AND SOFTWARE*, 1989.
- [52] T. Sjostrand, (1995), hep-ph/9508391.

- [53] OPAL, G. Alexander *et al.*, Z. Phys. **C69**, 543 (1996).
- [54] S. Jadach, Z. Was, R. Decker, and J. H. Kuhn, Comput. Phys. Commun. **76**, 361 (1993).
- [55] GEANT4, S. Agostinelli *et al.*, Nucl.Instrum.Meth. **A506**, 250 (2003).
- [56] F. Gaede, Nucl. Instrum. Meth. **A559**, 177 (2006).
- [57] J. S. Marshall and M. A. Thomson, Eur. Phys. J. **C75**, 439 (2015), 1506.05348.
- [58] J. S. Marshall, Presentation on pandorapfa with lc reconstruction, [https://github.com/PandoraPFA/Documentation/blob/master/Pandora\\_LC\\_Reconstruction.pdf](https://github.com/PandoraPFA/Documentation/blob/master/Pandora_LC_Reconstruction.pdf), 2017.
- [59] A. Sailer, Luminosities for ee, eg, and gg interactions, [https://indico.cern.ch/event/233706/contributions/499053/attachments/390186/542711/130514\\_LuminosityNormalisation.pdf](https://indico.cern.ch/event/233706/contributions/499053/attachments/390186/542711/130514_LuminosityNormalisation.pdf), 2013.
- [60] D. Schulte, (1999).
- [61] T. Barklow, D. Dannheim, M. O. Sahin, and D. Schulte, (2012).
- [62] G. F. Sterman and S. Weinberg, Phys. Rev. Lett. **39**, 1436 (1977).
- [63] S. Moretti, L. Lonnblad, and T. Sjostrand, JHEP **08**, 001 (1998), hep-ph/9804296.
- [64] G. P. Salam, Eur. Phys. J. **C67**, 637 (2010), 0906.1833.
- [65] A. Ali and G. Kramer, Eur. Phys. J. **H36**, 245 (2011), 1012.2288.
- [66] M. Cacciari, G. P. Salam, and G. Soyez, Eur. Phys. J. **C72**, 1896 (2012), 1111.6097.
- [67] M. Cacciari and G. P. Salam, Phys. Lett. **B641**, 57 (2006), hep-ph/0512210.
- [68] S. Catani, Y. L. Dokshitzer, M. H. Seymour, and B. R. Webber, Nucl. Phys. **B406**, 187 (1993).
- [69] S. D. Ellis and D. E. Soper, Phys. Rev. **D48**, 3160 (1993), hep-ph/9305266.
- [70] S. Catani, Y. L. Dokshitzer, M. Olsson, G. Turnock, and B. R. Webber, Phys. Lett. **B269**, 432 (1991).
- [71] M. Battaglia and F. P., CERN Report No. LCD-Note-2010-006, 2010 (unpublished).
- [72] A. Hocker *et al.*, PoS **ACAT**, 040 (2007), physics/0703039.

- [73] Y. Freund and R. E. Schapire, Journal of Computer and System Sciences **55**, 119 (1997).
- [74] T. Hastie, R. Tibshirani, and J. Friedman, *The Elements of Statistical Learning: Data Mining, Inference, and Prediction, Second Edition* Springer Series in Statistics (Springer New York, 2009).
- [75] G. Kačarević, Prelection for  $h \rightarrow \gamma \gamma$  at 3 tev, <https://indico.cern.ch/event/577810/contributions/2485070/attachments/1424897/2185427/GoranKacarevic.pdf>, 2017.
- [76] B. Xu, Improvement of photon reconstruction in PandoraPFA, in *Proceedings, International Workshop on Future Linear Colliders (LCWS15): Whistler, B.C., Canada, November 02-06, 2015*, 2016, 1603.00013.
- [77] E. Segrè, *Nuclei and particles: an introduction to nuclear and subnuclear physics* (W. A. Benjamin, 1977).
- [78] E. Longo and I. Sestili, Nucl. Instrum. Meth. **128**, 283 (1975), [Erratum: Nucl. Instrum. Meth. 135, 587(1976)].
- [79] M. J. Berger and S. M. Seltzer, NASA Special Publication **3012** (1964).
- [80] B. Rossi, *High-energy Particles* Prentice-Hall physics series (New York, 1952).
- [81] ALEPH collaboration, S. Schael *et al.*, Phys. Rept. **421**, 191 (2005).
- [82] S. Berge, W. Bernreuther, and S. Kirchner, Phys. Rev. **D92**, 096012 (2015).
- [83] DELPHI collaboration, P. Abreu *et al.*, Phys. Lett. **B267**, 422 (1991).
- [84] E. Farhi, Phys. Rev. Lett. **39**, 1587 (1977).
- [85] F. Gaede and J. Engels, EUDET Report (2007).
- [86] TMVA Core Developer Team, J. Therhaag, AIP Conf.Proc. **1504**, 1013 (2009).
- [87] A. Duperrin, Eur. Phys. J. **C59**, 297 (2009), 0805.3624.
- [88] D. Lyth, Journal de Physique Colloques **35**, C2 (1974).
- [89] S. Dittmaier *et al.*, (2012), 1201.3084.
- [90] A. Míznnich, CERN Report No. LCD-Note-2010-009, 2010 (unpublished).

- [91] CLICdp, A. Sailer and A. Sapronov, (2017), 1702.06945.
- [92] S. Lukić, Forward electron tagging in the  $h \rightarrow \mu \mu$  analysis at 1.4 tev, <http://indico.cern.ch/event/262809/contributions/1595499/attachments/464689/643931/electronTagging.pdf>, 2013.
- [93] T. Suehara and T. Tanabe, Nucl. Instrum. Meth. **A808**, 109 (2016), 1506.08371.
- [94] LCFI, D. Bailey *et al.*, Nucl. Instrum. Meth. **A610**, 573 (2009), 0908.3019.
- [95] H. Aihara *et al.*, (2009), 0911.0006.
- [96] G. Hanson *et al.*, Phys. Rev. Lett. **35**, 1609 (1975).
- [97] A. Buckley, The heptesis L<sup>A</sup>T<sub>E</sub>X class.

# List of Figures

2.1.	SM Higgs boson decay width and branching ratios . . . . .	16
2.2.	The main Feynman diagrams for the leading-order $e^+e^- \rightarrow HH\nu_e\bar{\nu}_e$ processes. . . . .	17
2.5.	Two-dimensional distribution of $Z \rightarrow \tau^+\tau^-$ and $H \rightarrow \tau^+\tau^-$ . . . . .	23
3.1.	Schematic layout of the International Linear Collider, indicating all the major subsystems (not to scale), taken from [29]. . . . .	26
3.2.	International Large Detector and the Silicon Detector for the International Linear Collider. . . . .	26
3.3.	A layout of the Compact Linear Collider at the final stage of a centre-of-mass of energy of 3 TeV, taken from [30]. . . . .	27
3.4.	Ideal W/Z separation as a function of jet mass resolution obtained using a Gaussian smearing of Breit-Wigner distribution, taken from [2]. . . . .	29
3.5.	The longitudinal cross section of top quadrant of the ILD, taken from [29]. From interaction point (IP) outwards, there are a tracking system comprising a large time projection chamber (TPC) augmented with silicon tungsten layer, highly granular electromagnetic calorimeters (ECAL) and hadronic calorimeters (HCAL), forward calorimeters (FCAL), magnetic coils, and muon chambers/iron yokes. The dimensions are in units of mm. . . . .	32
3.6.	Mechanical support structure of ILD vertex detector, taken from [35]. . . . .	34
3.7.	a) A top quadrant view of the ILD silicon envelope system, SIT, SET, ETD, and ETD, with TPC, ECAL, and HCAL, and b) a 3D detailed GEANT 4 simulation description of the silicon system as sketched in the quadrant view in a). Both plots are adapted from figures in [35]. . . . .	35

3.8. a) The electromagnetic calorimeter (in blue) within the ILD detector. b) A cross section through the electromagnetic calorimeter layers. Both plots are taken from [35]. . . . .	37
3.9. The schematic view of a CALICE analogue HCAL technological prototype module, taken from [29]. . . . .	38
3.10. Sensitive layers of the ILD muon system, taken from [29]. . . . .	39
3.11. The forward calorimeters of the ILD. . . . .	39
3.12. Impact parameter resolution of the ILD vertex detector for two different particle production angles ( $20^\circ$ and $85^\circ$ ), assuming the baseline point resolution given in table 3.3 for CMOS option (solid line), and the FPCCD option (dotted line). The curves with long dashes show the performance goal. The figure is taken from [35]. . . . .	40
3.13. The single jet energy resolution as a function of the number of longitudinal ECAL layers, with different total jet energy using $e^+e^- \rightarrow Z'Z'$ , where $Z' \rightarrow u\bar{u}/d\bar{d}/s\bar{s}$ sample at barrel region, taken from [35]. . . . .	41
3.14. The single jet energy resolution as a function of the hadronic calorimeter scintillator cell sizes, with different total jet energy using $e^+e^- \rightarrow Z'Z'$ , where $Z' \rightarrow u\bar{u}/d\bar{d}/s\bar{s}$ sample at barrel region, taken from [29]. . . . .	42
3.15. The longitudinal cross section of top quadrant the CLIC_ILD, taken from and [2]. For both plots, from interaction point (IP) outwards, there is a tracking system comprising a large time projection chamber (TPC) augmented with silicon tungsten layer, highly granular electromagnetic calorimeters (ECAL) and hadronic calorimeters (HCAL), forward calorimeters (FCAL), magnetic coils, and muon chambers/iron yokes. . . . .	43
4.1. Illustration of the cone based clustering algorithm, taken from [58] . . . . .	49
4.2. Illustration of the clustering algorithm used in the PandoraPFA, taken from [58] . . . . .	50
4.3. Topological association in the PandoraPFA. . . . .	51
4.4. Illustration of the re-clustering algorithm in PandoraPFA . . . . .	52
4.5. Effect of the suppression of the background with the tight PFO selection. . . . .	56

4.6. Example of model efficiency as function of the model complexity. Here the model is a boosted decision tree. The model parameter reflecting the model complexity is the depth of tree. The y-axis is the signal efficiency when the background efficiency is 1%. From the tree depth of six onwards, overfitting occurs. . . . .	62
4.7. Example of a decision tree. . . . .	65
5.1. Simulated longitudinal electromagnetic shower profile as a function of depth for electrons and photons. . . . .	73
5.2. A flow diagram of the PHOTON RECONSTRUCTION algorithm. . . . .	75
5.3. Example of projecting a large photon cluster containing two photons. . .	76
5.4. Flow chart for 2D PEAK FINDING algorithm neutral cluster variant. .	78
5.5. Flow chart for 2D PEAK FINDING algorithm. . . . .	82
5.6. Distributions for a) the start layer from the longitudinal shower profile ( $t_0$ ), b) the fractional difference of the observed shower profile to the expected EM shower profile ( $\delta l$ ), c) the energy weighted root-mean-squared distance of all bins in a SHOWER PEAK to its peak bin ( $\langle w \rangle$ ), and d) the distance between the photon candidate and the closest track projection in the front of the ECAL ( $d$ ) are shown. All plots are normalised that the area under curve is 1. The particle ID is determined using the truth information. All plots are generated with simulated 250 GeV $Z' \rightarrow u\bar{u}/d\bar{d}/s\bar{s}$ . . . . .	85
5.7. An event display of a typical 10 GeV photon shown in a), reconstructed into a main photon shown in b), and a photon fragment shown in c). . . . .	86
5.8. Illustration of distance metric, $d$ . . . . .	88
5.9. An event display of a typical 500 GeV photon, reconstructed into a main photon in the ECAL (yellow) and a neutral hadron fragment in the HCAL (blue). . . . .	92
5.10. Average number of photons using two photons of 500 and 50 GeV per event sample. . . . .	97
5.11. Jet energy resolution as a function of the total jet energy without and with photon related algorithms . . . . .	98

5.12. Average number of reconstructed photons and reconstructed particles, as a function of their true energy using single photon sample. . . . .	100
5.13. Average number of reconstructed photons and reconstructed particles, as a function of the MC distance separation. . . . .	100
5.14. Average fraction fragments energies of the total energy, as a function of the MC distance separation . . . . .	101
5.15. Jet energy resolution as a function of the di-jet energy . . . . .	102
5.16. Average number of photons, as a function of the MC distance separation for different algorithms combinations. . . . .	104
5.17. Single photon reconstruction efficiency as a function of energy. . . . .	105
5.18. Average numbers of photon (blue) and particle (orange), as a function of the Monte Carlo distance separation between the photon pair, using two photons of 500 and 50 GeV per event sample. . . . .	106
5.19. Average numbers of reconstructed photon for four different photon pairs: 500 - 50 GeV (blue), 500 - 500 GeV (orange), 100 - 10 GeV (green), and 10 - 10 GeV (red), as a function of the Monte Carlo distance separation between the photon pair. . . . .	107
6.1. An example event display of a simulated $e^+e^- \rightarrow \tau^+\tau^-$ event using the ILD detector model. The top half of the event is a tau lepton decaying into $\pi^-\pi^0\nu_\tau$ final state and the bottom half of the event is a tau lepton decaying into $\pi^+\pi^-\pi^-\pi^0\nu_\tau$ final state. The purple lines are the tracks left by $\pi^\pm$ in the tracking detectors. The purple clusters are the calorimeter hits of $\pi^\pm$ . And the yellow clusters are the calorimeter hits of photon from $\pi^0 \rightarrow \gamma\gamma$ . The blue region is the transverse cross section of the ECAL barrel part along the beam line direction. . . . .	112
6.2. Distribution for a) the number of charged particle ( $N_{\chi^+}$ ); b) the number of photons ( $N_\gamma$ ); c) the invariant mass of all non-neutrino decay products ( $m_{vis}$ ); and d) the invariant mass of the $a_1$ , reconstructed with $a_1(\pi^-\pi^0\pi^0)$ hypothesis. Area under the curve for each decay mode is normalised to 1. Decay modes in all plots are selected using the truth information. . . . .	118

6.3. The correct classification efficiency for tau hadronic decay final states as a function of the ECAL square cell sizes . . . . .	124
6.4. The tau hadronic decay efficiency as a function of the ECAL cell sizes at different $\sqrt{s}$ with the ILD detector model. . . . .	125
6.5. Two-dimensional histograms of $E_{\pi^+}/E\tau^+$ as a function of $E_{\pi^-}/E\tau^-$ obtained with $Z \rightarrow \tau^+\tau^-$ channel , selecting $\tau^- \rightarrow \pi^-\nu_\tau$ decay mode for both taus, for a) Monte Carlo particles, and b) simulated and reconstructed particles. . . . .	131
7.1. The main Feynman diagrams for the leading-order $e^+e^- \rightarrow HH\nu_e\bar{\nu}_e$ processes at CLIC. . . . .	134
7.2. Distributions shown for $p_T$ of identified electrons after $E$ and $r_0$ cuts, for a) $HH \rightarrow b\bar{b}W^+W^- \rightarrow b\bar{b}qqqq$ signal channel; and b) $e^+e^- \rightarrow qqqq\ell\nu$ background channel. Distributions shown for $23\text{ GeV}^{\frac{1}{2}} \times \sqrt{E_{cone1}} + 5\text{ GeV}$ as a function of $E$ after $E$ and $r_0$ cuts, for c) $HH \rightarrow b\bar{b}W^+W^- \rightarrow b\bar{b}qqqq$ signal channel; and d) $e^+e^- \rightarrow qqqq\ell\nu$ background channel. . . . .	140
7.3. Distributions to show isolation criterion. a) Distribution of $p_{Tcone}$ for isolation criteria 1 after $N_{cone1} = 0$ ; b) distribution of $r_0$ for isolation criteria 2 after $N_{X^+} = 1$ , $N_{cone1} = 1$ ; and c) distribution of $p_{Tcone}$ for isolation criteria 3 after $N_{X^+} = 3$ , $N_{cone1} = 1$ , $\theta_S < \cos^{-1}(0.9995)$ . . . . .	143
7.4. BeamCAL and LumiCAL electron tagging efficiency. . . . .	146
7.5. Example MC mass fit for jet optimisation in double Higgs analysis . . . . .	149
7.6. Fitted mass, and resolution of $H_{bb}$ , $H_{WW^*}$ and $W$ at $\sqrt{s} = 1.4\text{ TeV}$ . . . . .	151
7.7. Fitted mass peak positions and relative mass resolution of $H_{bb}$ , $H_{WW^*}$ and $W$ at $\sqrt{s} = 3\text{ TeV}$ . . . . .	152
7.8. Performance of b-jet tagging with $e^+e^- \rightarrow Z\nu\nu$ samples, where $Z$ decays to $b\bar{b}$ , $c\bar{c}$ , or $u\bar{u}/d\bar{d}/s\bar{s}$ at a) $\sqrt{s} = 1.4\text{ TeV}$ , and b) $\sqrt{s} = 3\text{ TeV}$ . . . . .	154
7.9. The distribution of the highest b-jet value for the $HH \rightarrow b\bar{b}W^+W^- \rightarrow b\bar{b}qqqq$ events at $\sqrt{s} = 1.4\text{ TeV}$ . Area under the curve is normalised to 1. . . . .	155
7.10. Sum of b-jet tag values as a function of $-\log(y_{34})$ at $\sqrt{s} = 1.4\text{ TeV}$ . . . . .	156

7.11. The distribution of $m_{H_{bb}}$ for a) the signal channel, hadronic $W^+W^-$ decay of $HH \rightarrow b\bar{b}W^+W^-$ , and b) the sum of all background channels normalised to the respective cross sections. The area under the curve is normalised to 1. All plots are shown for $\sqrt{s} = 1.4$ TeV. . . . .	159
7.12. Distributions of the invariant mass of the two Higgs system for $\sqrt{s} = 1.4$ TeV, assuming an intergraded luminosity of $1500 \text{ fb}^{-1}$ . . . . .	160
7.13. Distributions of the second highest b-jet tag value for $\sqrt{s} = 1.4$ TeV, assuming an intergraded luminosity of $1500 \text{ fb}^{-1}$ . . . . .	161
7.14. Distributions of the transverse momentum of the two Higgs system for $\sqrt{s} = 1.4$ TeV, assuming an intergraded luminosity of $1500 \text{ fb}^{-1}$ . . . . .	162
7.15. Distributions of the four variables with highest discriminating power: a) the invariant mass of $H_{bb}$ , b) the invariant mas of $H_{WW^*}$ , c) the acolinearity of the two jets associated with $H_{bb}$ , and d) the opening angles of the two jets associated with $H_{bb}$ in the decay rest frame of the $H_{bb}$ . All plots assumes an intergraded luminosity of $1500 \text{ fb}^{-1}$ at $\sqrt{s} = 1.4$ TeV after all pre-selection cuts applied before the MVA. . . . .	168
7.16. Sum of b-jet tag as a function of $y_{34}$ at $\sqrt{s} = 3$ TeV . . . . .	173
7.17. Distributions of the invariant mass of the two Higgs system for $\sqrt{s} = 3$ TeV, assuming an intergraded luminosity of $2000 \text{ fb}^{-1}$ . . . . .	174
7.18. Distributions of the highest b-jet tag value for $\sqrt{s} = 3$ TeV, assuming an intergraded luminosity of $2000 \text{ fb}^{-1}$ . . . . .	175
7.19. Cross section for the $e^+e^- \rightarrow HH\nu_e\bar{\nu}_e$ process as a function of the ratio $\lambda/\lambda_{SM}$ . . . . .	181
7.20. Normalised cross section for the $e^+e^- \rightarrow HH\nu_e\bar{\nu}_e$ process as a function of the $g_{HHH}/g_{HHHSM}$ and $g_{WWHH}/g_{WWHHS}$ at $\sqrt{s} = 3$ TeV. . . . .	183
7.21. The significance for the $e^+e^- \rightarrow HH\nu_e\bar{\nu}_e$ process as a function of the $g_{HHH}/g_{HHHSM}$ and $g_{WWHH}/g_{WWHHS}$ at $\sqrt{s} = 3$ TeV, using sub-channel hadronic $W^+W^-$ decay of $HH \rightarrow b\bar{b}W^+W^-$ , assuming an integrated luminosity of $3000 \text{ fb}^{-1}$ . . . . .	184
7.22. $\chi^2$ as a function of $g_{HHH}/g_{HHHSM}$ and $g_{WWHH}/g_{WWHHS}$ at $\sqrt{s} = 3$ TeV .	185

7.23. Normalised $\chi^2$ , after averaging the toy MC experiments, as a function of $g_{\text{HHH}}/g_{\text{HHHSM}}$ and $g_{\text{WWHH}}/g_{\text{WWHHS}}$ , combining hadronic decay $\text{HH} \rightarrow b\bar{b}W^+W^-$ and $\text{HH} \rightarrow b\bar{b}b\bar{b}$ sub-channels, assuming an integrated luminosity of $3000 \text{ fb}^{-1}$ . . . . .	186
7.24. Contour plot of 68% confidence ( $\chi^2 = 2.3$ ) , after averaging the toy MC experiments, as a function of $g_{\text{HHH}}/g_{\text{HHHSM}}$ and $g_{\text{WWHH}}/g_{\text{WWHHS}}$ , combining hadronic $W^+W^-$ decay of $\text{HH} \rightarrow b\bar{b}W^+W^-$ and $\text{HH} \rightarrow b\bar{b}b\bar{b}$ sub-channels, assuming an integrated luminosity of $3000 \text{ fb}^{-1}$ . . . . .	187



# List of Tables

2.1. Masses, spins, and charges of fundamental bosons in the SM. Values are taken from [6]. . . . .	6
2.2. Masses and charges of the fundamental fermions in the SM. All fermions are spin- $\frac{1}{2}$ particles. For each fermion in the SM, there is an anti-fermion with the same mass and spin, but opposite charge. Neutrinos are known to have non-zero mass from the observation of neutrino flavour oscillations. The upper bound on the neutrino mass is 2 eV. For the top quark mass, the statistical uncertainties is listed first, followed by systematic uncertainties. Values are taken from [6]. . . . .	7
2.3. Decay modes, final state particles and branching ratios of the seven major $\tau^-$ decays. . . . .	21
3.1. Contributions from the different particle components to the jet energy resolutions (all energies in GeV). The table lists the approximate fractions of charged particles, photons, and neutral hadrons in a jet of energy $E_j$ , and the assumed single particle energy resolutions. The table is adapted from [34]. . . . .	31
3.2. A comparison of key parameters of the ILD and CLIC_ILD detector concepts. . . . .	33
3.3. Key parameters for vertex detector in the ILC. The spatial resolution ( $\sigma$ ) and readout times are for the CMOS option. The table is adapted from [35]. . . . .	34
3.4. Main parameters of the central silicon systems (SIT, SET, and ETD) and the TPC. The table is adapted from [35]. . . . .	36
3.5. Comparison of the LumiCAL and the BeamCAL at the ILD and the CLIC_ILD. . . . .	40

4.1.	Luminosity ratio for processes with initial-state photons from Beamstrahlung.	54
4.2.	Masses of quarks and bosons used for generating Standard Model samples.	56
4.3.	The attribute of the PhD student class for the decision tree example shown in figure 4.7. . . . .	65
4.4.	The attribute of the undergraduates class for the decision tree example shown in figure 4.7. . . . .	66
5.1.	List of variables for the likelihood based photon ID test. . . . .	84
5.2.	The cuts for photon fragment removal algorithm in the ECAL. . . . .	90
5.3.	The cuts for photon fragment removal algorithm in the ECAL. . . . .	91
5.4.	Cuts for merging high energy photon fragment in the HCAL. . . . .	94
5.5.	Cuts for splitting photons. . . . .	95
5.6.	Photon confusion as a function of energy for reconstruction with and without photon algorithms. . . . .	99
6.1.	Decay modes, detectable final state particles and branching ratios of the seven major $\tau^-$ decays. . . . .	112
6.2.	Pre-selection cuts for tau lepton decay final state classification. . . . .	114
6.3.	The table shows the fraction of fraction of events passing successive cuts: no photon conversion in the tracking detector; total energy of non-neutrino decay products $> 5 \text{ GeV}$ ; and $0.6 >  \theta_{Z,MC}  > 0.3$ or $1.57 >  \theta_{Z,MC}  > 0.8$ . All cuts are based on the truth information. . . . .	114
6.4.	Variables used in the MVA classification for the tau lepton decay mode classification. . . . .	119
6.5.	Optimised parameters for the Boosted Decision Tree with Gradient boost multiclass classifier. See section 4.8.8 for a detailed explanation of variables.	120
6.6.	Classification efficiency for tau decay modes. . . . .	121
6.7.	Optimised parameters of PHOTONFRAGMENTREMOVAL algorithm as a function of the ECAL square cell size. . . . .	122

6.8. Optimised parameters of the modified ISOLATEDTAUIDENTIFIER . . . . .	127
7.1. Signal and background samples with the corresponding cross sections at $\sqrt{s} = 1.4 \text{ TeV}$ . . . . .	137
7.2. Optimised parameters for the ISOLATEDLEPTONFINDER processor . . . . .	138
7.3. Optimised parameters for ISOLATEDLEPTONIDENTIFIER . . . . .	141
7.4. Optimised parameters for the TAUFINDER processor . . . . .	142
7.5. Optimised parameters of ISOLATEDTAUIDENTIFIER processor . . . . .	144
7.6. The performances of the lepton finding algorithms for the signal events and selected background events at $\sqrt{s} = 1.4 \text{ TeV}$ . Numbers represent the fractions of events where no leptons are identified by the individual lepton finder . . . . .	146
7.7. The performances of the lepton finding algorithms for the signal events and selected background events at $\sqrt{s} = 3 \text{ TeV}$ . Numbers represent the fractions of events where no leptons are identified by the individual lepton finder . . . . .	147
7.8. The fitted mass parameters of optimal jet reconstruction at $\sqrt{s} = 1.4 \text{ TeV}$	150
7.9. The table show the expected number of events, before cuts and after successive cuts: the lepton veto, $\text{HH} \rightarrow b\bar{b}W^+W^-/\text{HH} \rightarrow b\bar{b}b\bar{b}$ separation, and valid jet pairing, for the signal and background events at $\sqrt{s} = 1.4 \text{ TeV}$ , assuming an integrated luminosity of $1500 \text{ fb}^{-1}$ . q can be u, d, s, b or t. Unless specified, q, $\ell$ and $\nu$ represent either particles or the corresponding anti-particles . . . . .	158
7.10. List of signal and background samples after pre-selection cuts at $\sqrt{s} = 1.4 \text{ TeV}$ . . . . .	163
7.11. Variables used in the MVA event selection for $\sqrt{s} = 1.4 \text{ TeV}$ . . . . .	167
7.12. Optimised parameters for the boosted decision tree classifier used in the MVA event selection. See section 4.8.8 for detailed explanations of variables.	170
7.13. Selection efficiency and number of events for signal and background at $\sqrt{s} = 1.4 \text{ TeV}$ . . . . .	171

7.14. Cross sections of samples at $\sqrt{s} = 3 \text{ TeV}$ . . . . .	172
7.15. List of signal and background selection efficiencies and event numbers after MVA application at $\sqrt{s} = 3 \text{ TeV}$ . . . . .	176
7.16. Variables used in the MVA event selection for the semi-leptonic $W^+W^-$ decay of $HH \rightarrow b\bar{b}W^+W^-$ analysis at $\sqrt{s} = 3 \text{ TeV}$ . . . . .	178
7.17. List of signal and background events with selection efficiency and number of events at $\sqrt{s} = 3 \text{ TeV}$ for semi-leptonic $W^+W^-$ decay of $HH \rightarrow b\bar{b}W^+W^-$ analysis , assuming a luminosity of $2000 \text{ fb}^{-1}$ . The number of events ( $N$ ), the selection efficiencies of pre-selection cuts ( $\varepsilon_{\text{presel}}$ ), the selection efficiencies of MVA after pre-selection cuts ( $\varepsilon_{\text{MVA}}$ ), and the number of events after MVA ( $N_{\text{MVA}}$ ) are shown. - represents a number less than 0.01. q can be u, d, s, b or t. Unless specified, q, $\ell$ and $\nu$ represent either particles or the corresponding anti-particles. $\gamma$ (BS) represents a real photon from beamstrahlung (BS). $\gamma$ (EPA) represents a “quasi-real” photon, simulated with the Equivalent Photon Approximation. . . . .	179
7.18. Number of signal and background events, and significance after MVA for all $HH \rightarrow b\bar{b}W^+W^-$ analyses. . . . .	180
A.1. The table shows the expected number of events, before cuts and after successive cuts: the lepton veto, $HH \rightarrow b\bar{b}W^+W^-/HH \rightarrow b\bar{b}b\bar{b}$ separation, and valid jet pairing, for the signal and background events at $\sqrt{s} = 3 \text{ TeV}$ , assuming an integrated luminosity of $2000 \text{ fb}^{-1}$ . q can be u, d, s, b or t. Unless specified, q, $\ell$ and $\nu$ represent either particles or the corresponding anti-particles. . . . .	192
A.2. The table shows the expected number of events after successive cuts: invariant mass of the two Higgs system $> 150 \text{ GeV}$ , and the highest b-jet tag value $> 0.7$ . All cuts include the lepton veto, $HH \rightarrow b\bar{b}W^+W^-/HH \rightarrow b\bar{b}b\bar{b}$ separation, and valid jet pairing. The table shows for the signal and background events at $\sqrt{s} = 3 \text{ TeV}$ , assuming an integrated luminosity of $2000 \text{ fb}^{-1}$ . q can be u, d, s, b or t. Unless specified, q, $\ell$ and $\nu$ represent either particles or the corresponding anti-particles. . . . .	193